Alma Mater Studiorum – Università di Bologna
Technische Universität Dortmund

Search for same-sign top quark pairs with the ATLAS detector at the LHC

Noemi Cavalli

PhD Coordinator:
Prof. Michele Cicoli

Supervisors:
Chiar.mo Prof. Maximiliano Sioli
Prof. Dr. Kevin A. Kröninger

Co-supervisor:
Dr. Matteo Negrini

2023

Abstract

In this thesis, a search for same-sign top quark pairs produced according to the Standard Model Effective Field Theory (SMEFT) is presented. The analysis is carried out within the ATLAS Collaboration using collision data at a center-of-mass energy of $\sqrt{s} = 13$ TeV, collected by the ATLAS detector during the Run 2 of the Large Hadron Collider, corresponding to an integrated luminosity of 140 fb^{-1}. Three SMEFT operators are considered in the analysis, namely $\mathcal{O}_{RR}$, $\mathcal{O}_{LR}^{(1)}$, and $\mathcal{O}_{LR}^{(8)}$. The signal associated to same-sign top pairs is searched in the dilepton channel, with the top quarks decaying via $t \longrightarrow W^+ b \longrightarrow \ell^+ \nu b$, leading to a final state signature composed of a pair of high-transverse momentum same-sign leptons and b-jets. Deep Neural Networks are employed in the analysis to enhance sensitivity to the different SMEFT operators and to perform signal-background discrimination. No significant excess with respect to the Standard Model predictions is observed, therefore upper limits are placed on the signal production cross section and on the Wilson Coefficients associated to the considered EFT operators. The observed upper limit at 95% of confidence level on same sign top pairs production cross section times Branching Ratio is 0.86 fb. The observed upper limits at 95% of confidence level on the SMEFT parameters are 0.005, 0.015 and 0.031 ([TeV/Λ]^2) for the Wilson Coefficients associated to $\mathcal{O}_{RR}$, $\mathcal{O}_{LR}^{(1)}$ and $\mathcal{O}_{LR}^{(8)}$ respectively. This is the first result of the ATLAS Collaboration concerning the search for same-sign top quark pairs production in proton-proton collision data at $\sqrt{s} = 13$ TeV, in the framework of the SMEFT.

Contents

Introduction

The field of particle physics aims to unveil the fundamental laws that govern the Universe at microscopic level. The Standard Model (SM) of particle physics serves as a framework for describing the interactions between elementary particles and for making predictions that can be tested at particle accelerator experiments. Over the course of the last century, the predictive power of the Standard Model has been confirmed through a multitude of experimental measurements, which have increasingly verified the theory with a higher degree of precision. However, experimental evidences related to phenomena that do not find a proper explanation within the SM have been found, unveiling the limits of the theory and therefore paving the way to new physics searches and theories Beyond the Standard Model (BSM). Various models have been proposed to extend the Standard Model. These BSM theories often predict the existence of new particles with masses around 1 TeV, that could be probed at the Large Hadron Collider experiments.

Currently, the Large Hadron Collider (LHC) at CERN in Geneva, Switzerland, is the largest and most powerful particle accelerator in operation, designed to accelerate and collide proton beams to energies up to about 14 TeV. Four main particle physics detectors are located at the interaction points of the LHC accelerating ring, performing measurements that confirm Standard Model predictions to an unprecedented level of precision. Among these, the ATLAS ("A Toroidal LHC ApparatuS") experiment uses a multi-purpose detector designed to measure the products of proton-proton interactions with exceptional accuracy. The high precision of measurements carried out within the ATLAS Collaboration allows the confirmation of SM predictions as well as the search for signatures related to new physics phenomena. New particles predicted by BSM theories can be directly searched for at the ATLAS experiment, assuming their mass values would lie within the LHC energy reach ($\sim$ TeV). On the other hand, if the new particles were too heavy to be directly probed at the LHC, signals related to BSM theories could be searched for indirectly, looking for deviations with respect to Standard Model predictions. While direct searches mostly rely on specific model assumptions to predict new particles and therefore new signatures to be probed, indirect searches can also adopt a model

independent approach through the Standard Model Effective Field Theory (SMEFT). Within the SMEFT, the Standard Model is assumed to be a low energy approximation to a more fundamental theory. SM predictions are therefore assumed to be valid up to the new physics energy scale, that would lie outside the experimental energy reach. Possible deviations from SM predictions can therefore be interpreted using the SMEFT framework. Furthermore, new physics phenomena either forbidden or highly suppressed within the SM could be directly explored in analyses using the SMEFT.

The analysis presented in this document is a search for same-sign top quark pairs produced according to the SMEFT. Due to its large mass with respect to the other SM fermions, the top quark is of particular interest, since it is closely linked to the Higgs boson and to the mechanism responsible for generating the masses of SM particles, known as the Higgs mechanism. The production of same-sign top pairs is highly suppressed within the SM, therefore evidence related to the process searched for in this analysis would directly point towards the existence of a more fundamental underlying theory. The same-sign top pairs search is carried out within the ATLAS Collaboration, using the collision data at a center-of-mass energy of $\sqrt{s} = 13$ TeV collected by the detector during the LHC Run 2 (from 2015 to 2018), corresponding to an integrated luminosity of 140 fb^{-1}.

Same-sign top pairs, generated within the SMEFT via a four-fermion pointlike interaction, are searched for in the dilepton channel, with the top quarks decaying leptonically according to $t \longrightarrow W^+ b \longrightarrow \ell^+ \nu b$. Same-sign top pairs generated by three different dim-6 EFT operators are considered in the analysis. The Warsaw basis is employed for the operator definition. Although the final state associated to the searched signal is rarely produced in SM processes, background events may arise from detector inefficiencies as well as from the mis-reconstruction of physics objects.

Several mutually exclusive analysis regions are defined in order to be enriched in either signal or background events. The expected background contributions in the selected collision data are estimated employing different techniques, based on both simulation and data. The extraction of the signal is performed through a statistical maximum likelihood fit performed on the full Run 2 dataset. Different sources of systematic uncertainties affecting the measurement are taken into account in the analysis. A first Deep Neural Network (DNN) is employed to build regions sensitive to same-sign top pairs generated by different EFT operators. A second DNN is subsequently employed to perform the signal-background discrimination. In the absence of any deviations from the Standard Model predictions, exclusion limits on the parameters associated with the three EFT considered operators are derived. This is the first search for same-sign top pairs carried out within the ATLAS Collaboration using the Standard Model Effective Field Theory

and proton-proton collision data at $\sqrt{s} = 13$ TeV.

The document is organized as follows. A brief summary of the Standard Model is presented in Chapter 1, while the Standard Model Effective Field Theory is described in Chapter 2. Details concerning the same-sign top pairs production within the SMEFT are reported in Chapter 3. An overview of the ATLAS experiment is presented in Chapter 4. Finally, the search for same-sign top pairs is reported in detail in Chapter 5. Auxiliary material related to the analysis can be found in Appendix C, D, E and F. The analysis reported in this document shares some common features with another search carried out within the ATLAS Collaboration by researchers belonging to the analysis team. Therefore, a brief description of this reference analysis is reported in Appendix A. Finally, additional research activity carried out on muon reconstruction and muon momentum calibration is described in Appendix B.

The analysis reported in this document has been carried out together with ATLAS Collaboration members affiliated with the Università di Bologna - Alma Mater Studiorum, the Technische Universität Dortmund, the Institut de Física d'Altes Energies (IFAE) and CERN. I am the main analyst for the work presented in this thesis and I am co-leading the ATLAS analysis team involved. Specifically, my personal contribution to the analysis concerns the definition and optimization of the analysis strategy as well as its development. I worked on the generation of the EFT signal samples, reported in Section 5.1.1, and on the definition of the analysis regions enriched in signal events, reported in Section 5.2.8 and 5.4. I performed the statistical analysis described in Section 5.7 whose results are presented in Section 5.8. I contributed to the definition and development of the NN-based strategy. The definition of the regions enriched in background events as well as the strategy employed to estimate the background contributions in the selected collision data, described in Section 5.5, has been originally developed for another analysis carried out within the ATLAS Collaboration to which I contributed to a lesser extent. This analysis involved the team members from IFAE and CERN and is summarized in Appendix A.

Chapter 1

The Standard Model of particle physics

Modern particle physics is outlined by the Standard Model of particle physics (SM), which gathers together relativistic quantum field theories that describe the interactions among elementary particles. Nowadays, SM predictions are still confirmed with experimental measurements carried out at particle accelerators experiments, which increasingly corroborate the validity of the theory with a higher degree of precision[1]. The SM is invariant under Lorentz transformations as well as $\mathrm{SU(3)}_C \times \mathrm{SU(2)}_L \times \mathrm{U(1)}_Y$ gauge transformations. The three gauge groups are related to the strong and electroweak interactions. The SM particle and interaction content is summarized in Section 1.1 and Section 1.2.

1.1 Quarks and leptons

Elementary particles that make up physical matter are described within the SM by fermionic fields. These are spin 1/2 particles classified as either quarks or leptons. Quarks exist within the SM in six different *flavors* (u, d, c, s, t, b) and are classified into three generations:

$$\begin{pmatrix} u \\ d \end{pmatrix} \quad \begin{pmatrix} c \\ s \end{pmatrix} \quad \begin{pmatrix} t \\ b \end{pmatrix} \tag{1.1}$$

Each generation contains one positive $(Q/|e| = +2/3)$ and one negative $(Q/|e| = -1/3)$ particle, where e is the electric charge of the electron. Specifically, u, c, t and d, s, b are

---

[1]However, some experimental evidences do not find a proper explanation within the SM, as reported in Section 1.4

positive and negative particles respectively. Quarks are also strongly interacting, since they carry a color charge (*red, green* or *blue*). They have quantum numbers related to the $SU(2)_L$ and $U(1)_Y$ gauge groups, that are the weak isospin I and hypercharge Y. These numbers are related to the electric charge as $Q = I_3 + Y/2$, being I_3 the third component of the weak isospin[2]. Specifically, left-handed and right-handed chiral components of quarks have $I = 1/2$ and $I = 0$ respectively, therefore left-handed quarks are gathered in weak isospin doublets $q_L = (u_L \ d_L)$, $(c_L \ s_L)$, $(t_L \ b_L)$ with the third isospin component $I_3 = +1/2, -1/2$ for u_L, c_L, t_L and d_L, s_L, b_L respectively. Right-handed quarks are instead weak isospin singlets $u_R, d_R, c_R, s_R, t_R, b_R$.

Together with quarks, other fermionic particles called leptons exist within the SM. There are six different lepton flavors $(e, \mu, \tau, \nu_e, \nu_\mu, \nu_\tau)$, arranged into three generations as follows:

$$\begin{pmatrix} \nu_e \\ e \end{pmatrix} \quad \begin{pmatrix} \nu_\mu \\ \mu \end{pmatrix} \quad \begin{pmatrix} \nu_\tau \\ \tau \end{pmatrix} \tag{1.2}$$

Each generation is composed by one neutral $(Q = 0)$ and one negative $(Q = -1)$ particle, with ν_e, ν_μ, ν_τ and e, μ, τ being neutral and negative respectively. Leptons are not charged under the strong interaction but, similarly to quarks, they are arranged into left-handed weak isospin doublets $l_L = (\nu_{eL} \ e_L)$, $(\nu_{\mu L} \ \mu_L)$, $(\nu_{\tau L} \ \tau_L)$ and right-handed singlets e_R, μ_R, τ_R[3].

In addition to the particles described above, the SM particle content includes anti-particles, that have opposite quantum numbers with respect to the ones associated to the fermions already presented. Leptons and quarks also carry a lepton L and baryon B number respectively. A Baryon number $B = 1/3, -1/3$ is associated to quarks and anti-quarks, since baryons are composed by either three quarks or three anti-quarks. Leptons and anti-leptons have respectively lepton number $L = 1, -1$. Although lepton and baryon numbers are not related to specific symmetries of the SM theory, they are conserved quantities in all SM interactions.

1.2 Standard Model interactions

Interactions among quarks and leptons are described within the SM by the exchange of vector bosons (spin 1 elementary particles) associated to the strong, weak and electromagnetic forces.

---

[2]The particle electric charge $Q/|e|$ from now on is referred as Q, by omitting the electron charge e for simplicity.

[3]It should be noted that right-handed neutrinos ν_R are neutral under all interactions described by the SM.

Electromagnetic interactions are described within the SM by the Quantum Electrodynamics (QED) and involve all electrically charged particles. According to QED, electromagnetic interactions are invariant under local U(1) gauge transformations and they conserve the electric charge Q. These interactions are described by the exchange of a photon γ, that is the massless neutral boson associated to electromagnetic interactions.

Quantum Chromodynamics (QCD) is the quantum field theory that describes the strong interaction, that is invariant under the $\mathrm{SU}(3)_C$ gauge symmetry. Strong interactions are described by the exchange of one among eight different massless neutral gluons g. These bosons carry different color-charges and they can interact with quarks as well as among themselves.

Weak interactions exhibit several differences with respect to both electromagnetic and strong forces. These interactions are mediated by massive gauge bosons, Z or $W^{\pm}$, with electric charge $Q = 0$ and $Q = \pm 1$ respectively. Furthermore, weak processes can violate parity and flavor conservation, while these characteristics are conserved by other SM interactions. Weak interactions respect the $\mathrm{SU}(2)_L \times \mathrm{U}(1)_Y$ gauge symmetry, unifying electromagnetic and weak forces within the electroweak (EW) gauge theory. Weak interactions only involve left-handed fermions (or right-handed anti-fermions) when mediated by the $W^{\pm}$ boson, while the Z boson can also interact with right-handed fermions.

All massive particles of the SM, from fermions to W, Z bosons, acquire mass following the Spontaneous Symmetry Breaking (SSB) of the EW symmetry though the Brout-Englert-Higgs mechanism. This is realized though the introduction of a scalar (spin 0) $\mathrm{SU}(2)_L$ doublet $\Phi = (\Phi^+ \Phi^0)$, called the Higgs doublet. After acquiring a *"vacuum expectation value"* (v.e.v.) $v = 246$ GeV, the Higgs field Φ leads to the breaking of the EW $\mathrm{SU}(2)_L$ and $\mathrm{U}(1)_Y$ symmetries. As a consequence of the SSB, the EW bosons as well as the Higgs boson h itself acquire masses. Fermion masses arise from the interaction between fermions and the Higgs boson through Yukawa couplings.

The entirety of SM interactions can be described by the following Lagrangian [1–3]:

$$
\begin{aligned}
\mathcal{L}_{\mathrm{SM}} = &-\frac{1}{4} B_{\mu\nu} B^{\mu\nu} - \frac{1}{4} W^I_{\mu\nu} W^{I\mu\nu} - \frac{1}{4} G^A_{\mu\nu} G^{A\mu\nu} \\
&+ i \left(\bar{u}_{\mathrm{R}} \slashed{D} u_{\mathrm{R}} + \bar{d}_{\mathrm{R}} \slashed{D} d_{\mathrm{R}} + \bar{e}_{\mathrm{R}} \slashed{D} e_{\mathrm{R}} \right) \\
&+ i \left(\bar{l}_{\mathrm{L}} \slashed{D} l_{\mathrm{L}} + \bar{q}_{\mathrm{L}} \slashed{D} q_{\mathrm{L}} \right) \\
&+ \left(D_\mu \phi \right)^\dagger \left(D^\mu \phi \right) + \mu^2 \phi^\dagger \phi - \lambda \left(\phi^\dagger \phi \right)^2 \\
&- \left(Y^u \bar{q}_{\mathrm{L}} \tilde{\phi} u_{\mathrm{R}} + Y^d \bar{q}_{\mathrm{L}} \phi d_{\mathrm{R}} + Y^e \bar{l}_{\mathrm{L}} \phi e_{\mathrm{R}} + \text{ h.c. } \right)
\end{aligned}
\tag{1.3}
$$

Here, the first line gathers the gauge kinetic terms related to the strong and electroweak interactions. The gauge field strength tensors $B_{\mu\nu}, W^I_{\mu\nu}, G^A_{\mu\nu}$ are related to the $\mathrm{U}(1)_Y$, $\mathrm{SU}(2)_L$ and $\mathrm{SU}(3)_C$ gauge groups respectively (I and A being the $\mathrm{SU}(2)_L$ and $\mathrm{SU}(3)_C$ related indices). The fermionic kinetic terms are given by the second and third lines in (1.3). Here, l_L and q_L are the $\mathrm{SU}(2)_L$ lepton and quark left-handed doublets, while the right-handed $\mathrm{SU}(2)_L$ singlets are u_R, d_R, e_R. These terms are assumed to be summed over the three fermion generations and also over different colors for quarks. The covariant derivative is denoted as D_μ. Finally, the last two lines in (1.3) are related to the Higgs field, with Φ being the $\mathrm{SU}(2)_L$ Higgs doublet and Y^i the matrices of Yukawa coupling constants that confer masses to the left- and right-handed SM fermions.

1.3 The top quark

Since its discovery in 1995 by the CDF and D0 experiments at FNAL [4, 5], the top quark t has been carefully studied and its proprieties have been and are still measured with increasing precision by particle accelerators experiments at FNAL and the LHC. The study of this particle is of great interest in the high energy physics field since the top quark exhibits distinctive features that are not held by any of the other SM quarks. Due to its large mass $m_t = (172.69 \pm 0.30)$ GeV [6], the top quark does not form hadrons, since it decays following the weak interaction into a W boson and a b quark before QCD hadronization can occur. Furthermore, the top quark is strictly linked to the Higgs mechanism and the electroweak SSB (EWSSB), since its Yukawa coupling to the Higgs boson is order of unity. Therefore precision measurements of its proprieties, such as production cross section, decay width, couplings, mass, *etc.*, provide key information on fundamental interactions at the EWSSB scale and beyond.

Thanks to the large number of top events produced in proton-proton collisions at the LHC particle accelerator, the data collected by the LHC experiments during Run 1 and Run 2 allowed thorough studies of top proprieties that resulted in exceptionally precise measurements. Through these measurements, experiments can both test the SM theory and simultaneously look for deviations with respect to SM predictions, that would be associated to the existence of new physics beyond or at the SM EW energy scale.

1.4 BSM Physics

Standard Model predictions have always been experimentally confirmed by numerous analyses, whose results reached a remarkably high precision. Nevertheless, experimental

evidences related to phenomena that do not find a proper explanation within the SM have been found, unveiling the limits of the theory and therefore paving the way to new physics searches and theories Beyond the Standard Model (BSM).

Among these experimental evidences for BSM physics one can find:

- **Dark Matter**. Experimental evidences related to the existence of Dark Matter (DM) have been collected from measurements of rotation velocities in spiral galaxies, Cosmic Microwave Background patterns and gravitational lensing [7, 8]. This non-luminous (therefore non electromagnetically interacting) matter is expected to make up 84.4% of the matter content of the Universe [6]. Several BSM theories that predict the existence of DM particles have been formulated. Within these theories, DM candidates exhibit different proprieties, leading to a various phenomenology that can be searched for at particle accelerators.

- **CP-violation**. The large asymmetry between the amount of matter and antimatter in the Universe is not explained within the SM theory. One of the requirements that need to be fulfilled by the theory to account for this unbalance is the violation of CP symmetry [9, 10]. Although some experimental measurements pointed out the existence of CP violating processes in the SM weak interactions [6], these do not suffice to account for the large matter-antimatter asymmetry observed. For this reason, other sources of CP violation are being theorized and searched for, such as CP violation in the neutrino sector or in the SM strong interaction [11].

- **Neutrino masses**. BSM theories are required to account for the existence of neutrino masses pointed out by the experimental evidence of neutrino oscillations [6]. The SM Higgs mechanism fails to generate neutrino masses in a "natural" way, since no experimental evidence related to the existence of right-handed neutrinos has yet been found. Furthermore, the large mass difference between neutrinos and charged leptons can be labeled as unnatural and gives rise to additional theoretical open questions.

In addition to the BSM experimental evidences listed above, the SM lacks a proper motivation for the wide mass range covered by fermions, related to Yukawa couplings ranging from $\sim 10^{-6}$ for the electron to ~ 1 for the top quark. Furthermore, a *fine-tuning* is required on SM fermions as well as the Higgs boson to cancel Next-to-Leading-Order (NLO) corrections on fermion masses that would push their values to the Planck scale [12]. This issue is referred as the *hierarchy problem* and represents a puzzling item related to the SM theory.

Finally, some recent experimental results show tensions with respect to SM predictions that could point to new physics processes. Lepton universality tests in $b \longrightarrow s\ell\ell$ decays have been carried out by the LHCb Collaboration resulting into more than 3 σ deviations with respect to SM predictions [13]. Another experimental result involving leptons that resulted in 4.2 σ deviations with respect to the SM is the measurement of the muon anomalous magnetic moment carried out by E821 at BNL and the Muon $g-2$ experiment at FNAL [14, 15].

1.5   Direct and indirect BSM searches

The previous section drew attention to the need for BSM theories to investigate new physics that could address and motivate the observed discrepancies with respect to SM predictions. Two different approaches can be adopted by physics analyses at the LHC to search for new physics.

If the BSM theory predicts new particles with mass values within the LHC energy reach, new physics signals can be searched for directly. Direct searches aim to measure either resonance peaks related to the BSM particles, or event yields produced by BSM processes involving the new particles. A detailed description of an illustrative BSM theory, called two-Higgs-doublet-model (2HDM), is reported in Appendix A as a reference.

On the other hand, if the new particles are outside the LHC energy reach, they can not be directly searched for. In this case, an indirect approach can be adopted to search for the effects related to the new physics in the experimental energy range. These effects would result in deviations with respect to SM predictions, such as deviations on cross sections and couplings values.

While direct searches mostly rely on specific model assumptions to predict new particles and therefore new signatures to be probed, indirect searches can also adopt a model independent approach through Effective Field Theories (EFT) [16–21]. Results obtained with model independent searches can then be reinterpreted with respect to specific BSM theories. A detailed description of the EFT approach applied to the SM is presented in Chapter 2.

Chapter 2

The Standard Model Effective Field Theory

Model independent searches for new physics at high energies can be carried out using the Standard Model Effective Field Theory (SMEFT). In this approach the Standard Model is assumed to be a leading order, low energy approximation to a more fundamental theory.

An historical as well as established example of an Effective Field Theory applied to particle physics is the Fermi Theory of weak interactions [22]. According to Fermi's theory the process $\mu^- \longrightarrow e^- \bar{\nu}_e \nu_\mu$ results from a pointlike interaction, as presented in Figure 2.1a, and is described by the following Lagrangian

$$\mathcal{L}_{eff} = -\frac{G_F}{\sqrt{2}} \mathcal{J}_\mu^\dagger \mathcal{J}^\mu \tag{2.1}$$

where the weak current is $\mathcal{J}_\mu = \bar{\nu}_l \gamma_\mu \left(1 - \gamma_5\right) l$ and G_F is the Fermi constant of weak interactions [20].

The same process is described by the electroweak gauge theory as an interaction involving the W boson, as shown in Figure 2.1b. Both the interaction vertices $\mu^- \nu_\mu W^-$ and $e^- \bar{\nu}_e W^-$ are described following a Lagrangian expressed in the form

$$\mathcal{L} = -\frac{g}{2\sqrt{2}} \mathcal{W}_\mu^\dagger \mathcal{J}^\mu \tag{2.2}$$

where $\mathcal{W}_\mu$ and g are the weak gauge field and coupling respectively. The overall process $\mu^- \longrightarrow e^- \bar{\nu}_e \nu_\mu$ is then described by also taking into account the W boson propagator $\frac{1}{M_W^2 - q^2}$, where q is the four-momentum carried by the weak boson.

Both theories are valid and predictive in the low energy regime, below the W boson
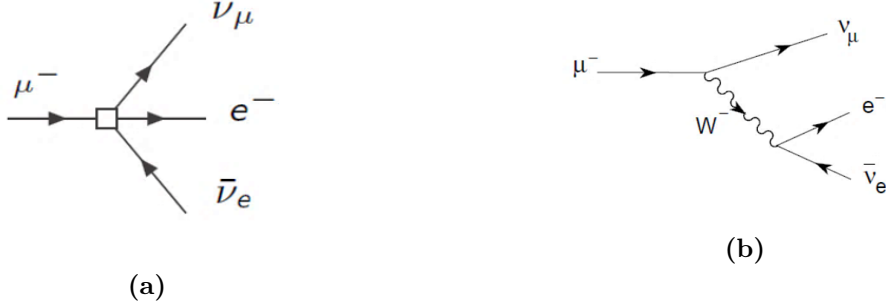
Figure 2.1: The $\mu^- \longrightarrow e^- \bar{\nu}_e \nu_\mu$ weak process described by the Fermi Theory (2.1a) and by the SM electroweak gauge theory (2.1b).

mass scale (where $q^2 \ll M_W^2$), and are linked through the following expression:

$$\frac{G_F}{\sqrt{2}} = \frac{g^2}{8M_W^2} \tag{2.3}$$

In the Fermi Theory, the constant G_F, that is the coupling of the weak pointlike interaction, encloses the information of the physics at the W boson energy scale (M_W, g). As a consequence, the Fermi Theory has been historically successful in studying EW experimental results before the W boson was discovered and measured.

The SMEFT has the same underlying approach as the Fermi Theory. In order to consider the SM as an effective theory, the new physics energy scale Λ is bound to be substantially larger than the SM EW scale $(\Lambda \gg v)$ [23]. Since no evidence for new particles above the EW scale has been found so far, the Λ scale is also assumed to be larger than the the current particle accelerators energy reach.

Being the new physics outside the experimental energy reach, it would not be possible to search for new resonances directly; instead, the new physics effects would appear as deviations from the SM predictions in high energy measurements carried out at particle accelerators. New physics therefore can be searched for using the SMEFT through an indirect approach. On the other hand, the new physics theory would also predict new final states either forbidden or highly suppressed within the SM, that could be directly explored in analyses.

The effective Lagrangian related to the SMEFT can be built by expanding $\mathcal{L}_{SM}$ reported in (1.3) with higher dimensional operators $O_i^{(D)}$, which are suppressed by inverse

powers of the new physics scale Λ [24]

$$\mathcal{L}_{\text{SMEFT}} = \mathcal{L}_{\text{SM}} + \sum_{i,D>4} \frac{c_i}{\Lambda^{D-4}} O_i^{(D)} \qquad (2.4)$$

The SMEFT Lagrangian only includes SM fields and is Lorentz invariant as well as invariant under SM gauge symmetries (SU(3)$_C \times$SU(2)$_L \times$U(1)$_Y$). The SM Higgs doublet is present in the EFT construction. The dimensionless Wilson Coefficients c_i associated to the EFT operators carry the information related to new physics [25], such as the mass value of a new particle and the coupling constant related to a new interaction, similarly to the Fermi constant G_F in the Fermi Theory described above.

Deviations from the SM predictions may arise when the EFT effects related to the higher order operators ($O_i^{(D)}$ with $D > 4$) become significant, with the expectation of larger effects to come from lower dimension operators.

The SM Lagrangian expansion is generally truncated, by considering only the contributions up to dimension 6 and assuming the effect of operators with higher dimension to be negligible (these operators are suppressed at least as $1/\Lambda^3$). By imposing also lepton and baryon number conservation, the only dimensional 5 operator that follows SM gauge symmetries has to be removed from the expansion. Minimal and complete sets (bases) of dimensional 6 (dim-6) EFT operators have been derived [24, 26–28]. Among these, the "Warsaw basis" is composed by 2499 baryon and lepton number conserving operators[1].

The new physics effects are then parametrized by the EFT operators that would affect SM processes and therefore modify experimental observables, such as production cross sections, decay widths and low energy constants. On the other hand, the EFT operators could give rise to new processes not allowed by the SM.

2.1 EFT reinterpretation of SM measurements

Precision measurements related to SM processes, such as total and differential production cross sections, can be reinterpreted using the SMEFT framework to investigate possible deviations with respect to SM predictions. These reinterpretations rely on the EFT parametrization of experimental observables.

Considering a process that can be produced from both SM and dim-6 EFT (BSM)

---

[1]The complete list of dim-6 EFT operators in the Warsaw basis can be found in [28].
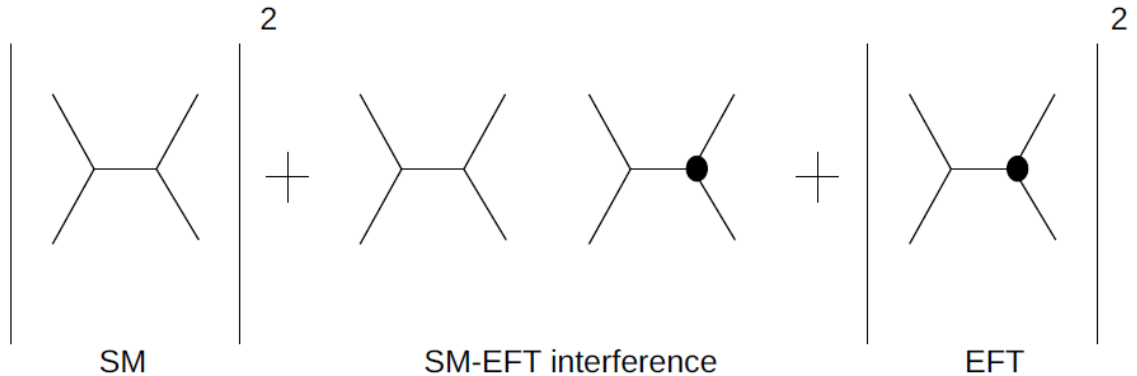
Figure 2.2: Schematic representation of the SM and EFT contributions to the squared amplitude $|\mathcal{M}|^2$ of a given process.

operators, its related amplitude $\mathcal{M}$ can be expressed as

$$\mathcal{M} = \mathcal{M}^{\text{SM}} + \frac{1}{\Lambda^2} \sum_i c_i \mathcal{M}_i^{\text{EFT}} + \mathcal{O}\left(\frac{1}{\Lambda^4}\right) \tag{2.5}$$

with the subleading $\mathcal{O}(1/\Lambda^4)$ contributions arising from multiple insertions of EFT operators within the same process not taken into account [29]. Experimental observables measured in analyses are described by events rates, that are proportional to the squared amplitude $|\mathcal{M}|^2$ related to the process of interest. Therefore, any given observable σ can be parametrized as

$$\sigma = \sigma^{\text{SM}} + \frac{1}{\Lambda^2} \sum_i c_i \sigma_i^{int} + \frac{1}{\Lambda^4} \sum_{i,j} c_i c_j \sigma_{i,j}^{EFT} \tag{2.6}$$

Here, σ^{SM} is the SM contribution, which corresponds to the value of the physics observable in the SM limit $c_i/\Lambda^2 \longrightarrow 0$ for any EFT operator $\mathcal{O}_i$. The component σ^{int} comes from the interference between the SM and the EFT amplitudes, while σ^{EFT} is the pure EFT contribution, arising from the squared amplitudes of the dim-6 operators considered and from the interference between EFT operators. A visual representation of the contributions to the squared amplitude of a given process is shown in Figure 2.2. Contributions arising from SM-EFT interference as well as pure EFT insertions of higher dimensional operators ($D > 6$) are here neglected in the EFT parametrization of the physics observable.

The sum $\sigma^{int} + \sigma^{EFT}$ constitutes the new physics signal, that is a deviation from the

SM predicted value σ^{SM}. Therefore, high SM precision measurements are essential to gain sensitivity to the new physics EFT effects.

2.2 LHC SMEFT measurements in the top quark sector

Due to its large mass, the top quark likely is the SM particle closest to new physics sectors. Therefore it is of great importance to thoroughly study its proprieties and couplings, since these measurements could shed light on new physics. SMEFT reinterpretations of top quark measurements are carried out at the LHC exploiting the large number of top events collected during the Run 1 and Run 2 by accelerator experiments, such as ATLAS and CMS, and therefore making the most of the precision achieved by SM measurements in the top sector [30–32].

Searches for new physics processes either forbidden or suppressed within the SM, such as top flavor changing neutral current (tFCNC) interactions, are as well performed within the SMEFT framework.

2.2.1 SMEFT searches in SM processes involving the top quark

Many EFT reinterpretation analyses are carried out exploiting top processes using LHC collision data, such as inclusive and differential cross section, charge asymmetry and decay width measurements [33–44]. Among these, differential measurements are of great interest since they can constraint multiple Wilson Coefficients (WCs) at the same time.

The full parametrization reported in eq.(2.6) can be known for a given set of EFT operators if more than one observable is measured. This is indeed the case for differential measurements, where each bin related to a physics kinematic distribution can be considered as an observable. However, constraining the whole set of EFT operators affecting one top process is still a task that cannot be accomplished by a single (even if differential) analysis.

Multiple operators affecting top processes, from its production to its decay are constrained in global fits, that gather results from many different top EFT analyses (see section 2.2.3 for a more detailed description of global fits in the top sector).

2.2.2 SMEFT searches in new final states involving the top quark

The SMEFT framework can also be employed to search for processes either forbidden or suppressed by the SM [45–47].

Concerning top processes, this is the case for top flavor changing neutral current interactions. These processes are highly suppressed in the SM by the GIM mechanism [48]. The branching ratios related to tFCNC decays have values of order $10^{-12} - 10^{-15}$, therefore any experimental evidence related to tFCNC interactions would directly point towards new physics [49].

When performing new physics searches using the SMEFT, the parametrization expression (2.6) is simplified, since no SM operator can produce the targeted process. In this case, the number of events is the studied physics observable σ and it is parametrized by only taking into account pure EFT contributions, as

$$\sigma = \frac{1}{\Lambda^4} \sum_{i,j} c_i c_j \sigma_{i,j}^{EFT} \tag{2.7}$$

Being the number of events a single physics observable, SMEFT searches are generally not suited to constraint more than one EFT operator at the same time, but results achieved through these analyses still play a fundamental role in EFT global fits.

2.2.3 Global EFT fits in the top sector

The results obtained from the many EFT analyses carried out by LHC experiments are then combined in global fits, that allow to place limits on several EFT operators at once. These limits are usually less stringent with respect to the ones resulting from individual analyses, but they are more general and can therefore be employed as a reference for any other EFT analysis targeting a specific process.

Concerning the top sector, a global fit has been recently performed [50] gathering measurements carried out by ATLAS and CMS. Several measurements have been employed: $t\bar{t}$, $t\bar{t}W$, $t\bar{t}Z$, single and associated top production, top decay and charge asymmetry. The full set of dim-6 operators affecting top physics has been employed in the fit.

Since the overall number of parameters related to top processes is too large to be efficiently taken into account in global fits (1179), a "flavor assumption" has been placed on the SMEFT physics. Specifically, the quarks belonging to the first two generations are required to follow an $U(2)_q \times U(2)_u \times U(2)_d$ symmetry (an $U(2)$ symmetry for each field q_L, u_R, d_R) while no restriction is placed on the third quark generation. The Wilson

Coefficients related to operators involving quarks are therefore forced to be identical for the first and second generation thus reducing the overall number of coefficients within the theory[2]. Furthermore, only CP-conserving operators are taken into account and operators that do not have a sizeable effect on the considered observables or are strongly constrained by other measurements (not top-related) are not taken into account[3]. Finally, operators involving leptons are not taken into account in the fit. With these restrictions, the number of parameters to be considered in the global fit is reduced to 22.

The global EFT fit results are reported in Figure 2.3. Here, some of the EFT operators are defined as linear combinations of the Warsaw basis operator definitions (see [50] for a detailed review of the relations between the operator definitions employed in the global fit and the Warsaw basis).

Some among the EFT operators constrained in top analyses can also be targeted in Higgs and B-physics measurements, with the same operators affecting processes involving either the top quark, the Higgs boson or B-mesons. Therefore, SMEFT top, Higgs and B-physics measurements can be combined together as well in global fits, resulting in even more general constraints on EFT operators with respect to the ones presented in this Section [51]. The constraints resulting from these wider combinations of measurements can then be employed in a significantly broad number of analyses.

2.3 Matching SMEFT constraints to BSM theories

Due to the model independent approach of the SMEFT, results related to SMEFT searches can be reinterpreted using multiple distinct BSM theories.

Processes targeted in SMEFT searches are usually also predicted by BSM theories through interactions involving SM particles and new physics mediators. Similarly to what has been described in Section 2 related to the Fermi Theory of weak interactions, SMEFT and BSM theories can be linked together (*matched*) by assuming the mass of the BSM mediator to be substantially larger than the energy scale associated to the targeted process [25, 32]. By *matching* the two theories, their associated parameters, namely the Wilson Coefficients and the mass and coupling of the BSM mediator, are brought into relation through expressions similar to the one reported in eq.(2.3), with G_F being the WC and M_W and g the mass and coupling related to the BSM mediator. These relations can then be used to translate limits on WCs resulting from model-independent SMEFT searches into constraints on new particles masses and couplings.

---

[2]Other flavor assumptions defined concerning quarks and leptons are described in [30].

[3]Concerning CP-violating operators, these are constrained in top polarization, spin correlation and B meson decays measurements.
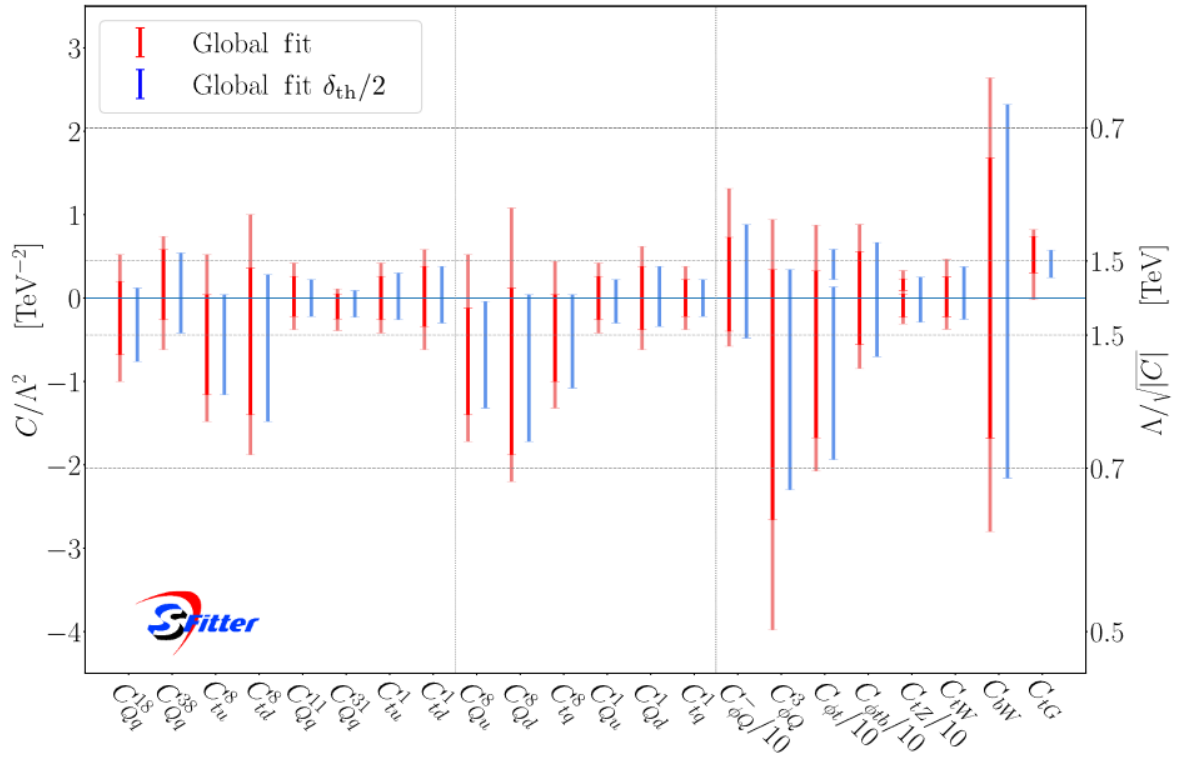
Figure 2.3: Bounds on SMEFT operators resulting from the global EFT fit in the top sector [50].

Chapter 3

Same-sign top quark pairs production

Same-sign top pairs production is forbidden in the SM at Leading-Order (LO). This process can happen at the lowest perturbative order through the Feynman diagram in Figure 3.1 with the exchange of two W bosons. Therefore, same-sign top pairs production is highly suppressed in the SM by the GIM mechanism [48], due to the large value of the square of the b quark mass. The SM cross section related to this process has been computed in [52] for proton-proton interactions at $\sqrt{s} = 13$ TeV to be $\sigma(pp \longrightarrow tt)_{SM} \simeq 4 \cdot 10^{-15}$ pb.

Due to its suppression in the SM, same-sign top pairs production is not expected to be observed with the available LHC data, therefore its experimental observation would directly point to the existence of new physics. Several BSM theories predict same-sign top pairs production, such as 2HDMs, models with an extra U(1) gauge group as well as baryon and lepton number violating theories [53]. Within these theories, same-sign top
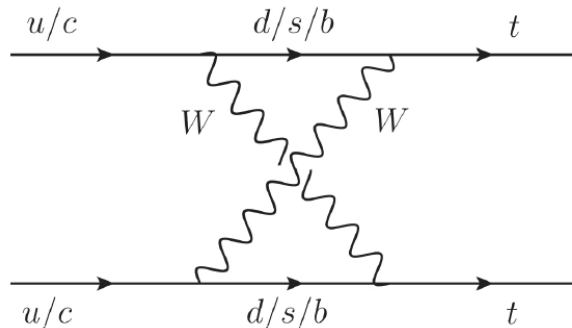
Figure 3.1: SM production of same-sign top pairs.
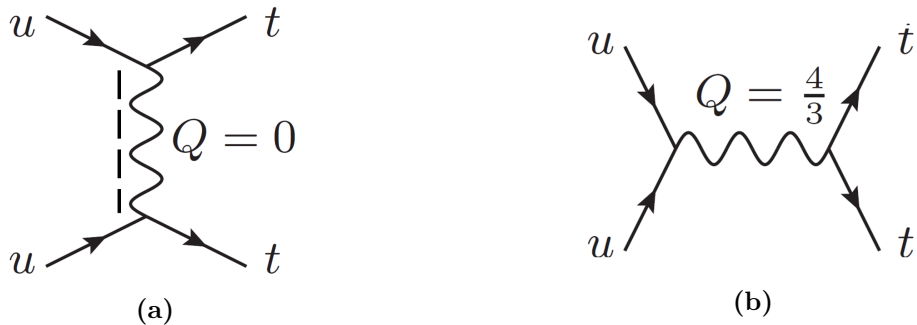
Figure 3.2: Same-sign top pairs *t-channel* (3.2a) and *s-channel* (3.2b) production.
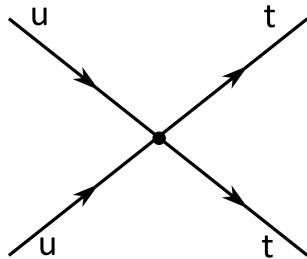
Figure 3.3: Same-sign top pairs production as a pointlike EFT four-fermion interaction.

pairs can be produced in *t-channel* and *s-channel* processes, as shown in Figure 3.2.

Considering *t-channel* processes, same-sign top pairs are produced in top flavor changing neutral current processes through the exchange of a neutral BSM scalar or vector mediator, such as heavy Z' or heavy Higgses H predicted in extra U(1) models and 2HDMs respectively.

On the other hand, the *s-channel* process would require the on-shell production of a BSM particle with electric charge $Q = +4/3$.

3.1 EFT production of same-sign top quark pairs

Instead of relying on a specific BSM theory, same-sign top pairs production can be described using the SMEFT framework as a pointlike interaction involving four up-like fermions, as shown in Figure 3.3.

Among the complete set of dim-6 EFT operators expressed in the Warsaw basis, only five can be responsible for same-sign top pairs production [54], assuming flavor

universality:

$$\mathcal{O}_{RR} = [\bar{t}_R \gamma^\mu u_R] [\bar{t}_R \gamma_\mu u_R]$$
$$\mathcal{O}_{LL}^{(1)} = [\bar{Q}_L \gamma^\mu q_L] [\bar{Q}_L \gamma_\mu q_L]$$
$$\mathcal{O}_{LL}^{(3)} = [\bar{Q}_L \gamma^\mu \sigma^a q_L] [\bar{Q}_L \gamma_\mu \sigma^a q_L] \qquad (3.1)$$
$$\mathcal{O}_{LR}^{(1)} = [\bar{Q}_L \gamma^\mu q_L] [\bar{t}_R \gamma_\mu u_R]$$
$$\mathcal{O}_{LR}^{(8)} = [\bar{Q}_L \gamma^\mu T^A q_L] [\bar{t}_R \gamma_\mu T^A u_R]$$

Here, Q_L and t_R are the third quark generation left-handed doublet and right-handed singlet, while q_L and u_R are related to the first two generations. The production of a pair of right-handed same-sign quarks via the four-fermion interaction $u_R u_R \longrightarrow t_R t_R$ (with $u_R = u, c$) is described by the $\mathcal{O}_{RR}$ operator, while two different operators $\mathcal{O}_{LL}^{(1)}$, $\mathcal{O}_{LL}^{(3)}$ can originate left-handed same-sign top quarks via $u_L u_L \longrightarrow t_L t_L$, with the Pauli matrices σ^a entering the $\mathcal{O}_{LL}^{(3)}$ definition. Same-sign top pairs with mixed chirality can be generated via $u_L u_R \longrightarrow t_L t_R$. The $\mathcal{O}_{LR}^{(1)}$ and $\mathcal{O}_{LR}^{(8)}$ operators can originate this process, with the SU(3)$_C$ generators T^A entering the $\mathcal{O}_{LR}^{(8)}$ operator definition.

It should be noticed that without the flavor universality assumption 15 operators could generate same-sign top pairs. In this case, each of the five operators listed above would represent 3 different operators depending on the initial state quark flavor. $\mathcal{O}_{RR}$ would be either $[\bar{t}_R \gamma^\mu u_R] [\bar{t}_R \gamma_\mu u_R]$, $[\bar{t}_R \gamma^\mu u_R] [\bar{t}_R \gamma_\mu c_R]$ or $[\bar{t}_R \gamma^\mu c_R] [\bar{t}_R \gamma_\mu c_R]$ corresponding to $u_R u_R \longrightarrow t_R t_R$, $u_R c_R \longrightarrow t_R t_R$ or $c_R c_R \longrightarrow t_R t_R$ respectively. Analogous considerations apply to the other operators in (3.1).

The same-sign top pairs production effective Lagrangian, related to the EFT operators in (3.1), is expressed as

$$\mathcal{L}_{\text{D}=6}^{qq \to tt} = \frac{1}{\Lambda^2} \left(c_{RR} \mathcal{O}_{RR} + c_{LL}^{(1)} \mathcal{O}_{LL}^{(1)} + c_{LL}^{(3)} \mathcal{O}_{LL}^{(3)} \right.$$
$$\left. + c_{LR}^{(1)} \mathcal{O}_{LR}^{(1)} + c_{LR}^{(8)} \mathcal{O}_{LR}^{(8)} \right) + h.c. \qquad (3.2)$$

with c_{RR}, $c_{LL}^{(1)}$, $c_{LL}^{(3)}$, $c_{LR}^{(1)}$ and $c_{LR}^{(8)}$ being the Wilson Coefficients related to the EFT operators. In this work only $\mathcal{O}_{RR}$, $\mathcal{O}_{LR}^{(1)}$, $\mathcal{O}_{LR}^{(8)}$ are taken into account, since $\mathcal{O}_{LL}^{(1)}$ and $\mathcal{O}_{LL}^{(3)}$ also contain $[b_L \gamma^\mu d_L] [b_L \gamma_\mu d_L]$, already constrained by B_d mixing and di-jet production measurements. The upper bound placed on the linear combination $c_{LL} = c_{LL}^{(1)} + c_{LL}^{(3)}$ with B_d mixing measurements is [55]

$$|c_{LL}| \left(\frac{1\text{TeV}}{\Lambda} \right)^2 < 2.1 \times 10^{-4} \qquad (3.3)$$

23

Since this work presents a search for same-sign top pairs production using the SMEFT framework, the experimental observable of interest is the production cross section $\sigma_{pp\longrightarrow tt}$. Its EFT parametrization can be obtained from (2.6) using $\mathcal{O}_{RR}$, $\mathcal{O}_{LR}^{(1)}$ and $\mathcal{O}_{LR}^{(8)}$ as

$$\sigma_{pp\longrightarrow tt} = \frac{1}{\Lambda^4} \left[c_{RR}^2 \sigma_{RR} + c_{LR^{(1)}}^2 \sigma_{LR^{(1)}} + c_{LR^{(8)}}^2 \sigma_{LR^{(8)}} + c_{LR^{(1)}} c_{LR^{(8)}} \sigma_{LR^{(1)}-LR^{(8)}} \right] \quad (3.4)$$

where the contributions to the cross section parametrization stem only from the squared amplitudes related to the three EFT operators considered and from the interference between $\mathcal{O}_{LR}^{(1)}$ and $\mathcal{O}_{LR}^{(8)}$, reported as $\sigma_{LR^{(1)}-LR^{(8)}}$ in eq (3.4) [1].

SM same-sign top pairs production is negligible, therefore the cross section parametrization only contains pure EFT contributions, coming from the squared amplitudes of single EFT insertions and from the interference between the two $\mathcal{O}_{LR}$ operators.

3.2   State of the art

Same-sign top pairs have been searched for using Tevatron and LHC data [56–68]. Many different BSM theories, such as extra U(1) SM extensions, SUSY, 2HDMs, baryon and lepton number violating theories, have been employed to perform both searches and phenomenological studies related to same-sign top pairs production.

Experimental searches usually focus on the dilepton decay channel of the top pair, since final states involving two leptons with same electric charge and b-jets are rarely produced by SM processes. Therefore this decay channel has a low expected background contamination.

Same-sign top pairs have been searched for using LHC data at 7, 8 and 13 TeV by the ATLAS and CMS Collaborations. The most stringent limits on model independent tt production are reported in Table 3.1. These limits resulted from an ATLAS analysis carried out using collision data at 8 TeV [67]. Different simulated signal samples have been employed for the different chirality of the same-sign top pair, resulting in different upper limits on the signal cross section.

A more recent ATLAS analysis has been carried out using collision data at 13 TeV corresponding to an integrated luminosity of 36.1 fb^{-1} and resulted in an upper limit on the same-sign top production cross section $\sigma(uu \longrightarrow tt) = 89$ fb. Here, a BSM vector mediator with $M = 1$ TeV has been assumed [64]. The search has not been performed over the different chirality states of the same-sign top pair, therefore resulting in a limit

---

[1]It should be noticed that the RR operator does not interfere with any of the two LR operators, due to the different chirality configurations.

quark chirality	UL on $\sigma(pp \longrightarrow tt)$ [fb]
LL	62
LR	53
RR	40

Table 3.1: Most stringent model independent limits at 95% CL on same-sign top pairs production cross section. The three rows are associated to the different chirality states of the top pair [67].

on the total cross section related to the process.

The SMEFT approach has been also adopted by some analyses to search for same-sign top pairs, resulting in limits on the Wilson Coefficients related to the EFT operators affecting the process [57, 66–68]. The most stringent upper limits are reported in Table 3.2 and resulted from the above mentioned ATLAS analysis carried out using collision data at 8 TeV. A different operator basis has been adopted with respect to the Warsaw basis, used instead in the work presented in this document. Specifically, four dim-6 EFT operators are related to same-sign top pairs production in the basis used to evaluate the limits reported in Table 3.2: one LL operator, two LR operators and one RR operator. The two LR operators give rise to kinematically equivalent events, therefore only one Wilson Coefficient associated to the LR operators has been considered.

quark chirality	UL on the Wilson Coefficients $|c|$ $(\text{TeV}/\Lambda)^2$
LL	0.053
LR	0.137
RR	0.042

Table 3.2: Most stringent upper limits at 95% CL on the Wilson Coefficients associated to the four-fermion operators affecting sign top pair production [67].

The Warsaw basis, employed in the analysis reported in this thesis, has been instead used to perform the global fit in the top sector reported in Section 2.2.3. Although a more restrictive flavor scenario has been assumed in the global fit with respect to the one employed in the analysis presented in Chapter 5, the resulting limits can still be employed as a guideline for choosing the analysis signal benchmark. Among the 22 coefficients constrained in the global fit (as reported in Figure 2.3) C_{tu}^1, C_{tu}^8, C_{Qu}^1, C_{Qu}^8, C_{tq}^1 and C_{tq}^8 are related to the three EFT operators taken into account in the analysis: $\mathcal{O}_{RR}$, $\mathcal{O}_{LR}^{(1)}$ and $\mathcal{O}_{LR}^{(8)}$. Specifically, the associated operators are defined as

$$O_{tu}^1 = \mathcal{O}_{RR}^{[33ii]}$$

$$O_{tu}^8 = -\frac{1}{6}\mathcal{O}_{RR}^{[33ii]} + \frac{1}{2}\mathcal{O}_{RR}^{[3ii3]}$$

$$O_{Qu}^1 = \mathcal{O}_{LR}^{(1)[33ii]}$$

$$O_{Qu}^8 = \mathcal{O}_{LR}^{(8)[33ii]} \qquad (3.5)$$

$$O_{tq}^1 = \mathcal{O}_{LR}^{(1)[ii33]}$$

$$O_{tq}^8 = \mathcal{O}_{LR}^{(8)[ii33]}$$

where the flavor indices are specified in square parentheses with $i = 1, 2$. The corresponding upper limits on the Wilson Coefficients resulting from the global fit at 95% confidence level are reported in Table 3.3.

Wilson Coefficient	95% UL $(\mathrm{TeV}/\Lambda)^2$
O_{tu}^1	0.42
O_{tu}^8	0.52
O_{Qu}^1	0.42
O_{Qu}^8	0.52
O_{tq}^1	0.38
O_{tq}^8	0.44

Table 3.3: Upper limits on the Wilson Coefficients at 95% CL resulting from the global fit performed in the top sector [50]. Only the operators linked to the ones employed in the presented analysis are reported.

Chapter 4

The ATLAS experiment at the LHC

4.1   The Large Hadron Collider

The Large Hadron Collider (LHC) at CERN [69] is the most energetic particle accelerator in the world, able to accelerate proton beams up to 6.8 TeV. The LHC accelerator system that allows to reach such an energy is composed by several machines operating in an acceleration chain.

Protons are first produced by applying an electric field to a tank of hydrogen gas and then injected in the Linac2 linear accelerator, that boosts protons up to 50 MeV. The particles are then injected in the first circular accelerator, the Proton Synchrotron Booster (PS Booster) where they reach 1.4 GeV. The proton beam is further accelerated in the circular Proton Synchrotron (PS) and Super Proton Synchrotron (SPS) reaching 25 GeV and 450 GeV in the first and second accelerator respectively. Finally, protons are injected from the SPS to the LHC ring into two beam pipes where they circulate in opposite directions. The two proton beams were accelerated up to 6.5 TeV during Run 2, nowadays they reach 6.8 TeV. Protons are arranged in bunches within the accelerated beams, and once the beams reach the maximum energy in the LHC, they collide in four interaction points (IPs), where the ATLAS, CMS, ALICE and LHCb detectors are located. During LHC Run 2 the proton-proton collisions were carried out with a resulting center-of-mass energy of $\sqrt{s} = 13$ TeV and with a maximum rate of bunch crossing of 40 MHz and a maximum instantaneous luminosity of 1.4×10^{34} cm^{-2} s^{-1} [70].

4.2 Overview of the ATLAS detector

The ATLAS detector [71–73] is one of the four large experiments located at one IP of the LHC. It is a multipurpose particle detector with a forward-backward symmetrical geometry and nearly 4π coverage in solid angle. The detector coverage description is based on a right-handed coordinate system with its origin at the IP, corresponding to the center of the detector itself. The $z-$axis is along the beam pipe while the $x-$ and $y-$axes point from the IP to the LHC ring center and upwards respectively. Particle events within the detector volume are described using cylindrical coordinates (r, ϕ), with ϕ being the azimuthal angle around the $z-$axis. The polar angle θ is used to define the pseudorapidity as $\eta = -\ln\tan(\theta/2)$. Angular distances between objects are then defined as $\Delta R = \sqrt{(\Delta\eta)^2 + (\Delta\phi)^2}$.

The ATLAS detector, shown in Figure 4.1, is composed by several subdetectors. The inner tracking detector is the subdetector closest to the IP, surrounded by a thin superconducting solenoid that provides a 2 T axial magnetic field. Two calorimeters, one electromagnetic and one hadronic are placed outside the solenoid. The outermost part of the detector is composed by a muon spectrometer and toroid magnets placed in the detector barrel and end-caps providing a 0.5 T and 1 T magnetic field respectively. The ATLAS detector structure employed to collect collision data during LHC Run 2 is described in the following sections.

4.3 The inner tracking system

The Inner Detector (ID) is designed to track charged particles produced at the interaction point and measure their transverse momenta through the curvature of trajectories caused by the axial magnetic field. Its overall coverage is $|\eta| < 2.5$. Thanks to its high tracking precision, the ID allows to reconstruct primary as well as possible secondary decay vertices associated to the particles generated from proton-proton collisions. Being located in the innermost part of ATLAS, the ID is composed by radiation hard material with an high spatial resolution.

Four different subdetectors form the ATLAS ID: the Insertable B-Layer, the Pixel Detector, the Semiconductor Tracker and the Transition Radiation Tracker.

The Insertable B-Layer (IBL) is the innermost subdetector. It is composed by one single silicon pixel layer with high granularity designed to measure the impact parameter as well as to get track information related to short-lived particles that decay in proximity of the IP. Therefore, it is a key detector for the b-tagging of particle jets. Its spatial resolution is 10 μm and 60 μm in the transverse plane and along the $z-$axis direction
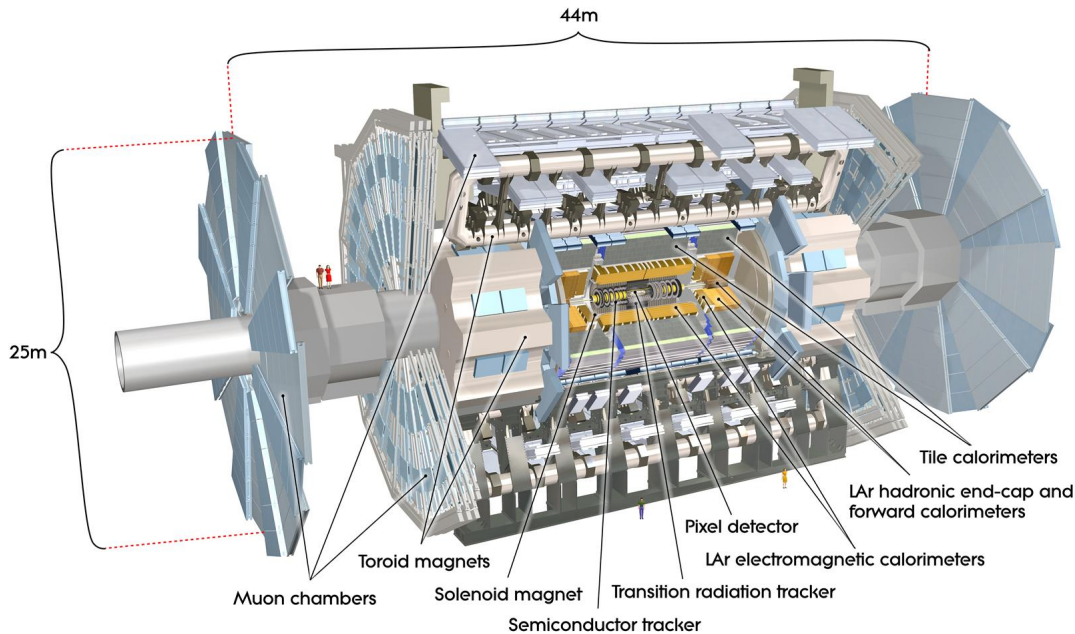
Figure 4.1: Schematic cut-away view of the ATLAS detector during the LHC Run 2 data taking period.

respectively.

The Pixel Detector is located outside the IBL and it is composed by three layers of silicon pixel detectors with high granularity. Specifically, three cylindrical layers and three disks are placed in the barrel and in each end-cap respectively. The Pixel Detector size has been optimized to maximise the probability for a particle to cross all three layers. Its spatial resolution is 10 μm and 115 μm in the transverse plane and along the $z-$axis direction respectively.

Outside the Pixel Detector, the Semiconductor Tracker (SCT) is located. It is composed by many silicon microstrip sensors arranged in four coaxial cylinders in the barrel and nine disks in each end-cap. Its spatial resolution is 17 μm in the transverse plane and 580 μm along the $z-$axis.

Finally, the Transition Radiation Tracker (TRT) makes up the outermost part of the ID. It is composed by straw tubes filled with a gas mixture and arranged in three coaxial cylinders in the barrel. The straws are embedded in propylene fibers employed as transition radiation material. The transition radiation as well as the tracks associated to charged particles are measured by the detector to allow electron identification, transverse momentum measurement and e/π discrimination. The spatial resolution of the TRT is

130 μm in the transverse plane.

4.4 The calorimeters

ATLAS electromagnetic and hadronic calorimeters are designed to perform precise measurements of the energy of particles transversing the detector, such as electrons, photons and jets. The calorimeters are made of alternating layers of absorbing and active materials so that a transversing particle would generate other particles in a shower-like signature and deposit all its energy in the detector. The energy deposit is measured in the active layers. Since the particle transversing the calorimeters is stopped within the detector material and all its energy is measured, calorimeters allow also for a precise measurement of the missing transverse momentum E_T^{miss} associated to the event generated at the interaction point. ATLAS calorimeters are located outside the Inner Detector, both in the barrel and in the end-caps, with a coverage of $|\eta| < 4.9$.

The electromagnetic calorimeter (ECAL) is made of alternating layers of lead and liquid argon (LAr) as absorbing and active materials respectively, arranged in an accordion shape that allows a complete azimuthal symmetry of the detector without any crack. The LAr radiation hardness, its steady response stability and its intrinsic linear behavior ensure a stable performance of the calorimeter over time. To allow precise measurements of photons and electrons, the electromagnetic calorimeter has a finer granularity within the ID acceptance ($|\eta| < 2.5$).

The energy deposit of hadrons is measured by two different hadronic calorimeters: the Tile Calorimeter (HTC) and the end-cap calorimeter (HEC). These subdetectors are built in order to contain particle showers generated by hadrons transversing the calorimeters. The HTC is placed outside the electromagnetic calorimeter and is composed by three barrel layers. Steel and scintillating tiles are employed as absorbing and active materials respectively. The HEC is instead composed by copper plates and liquid argon as absorbing and active layers. It is arranged in two wheels per end-cap placed outside the ECAL.

Finally, the forward calorimeter (FCal) is located in the forward region of the detector with respect to the interaction point, with a coverage of $3.1 < |\eta| < 4.9$. It is composed by three modules per end-cap. The first and second/third modules are built to contain and measure electromagnetic and hadronic forward showers respectively. Liquid argon is used as active material in all modules. In the first module copper is used as absorbing material, while the other modules employ tungsten.

4.5   The muon spectrometer

The outermost ATLAS subdetector is the Muon Spectrometer (MS), designed to track muons leaving the calorimeters and to measure their transverse momenta. The momentum measurement is performed using muon trajectories that are bent by the magnetic fields generated by the barrel and end-cap toroid magnets. The MS is composed by different types of muon chambers, designed to either perform precise track measurements or to work as muon triggers. The chambers are arranged in three barrel layers, called *stations* and in three wheels per end-cap. Both barrel and end-cap chambers are arranged into 18 sectors in the azimuthal plane.

Muon trajectories are measured by Monitored Drift Tubes (MDTs) and Cathode Strip Chambers (CSCs). MDTs are employed to measure muon tracks in the $|\eta| < 2.7$ region with a single-hit resolution of ~ 80 μm per chamber in the bending plane. They are filled with a gas mixture of argon and carbon dioxide, chosen for its good ageing proprieties. Each MDT chamber allow six to eight η measurements along the muon track.

In the innermost end-cap station CSCs are employed instead of MDTs to cover the $2 < |\eta| < 2.7$ range, since CSCs have a higher rate capability with respect to MDTs. CSCs are multiwire proportional chambers filled with the same gas mixture employed for MDTs. Each CSC provides four simultaneous η and ϕ measurements. Their single-hit resolution is 60 μm and 5 mm per chamber in the bending and transverse planes respectively.

The chambers alignment is based on optical sensors to achieve a 10% resolution on the transverse momentum of 1 TeV muons.

Resistive Plate Chambers (RPCs) and Thin Gap Chambers (TGCs) are used to trigger on muons transversing the spectrometer. RPCs are employed in the barrel and cover the $|\eta| < 1.05$ region. They are gaseous parallel electrode-plate chambers with a time resolution of ~ 2 ns. RPCs are arranged into three coaxial layers. TGCs make up the trigger system in the end-caps ($1.05 < |\eta| < 2.4$). They are multi wire proportional chambers with a time resolution of $15 - 18$ ns.

Both RPCs and TGCs are also employed to perform track measurements in the azimuthal plane complementary to MDTs, with spatial resolution ranging from 5 to 10 mm.

4.6   Trigger and readout systems

In order to manage the large amount of data collected by the ATLAS detector in an efficient way, two different trigger levels are employed by ATLAS readout system [74]. A first hardware-based trigger level, called *Level 1* trigger (L1), only selects events that exhibit an interesting topology. This selection is based on information collected by the calorimeters and the muon spectrometer. L1 trigger reduces the event rate from 40 MHz to 100 kHz. A following software-based trigger level, called High Level Trigger (HLT), further reduces the event rate down to 1 kHz, by using finer-granularity information collected by ATLAS subdetectors, such as the ID, calorimeters and the MS. Events passing the HLT selection are then stored to be employed in physics analyses.

Chapter 5

Same-sign top quark pairs search

A search for same-sign top quark pairs decaying leptonically is presented in this Chapter. The full Run 2 dataset collected by the ATLAS detector from 2015 to 2018 from proton-proton collisions at $\sqrt{s} = 13$ TeV is employed, corresponding to an integrated luminosity of 140 fb^{-1}. The Standard Model Effective Field Theory is used to obtain predictions associated to the production of same-sign top pairs. Alongside signal simulated samples, background processes are taken into account, since SM processes together with detector inefficiencies and object mis-reconstruction could result in events with signatures similar to the signal of interest. A detailed description of the signal and background processes considered in this analysis is presented in Section 5.1.

Several mutually exclusive analysis regions are defined in order to be enriched in either signal or background events. The analysis regions are defined based on the predictions resulting from the simulation of signal and background events as well as on the simulation of the ATLAS detector. The event selection is based on kinematic and reconstruction-related variables. Collision data events are not employed in the definition of the analysis regions to avoid introducing biases in the final result. This *blinded* approach is also employed after the analysis regions have been defined, to properly develop the analysis framework and strategy. Specifically, a strategy is defined to partially blind data events in regions sensitive to the searched signal.

Signal Regions (SRs) are defined to include as many signal events as possible, with a low contamination coming from background events. A preliminary selection of signal-like events is performed as reported in Section 5.2.8. The selected events are then employed to train a Deep Neural Network (DNN) in order to build separate SRs, enriched in same-sign top events resulting from different EFT operators. Within each defined SR, a second DNN is trained to perform signal-background discrimination. Details on the Neural Networks employed are reported in Section 5.3. One final selection requirement is

defined based on the azimuthal distance between the two same-sign leptons $\Delta\Phi(\ell^\pm, \ell^\pm)$ to finalize the definition of the analysis Signal Regions. This requirement allows the definition of Validation Regions (VRs), that are built using the SR selection with an opposite requirement on $\Delta\Phi(\ell^\pm, \ell^\pm)$, as reported in Section 5.4. The VRs are not used to perform the statistical analysis and are instead employed to validate the resulting background estimates.

Several different techniques (data-driven, semi data-driven or based only on simulation) are employed to estimate the background contributions in the SRs. Control Regions (CRs) are defined to be enriched in events related to specific background processes and have a negligible contribution coming from signal events, as reported in Section 5.5.

A study on the expected sensitivity of the analysis is performed using a "realistic" Asimov pseudo-dataset, as described in Section 5.7.2. The pseudo-background events in the Asimov dataset are generated following the results of a fit performed on data events assuming a background-only hypothesis, reported in Section 5.7.1.

Same-sign top pairs are finally searched for by performing a fit on collision data events (*unblinded* fit) over all SRs and CRs, with the expected signal normalized according to the results of the sensitivity study. The same-sign top pairs search results are reported in Section 5.8.

5.1 Signal and background processes and samples

Monte Carlo (MC) simulated samples related to signal and background processes relevant for the analysis are employed. MC events are classified according to three simulation campaigns: mc16a, mc16d and mc16e (related to the 2015-2016, 2017 and 2018 LHC data taking years respectively). In these samples, events are generated according to the SMEFT and SM predictions for signal and background samples respectively. Pile-up effects are modelled using events originating from minimum-bias interactions generated with Pythia 8.186 [75] using the NNPDF2.3LO set of Parton Distribution Functions (PDFs) and the A3 set of tuned parameters [76].

The MC generated events are then processed through the simulation of the ATLAS detector geometry [77] and response using GEANT4 [78] and then through the reconstruction software that is also employed for data events. Correction factors are applied to the simulated samples on objects reconstruction efficiencies, energy and momentum scales and resolutions to match the values obtained from dedicated data samples. More details concerning the evaluation of the correction factors related to muons are presented in Appendix B.

5.1.1 Same-sign top signal

Signal events have been generated using MadGraph5_aMC@NLO [79] v2.9.3 together with the SMEFTsim3.0 framework [80, 81]. The computation of the matrix element for EFT processes at NLO is not currently supported by SMEFTsim3.0, therefore signal events have been generated at LO. The set of PDFs used is NNPDF30LO [82]. Only the leptonic decays of the top quark have been generated ($t \longrightarrow bW$, with $W \longrightarrow \ell\nu_\ell$) and parton showering has been performed using Pythia 8.245 [75] with the A14 set of tuned parameters [83]. Decays of bottom and charm hadrons have been simulated with EvtGen 1.6.0 [84]. The m_W electroweak input scheme [81] is employed within the used SMEFTsim EFT model, where G_F, m_Z, m_W are used as input parameters in the EFT. The mass of the top quark is set to be 172.5 GeV.

The EFT model employed is based on a general flavor assumption, that allows all possible flavor combinations related to the defined EFT operators. Therefore the complete set of dim-6 operators expressed in the Warsaw basis is included in the model.

Out of the five four-fermion operators that can produce same-sign top quark pairs, only three are considered in this analysis, as reported in Chapter 3:

$$
\begin{aligned}
\mathcal{O}_{RR} &= [\bar{t}_R \gamma^\mu u_R] [\bar{t}_R \gamma_\mu u_R] \\
\mathcal{O}_{LR}^{(1)} &= [\bar{Q}_L \gamma^\mu q_L] [\bar{t}_R \gamma_\mu u_R] \\
\mathcal{O}_{LR}^{(8)} &= [\bar{Q}_L \gamma^\mu T^A q_L] [\bar{t}_R \gamma_\mu T^A u_R]
\end{aligned}
\tag{5.1}
$$

A flavor restriction is then placed over the above listed operators. Specifically, the analysis is carried out assuming flavor universality for the EFT production of same-sign top pairs. Therefore the Wilson Coefficients (WCs) related to the *uutt*, *uctt*, *cctt* vertices are bound to have the same value regardless of the flavor of the initial state quarks in the interaction. The WCs related to the three operators are referred as c_{RR}, $c_{LR}^{(1)}$, $c_{LR}^{(8)}$.

Two nominal signal samples have been generated for tt and $\bar{t}\bar{t}$ EFT production with the following values associated to the WCs: $c_{RR} = 0.04$, $c_{LR}^{(1)} = 0.1$, $c_{LR}^{(8)} = 0.1$. The resulting cross section times Branching Ratio values are[1]:

$$
\begin{aligned}
\sigma(pp \longrightarrow tt) \times BR(t \longrightarrow W^+ b, W^+ \longrightarrow \ell^+ \nu_\ell) &= 97.6 \text{ fb} \\
\sigma(pp \longrightarrow \bar{t}\bar{t}) \times BR(\bar{t} \longrightarrow W^- \bar{b}, W^- \longrightarrow \ell^- \bar{\nu}_\ell) &= 2.4 \text{ fb}
\end{aligned}
\tag{5.2}
$$

The benchmark employed to generate the nominal samples has been chosen taking as a reference a BSM search carried out, within the ATLAS Collaboration, by researchers

---

[1]The associated errors are negligible and therefore omitted.

involved in the analysis presented in this Chapter. The reference analysis, based on a 2HDM, is a search for BSM processes involving an heavy Higgs boson and it is summarized in Appendix A. Same-sign top pairs *t-channel* production is among the searched processes. The EFT benchmark reported in (5.2) and used to generate the nominal samples has therefore been chosen so that the signal cross section would be consistent with the expected sensitivity to tt production resulting from the 2HDM search.

Among the three WCs c_{RR}, $c_{LR}^{(1)}$ and $c_{LR}^{(8)}$, the first one has been set to a lower value (0.04) to balance the contributions to the same-sign top pairs production cross section coming from the three different operators, given the larger effect stemming from $\mathcal{O}_{RR}$.

The nominal samples are employed in the optimization of the analysis strategy and to get the MC signal predictions used to perform the new physics search, as described in this Chapter.

Instead of generating multiple signal samples related to different assumptions on the WCs values, the MadGraph5_aMC@NLO reweighting tool [85, 86] has been employed to get different signal predictions within the nominal samples. The event weights related to the different EFT assumptions considered (therefore to the different sets of WCs values) are obtained through the re-computation of the same-sign top pairs production matrix element as:

$$W_{new} = \frac{|M_{new}|^2}{|M_{orig}|^2} \cdot W_{orig} \qquad (5.3)$$

where M_{new} is the re-computed matrix element, while M_{orig} and W_{orig} are the matrix element and the weight associated to the event in the original nominal sample.

The complete list of the different EFT benchmarks obtained through the reweighting procedure is reported in Table 5.1. The cross sections related to the various assumptions on the WCs values range between $\sim$10 fb and $\sim$100 fb for tt production times BR. Different ranges for the WCs values have been chosen for each EFT operator among the three considered. Specifically, the ranges related to c_{RR}, $c_{LR}^{(1)}$ and $c_{LR}^{(8)}$ are $[0.01; 0.05]$, $[0.05; 0.15]$ and $[0.1; 0.3]$ respectively. As occurred for the nominal samples, the values have been chosen to balance the contributions to the same-sign top pairs production cross section coming from the three different operators. The same EFT benchmarks have been employed for both tt and $\overline{tt}$ nominal samples.

To assess the validity of the reweighting procedure applied on signal events, additional tt signal samples have been generated assuming different WCs values for the three operators. For each additional sample, the reweighting validation has been performed by comparing the resulting kinematic distributions associated to same-sign top events with the same distributions resulting from the nominal sample after applying the weights related to the matching EFT assumption.

36

c_{RR}	$c_{LR}^{(1)}$	$c_{LR}^{(1)}$
0.02	0	0
0.03	0	0
0.04	0	0
0.05	0	0
0	0.05	0
0	0.07	0
0	0.1	0
0	0.15	0
0	0	0.1
0	0	0.2
0	0	0.25
0	0	0.3
0.01	0.05	0
0.01	0.1	0
0.01	0	0.2
0.01	0	0.3
0.01	0.05	0.2
0.01	0.05	0.3
0.01	0.1	0.2
0.01	0.1	0.3
0.02	0.05	0
0.02	0.1	0
0.02	0	0.2
0.02	0	0.3
0.02	0.05	0.2
0.02	0.05	0.3
0.02	0.1	0.2
0.02	0.1	0.3
0	0.05	0.2
0	0.05	0.3
0	0.1	0.2
0	0.1	0.3

Table 5.1: The full list of the EFT benchmarks obtained through the reweighting procedure for the nominal tt and $\overline{tt}$ signal samples.

The validation has been performed on tt events at *truth level*, without the detector simulation, employing additional samples generated with the WCs values reported in Table 5.2. The reweighting validation has also been performed at *reconstruction (reco)*

c_{RR}	$c_{LR}^{(1)}$	$c_{LR}^{(1)}$	level
0.04	0	0	truth, reco
0	0.1	0	truth, reco
0	0	0.1	truth, reco
0	0.1	0.2	truth
0.01	0.05	0	truth
0.02	0	0.3	truth
0.01	0.1	0.3	truth

Table 5.2: Values related to the WCs used to generate the additional tt samples employed for the reweighting validation at *truth* and *reco level*.

level, where the simulation of the detector geometry and response has been taken into account as well. Three additional samples have been employed to perform the *reco level* validation, related to assumptions of only one non-zero WC among c_{RR}, $c_{LR}^{(1)}$ and $c_{LR}^{(8)}$, as reported in the first three rows of Table 5.2.

No significant discrepancy has been observed between the compared distributions on both levels, as can be seen from the validation results reported in Appendix C.

Signal normalization

Since the final state topologies related to same-sign top pairs and SM $t\bar{t}W$ events share common features, the signal searched in this analysis could contribute to an excess of events at the level of $\sim 40\%$ with respect to $t\bar{t}W$ NLO predictions, observed in previous analyses carried out within the ATLAS Collaboration, targeting $t\bar{t}W/t\bar{t}H$ processes [87, 88]. Therefore, signal EFT predictions in the tt and $\bar{t}\bar{t}$ nominal samples have been scaled down to reproduce the observed excess, resulting in the following signal cross sections:

$$
\sigma(pp \longrightarrow tt) \times BR(t \longrightarrow W^+ b, W^+ \longrightarrow \ell^+ \nu_\ell) = 38.8 \text{ fb}
$$
$$
\sigma(pp \longrightarrow \bar{t}\bar{t}) \times BR(\bar{t} \longrightarrow W^- \bar{b}, W^- \longrightarrow \ell^- \bar{\nu}_\ell) = 0.96 \text{ fb}
$$
(5.4)

This signal benchmark has been employed in the optimization of the analysis strategy to ensure blinding with respect to the already observed $t\bar{t}W$ excess, in the event that the searched same-sign top signal would make up part of it. Once the analysis strategy has been optimized and a first estimate of the $t\bar{t}W$ background has been obtained, as reported in Section 5.7.1, resulting in an excess with respect to the SM predictions, the signal benchmark has been changed. Specifically, the signal normalization has been tuned according to the analysis expected sensitivity, as reported in Section 5.7.2. Pseudo-data events have been used to evaluate the expected sensitivity related to analysis framework.

The signal normalization that resulted in an expected significance of $\approx 3\sigma$ has been chosen as final benchmark and has been employed to perform the same-sign top pairs search using the complete set of Run 2 collision data events (*unblinded*). The associated signal cross sections are:

$$\sigma(pp \longrightarrow tt) \times BR(t \longrightarrow W^+b, W^+ \longrightarrow \ell^+\nu_\ell) = 1.94 \text{ fb}$$
$$\sigma(pp \longrightarrow \overline{tt}) \times BR(\overline{t} \longrightarrow W^-\overline{b}, W^- \longrightarrow \ell^-\overline{\nu}_\ell) = 0.048 \text{ fb}$$

(5.5)

5.1.2 Background processes

Together with the signal samples described above, other simulated samples related to background processes are employed in the analysis. Among the SM processes that can mimic the final state signature produced by signal same-sign top events one can find $t\bar{t}W$, $t\bar{t}(Z/\gamma)$, $t\bar{t}H$, $t\bar{t}t\bar{t}$, WZ+jets and ZZ+jets. Furthermore, rare background processes such as tZ+jets, $t\bar{t}WW$, $t\bar{t}HH$, $t\bar{t}WH$, $t\bar{t}ZZ$, WtZ, ttt and VVV (with $V = W, Z$) are considered in the analysis. All the processes listed above are referred as *irreducible backgrounds*.

Events related to $t\bar{t}W$ have been generated with NLO accuracy in the strong coupling constant α_S for $t\bar{t}W + 0, 1$ j and LO accuracy for $t\bar{t}W + 2$ j. A dedicated sample has been separately generated to evaluate LO electroweak contributions to the process. The $t\bar{t}(Z/\gamma)$ sample has been generated with NLO[2] and LO accuracy for $t\bar{t}(Z/\gamma) + 0, 1$ j and $t\bar{t}(Z/\gamma) + 2$ j respectively. Four top, $t\bar{t}H$ and diboson (WZ, ZZ) events have been generated at NLO. The highest available level of accuracy (NLO or LO) has been employed to generate rare background processes.

Besides the irreducible backgrounds listed above, other background events can produce the searched final state signature due to detector inefficiencies. Jets can be mis-reconstructed as leptons and lepton candidates can be reconstructed with the wrong electric charge. Furthermore, leptons originating from the decays of hadrons can be mis-reconstructed as *prompt* leptons (produced at the interaction vertex). This is also the case for electrons originating from photon conversion, that might as well be incorrectly reconstructed as *prompt*. Simulated samples related to $Z \longrightarrow \ell^+\ell^-$, $t\bar{t}$, single top and Wt processes have been generated at NLO and employed to estimate these backgrounds, referred as *reducible backgrounds*.

The cross section values related to the background processes taken into account in the analysis are reported in Table 5.3 with the associated uncertainties.

---

[2]For simplicity reasons, in the following the NLO accuracy is considered related to the QCD contribution, if not stated otherwise.

Process	Precision order	Cross section central value	Cross section uncertainty
MC samples contributing to reducible backgrounds			
$t\bar{t}$	NNLO+NNLL	832 pb [89]	-
s-, t-channel single top	NLO	227 pb [90, 91]	-
Wt single top	NNLO approx	71.7 pb [92]	-
$Z \longrightarrow l^+l^-$	NNLO	1.98 nb [93]	-
Irreducible backgrounds MC samples			
$t\bar{t}$ W	NLO	722.4 fb [94]	-
$t\bar{t}t\bar{t}$	NLO	12 fb [95]	20%
$t\bar{t}(Z/\gamma^* \longrightarrow l^+l^-)$	NLO	839 fb [96]	-
$t\bar{t}H$	NLO	507 fb [92]	11%
VV, $qqVV$	NLO	104 pb	-
tZ	NLO	33.3 fb	50%
$t\bar{t}t$	LO	1.6 fb	50%
WtZ	NLO	16 fb	50%
$t\bar{t}W^+W^-$	NLO	9.9 fb	50%
$t\bar{t}HH$	NLO	0.76 fb [96]	50%
$t\bar{t}WH$	NLO	1.6 fb [96]	50%
VVV	NLO	13.7 fb	50%

Table 5.3: Cross section values and their related uncertainties for the background samples used in the analysis. The cross section uncertainties related to the samples contributing to reducible backgrounds as well as to $t\bar{t}W$, $t\bar{t}(Z/\gamma*)$ and diboson are directly estimated in the analysis and therefore omitted in the table.

Additional simulated samples have been employed to estimate systematic uncertainties related to some of the background processes, as described in Section 5.6. A summary of the MC generators employed for irreducible and reducible backgrounds is reported in Appendix D together with details on the samples used to evaluate the systematic uncertainties.

5.2   Object reconstruction and event selection

The final state signature selected in the analysis, resulting from the fully leptonic decay of same-sign top quark pairs, produced at the interaction vertex in proton-proton collisions, consists of a pair of light leptons (e, μ) with same electric charge, two b-jets and missing transverse momentum associated to the two neutrinos originated from the W bosons decay. These objects are reconstructed with dedicated algorithms by processing signals produced by particles transversing ATLAS subdetectors. The following sections summarize the techniques and algorithms employed to reconstruct the final state objects relevant for the analysis: electrons, muons, jets, b-jets and missing transverse momentum. An overview of the selection criteria applied to the reconstructed objects to perform the analysis is reported as well.

Since some studies on the evaluation of muon reconstruction efficiencies and muon momentum calibration have been carried out as reported in Appendix B, a detailed description of muon reconstruction is presented in the next section.

5.2.1   Muons

Muon reconstruction and identification are performed based on the information of ATLAS Inner Detector (ID), calorimeters and Muon Spectrometer (MS) [97]. Muon candidates are reconstructed from tracks down to $p_T = 2$ GeV. Five types of muons are defined, depending on the available information related to the candidate:

- **Combined muon** candidates (CB) are reconstructed by matching MS tracks to ID tracks. This is performed through a track fit based on MS and ID hits, taking into account the energy loss in the calorimeters. Following the fit result, MS hits associated to the track might be updated and the fit repeated. This is the most commonly used muon type in ATLAS physics analyses. In the forward detector region $|\eta| > 2.5$, MS tracks can be combined with segments reconstructed from hits in the pixel and SCT detectors. This subset of CB muons is referred as silicon-associated forward muons (SiF).

- **Inside-out combined muon** candidates (IO) are reconstructed by matching ID tracks to MS hits. A track fit is performed based on the ID track, MS hits and energy loss in the calorimeters. Since the fit does not require an MS track to be reconstructed, this muon type is characterized by a higher efficiency with respect to CB muons.

41

- **Muon Extrapolated** candidates (ME) are reconstructed from a track in the MS extrapolated to the IP, without requiring a match with an ID track. By exploiting the whole MS coverage, muon candidates are reconstructed up to $|\eta| = 2.7$.

- **Segment-Tagged muon** candidates (ST) are identified only from ID track information, requiring the ID track to match a reconstructed segment in the MS.

- **Calo-Tagged muon** candidates (CT) are reconstructed from an ID track matched to an isolated energy deposit in the calorimeter consistent with a minimum ionizing particle. The lower p_T threshold for CT candidates is increased from 2 to 5 GeV due to the large background contamination at lower p_T values.

In order to provide high-quality muons to be employed in physics analyses, further requirements are applied on muon candidates. These requirements involve the number of hits in the ID and MS, the reconstructed track quality and other proprieties related to the reconstructed muon. Five different *Working Points* (WPs) are defined based on different requirements placed on the reconstructed candidate, enhancing purity, efficiency or targeting specific regions at very high or very low p_T values. Specifically, the efficiency of a WP represents the probability of a reconstructed prompt muon to satisfy the WP selection criteria, while the purity of a WP is one minus the fraction of light hadrons mis-reconstructed as muons satisfying the WP selection.

The following muon WPs are defined:

- The **Medium** WP selection is based on CB and IO muons with at least 2 MDT or CSC stations with three or more hits, except for the $|\eta| < 0.1$ region, where only 1 station with at least three hits is allowed, and for the $2.5 < |\eta| < 2.7$ region, where ME and SiF muons are employed instead. To suppress fake muons, a loose selection based on the compatibility of the momentum measured from ID and MS information is applied. This is the most used WP in physics analyses since it results in good efficiency, a per-mill fake rate and small systematic uncertainties related to the muon reconstruction.

- The **Loose** WP is defined in order to maximize selection efficiency. All muons classified as `Medium` also satisfy the `Loose` WP requirements. Together with IO muons, ST and CT muons are employed as well in the $|\eta| < 0.1$ region to recover the efficiency loss in the `Medium` WP due to a gap in the MS coverage. In the $|\eta| < 1.3$ region, to increase the selection efficiency of low-p_T muons, only one station with at least three hits is required for muons with $p_T < 7$ GeV, if they are also independently reconstructed as ST muons.

- The **Tight** WP is defined to maximize purity. The WP selection is based only on CB and IO muons with at least two MDT os CSC stations with three or more hits. A requirement is placed on the value of the normalized χ^2 resulting form the track fit to reject bad reconstructed tracks caused by in-flight hadron decays. To enhance background rejection a selection is placed on the compatibility of the momentum measurements in the ID and MS.

- The **Low-p_T** WP is defined to target muons with low p_T that may lose all their energy in the calorimeter and therefore may not reach the outer MS stations. For this reason, `Low-`p_T muons are mainly defined from IO reconstructed muons, although also CB muons are employed. To enhance purity, IO muons are required to be also independently reconstructed as ST. At least one station is required to have three or more hits, except in the $|\eta| > 1.3$ region, where two stations are required. The `Low-`p_T WP definition corresponds to the `Medium` one for $p_T \geq 18$ GeV. Further requirements are placed to reject the background coming from light hadrons decays. Two different `Low-`p_T WPs are defined: a cut-based WP and a multivariate-based WP. The first one is defined to reduce kinematic dependencies of background efficiencies, while the second one maximizes the overall `Low-`p_T muon identification performance.

- The **High-p_T** WP is defined to target muons with very high p_T that exhibit almost straight trajectories when transversing the ATLAS detector. The WP selection is based on CB and IO muons passing the `Medium` WP requirements. Furthermore, only muons with at least three MDTs or CSCs with three or more hits are accepted. All muons falling into the barrel-end-cap overlapping region ($1.0 < |\eta| < 1.1$) are rejected, since there the alignment between different chambers is known with less precision.

A detailed review of the evaluation of muon reconstruction efficiencies for the five defined WPs is reported in Appendix B, together with a description of the procedure applied for the muon momentum calibration.

All muon candidates employed in the analysis are required to have $|\eta| < 2.5$ and $p_T > 10$ GeV. They additionally have to satisfy the *FCLoose* isolation WP. A selection is also placed on the impact parameter significance ($d_0/\sigma_{d_0} < 3$) and on the longitudinal impact parameter value ($|z_0 sin\theta| < 0.5$ mm). Muons that satisfy the previous requirements and the `Loose` identification WP are pre-selected in the analysis and employed within the overlap removal algorithms, as reported in Section 5.2.6. Subsequently, candidates that satisfy the `Medium` identification WP are selected and different categories of muons are

defined and employed in the analysis based on looser or tighter isolation requirements, as reported in Section 5.2.3.

5.2.2 Electrons

Electrons are reconstructed as Inner Detector charged tracks that match clusters of energy deposit in the electromagnetic calorimeter [98]. Electron candidates employed in the analysis are required to satisfy $p_T > 10$ GeV, $|\eta| < 2.47$ and the `FCLoose` isolation WP. Candidates in the transition region between different components of the electromagnetic calorimeter ($1.37 < |\eta| < 1.52$) are vetoed. Only candidates with the ID track reconstructed as originating from the primary vertex of the proton-proton interaction are considered. The same requirement on the longitudinal impact parameter is placed on electron candidates as described above for muons ($|z_0 sin\theta| < 0.5$ mm), while a looser selection is applied to the impact parameter significance: $d_0/\sigma_{d_0} < 5$. Different categories of electrons are defined in Section 5.2.3 and employed in the analysis. Looser or tighter isolation and identification requirements are placed on electron candidates according to the different categories, with the loosest category (`Loose` identification WP) employed within the overlap removal algorithms reported in Section 5.2.6. Electrons are also classified based on the scores of Boosted Decision Trees (BDTs) trained to reject candidates reconstructed with the wrong electric charge. Finally, additional requirements are placed on some categories to suppress electrons originating from photon conversion.

5.2.3 Lepton categories employed in the analysis

Muons and electrons, reconstructed and selected following the requirements presented in the previous sections, are classified according to different lepton categories defined in the analysis. Four categories are defined for both electrons and muons: Loose inclusive (Linc), Medium inclusive (Minc), Medium (M) and Tight (T), as summarized in Table 5.4. Linc leptons are defined following the selection criteria presented in the previous sections. The `Loose` identification WP is used for Linc electron candidates, while the `Tight` identification WP is required for electrons in the other 3 categories. The `Medium` identification WP is employed for muons in all the defined categories.

For both electron and muon candidates, a multivariate-based algorithm, called *Prompt Lepton Improved Veto* (PLIV) is employed in the analysis to either select or reject *non-prompt* leptons. These are mainly generated in the decays of light,*c*- and *b*-hadrons. Although non-prompt leptons might satisfy the selection criteria described in the previous sections, they can be identified using their lifetime information and tracing them

back to the displaced decay vertices associated to the hadrons that originated them. The PLIV multivariate algorithm is based on BDTs and makes use of many variables to perform the non-prompt lepton identification: impact parameter, lifetime, isolation, secondary vertex and track information related to the lepton candidate. The algorithm is separately optimized for electrons and muons.

Both PLIV Working Points, defined based on the BDTs output scores, are employed in the analysis: PLIV *Tight* and *VeryTight*. Since prompt and non-prompt lepton efficiencies are p_T-dependant, these WPs are defined by applying different cuts on the BDTs scores depending on the lepton candidate p_T to gain uniformity in the WP efficiency. Specifically, both working points exhibit almost uniform prompt muon efficiencies with values above 90% for $p_T > 40$ GeV and non prompt muon efficiencies ranging from $\simeq 2\%$ to $\simeq 3\%$ for PLIV *Tight* and from $\simeq 1\%$ to $\simeq 2\%$ for PLIV *VeryTight* depending on the transverse momentum of the lepton. Prompt electron efficiencies range from 70% to values above 90%, with the lower efficiency values associate to the *VeryTight* WP. Efficiencies related to non prompt electrons range from $\simeq 2\%$ to $\simeq 5\%$ for electrons satisfying the PLIV *Tight* WP and from $\simeq 1\%$ to $\simeq 3\%$ for the PLIV *VeryTight*.

The PLIV *Tight* and *VeryTight* are related to the Minc and T lepton categories respectively. One additional PLIV WP *Tight-not-VeryTight*, related to the M category, has been defined to select lepton candidates that satisfy *Tight* but do not pass the *VeryTight* selection.

Leptons classified according to the above mentioned categories are employed within the analysis to select signal-like events in the Signal Regions and also to build Control Regions enriched in non-prompt leptons.

Additional selection requirements are applied to electrons in the Minc, M and T categories.

To reject the background coming from electrons with a mis-identified electric charge, a BDT based algorithm, referred as ECIDS, is employed. Six variables, listed in Table 5.5, are used for the BDT training to identify and suppress electron candidates reconstructed with the wrong charge. A BDT score of at least 0.7 is required for Minc, M and T electron candidates, corresponding to a 92.5% efficiency on the selection of electrons with the correct electric charge assigned.

To suppress background electrons originated from photon conversion taking place at the interaction point or in the detector material, a selection is applied based on the invariant mass value of the electron candidate and its closest track evaluated at the primary and conversion vertices ($m_{trk-trk,PV}$, $m_{trk-trk,CV}$). Specifically, electron candidates with a conversion vertex at $r > 20$ mm and $0 < m_{trk-trk,CV} < 100$ MeV are vetoed, since they are classified as candidates coming from photon conversion in the

45

	e				μ			
	Linc	Minc	M	T	Linc	Minc	M	T
`FCLoose` isolation		Yes				Yes		
PLIV WP	No	*Tight*	*Tight-not-VeryTight*	*VeryTight*	No	*Tight*	*Tight-not-VeryTight*	*VeryTight*
Identification	Loose		Tight			Medium		
Charge mis-assignment veto (ECIDS)	No		Yes			N/A		
IntCo, ExtCO veto	No		Yes			N/A		
pseudorapidity η	$(|\eta| < 1.37)\|\|(1.52 < |\eta| < 2.47)$				$|\eta| < 2.5$			
Transverse impact parameter significance $|d_0|/\sigma_{d_0}$	< 5				< 3			
Longitudinal impact parameter $|z_0 \sin\theta|$	< 0.5 mm							

Table 5.4: Summary of the definition of the lepton categories employed in the analysis. Loose inclusive (Linc), Medium inclusive (Minc), Medium (M), and Tight (T).

Variable	Description
p_T	Transverse momentum
η	Pseudorapidity
charge$\times d_0$	Electric charge times the transverse impact parameter
E/p	Ratio of the cluster energy to the track momentum
$\Delta\Phi$	$\Delta\Phi$ between the cluster position in the middle layer and the extrapolated track
Weighted average charge	Charge weighted by the sum over all associated track particles

Table 5.5: Variables used to train the electron ECIDS BDT discriminant.

detector material (referred as $MatCO$ e). Electrons that do not satisfy the previous selection, but have $0 < m_{trk-trk,PV} < 100$ MeV, are classified as resulting from photon conversion taking place at the interaction point (referred as $IntCO$ e), and therefore are vetoed as well.

5.2.4 Jets and b-jets

Particle jets are generated by the hadronization of high-p_T quarks and gluons. They are reconstructed as a collection of tracks in the Inner Detector and clusters of energy deposit in both the electromagnetic and the hadronic calorimeters. Specifically, the anti-k_T algorithm with $\Delta R = 0.4$ on particle-flow objects [99, 100](`AntiKt4EMPFlowJets`) is employed to perform the jet reconstruction. Jet candidates are required to satisfy $|\eta| < 4.5$ and $p_T > 25$ GeV. The Jet Vertex Tagger (JVT) algorithm [101] is employed to reject jets originating from the pile-up for candidates with $|\eta| < 2.4$ and $p_T < 60$ GeV. Specifically, the `JVT Tight` WP is required.

Jets originating from b quarks are identified (*b-tagged*) using the DL1r multivariate-based algorithm, that makes use of the information related to displaced tracks within the jet to reconstruct secondary and tertiary decay vertices [102]. Two b-tagging WPs are employed in the analysis, corresponding to an average efficiency of 60% and 77% for b-jets with $p_T > 20$ GeV and $|\eta| < 2.5$ in $t\bar{t}$ events. The 77% WP is employed to select events in all Signal Regions and in Control Regions related to non-prompt lepton backgrounds, while the 60% WP is used to build Control Regions enriched in VV and $t\bar{t}Z$ events.

A summary of the jet and b-jet selection requirements employed in the analysis is reported in Table 5.6.

Algorithm details	Anti-k_T
	$\Delta R = 0.4$
	PFlow
Selection requirements	
p_T	> 25 GeV
$|\eta|$	< 2.5
JVT	> 0.5 for $p_T < 60$ GeV, $|\eta| < 2.4$
b-tagging requirements	
Algorithm	DL1r
	Eff = 60,77%

Table 5.6: Jet, b-jet reconstruction and selection criteria.

5.2.5 Missing transverse momentum

The missing transverse momentum E_T^{miss} is defined as the magnitude of the negative vector sum of the transverse momenta of all reconstructed objects in an event, taking also into account the energy deposits that have not been associated to any physical object [103]. This variable is employed in the analysis to build Control Regions to estimate the background related to non-prompt leptons.

5.2.6 Overlap removal

To prevent a particle from being reconstructed as two different objects in the same event, overlap removal algorithms are applied. These techniques allow to avoid double counting and at the same time to retain reconstructed close-by objects. Concerning leptons, the overlap removal algorithms are applied to muons and electrons that satisfy the loosest

selection requirements reported in Section 5.2.1 and Section 5.2.2 respectively. The procedures employed are tailored on different reconstructed object pairs:

- Electron/Muon: `Loose` muons reconstructed from CT tracks in the $\eta \approx 0$ region can be also reconstructed as electrons. If an electron and a muon are reconstructed within $\Delta R < 0.01$ the muon is removed if it is calo-tagged, otherwise the electron is removed.

- Electron/Jet: if an electron and a jet are reconstructed within $\Delta R < 0.2$, the jet is removed if it is not b-tagged and its transverse momentum is lower than 200 GeV. Above this p_T threshold, the jet is removed regardless of the b-tagging.

- Muon/Jet: if a muon and a jet are reconstructed within $\Delta R < 0.4$, the jet candidate is removed if it is not b-tagged and has less than 3 tracks with $p_T < 500$ MeV.

- Jet/Lepton: if a jet candidate is not removed based on the previous conditions and it is reconstructed within $\Delta R < 0.04 + 10$ GeV$/p_{T,lepton}$ from a lepton candidate (up to a maximum value $\Delta R = 0.4$), the lepton is removed.

5.2.7 Primary vertex and triggers

Only events with a reconstructed primary vertex [104] are employed in the analysis. The primary vertex is chosen as the one with the largest value of $\sum p_T^2$ related to the tracks associated to the vertex, with each track satisfying $p_T > 0.5$ GeV.

Furthermore, all events are required to fire single lepton (e, μ) or dilepton ($e\mu$, ee, $\mu\mu$) triggers. The complete list of lepton High Level Triggers (HLT) employed for the different data taking years is reported in Table 5.7.

5.2.8 Preliminary selection of signal-like events

A preliminary selection of signal-like events is performed by applying additional requirements on the final state objects described in the previous sections. Events passing this selection are used to train the Neural Networks employed in the analysis, as described in Section 5.3. Signal Regions are then defined, as reported in Section 5.4, by adding further requirements to the preliminary selection reported in this section.

Signal-like events are required to have two light leptons ($\ell = e$, μ) with same electric charge. Both leptons have to satisfy $p_T(\ell) > 20$ GeV. At least two jets are required in the event and two different combinations of PLIV and b-jet requirements are employed in the signal selection. Specifically, only events with both leptons classified as Minc (PLIV

48

	Single lepton triggers (2015)
μ	`HLT_mu20_iloose_L1MU15, HLT_mu50`
e	`HLT_e24_lhmedium_L1EM20VH, HLT_e60_lhmedium, HLT_e120_lhloose`

	Dilepton triggers (2015)
$\mu\mu$	`HLT_mu18_mu8noL1`
ee	`HLT_2e12_lhloose_L12EM10VH`
$e\mu, \mu e$	`HLT_e17_lhloose_mu14`

	Single lepton triggers (2016)
μ	`HLT_mu26_ivarmedium, HLT_mu50`
e	`HLT_e26_lhtight_nod0_ivarloose, HLT_e60_lhmedium_nod0,` `HLT_e140_lhloose_nod0`

	Dilepton triggers (2016)
$\mu\mu$	`HLT_mu22_mu8noL1`
ee	`HLT_2e17_lhvloose_nod0`
$e\mu, \mu e$	`HLT_e17_lhloose_nod0_mu14`

	Single lepton triggers (2017 / 2018)
μ	`HLT_mu26_ivarmedium, HLT_mu50`
e	`HLT_e26_lhtight_nod0_ivarloose, HLT_e60_lhmedium_nod0,` `HLT_e140_lhloose_nod0`

	Dilepton triggers (2017 / 2018)
$\mu\mu$	`HLT_mu22_mu8noL1`
ee	`HLT_2e24_lhvloose_nod0`
$e\mu, \mu e$	`HLT_e17_lhloose_nod0_mu14`

Table 5.7: Single lepton and dilepton triggers employed to select events for the different data taking years.

Tight) and at least 2 *b*-jets passing the 77% *b*-tagging WP or events with both T leptons (PLIV *VeryTight*) and exactly one *b*-tagged jet passing the 77% WP are selected. This PLIV and *b*-tagging requirements have been chosen to enhance the efficiency and purity in the Signal Regions and at the same time to ensure mutual exclusion with respect to the analysis Control Regions, defined as reported in Section 5.5 to accurately estimate background contributions.

A summary of the preliminary selection of signal-like events is reported in Table 5.8.

Signal-like event selection	
Number of leptons	$N_\ell = 2$
Total lepton charge	+2 and -2
Lepton p_T	$p_T(\ell) > 20$ GeV
Lepton pseudorapidity	$e : |\eta| < 1.37$ && $1.52 < |\eta| < 2.47$, $\mu : |\eta| < 2.5$
Lepton ID	$e : $ `Tight`, $\mu : $ `Medium`
Number of jets	$N_{jets} \geq 2$
Jet pseudorapidity	$|\eta| < 4.5$
Jet p_T	$p_T(j) > 25$ GeV
PLIV and b-jet requirements	MincMinc with ≥ 2 b-jets at 77% WP OR TT with $= 1$ b-jet at 77% WP

Table 5.8: Summary of the preliminary selection of signal-like events.

5.3 Neural Network based strategy

Events passing the signal preselection described in the previous section are employed to train a Deep Neural Network (DNN) in order to build separate Signal Regions enriched in same-sign top events resulting from different EFT operators (one for the RR operator $\mathcal{O}_{RR}$ and one for the two LR operators $\mathcal{O}_{LR}^{(1)}$ and $\mathcal{O}_{LR}^{(8)}$). Events are then additionally split according to the same-sign lepton charge, resulting in four Signal Regions. Within each defined SR, a second DNN is trained to perform signal-background discrimination.

5.3.1 Deep Neural Network architecture

The DNNs employed in the analysis are based on `KERAS` library [105] with `TENSORFLOW` as backend [106] and have an identical architecture, with one input layer and five hidden layers consisting of 128, 64, 32, 16 and 8 nodes respectively. The NNs are employed as classifiers, therefore the output layer consists of a single node. The `SIGMOID` activation function is used for the output node, while the `RELU` function is employed in all the other layers. Binary Cross Entropy is used as loss function with the `ADAM` optimizer [107]. The input variables are scaled to improve the NN convergence with a standard `SCIKIT-LEARN` [108] scaler.

To make use of all generated events in the training of each NN, the simulated signal and background samples are split, based on the event run number[3], in two subsamples *even* and *odd*. Each NN is trained using the *even* and *odd* subsamples separately, with 80% and 20% of the events in each subsample used for training and validation respectively. Then, the performance of the NN trained on even events is tested using the odd subsample, and viceversa for the NN trained on odd events. This procedure is referred as *even-odd cross validation*. Collision data events with an even(odd) run number are then classified using the odd(even) trained NN when performing the analysis. This procedure is carried out for every NN employed in the analysis.

5.3.2 DNN for signal categorization

In order to build different Signal Regions related to either the RR chirality operator $\mathcal{O}_{RR}$ or the two LR operators $\mathcal{O}_{LR}^{(1)}$, $\mathcal{O}_{LR}^{(8)}$ a DNN, referred as NN$^{\text{SvsS}}$, has been trained to discriminate same-sign top pairs generated by the different EFT operators. The classification is performed exploiting the kinematic differences of same-sign top events generated by $\mathcal{O}_{RR}$ or $\mathcal{O}_{LR}^{(1)}$ and $\mathcal{O}_{LR}^{(8)}$. Signal events in the nominal tt and $\overline{tt}$ samples have

---

[3]One random run number is associated to each simulated event, while the actual run number related to the data taking periods is associated to data events.

been weighted first according to the EFT benchmark $c_{RR} = 0.04, c_{LR}^{(1)} = 0, c_{LR}^{(8)} = 0$ and then using the benchmark $c_{RR} = 0, c_{LR}^{(1)} = 0.1, c_{LR}^{(8)} = 0.2$. The weighted events are then used to train and test the NN^{SvsS}. It should be noticed that the WCs values employed in the NN^{SvsS} training are different with respect to the ones used to generate the nominal signal samples ($c_{RR} = 0, c_{LR}^{(1)} = 0.1, c_{LR}^{(8)} = 0.1$). Among the different benchmarks with $c_{RR} = 0$ obtained through the reweigthing (see Table 5.1 in Section 5.1), the one that resulted in the largest kinematic difference between same-sign top pairs generated by the RR operator or the two LR operators has been employed to train the NN^{SvsS}.

The classification is based on the 9 input variables listed in Table 5.9. The kinematic distributions related to the input variables for RR and LR signal events can be found in Appendix E together with their importance ranking. The data/MC agreement related to the input variables has been checked in the unblinded bins of the distributions to assess the good modelling provided by the simulation, as reported in Appendix E as well.

Signal categorisation Neural Network input variables
$\Delta\Phi$, $\Delta R, \Delta\eta$ between the two same-sign leptons
Invariant mass $M_{\ell\ell}$ of the two same-sign leptons
Sum of the p_T of jets and leptons ($H_{T,jet}, H_{T,lep}$)
p_T of the leading jet
Missing transverse momentum E_T^{miss}
Transverse mass of leptons and missing transverse momentum ($M_{T,lep-met}$) [4]

Table 5.9: Input variables for the NN^{SvsS}.

The NN^{SvsS} output distribution is reported in Figure 5.1 for simulated signal events. Output values close to 0 and 1 correspond to RR- and LR-like events. The NN^{SvsS} output is employed to define two Signal Regions SR_{RR} and SR_{LR} by requiring its value to be ≤ 0.538 and > 0.538 respectively. This value maximises the sum of the classification efficiencies for both RR and LR signals and corresponds to a classification accuracy of 65% for bot RR and LR categories. The ROC curve associated to the NN is shown in Figure 5.2 for separate and combined even/odd trainings. All signal simulated events have been employed to evaluate the combined ROC curve, with even events being processed by the odd trained NN and viceversa. It can be seen that the performance of the NN is comparable for the even and odd trainings, as expected. The NN^{SvsS} exhibits a good discrimination performance, despite the similarity of the signal events generated by the O_{RR} or the $O_{LR}^{(1)}, O_{LR}^{(8)}$ operators.

---

[4]The transverse mass is defined as: $M_T = \sqrt{E^2 - p_z^2}$
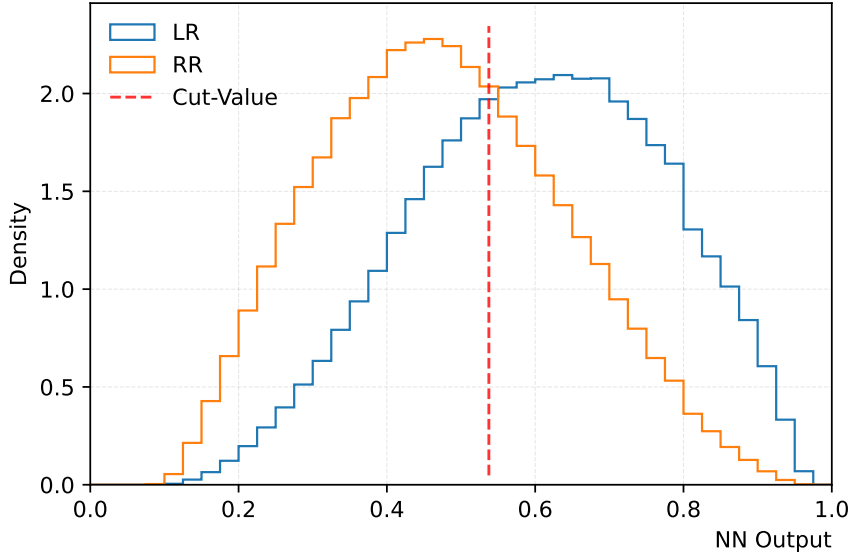
Figure 5.1: NN$^{\text{SvsS}}$ output distribution for RR and LR same-sign top signal events. Two Signal Regions SR_{RR} and SR_{LR} are defined based on the output value. The dashed red line shows the output value 0.0538 chosen to define the regions. Specifically, events resulting in an output lower or higher than the cut-value are classified as belonging to SR_{RR} and SR_{LR} respectively.

Figure 5.3a shows the NN$^{\text{SvsS}}$ output distribution for signal (RR and LR) and background simulated events. As it can be seen, background events are mostly classified by the NN as LR-like. This behaviour is caused by the background kinematic distributions being more similar to the ones related to the LR operators than to the RR one, as can be seen from the distributions reported in Appendix E. The same behaviour is exhibited by all background processes, as shown in Figure 5.3b, and even more pronounced for $t\bar{t}W$ events.
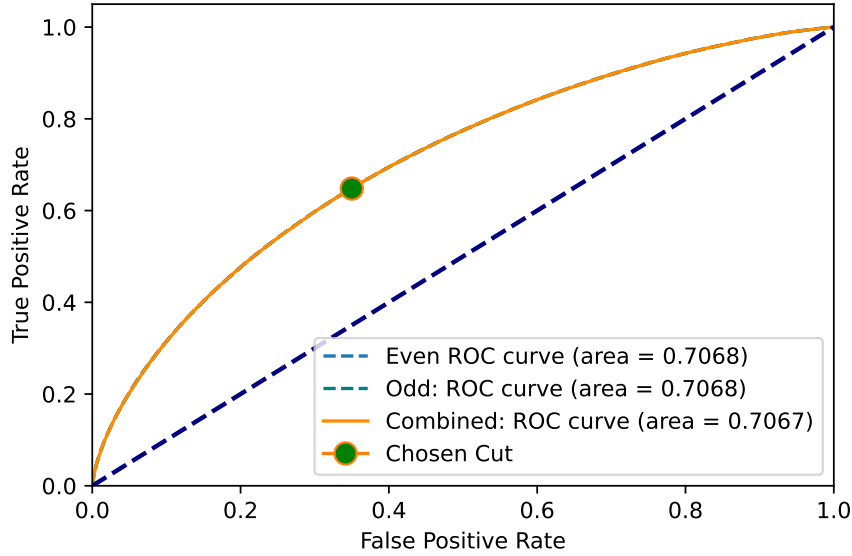
Figure 5.2: NN$^{\text{SvsS}}$ ROC curve. It can be seen that the performance of the NN is comparable for the even and odd trainings, as expected. The green dot corresponds to the NN$^{\text{SvsS}}$ output cut chosen to define SR_{RR} and SR_{LR}.
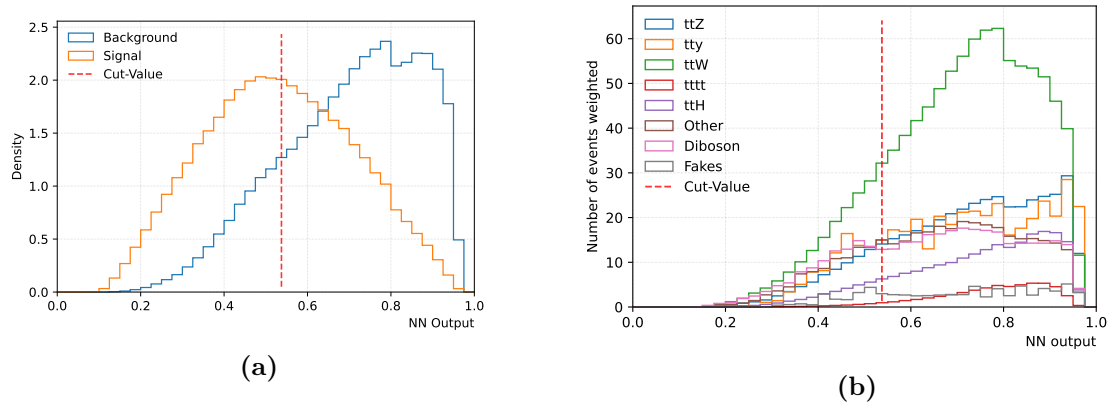
Figure 5.3: NN$^{\text{SvsS}}$ output distribution for signal (RR and LR) and background events (a) and for the different background processes considered in the analysis (b). The dashed red line shows the output value 0.0538 chosen to define the SR_{RR} and SR_{LR} regions. Specifically, events resulting in an output lower or higher than the cut-value are classified as belonging to SR_{RR} and SR_{LR}.

5.3.3 DNN for SvsB discrimination

A second DNN, referred as NN$^{\text{SvsB}}$, is trained separately on the SR_{RR}, SR_{LR} Signal Regions defined in the previous section to discriminate signal from background events. The kinematic distributions associated to tt and $\overline{tt}$ events exhibit significant differences as it can be seen from Figure 5.4. Therefore, to gain a high discriminating power for both tt and $\overline{tt}$, SR_{RR} and SR_{LR} are further divided, before training the second NN, into SR_{RR}^{++}, SR_{RR}^{--} and SR_{LR}^{++}, SR_{LR}^{--} based on the electric charge of the two same-sign leptons. Training the NN over tt and $\overline{tt}$ events at the same time would have resulted in a NN performance predominantly based only on tt events, due to the cross section unbalance between the two processes. As a consequence, the discriminating power for $\overline{tt}$ events would have been lower[5].
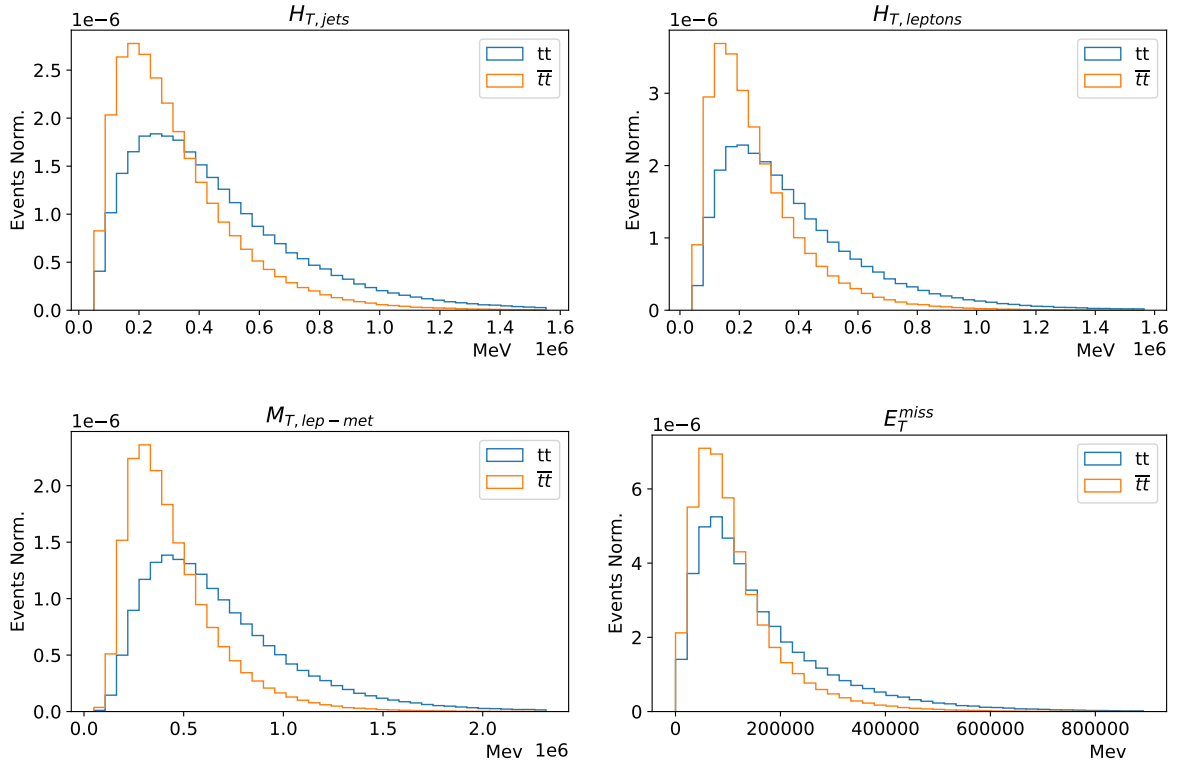
Figure 5.4: The kinematic distributions associated to tt and $\overline{tt}$ events are shown as blue and orange lines respectively. From top left to bottom right: $H_{T,jets}$, $H_{T,leptons}$, $M_{T,lep-met}$ and E_T^{miss}.

---

[5]The charge split has not been applied before training the NN$^{\text{SvsS}}$ since it was found to be ineffective for the discrimination of RR and LR signal events.

The NN$^{\text{SvsB}}$ is trained using 6 input variables, listed in Table 5.10. The associated kinematic distributions for signal ($tt + \overline{tt}$) and background events are reported in Appendix E together with their importance ranking. Although kinematic variables related to the dilepton system, such as $\Delta\Phi(\ell, \ell)$, $\Delta R(\ell, \ell)$ and $M(\ell, \ell)$, display significant differences in signal and background events, they are not employed as NN$^{\text{SvsB}}$ input variables. Instead, a cut-based selection is applied on events, after the NN training, based on the value of $\Delta\Phi(\ell, \ell)$ to reject background events and therefore enhance the purity of the SRs. This way, the NN$^{\text{SvsB}}$ performance is unbiased with respect to the value of $\Delta\Phi(\ell, \ell)$ and Validation Regions can be also built based on the lepton azimuthal distance, as reported in the next section.

Signal vs Background Neural Network input variables
Sum of the p_T of leptons ($H_{T,lep}$)
B-tagging score of 1st and 2nd leading jet
p_T of the leading jet
Transverse mass of leptons and missing transverse momentum ($M_{T,lep-met}$)
Number of jets (N_{jets})

Table 5.10: Input variables for the NN$^{\text{SvsB}}$.

The NN$^{\text{SvsB}}$ output distributions for simulated signal and background events are reported in Figure 5.6 for the 4 defined SRs. The associated ROC curves are reported in Figure 5.7 for separate and combined even/odd trainings in each SR. All signal simulated events have been employed to evaluate the combined ROC curve, with even events being processed by the odd trained NN and viceversa. As expected, the NN performance is comparable for even and odd trainings. It can be noticed that the discriminating performance is lower for negative events in both SR_{RR}^{--} and SR_{LR}^{--} than in the corresponding positive regions. This is due to the kinematic distributions of the input variables, which are found to be less dissimilar from the backgrounds for $\overline{tt}$ events, as can be seen from Figure 5.5 showing the normalized distribution of $M_{T,lep-met}$ for tt, $\overline{tt}$ and background events in SR_{RR} and SR_{LR}. The distributions related to all the NN$^{\text{SvsB}}$ input variables are reported in Appendix E.

The NN$^{\text{SvsB}}$ output distributions obtained from MC samples are employed in the statistical analysis to search for signal events in the collected data, as reported in detail in Section 5.7.
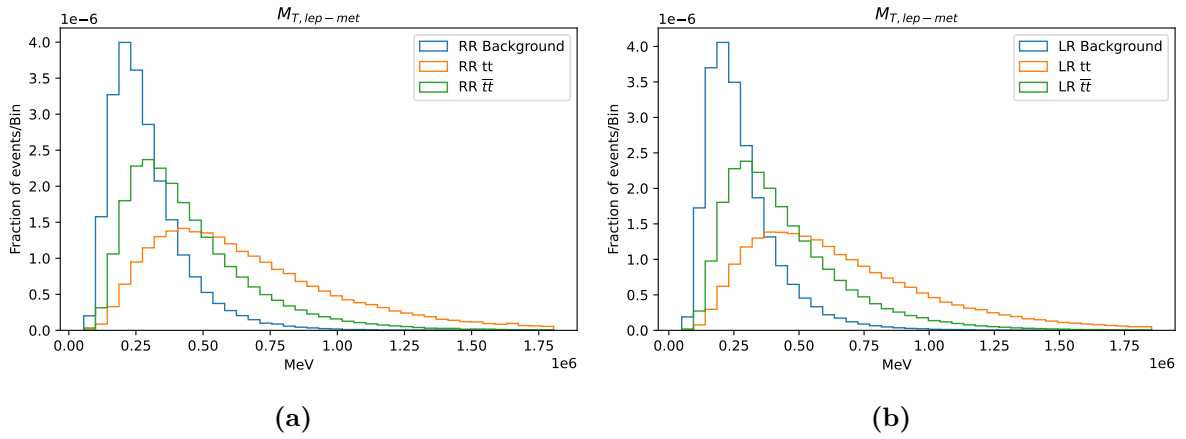
Figure 5.5: Normalized distribution of the NN$^{\text{SvsS}}$ input variable $M_{T,lep-met}$ for SR_{RR} (a) and SR_{LR} (b). The distributions related to tt, $\overline{tt}$ and background events are reported in orange, green and blue respectively.
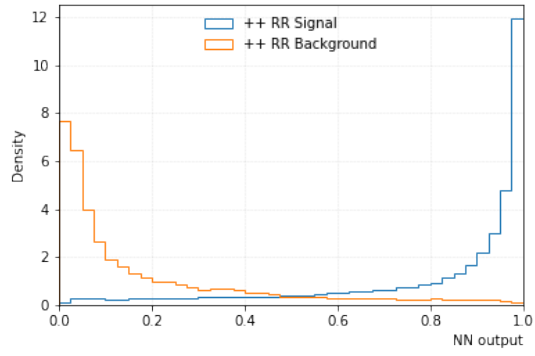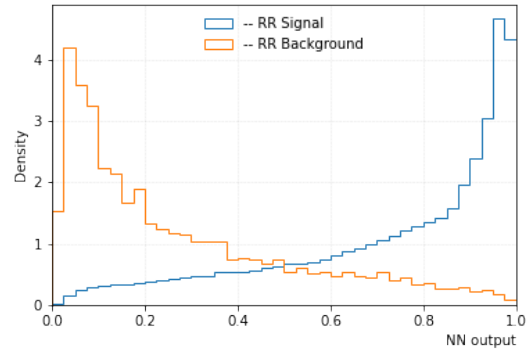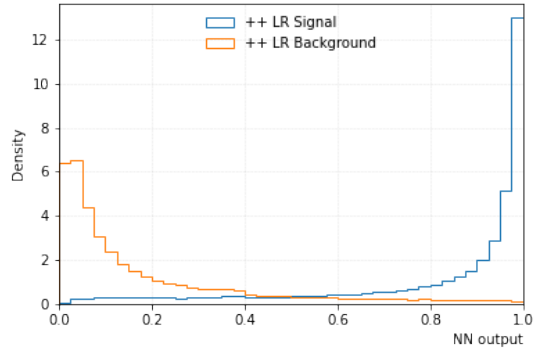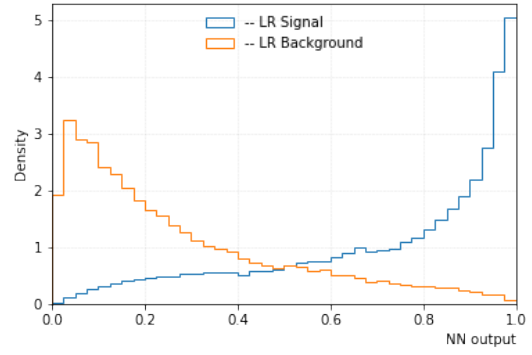
Figure 5.6: NN^{SvsB} output distributions for signal and background events for SR_{RR}^{++} (a), SR_{RR}^{--} (b), SR_{LR}^{++} (c) and SR_{LR}^{--} (d).
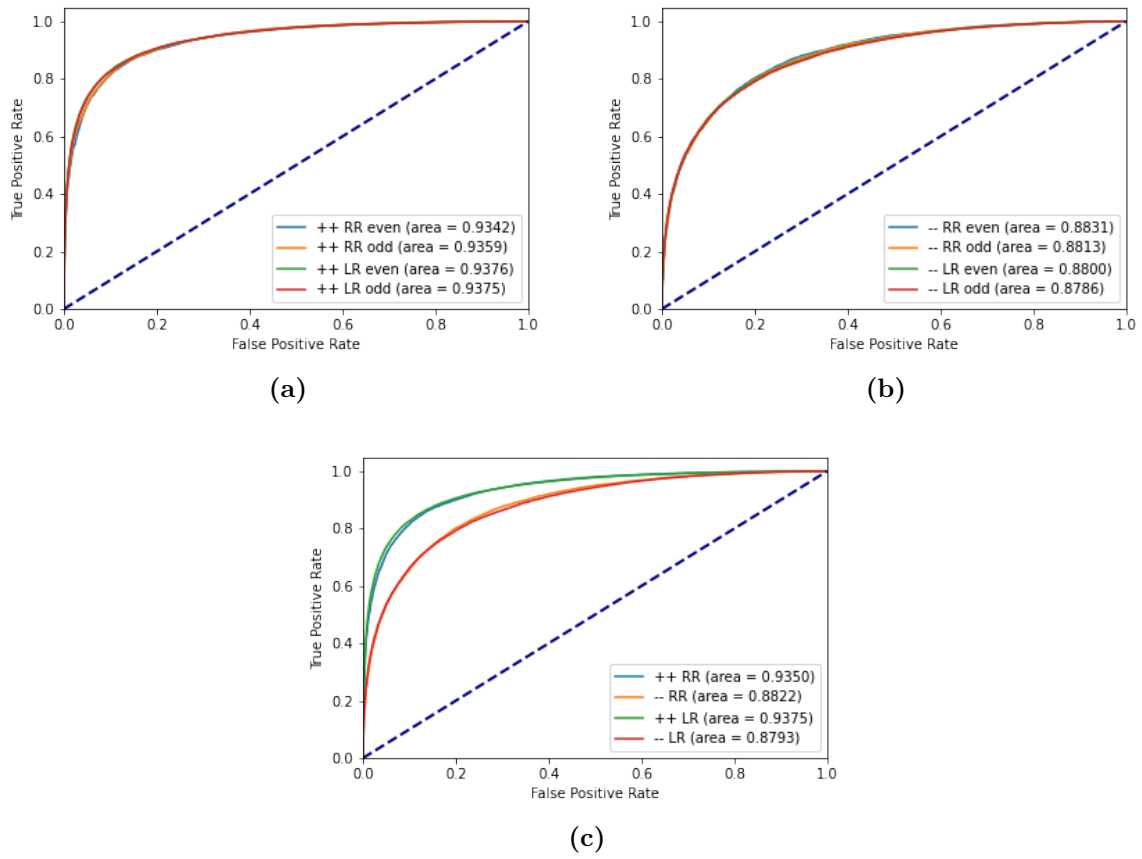
Figure 5.7: NN$^{\mathrm{SvsB}}$ ROC curves related to the even and odd trainings for $SR_{RR}^{++}, SR_{LR}^{++}$ (a) and for $SR_{RR}^{--}, SR_{LR}^{--}$ (b). It can be seen that the performance for the even and odd trainings are comparable, as expected. The combined ROC curves are reported in (c) for the 4 SRs.

5.4 Signal and Validation Regions

Once the DNNs described in the previous sections have been trained to define the four SR_{RR}^{++}, SR_{RR}^{--}, SR_{LR}^{++}, SR_{LR}^{--} regions and to perform signal-background discrimination within them, one additional selection requirement is placed on the azimuthal distance between the two same-sign leptons in the final states $\Delta\Phi(\ell,\ell)$ to further reject background events, and therefore enhance the SRs purity. The distribution related to $\Delta\Phi(\ell,\ell)$ is remarkably different for signal and background events in SR_{LR}^{++} and SR_{LR}^{--}, as it can be seen from Figure 5.8. Furthermore, at high $\Delta\Phi(\ell,\ell)$ values the ratio between signal and background expected yields S/B in SR_{RR}^{++} and SR_{RR}^{--} increases significantly, as shown in Figure 5.9. Therefore, events falling into the four defined Signal Regions are also required to have $\Delta\Phi(\ell,\ell) \geq 2.5$ to further suppress the backgrounds. This last selection requirement finalizes the definition of the SRs employed in the statistical analysis. A summary of the analysis SR selection is reported in Table 5.11 while a schematic representation of the strategy followed to define the analysis SRs is shown in Figure 5.10. The NN^{SvsB} output distributions for data and simulated events in the finalized SRs are shown in Figure 5.11. Collision data events in bins where the ratio of expected signal and background events is $S/B > 5\%$ are not shown in the distributions. Signal and background yields associated to the SRs are reported in Table 5.12. The yields are also shown for collision data taking only into account the *unblinded* bins of the SR distributions.

Signal Regions event selection

SR	SR_{RR}^{++}	SR_{RR}^{--}	SR_{LR}^{++}	SR_{LR}^{--}
Number of leptons		$N_\ell = 2$		
Lepton p_T		$p_T(\ell) > 20$ GeV		
Number of jets		$N_{jets} \geq 2$		
Jet p_T		$p_T(j) > 25$ GeV		
PLIV and *b*-jet requirements		MincMinc with ≥ 2 *b*-jets at 77% WP		
		OR		
		TT with $= 1$ *b*-jet at 77% WP		
Total lepton charge	+2	-2	+2	-2
NN^{SvsS} output		≤ 0.538	> 0.538	
Lepton azimuthal distance		$\Delta\Phi \geq 2.5$		

Table 5.11: Summary of the four Signal Regions selection requirements.

Since the kinematic variables related to the two same-sign leptons have not been employed in the NN^{SvsB} training, 4 Validation Regions are built by applying the same requirements used for the Signal Regions definition, with an opposite selection based on
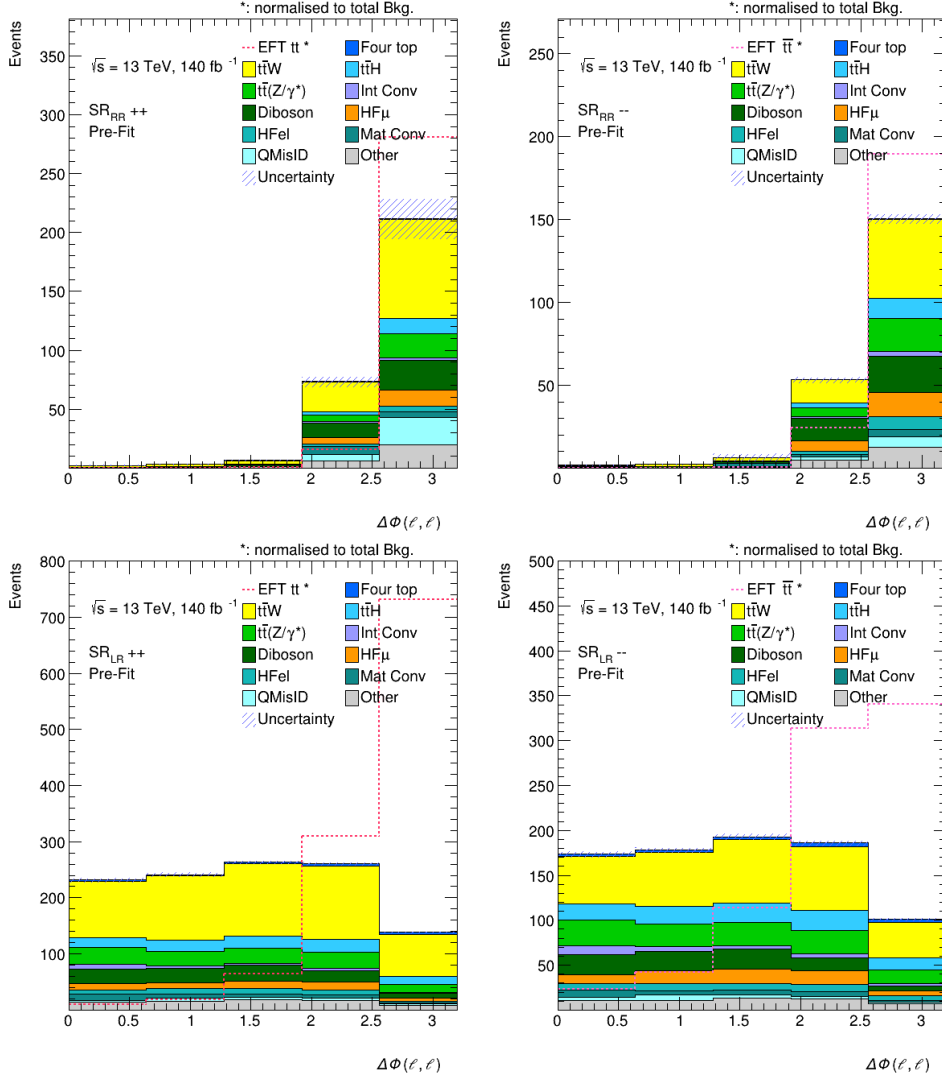
Figure 5.8: $\Delta\Phi(\ell,\ell)$ distribution in the 4 defined SR_{RR}^{++}, SR_{RR}^{--}, SR_{LR}^{++}, SR_{LR}^{--} regions for simulated signal and background events. Signal distributions (shown as dashed lines) are normalized to the total number of background yields. The statistical uncertainty is shown as blue dashed band.

$\Delta\Phi$ ($\Delta\Phi(\ell,\ell) < 2.5$). These regions are referred as VR_{RR}^{++}, VR_{RR}^{--}, VR_{LR}^{++} and VR_{LR}^{--} and are reported in Figure 5.12. The NN$^{\text{SvsB}}$ output distributions in VR_{LR}^{++} and VR_{LR}^{--} are then employed to validate the background estimates resulting from the statistical analysis reported in Section 5.7. These regions are expected to be highly dominated by $t\bar{t}W$ events, as can be seen from Figure 5.3b. On the other hand, VR_{RR}^{++} and VR_{RR}^{--} cannot be employed to validate the NN$^{\text{SvsB}}$ output shape due to the limited number of events
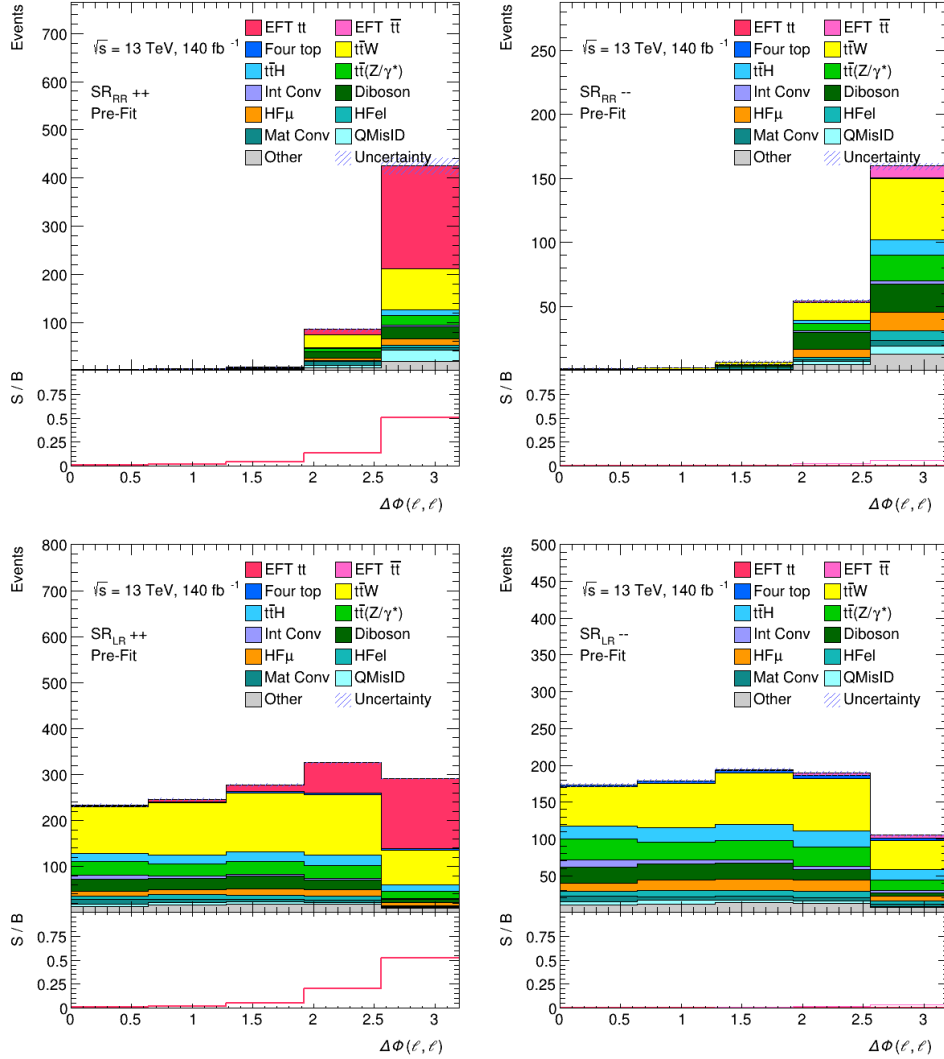
Figure 5.9: $\Delta\Phi(\ell,\ell)$ distribution of the expected signal and background yields in the 4 defined SR_{RR}^{++}, SR_{RR}^{--}, SR_{LR}^{++}, SR_{LR}^{--} regions. The statistical uncertainty is shown as blue dashed band in the top panels. The bottom panels show the S/B value.

and are therefore used as one-bin regions for the validation.

Signal and background yields associated to the VRs are reported in Table 5.13. The yields are also shown for collision data taking only into account the *unblinded* bins of the related distributions.

Figure 5.10: Schematic representation of the strategy followed to define the analysis SRs. First signal-like events are selected according to the criteria presented in Section 5.2.8. Events satisfying the preliminary selection requirements are employed to train the NN$^{\text{SvsS}}$ to discriminate signal events originating from the RR or the two LR EFT operators. Four Signal Regions are defined based on the NN$^{\text{SvsS}}$ output and on the charge of the same-sign leptons. A second NN$^{\text{SvsB}}$ is trained over each SR to perform signal-background discrimination. A final selection requirement on $\Delta\Phi(\ell^{\pm}, \ell^{\pm})$ is used to complete the definition of the 4 analysis SRs.

	SR_{RR} ++	SR_{RR} −	SR_{LR} ++	SR_{LR} −
EFT tt	216 ± 10	0 (0)	165 ± 12	0 (0)
EFT $\bar{t}\bar{t}$	0 (0)	9.49 ± 0.35	0 (0)	4.11 ± 0.25
Four top	0.70 ± 0.16	0.68 ± 0.17	4.1 ± 0.9	4.0 ± 0.9
$t\bar{t}W$	90 ± 60	50 ± 33	90 ± 50	45 ± 28
$t\bar{t}H$	13 ± 9	13 ± 9	16 ± 12	16 ± 11
$t\bar{t}Z/\gamma$	21.9 ± 1.5	21.1 ± 1.4	17.0 ± 1.5	16.6 ± 1.7
Int Conv	2.7 ± 1.5	3.1 ± 1.8	2.2 ± 1.3	2.8 ± 1.6
Diboson	26.9 ± 2.3	23.9 ± 1.9	9.4 ± 0.7	6.3 ± 0.5
HFμ	14.0 ± 3.5	16 ± 4	6.7 ± 2.2	6.5 ± 2.2
HFel	5.2 ± 2.9	8 ± 4	3.4 ± 1.8	5.4 ± 3.5
Mat Conv	6.6 ± 2.2	4.6 ± 1.4	2.3 ± 0.7	2.9 ± 1.0
QMisID	$< 10^{-4}$	$< 10^{-4}$	$< 10^{-4}$	$< 10^{-4}$
Other	21 ± 4	13.8 ± 2.5	9.7 ± 1.4	7.6 ± 1.5
Total	420 ± 60	164 ± 35	320 ± 60	117 ± 31
Data	109	131	83	109
(partially unblinded)				

Table 5.12: Yields of the analysis Signal Regions. Only data events related to the *unblinded* bins of the SR distributions are taken into account.
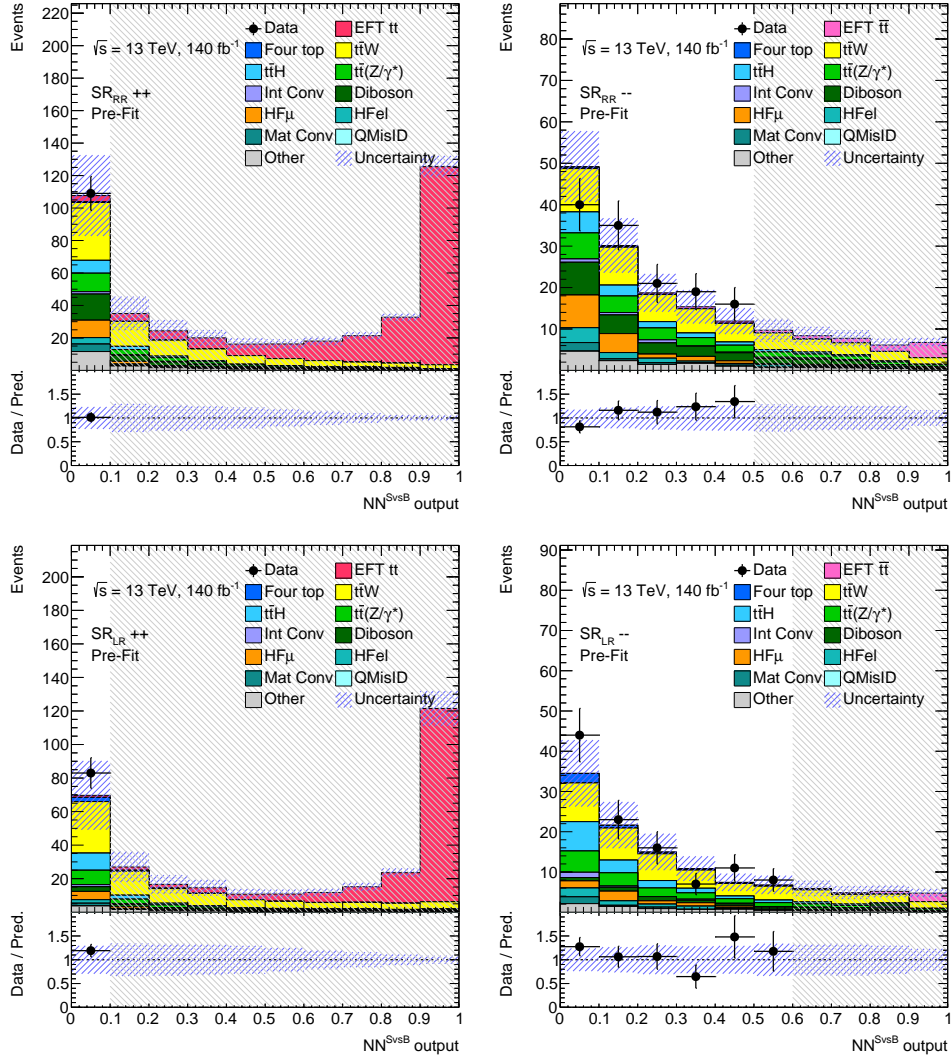
Figure 5.11: NN^SvsB output distribution for data and MC events in the 4 defined Signal Regions: SR_{RR}^{++}, SR_{RR}^{--}, SR_{LR}^{++}, SR_{LR}^{--}. Data events are not shown in bins with $S/B > 5\%$. The bottom panels show the data/MC agreement. The blue dashed band includes both statistical and systematic uncertainties.
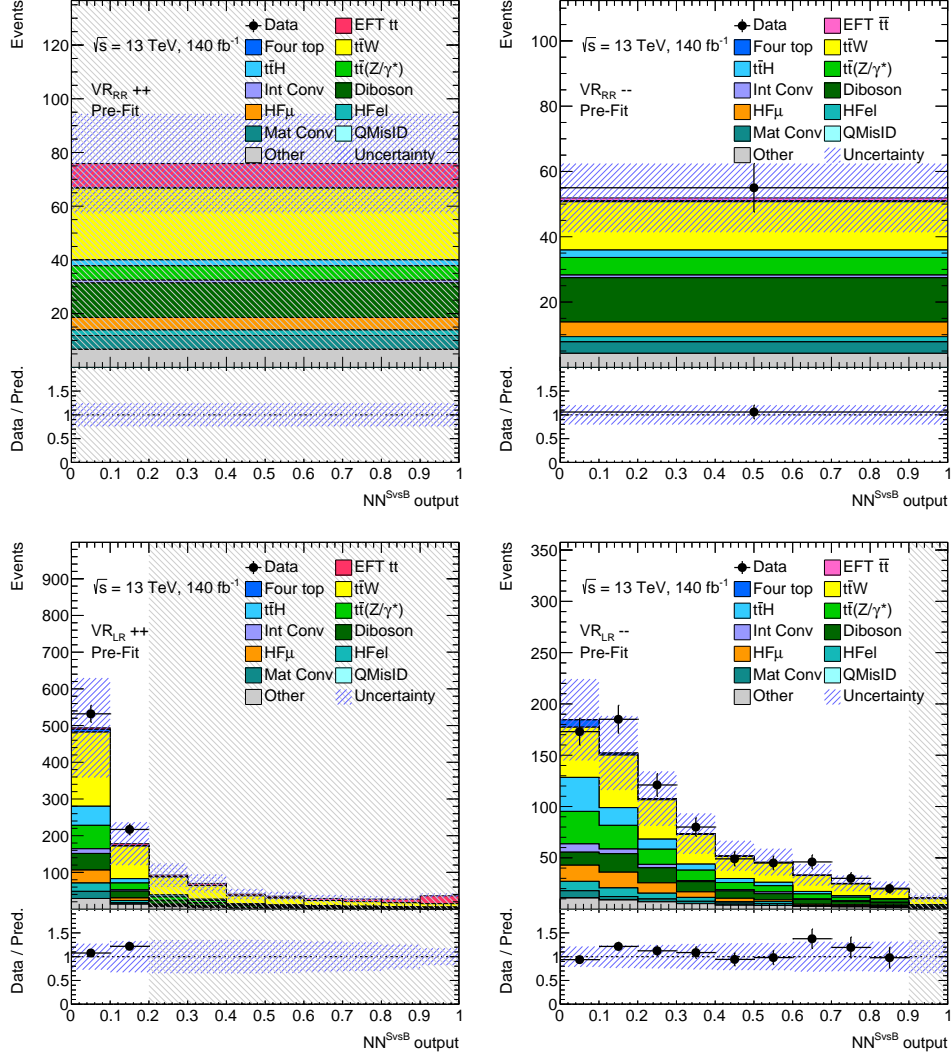
Figure 5.12: NN^{SvsB} output distribution for data and MC events in the 4 defined Validation Regions: VR_{RR}^{++}, VR_{RR}^{--}, VR_{LR}^{++}, VR_{LR}^{--}. Data events are not shown in bins with $S/B > 5\%$. The bottom panels show the data/MC agreement. Only one bin is employed in VR_{RR}^{++} and VR_{RR}^{--} due to the low statistic. The blue dashed band includes both statistical and systematic uncertainties.

	$VR_{RR}\,++$	$VR_{RR}\,-$	$VR_{LR}\,++$	$SR_{VR}\,-$
EFT tt	8.9 ± 0.4	$0\ (0)$	73 ± 4	$0\ (0)$
EFT $\overline{tt}$	$0\ (0)$	0.906 ± 0.030	$0\ (0)$	4.83 ± 0.19
Four top	0.29 ± 0.08	0.28 ± 0.07	10.8 ± 2.3	11.1 ± 2.3
$t\bar{t}W$	27 ± 18	15 ± 10	460 ± 300	250 ± 160
$t\bar{t}H$	2.2 ± 1.6	2.3 ± 1.5	80 ± 60	80 ± 60
$t\bar{t}Z/\gamma$	5.3 ± 0.5	5.4 ± 0.5	109 ± 8	104 ± 8
Int Conv	1.0 ± 0.7	0.8 ± 0.8	19 ± 10	23 ± 12
Diboson	12.8 ± 1.0	13.6 ± 1.7	99 ± 6	80 ± 5
HFμ	4.7 ± 1.4	4.5 ± 1.4	48 ± 13	55 ± 13
HFel	2.1 ± 1.7	1.6 ± 1.1	34 ± 18	31 ± 17
Mat Conv	5 ± 4	3.5 ± 2.2	29 ± 5	22 ± 4
QMisID	$< 10^{-4}$	$< 10^{-4}$	$< 10^{-4}$	$< 10^{-4}$
Other	6.7 ± 1.3	4.3 ± 0.9	64 ± 7	46 ± 7
Total	76 ± 19	52 ± 11	1030 ± 310	710 ± 170
Data (partially unblinded)	0	55	749	749

Table 5.13: Yields of the analysis Validation Regions. Only data events related to the *unblinded* bins of the VRs distributions are taken into account.

5.5 Background estimation

Different techniques have been employed in the analysis to estimate the background contamination. Most of the background processes have been estimated by only relying on MC simulation, while some background contributions have been evaluated though data-driven methods. A semi-data driven technique has been employed to estimate non-prompt leptons as well as events originated from $t\bar{t}Z(\gamma)$, $t\bar{t}W$ and VV (WZ, ZZ) SM processes. Specifically, a fit is performed over data events in dedicated Control Regions related to the above mentioned backgrounds with the Normalization Factors (NFs) associated to those processes left free floating, as described in Section 5.7.

5.5.1 Irreducible background estimation

Background events that satisfy the Signal Regions selection criteria can originate from SM processes that result in a final state topology similar to the one generated by signal events, consisting of two same-sign prompt leptons and b-jets. These *irreducible* background processes are $t\bar{t}Z, t\bar{t}W, t\bar{t}H, t\bar{t}\gamma, VV, t\bar{t}t\bar{t}$[6]. Other rare processes, such as tZ+jets, $t\bar{t}WW$, $t\bar{t}HH$, $t\bar{t}WH$, $t\bar{t}ZZ$, WtZ, ttt and VVV are considered as well. The estimation of these backgrounds is performed based on the good modelling of the processes, therefore it strongly relies on MC simulations, except for $t\bar{t}W, t\bar{t}Z$ and VV, that are the dominant irreducible backgrounds. The contribution related to these processes is estimated through a fit performed over dedicated regions as described in Section 5.7.

The Control Regions defined for $t\bar{t}Z$ and VV share some common selection requirements. Specifically, only events with three leptons in the final state are selected, with an opposite sign (OS), same flavor lepton pair and one extra charged lepton. The transverse momenta of the OS lepton and the two same-sign leptons are required to be $p_T(OS) > 10$ GeV and $p_T(SS) > 20$ GeV respectively. Furthermore, both leptons of the same-sign pair have to be classified as Minc (according to the lepton categories defined in Section 5.2.3), while the opposite sign lepton is required to be Linc. To select events with a Z boson decaying into a pair of leptons, in both CRs the invariant mass of the opposite sign, same flavor lepton pair is required to be within 10 GeV from the Z boson mass m_Z. The number of jets required is instead different for the two CRs. Specifically, only events with at least 4 jets are selected for the $t\bar{t}Z$ CR, while events with either 2 or 3 jets are selected for the VV CR. Finally, both regions require either 1 jet to pass the 60% b-tagging WP, or at least two b-jets at the 77% WP. A summary of the selection

---

[6]The $t\bar{t}Z(\gamma)$ processes will be referred as $t\bar{t}Z$ from now on for simplicity, while diboson processes VV will denote WZ and ZZ.

requirements used to define these Control Regions is reported in Table 5.14, while the distributions of the variables employed in the fit performed to extract the yields of these background processes are reported in Figure 5.13.

The distribution associated to the number of b-jets is employed in the fit for the two Control Regions defined for $t\bar{t}Z$ and VV processes, while the $t\bar{t}W$ contribution is estimated using the NN$^{\text{SvsB}}$ output distribution in the SRs. Since a large number of $t\bar{t}W$ events is expected to satisfy the SRs selection criteria, as it can be seen from the associated yields in Figure 5.11 and Table 5.12, the first bins of the NN$^{\text{SvsB}}$ output distribution in the defined SRs are employed in the fit to estimate the $t\bar{t}W$ contribution.

Prior to the analysis fit, a correction on the jet multiplicity is applied to VV events to correct data/MC mis-modelling exhibited by the N_{jets} distribution in a dedicated VV-enriched region, as reported in Appendix F.

5.5.2 Reducible background estimation

Reducible background events are related to either fake/non-prompt leptons or to lepton charge mis-identification. Backgrounds originating from events containing at least one non-prompt lepton mis-reconstructed as a prompt e, μ are accurately estimated through a semi data-driven method. Eight Control Regions enriched in non-prompt lepton events are built, using $t\bar{t}, Z + jets, W + jets$ and single top Monte Carlo simulations, with the main contribution to the lepton fake background originating from $t\bar{t}$ events. Among these regions, six are defined for non-prompt leptons coming from the decay of $b-,c-$ and light hadrons, while two are built to constrain electrons originating from photon conversion that can occur either in the detector material or at the interaction point.

Events with a pair of same-sign leptons are employed to define the six CRs used to estimate the non-prompt lepton background originating from hadrons decays, with three regions related to electrons and three to muons. These regions are referred as *Heavy Flavor HF*-CRs and share several selection requirements. Both final state leptons are required to have $p_T(\ell) > 20$ GeV and only events with at least 2 jets are selected. Each $e(\mu)$ region requires the same-sign leptons to be classified according to different categories among the ones defined for the analysis. Specifically, the TM, MT and MM combinations are employed. The subleading lepton is required to be an electron (muon) in all three e (μ) related CRs. To suppress the $t\bar{t}W$ contamination in these regions, only events with exactly one jet b-tagged at the 77% WP are selected. One further requirement $M_{T(lep,met)} < 250$ GeV is placed on the TM and MT regions for the same purpose. The transverse momentum of the subleading lepton is employed to estimate these backgrounds in the fit, by leaving the associated Normalization Factors free floating. Specifically, only

two NFs are employed, one for HFe and one for $HF\mu$.

While electron candidates identified as originated from photon conversion, according to the criteria described in Section 5.2, are vetoed in all the above mentioned analysis regions, two additional Control Regions are specifically defined to accurately estimate the photon conversion background. These regions are based on three lepton events including a pair of same-sign leptons and one opposite sign lepton, with at least one electron in the final state. The transverse momenta of the same-sign leptons is required to be $p_T(SS) > 20$ GeV, while $p_T(OS) > 10$ GeV has to be fulfilled by the opposite sign lepton. Both leptons of the same-sign pair have to be classified as Minc (according to the lepton categories defined in Section 5.2.3), while the opposite sign lepton is required to be Linc. A veto is applied on events with b-jets passing the 77% WP. In order to veto events with a Z boson decaying leptonically, a requirement is placed on the invariant mass of the opposite sign, same flavor lepton pair: $|m_{OSSF} - m_Z| > 10$ GeV. Furthermore, the invariant mass of the trilepton system and the missing transverse momentum are required to satisfy $|m_{\ell\ell\ell} - m_Z| < 10$ GeV and $E_T^{miss} < 50$ GeV respectively. All these selection requirements are placed on both CRs related to photon conversion. In order to build two separate regions, the events passing the selection criteria described above are also required to contain one electron candidate originating from photon conversion in the detector material or at the interaction point. These specific electron candidates are identified based on the values of the conversion radius and the invariant mass associated to the electron and its closest track, as described in Section 5.2. The number of events satisfying these CRs selection requirements is employed to estimate the photon conversion background.

A summary of the selection requirements related to the 8 Control Regions employed in the analysis to estimate non-prompt leptons is reported in Table 5.14 and 5.15, while the distributions of the associated variables employed in the analysis fit are reported in Figure 5.13 and 5.14. Background yields and data events related to the CRs are reported in Table 5.16.

Another source of *reducible* background is related to charge mis-identified electrons, originating mainly from $t\bar{t}$ events (muon charge flip has been estimated to be $\sim 10^{-5}$ and therefore is negligible for this analysis). The estimation of this background is carried out with a data driven method. $Z \longrightarrow e^+e^-$ data events are employed to measure the electron charge flip rate, which is then used to estimate the background contribution in all analysis regions. The charge flip rate associated to electrons reconstructed as originating from photon conversion ranges from 10^{-3} to 0.03, while lower values ranging from 10^{-5} to 0.004 are associated to prompt electron candidates. The charge flip rate increases with the transverse momentum of the reconstructed electron and with the absolute value of

3ℓ CRs	VV CR	$t\bar{t}Z$ CR	IntCO CR	MatCO CR
N_ℓ		3		
$p_{T,\ell}$ [GeV]		>20 (SS), >10 (OS)		
PLIV WPs		MincMinc (SS), LincLinc (OS)		
Total charge		± 1		
Electron CO candidate		!MatCO and !IntCO	IntCO	MatCO
Njets	2 or 3	≥ 4		≥ 0
Nbjets	1 b-jet at 60% WP $\|| \geq 2$ b-jets at 77% WP			0 at 77%
$|m_{SFOS} - m_Z|$		< 10 GeV		> 10 GeV
$|m(\ell\ell\ell) - m_Z|$	-	-		< 10 GeV
E_T^{miss}	-	-		< 50 GeV
Fitted variable		N_{b-jets}		N_{events}

Table 5.14: Summary of the event selection in the VV, $t\bar{t}Z$, Int/MatCO Control Regions.

$2\ell SS$ CRs	HF TM	HF MT	HF MM
N_ℓ		2	
$p_{T,\ell}$ [GeV]		>20	
PLIV WPs	TM	MT	MM
Njets		≥ 2	
Nbjets		1 at 77%	
Total lepton charge		++ or - -	
Electron CO candidate		!MatCO and !IntCO	
Additional cuts	$M_{T,lep-met} < 250$ GeV		-
Fitted variable		p_T (subleading ℓ)	

Table 5.15: Summary of the event selection in the HF Control Regions. Each TM, MT, and MM region is split in a muon channel ($\mu\mu + e\mu$) and an electron channel ($\mu e + ee$).

the pseudorapidity for both prompt and non-prompt electron candidates.

	CR HFel TM 2lSS	CR HFel MT 2lSS	CR HFel MM 2lSS
Four top	0.067 ± 0.020	0.041 ± 0.017	0.036 ± 0.014
$t\bar{t}W$	11 ± 5	4.8 ± 2.4	2.0 ± 0.9
$t\bar{t}H$	4.3 ± 2.8	2.2 ± 1.6	1.0 ± 0.7
$t\bar{t}Z/\gamma$	7.4 ± 1.4	1.35 ± 0.28	1.69 ± 0.30
Int Conv	5.7 ± 3.1	2.9 ± 1.6	0.5 ± 0.4
Diboson	12.7 ± 1.7	5.0 ± 1.3	2.0 ± 0.5
HFμ	2.4 ± 0.9	10.3 ± 1.8	4.1 ± 1.2
HFel	41 ± 21	7.2 ± 3.1	5.0 ± 2.5
Mat Conv	3.2 ± 2.0	1.9 ± 1.9	1.2 ± 0.4
QMisID	5.1 ± 2.9	3.3 ± 2.1	1.6 ± 1.1
Other	4.2 ± 0.7	1.69 ± 0.21	0.63 ± 0.12
Total	97 ± 23	41 ± 6	20 ± 4
Data	95	32	19

	CR HFmu TM 2lSS	CR HFmu MT 2lSS	CR HFmu MM 2lSS
Four top	0.11 ± 0.04	0.072 ± 0.035	0.046 ± 0.019
$t\bar{t}W$	16 ± 8	7.6 ± 3.5	2.7 ± 1.3
$t\bar{t}H$	6 ± 4	3.4 ± 2.4	1.4 ± 0.9
$t\bar{t}Z/\gamma$	10.9 ± 1.2	5.6 ± 0.7	2.3 ± 0.4
Int Conv	0.6 ± 0.5	1.8 ± 1.1	0.31 ± 0.27
Diboson	16.5 ± 3.4	7.3 ± 0.9	3.3 ± 0.6
HFμ	92 ± 9	24 ± 5	14.1 ± 2.4
HFel	1.5 ± 1.0	7 ± 4	2.0 ± 1.2
Mat Conv	1.3 ± 0.8	1.0 ± 0.7	1.4 ± 1.2
QMisID	0.25 ± 0.12	0.8 ± 0.5	0.38 ± 0.26
Other	5.2 ± 1.0	2.7 ± 0.4	0.82 ± 0.14
Total	151 ± 14	61 ± 8	29 ± 4
Data	150	57	28

	CR IntCO 3l	CR MatCO 3l	CR ttZ 3l	CR VV 3l,
Four top	0 (0)	0 (0)	1.60 ± 0.32	0.089 ± 0.035
$t\bar{t}W$	0 (0)	0 (0)	6.4 ± 3.0	18 ± 9
$t\bar{t}H$	0 (0)	0 (0)	11 ± 8	7 ± 5
$t\bar{t}Z/\gamma$	0 (0)	0 (0)	334 ± 31	194 ± 14
Int Conv	40 ± 6	14 ± 4	0.14 ± 0.24	1.8 ± 1.0
Diboson	0.036 ± 0.025	2.0 ± 0.8	43 ± 4	131 ± 5
tZ	0 (0)	0 (0)	31.5 ± 3.0	156.6 ± 3.0
HFμ	0 (0)	0 (0)	1.2 ± 0.5	8.5 ± 3.1
HFel	0 (0)	0 (0)	0.6 ± 0.5	10 ± 7
Mat Conv	1.2 ± 0.9	31.5 ± 3.0	0.5 ± 0.4	1.8 ± 1.0
QMisID	0 (0)	0 (0)	0.24 ± 0.24	0.8 ± 0.5
Other	0 (0)	0 (0)	46 ± 21	49 ± 23
Total	41 ± 6	48 ± 5	480 ± 40	578 ± 30
Data	44	55	494	605

Table 5.16: Background yields in the analysis CRs
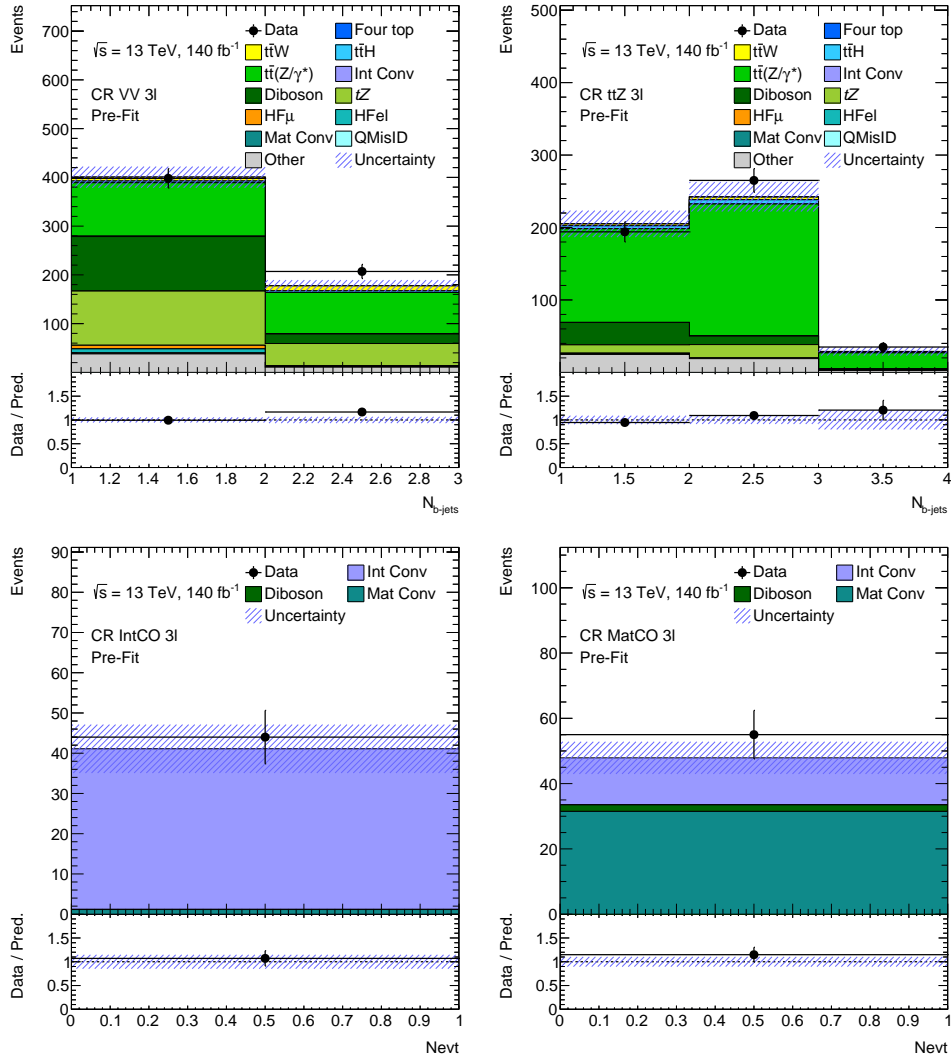
Figure 5.13: Distributions of the variables related to the CRs used in the analysis to estimate the backgrounds related to $t\bar{t}Z$ and VV processes (top row) and non-prompt leptons from photon conversion (bottom row). The blue hashed band includes both statistical and systematic uncertainties. The bottom panels display the data/MC ratio.
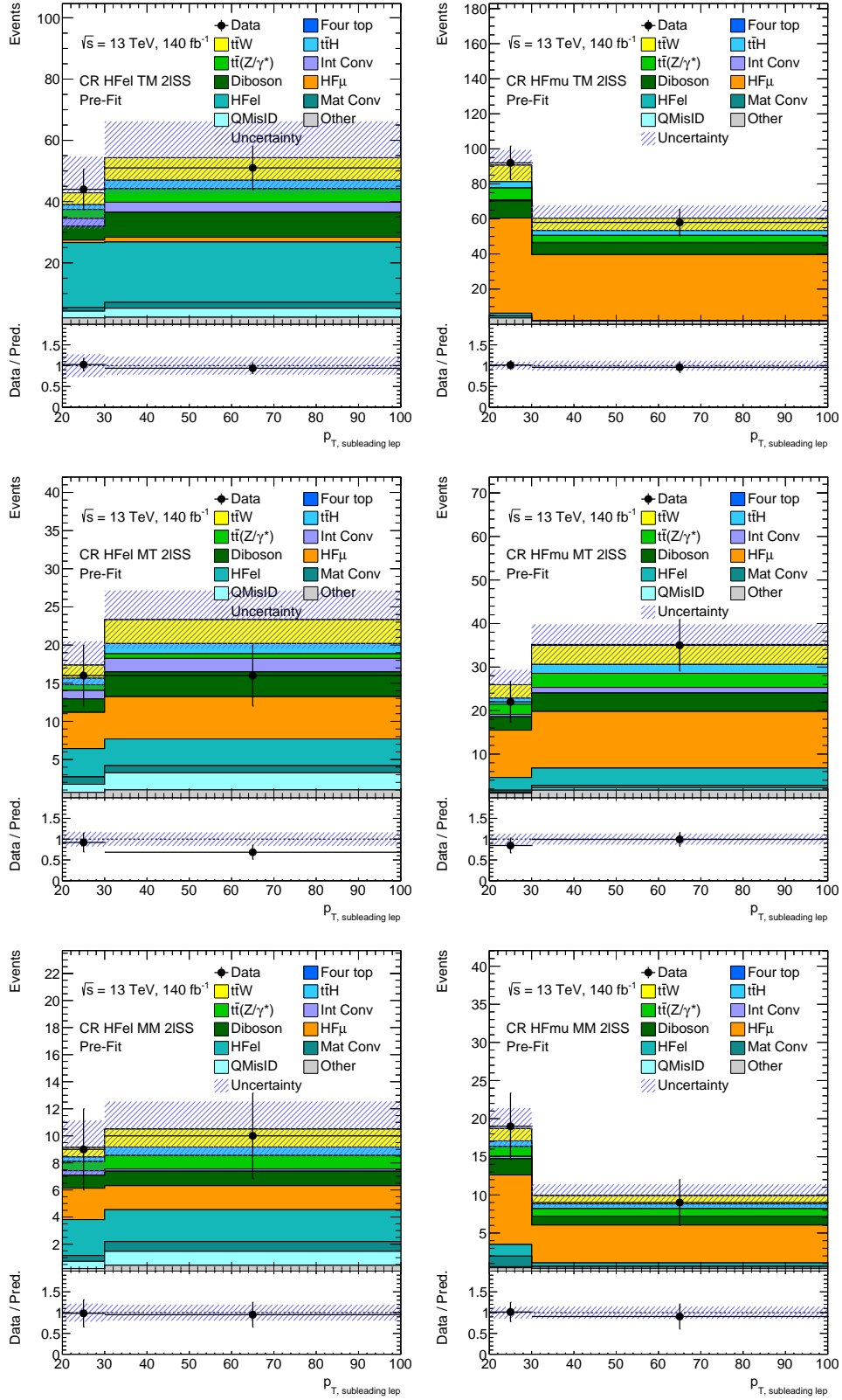
Figure 5.14: Distributions of the variables related to the CRs used in the analysis to estimate the backgrounds related to non-prompt leptons from heavy hadrons decay. From top left to bottom right: HFe TM, $HF\mu$ TM, HFe MT, $HF\mu$ MT, HFe MM and $HF\mu$ MM. The blue hashed band includes both statistical and systematic uncertainties. The bottom panels display the data/MC ratio.

5.6 Systematic uncertainties

Systematic uncertainties can impact the estimated signal and background yields as well as the shape of the distributions used in the analysis. Different systematic errors are taken into account, originating from the modelling of the various background processes considered, as well as from the methods employed for their estimation. Other systematic uncertainties are linked to object reconstruction, originating from both detector limitations and from the specific algorithms employed in the reconstruction.

All systematic uncertainties are incorporated in the likelihood function used to perform the analysis fit on collision data to extract the signal and some of the background contributions[7]. Specifically, one or more Nuisance Parameters (NPs) are associated to each systematic source considered in the analysis. The pre-fit values and $\pm 1\sigma$ variations of each NP are either provided by the ATLAS Collaboration performance groups or evaluated specifically for this analysis. When performing the maximum likelihood fit, the NPs are estimated together with the yields associated to the signal and to the main backgrounds. The NPs values and uncertainties resulting from the fit represent the estimates related to the systematic uncertainties.

A summary of the experimental and background modelling systematic errors taken into account in the analysis is reported in Table 5.17 with the associated number of NPs.

5.6.1 Experimental systematic uncertainties

Leptons systematic uncertainties

Experimental systematic uncertainties related to leptons are linked to trigger, reconstruction and identification efficiencies as well as to the scale and resolution associated to the measured lepton p_T and E for muons and electrons respectively. These uncertainties are evaluated, using $Z \longrightarrow \mu\mu(ee)$ and $J/\Psi \longrightarrow \mu\mu(ee)$ events as reported in [97, 98, 109], by performance groups within the ATLAS Collaboration.

Concerning muons, systematic variations related to the efficiency originate from muon reconstruction and identification as well as from the track-to-vertex association. Scale and resolution systematic uncertainties are instead linked to the muon p_T measurement and account also for charge dependent effects originating from the detector misalignment.

Systematic variations related to electrons originate similarly from reconstruction, identification and isolation efficiencies, while the scale and resolution systematic errors are linked to the electron energy measurement.

---

[7]Only the yields associated to the backgrounds with the normalization factors left free floating in the fit, as reported in Section 5.5, are extracted from the statistical analysis.

Systematic uncertainties associated to the trigger efficiency are evaluated for muons and electrons, following the procedures reported in [110, 111].

Jets systematic uncertainties

Systematic uncertainties related to jets are linked to the energy scale, resolution and to the jet-vertex-tagger. Different sources of systematic errors associated to the energy scale are considered to account for different jet flavor, pile-up effects and different calibration methods, as described in [112].

Systematic sources related to the b-tagging of jets are also considered [102]. These uncertainties are evaluated based on the b-tagging efficiencies related to b-,c- and light flavored jets. Since the searched signal generates b-jets with p_T up to $\sim$ TeV but the $b-$tagging efficiency WPs are defined for $p_T < 300$ GeV, additional systematic sources have been evaluated to account for the extrapolation of the b-tagging uncertainties at higher p_T values.

Other experimental systematic sources

In addition to the uncertainties described above, other sources of experimental systematic errors are considered. Their values are provided by performance groups within the Collaboration. Specifically, uncertainties related to the energy scale and resolution of the missing transverse momentum E_T^{miss} are considered. Finally, the uncertainties on the integrated luminosity corresponding to the dataset collected by the ATLAS detector in LHC Run-2 [113] and on the pile-up determination are taken into account as well.

5.6.2   Background modelling systematic uncertainties

Irreducible background modelling systematic uncertainties

Several sources of systematic uncertainties related to the modelling of the irreducible background processes considered in the analysis are taken into account. Systematic uncertainties related to $t\bar{t}Z, t\bar{t}W, t\bar{t}H$ and $t\bar{t}t\bar{t}$ are evaluated using alternative simulated samples that have been produced using different MC matrix element or parton shower generators with respect to the ones employed for the nominal background samples. Samples with variations of α_S are additionally considered to estimate the uncertainty associated to the modeling of Initial State Radiation (ISR) in $t\bar{t}Z$ events. Details on the alternative samples are reported in Appendix D.

Uncertainties related to the variation of the renormalization and factorization scale are also taken into account for $t\bar{t}W$, $t\bar{t}Z$, $t\bar{t}H$ and VV processes. An additional 50%

uncertainty is assigned to the HF jets contribution to $t\bar{t}W$, $t\bar{t}Z$, $t\bar{t}H$ and $t\bar{t}$ processes. Furthermore, systematic variations associated to the normalization of background events are evaluated for each process excluding $t\bar{t}W$, $t\bar{t}Z$ and VV, since the related normalization factors are left free-floating in the analysis fit.

One last source of uncertainty is considered, related to the N_{jets} correction applied to diboson events, as reported in Section 5.5.

Reducible background modelling systematic uncertainties

While several systematic uncertainties related to the PLIV algorithm are provided by performance groups and employed in the analysis, additional sources of systematic errors have been specifically defined and evaluated concerning the estimation of the non-prompt lepton background in the analysis. Uncertainties related to differences in the definition of the *VeryTight* and *Tight* PLIV WPs are taken into account as shape-only systematic variations based on the residual data/MC disagreement exhibited by the variables employed as input in the PLIV BDTs.

Since only two normalization factors are associated to the non-prompt background estimation based on the fit over the 6 HF-CRs defined in Section 5.5, two additional systematic uncertainties are defined to account for differences in the fakes rate in the three TM, MT and MM e, μ CRs.

Additional uncertainties are defined to account for the mis-modelling of the $t\bar{t}$+HF process and for the extrapolation of the photon conversion background from Z enriched regions to the $t\bar{t}$ enriched regions employed in the analysis.

Finally, three uncertainties associated to the modelling of charge mis-identification background are evaluated and their sum in quadrature is taken as associated systematic variation:

- the difference between the charge mis-reconstruction rate estimated in the analysis and the rate obtained from *truth-matching* performed with simulated $Z \longrightarrow ee$ events;

- the variation of the charge mis-reconstruction rate with the Z boson mass window;

- the uncertainty resulting from the data driven method employed in the analysis to estimate the rate.

Category	Type	Nuisance Parameters
	Luminosity	1
	Pile-up reweighting	1
Theory uncertainties	$t\bar{t}W$ EW cross section	1
	$t\bar{t}Z$, $t\bar{t}H$, VV and rare processes cross sections	9
	$t\bar{t}Z+$ HF-jets cross section	1
	$t\bar{t}H+$ HF-jets cross section	1
	$t\bar{t}+$HF-jets cross section	2
	Charge mis-identification cross section	1
Modelling of reducible backgrounds	PLIV input variables	8
	PLIV extrapolation	4
	Photon conversion	2
	$t\bar{t}$ alternative shower	2
	Data-driven charge mis-identification	4
Modelling of irreducible backgrounds	jet multiplicity correction	3
	$t\bar{t}Z$ alternative shower	3
	$t\bar{t}Z$ α_S variation for ISR modeling	3
	$t\bar{t}Z$ renormalization and factorization scale variation	2
	$t\bar{t}W$ alternative generator	2
	$t\bar{t}W$ alternative shower	2
	$t\bar{t}W$ renormalization and factorization scale variation	3
	$t\bar{t}t\bar{t}$ alternative generator	1
	$t\bar{t}H$ alternative generator	1
	$t\bar{t}H$ alternative shower	1
	$t\bar{t}H$ renormalization and factorization scale variation	1
	VV renormalization and factorization scale variation	1
Jet reconstruction and measurement	Jet Vertex Tagger	1
	Jet flavor tagging	60
	Jet energy scale	30
	Jet energy resolution	12
	b-tagging high-p_T extrapolation	3
Muon reconstruction and measurement	Momentum scale and resolution	4
	Reconstruction and ID	4
	Isolation	2
	Track-to-vertex association	2
	PLIV	20
Electron and γ reconstruction and measurement	Energy scale and resolution	2
	Reconstruction and ID	2
	Isolation	1
	PLIV	14
E_T^{miss} reconstruction and measurement	Scale and resolution	3
	Trigger	3

Table 5.17: Summary of the systematic sources considered in the analysis with the associated Nuisance Parameters.

5.7 Fit

The extraction of same-sign top signal yields and background yields related to $t\bar{t}Z$, VV, $t\bar{t}W$, and non-prompt leptons is based on on a maximum likelihood method. The statistical analysis is carried out using the TRExFitter framework [114] with the statistical model built according to HistFactory [115]. The negative log-likelihood minimization is performed using MINOS.

Section 5.7.1 presents the results of a first fit performed to get the background estimates related to non-prompt leptons, $t\bar{t}Z$, VV and $t\bar{t}W$ processes, whose normalization factors are left free floating. The fit is performed on data events over regions with an expected negligible contribution coming from signal events, with the signal normalization set to reproduce the $t\bar{t}W$ excess, as reported in Section 5.1.1. The post-fit data/MC agreement of background events is examined to asses the goodness of the resulting background estimates. This fit is performed following a background-only hypothesis.

A "realistic" Asimov dataset is built following the results of the background-only fit and employed to estimate the expected sensitivity of the analysis, as reported in Section 5.7.2. The expected upper limit on the signal cross section is evaluated following the results obtained using the Asimov dataset. The signal normalization is finally tuned so that a fit performed on the Asimov dataset assuming a signal+background hypothesis would result in an expected discovery significance of $\sim 3\sigma$.

The new signal normalization is then employed to perform the search for same-sign top pairs using the full Run 2 dataset. The search is carried out through a fit performed over the unblinded data distributions in all 14 analysis regions (10 CRs and 4 SRs), following a signal+background hypothesis. The search results are reported in Section 5.8.

The distributions of different variables are used as inputs in the fits to extract the yields related to the processes of interest, depending on the analysis regions. The NN^{SvsB} output distribution is used for the 4 SRs. The subleading lepton p_T is employed in the 6 HF CRs, while the number of b-jets is used in VV and $t\bar{t}Z$ CRs. For the IntCO and MatCO CRs only the event yields are used in the fit, given the small number of events populating these regions.

A summary of the selection requirements related to the analysis Signal and Control Regions is reported in Table 5.18.

The likelihood function employed in the analysis fits $\mathcal{L}(\mu, \vec{\lambda}, \vec{\theta})$ depends on $\mu, \vec{\lambda}, \vec{\theta}$. The signal strength parameter μ is a multiplicative factor applied to the signal yields predicted by the model (which is related to the chosen normalization and EFT benchmark), while $\vec{\lambda}$ are the normalization factors related to the backgrounds described in Section 5.5. The Nuisance Parameters (NPs) $\vec{\theta}$ are linked to the systematic uncertainties described in

SR	SR_{RR}^{++}	SR_{RR}^{--}	SR_{LR}^{++}	SR_{LR}^{--}
N_ℓ		2		
$p_T(\ell)$ [GeV]		> 20		
N_{jets}		≥ 2		
PLIV and b-jet requirements		MincMinc with ≥ 2 b-jets at 77% WP		
		OR		
		TT with $= 1$ b-jet at 77% WP		
Total lepton charge	+2	-2	+2	-2
NN$^{\mathrm{SvsS}}$ output		≤ 0.534		> 0.534
$\Delta\Phi(\ell,\ell)$		≥ 2.5		
Fitted variable		NN$^{\mathrm{SvsB}}$ output		

$2\ell SS$ CRs	HF TM	HF MT	HF MM
N_ℓ		2	
$p_T(\ell)$ [GeV]		>20	
Njets		≥ 2	
Nbjets		1 at 77%	
PLIV WPs	TM	MT	MM
Total lepton charge		++ or - -	
Electron CO candidate		!MatCO and !IntCO	
$M_{T,lep-met}$ [GeV]		< 250	-
Fitted variable		p_T (subleading ℓ)	

3ℓ CRs	VV CR	$t\bar{t}Z$ CR	IntCO CR	MatCO CR
N_ℓ		3		
$p_T(\ell)$ [GeV]		>20 (SS pair), >10 (OS)		
Njets	2 or 3	≥ 4	≥ 0	
Nbjets	1 b-jet at 60% WP $\|| \geq 2$ b-jets at 77% WP		0 at 77%	
PLIV WPs		MincMinc (SS), LincLinc (OS)		
Total charge		± 1		
Electron CO candidate		!MatCO and !IntCO	IntCO	MatCO
$|m_{SFOS} - m_Z|$		< 10 GeV	> 10 GeV	
$|m(\ell\ell\ell) - m_Z|$	-	-	< 10 GeV	
E_T^{miss}	-	-	< 50 GeV	
Fitted variable		N_{b-jets}	N_{events}	

Table 5.18: Summary of the analysis regions selection requirements. The symbol "$-$" is reported when the selection is not applied.

Section 5.6 affecting signal and/or background predictions.

Nuisance Parameters enter the fit with associated initial values and uncertainties either provided by the ATLAS Collaboration performance groups or specifically evaluated for the analysis, as reported in Section 5.6. After performing the fit, the NPs might result in different values with respect to the initial ones. Furthermore, the uncertainty on the NPs resulting from the fit could be lower with respect to the initial one. In the first and second case the NP is referred as *pulled* and *over-constrained* respectively.

The Likelihood $\mathcal{L}(\mu, \vec{\lambda}, \vec{\theta})$ is constructed as product of Poisson probabilities over all N bins of the distributions fitted in the statistical analysis:

$$\mathcal{L}(\mu, \vec{\lambda}, \vec{\theta}) = \prod_{i=1}^{N} \frac{\left(\mu s_i(\vec{\theta}) + b_i(\vec{\lambda}, \vec{\theta})\right)^{n_i}}{n_i!} e^{-\left(\mu s_i(\vec{\theta}) + b_i(\vec{\lambda}, \vec{\theta})\right)} \tag{5.6}$$

where n_i are the measured yields in each bin i. The expectation value is expressed as $E[n_i] = \mu s_i(\vec{\theta}) + b_i(\vec{\lambda}, \vec{\theta})$, where $\mu = 0$ and $\mu = 1$ correspond to the background-only and signal+background hypotheses respectively. The values $s_i(\vec{\theta})$ and $b_i(\vec{\lambda}, \vec{\theta})$ depend on the probability density functions (pdf) for signal and background events. Eq.(5.6) is related to a single Signal Region. The complete likelihood function employed in the fit over all analysis regions is built as a product of likelihoods expressed as eq.(5.6) for each region, with all SRs sharing the same μ parameter. The likelihoods related to Control Regions are built assuming only background contributions ($\mu = 0$) and therefore are expressed as:

$$\mathcal{L}(\vec{\lambda}, \vec{\theta}) = \prod_{j=1}^{M} \frac{b_j(\vec{\lambda}, \vec{\theta})^{m_i}}{m_j!} e^{-b_j(\vec{\lambda}, \vec{\theta})} \tag{5.7}$$

The profile likelihood ratio is employed to test the signal hypothesis related to the signal strength value. The test statistic q_μ is defined as:

$$q_\mu = -2\ln\left(\mathcal{L}\left(\mu, \hat{\hat{\vec{\lambda}}}_\mu, \hat{\hat{\vec{\theta}}}_\mu\right) / \mathcal{L}\left(\hat{\mu}, \hat{\vec{\lambda}}_{\hat{\mu}}, \hat{\vec{\theta}}_{\hat{\mu}}\right)\right) \tag{5.8}$$

where the $\hat{\mu}, \hat{\vec{\lambda}}_{\hat{\mu}}, \hat{\vec{\theta}}_{\hat{\mu}}$ parameters maximize the likelihood, while $\hat{\hat{\vec{\lambda}}}_\mu, \hat{\hat{\vec{\theta}}}_\mu$ maximize the likelihood for a given μ value.

5.7.1 Background only fit in CRs and unblinded bins of SRs

To assess the control over the main background processes, a maximum likelihood fit is performed on data events assuming a background-only hypothesis and it is carried out over the Control Regions and the unblinded bins of the Signal Regions, where the blinding threshold is set according to the $S/B > 5\%$ requirement (with S and B being the expected signal and background yields). These bins serve as CR for $t\bar{t}W$.

The fit results in an estimate of the normalization factors related to $t\bar{t}W$, $t\bar{t}Z, VV$ and non-prompt lepton processes and it is employed to assess the control over these backgrounds by checking the post-fit data/MC agreement.

The normalization factors (NFs) resulting from the fit are reported in Figure 5.15

with their associated uncertainties. It should be noticed that the $t\bar{t}W$ NF is 1.66 ± 0.33, slightly in tension with respect to the SM prediction (NF = 1). This excess has already been measured in dedicated $t\bar{t}W$ analyses [87, 88], and therefore is expected.
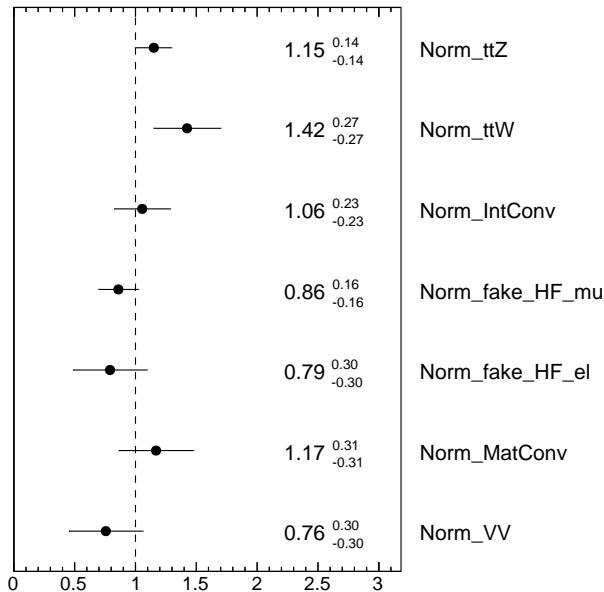
Figure 5.15: Normalization factors resulting from the background-only fit to CRs and to the unblinded bins of the SRs with statistical and systematic uncertainties. The normalization factors are related to the non-prompt leptons, diboson, $t\bar{t}Z$ and $t\bar{t}W$ backgrounds and are left free-floating in the fit.

The post-fit distributions of the variables employed in the fit related to the analysis regions are shown in Figure 5.16, 5.17 for CRs and in Figure 5.18 for SRs. The bottom panels display the post-fit ratios of data/MC yields, whose values are approximately 1 in each bin, therefore showing a good agreement between data and simulation. Summaries of the pre- and post-fit yields are reported in Figure 5.19 and Figure 5.20 respectively. The data/MC agreement is also checked in the 4 Validation Regions defined in Section 5.4, as it can be seen from Figure 5.21. These regions are $t\bar{t}W$ dominated, and therefore are employed to further validate the resulting $t\bar{t}W$ estimate. All displayed distributions have been obtained including both statistical and systematic uncertainties. The post-fit event yields related to the different background processes are reported in Table 5.19 for all CRs.

Figure 5.22 and 5.23 show the systematic pulls and over-constraints resulting from the fit. Some NPs are pulled after the fit, however the deviation is not significant. The most

pulled NPs are related to $t\bar{t}Z$ and $t\bar{t}W$ modelling as well as to the charge mis-identification estimation. Some among the jet-related NPs are pulled as well. One parameter related to $t\bar{t}H$ modelling is over-constrained by the fit.
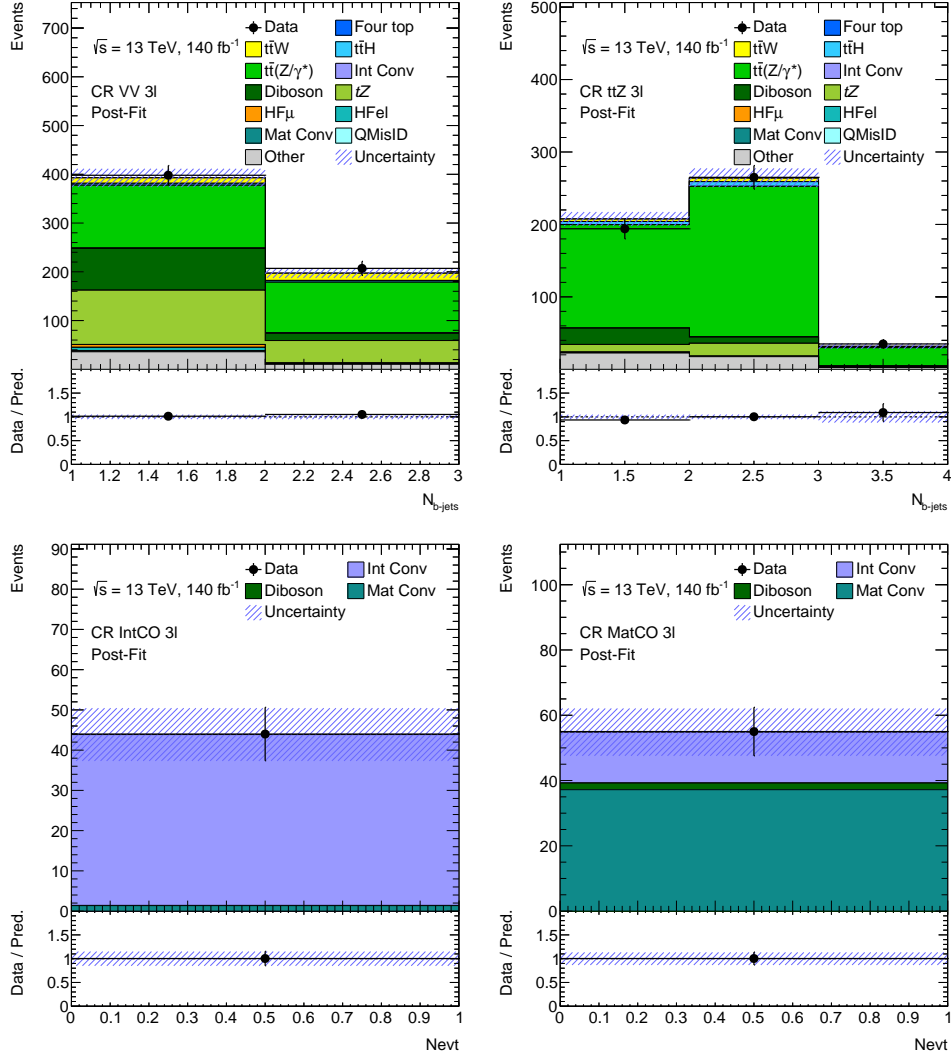
Figure 5.16: Post-fit distributions in VV, $t\bar{t}Z$, IntCO and MatCO CRs of the variables used in the background-only fit performed over the CRs and the unblinded bins of the SRs. The blue hashed band includes both statistical and systematic uncertainties. The bottom panels display the ratio between observed and expected event yields, used to assess the post-fit data/MC agreement.
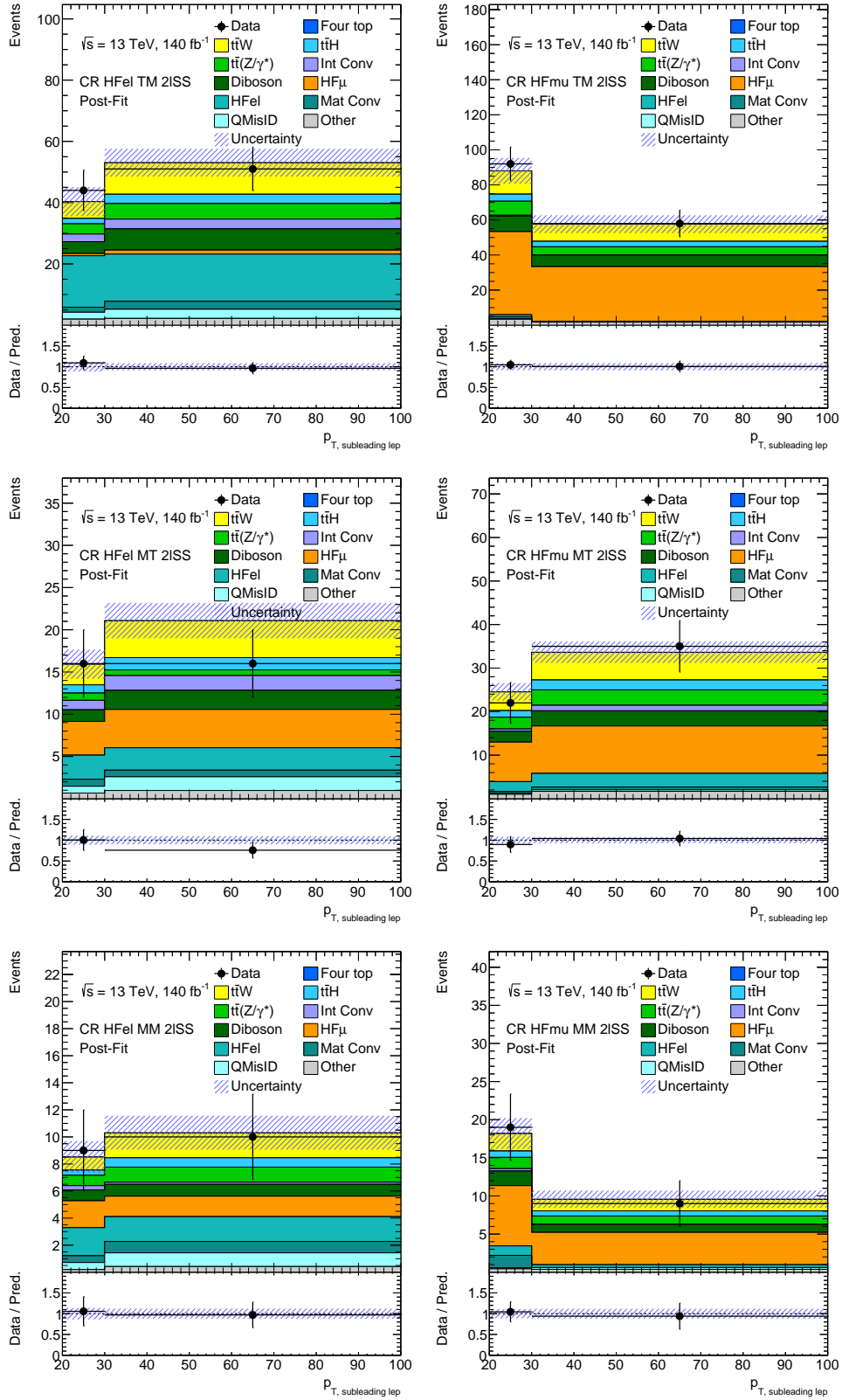
Figure 5.17: Post-fit distributions in the *HF*-CRs of the variables used in the background-only fit performed over the CRs and the unblinded bins of the SRs. The blue hashed band includes both statistical and systematic uncertainties. The bottom panels display the ratio between observed and expected event yields, used to assess the post-fit data/MC agreement.
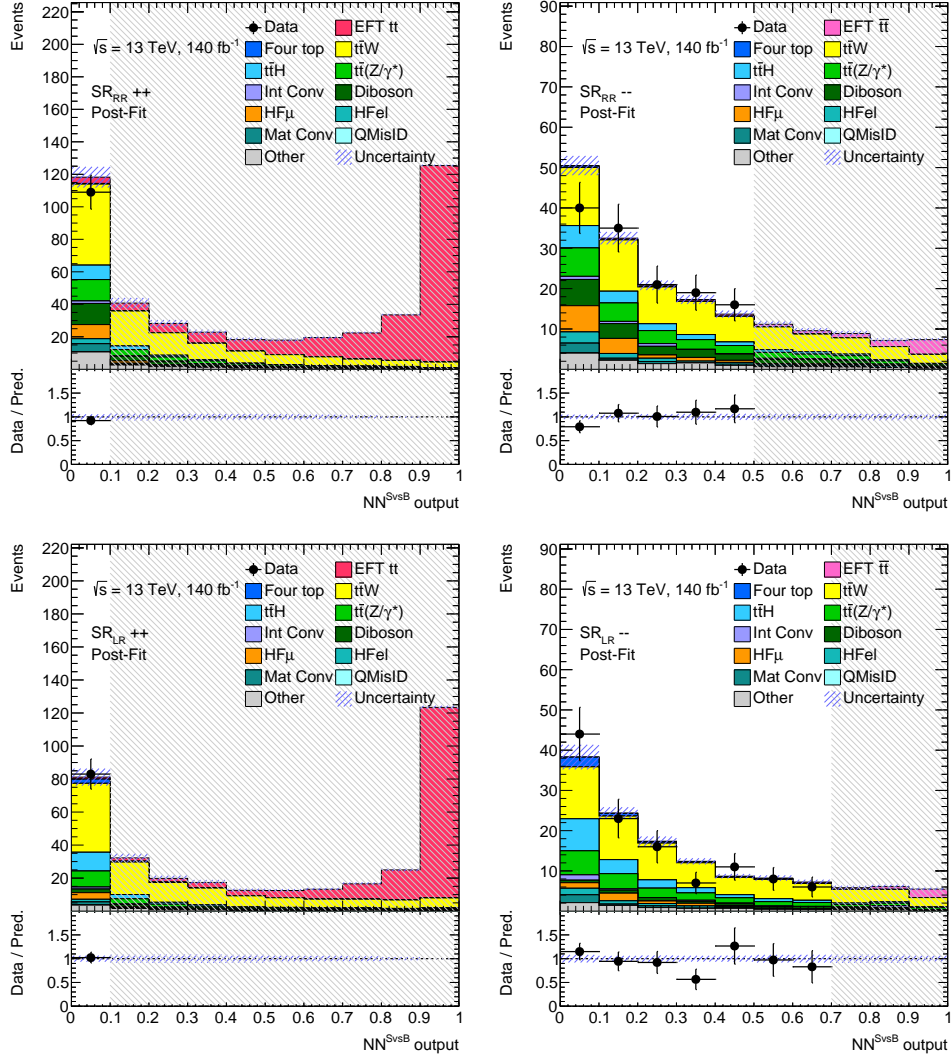
Figure 5.18: Post-fit distributions in the analysis SRs of the NN$^{\text{SvsB}}$ output used in the background-only fit performed over the CRs and the unblinded bins of the SRs. The blue hashed band includes both statistical and systematic uncertainties. The bottom panels display the ratio between observed and expected event yields, used to assess the post-fit data/MC agreement. Data events are displayed only in bins with $S/B < 5\%$.
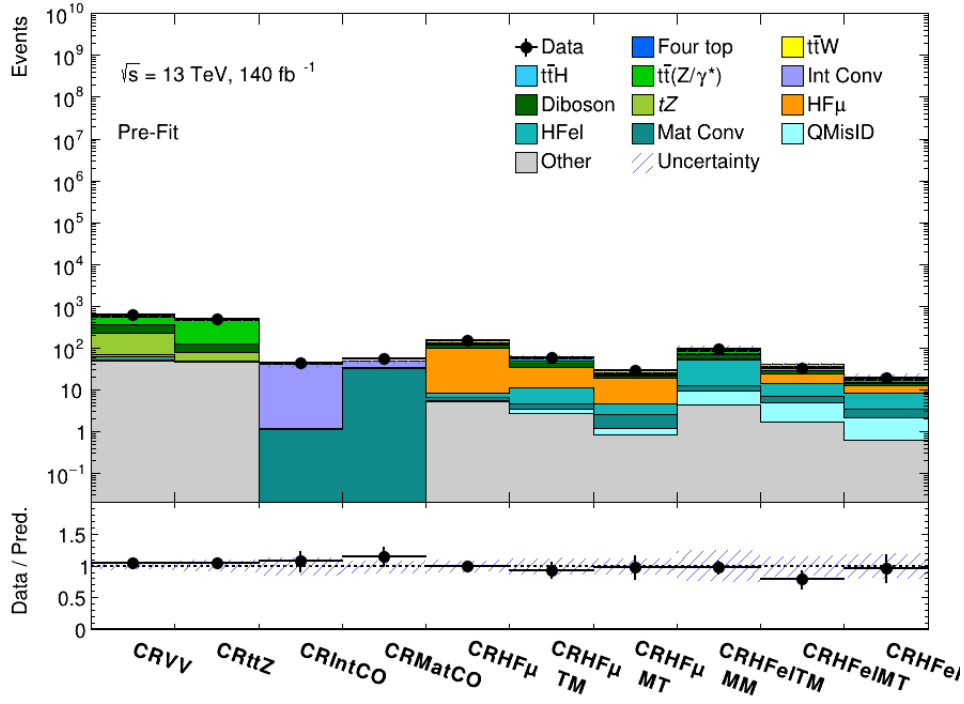
Figure 5.19: Summary of the pre-fit data and MC yields in the analysis CRs. The blue hashed band includes both statistical and systematic uncertainties. The bottom panels display the ratio between data and MC yields.
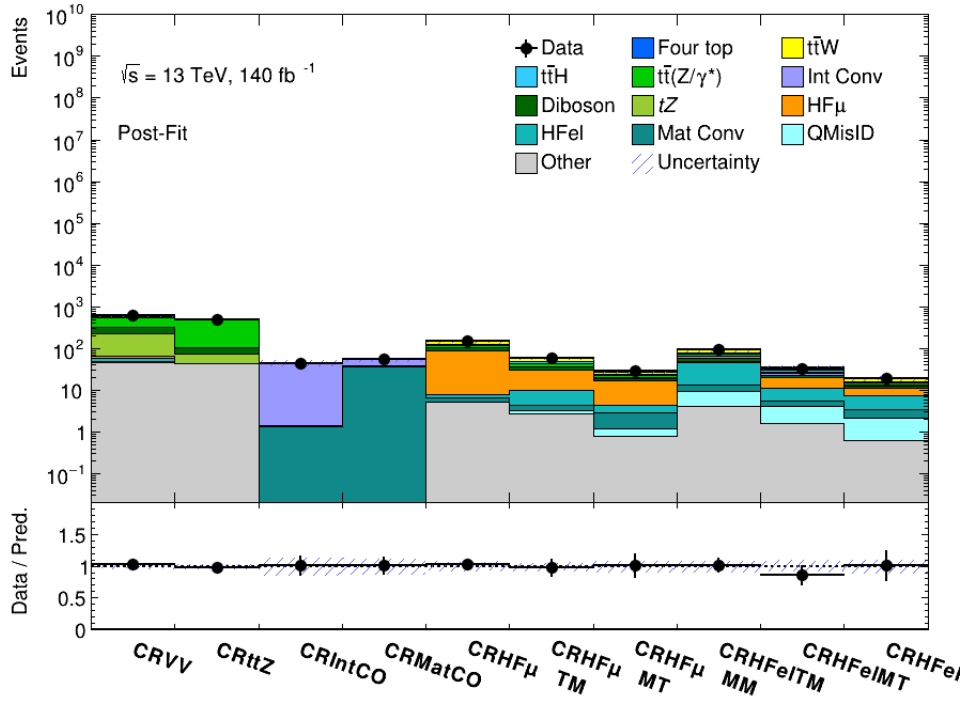
Figure 5.20: Summary of the post-fit data and MC yields in the analysis CRs. The background-only fit has been performed over the CRs and the unblinded bins of the SRs. The blue hashed band includes both statistical and systematic uncertainties. The bottom panels display the ratio between data and MC yields.
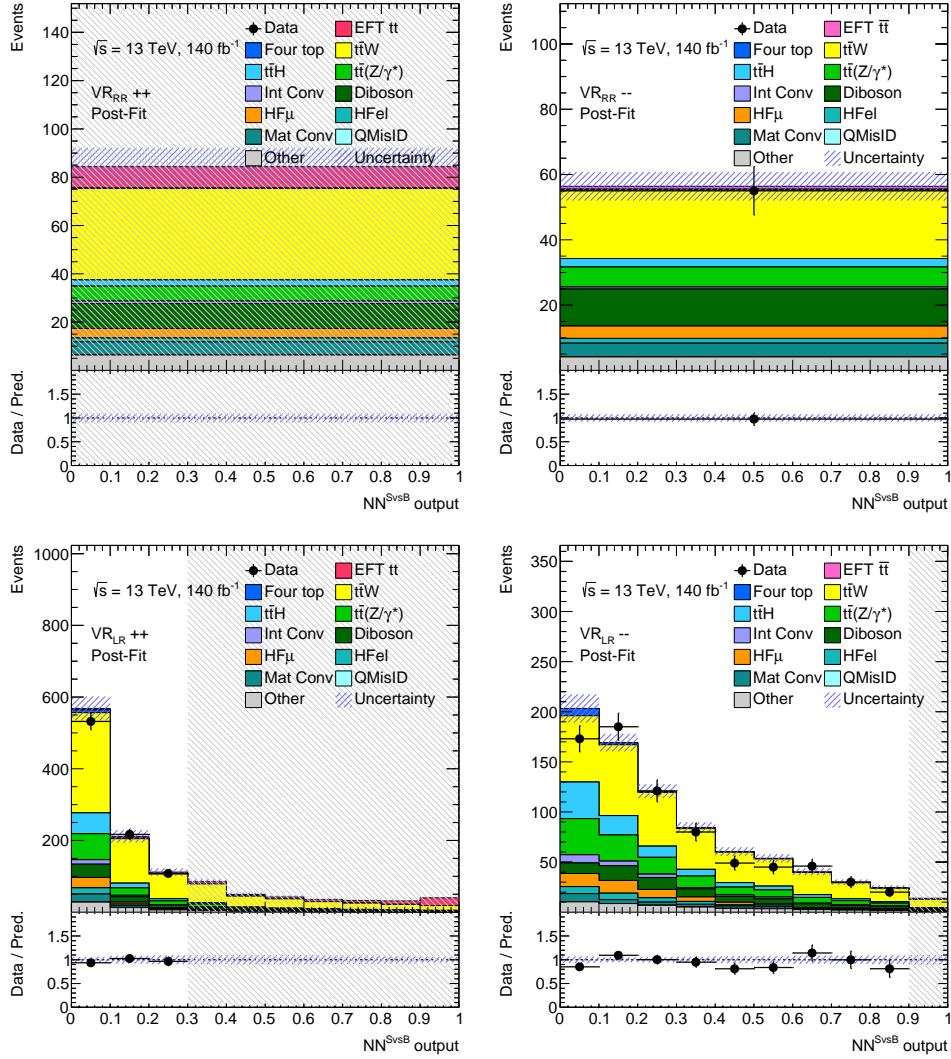
Figure 5.21: Post-fit distributions in the analysis VRs. The background-only fit has been performed over the CRs and the unblinded bins of the SRs. The blue hashed band includes both statistical and systematic uncertainties. The bottom panels display the ratio between observed and expected event yields. Data events are displayed only in bins with $S/B < 5\%$.
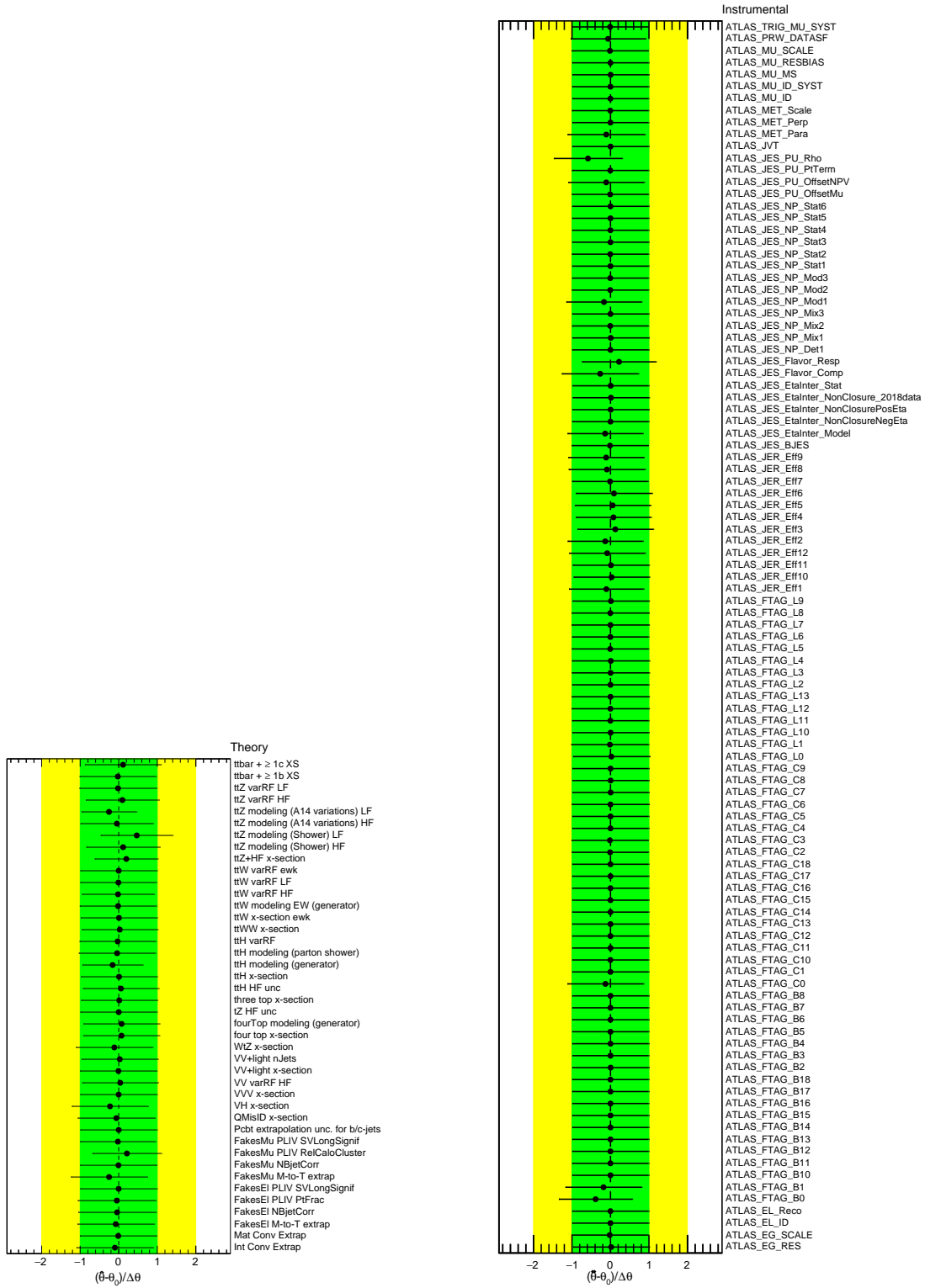
Figure 5.22: Pulls and constraints on the theory nuisance parameters (left) and on the instrumental nuisance parameters (right) resulting from a background-only fit performed over the 10 CRs and the unblinded bins of the SRs.

Muon
PLIV Muon Statistical [M]
PLIV Muon Probe Quality [M]
PLIV Muon M_t Window [M]
PLIV Muon Sherpa vs. Powheg [T]
PLIV Muon Sherpa vs. Powheg [M]

$(\theta-\theta_0)/\Delta\theta$

Electron
PLIV Electron Statistical [M]
PLIV Electron Pileup [T]
PLIV Electron Pileup [M]
PLIV Electron Jet Modeling [T]
PLIV Electron Jet Modeling [M]

$(\theta-\theta_0)/\Delta\theta$

DataDriven
QMisIDReco TM
QMisIDReco MT
QMisIDReco MM

$(\theta-\theta_0)/\Delta\theta$
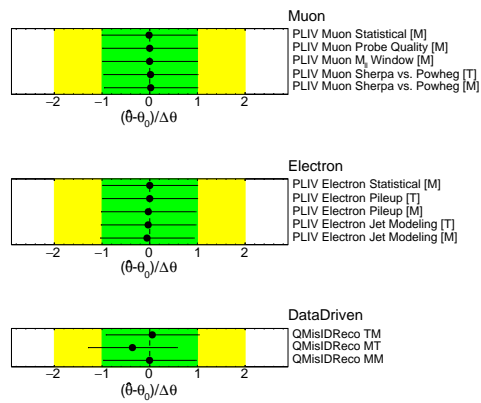
Figure 5.23: Pulls and constraints on the muon (top) and electron (middle) PLIV as well as on the data driven QMisID (bottom) related nuisance parameters resulting from a background-only fit performed over the 10 CRs and the unblinded bins of the SRs.

	CR IntCO 3l	CR MatCO 3l	CR ttZ 3l	CR VV 3l,
Four top	0 (0)	0 (0)	1.63 ± 0.32	0.094 ± 0.035
$t\bar{t}W$	0 (0)	0 (0)	8.4 ± 1.7	26 ± 5
$t\bar{t}H$	0 (0)	0 (0)	12 ± 6	7 ± 4
$t\bar{t}Z/\gamma$	0 (0)	0 (0)	376 ± 31	233 ± 28
Int Conv	42 ± 7	16 ± 4	0.14 ± 0.08	1.7 ± 1.0
Diboson	0.036 ± 0.021	2.03 ± 0.26	32 ± 13	100 ± 40
tZ	0 (0)	0 (0)	29.5 ± 2.4	157.3 ± 3.2
HFμ	0 (0)	0 (0)	1.01 ± 0.33	7 ± 5
HFel	0 (0)	0 (0)	0.37 ± 0.27	7.8 ± 3.0
Mat Conv	1.4 ± 1.0	37 ± 8	0.51 ± 0.33	2.2 ± 0.8
QMisID	0 (0)	0 (0)	0.19 ± 0.14	0.9 ± 0.4
Other	0 (0)	0 (0)	42 ± 20	46 ± 22
Total	44 ± 7	55 ± 7	504 ± 21	590 ± 22
Data	44	55	494	605

	CR HFel TM 2lSS	CR HFel MT 2lSS	CR HFel MM 2lSS
Four top	0.070 ± 0.019	0.042 ± 0.016	0.036 ± 0.012
$t\bar{t}W$	15.7 ± 3.0	6.8 ± 1.4	2.8 ± 0.6
$t\bar{t}H$	4.8 ± 2.4	2.4 ± 1.3	1.1 ± 0.6
$t\bar{t}Z/\gamma$	8.4 ± 1.7	1.54 ± 0.35	1.88 ± 0.33
Int Conv	5.7 ± 3.2	2.9 ± 1.6	0.48 ± 0.30
Diboson	10.8 ± 2.4	3.6 ± 1.1	1.7 ± 0.5
HFμ	2.0 ± 1.1	8.5 ± 2.2	3.5 ± 1.5
HFel	32 ± 11	5.5 ± 2.2	3.9 ± 1.4
Mat Conv	4.2 ± 2.2	1.6 ± 1.3	1.4 ± 0.4
QMisID	5.2 ± 2.9	2.4 ± 1.6	1.5 ± 1.0
Other	4.2 ± 0.5	1.64 ± 0.18	0.62 ± 0.09
Total	93 ± 9	37.0 ± 3.2	18.8 ± 2.1
Data	95	32	19

	CR HFmu TM 2lSS	CR HFmu MT 2lSS	CR HFmu MM 2lSS
Four top	0.11 ± 0.04	0.068 ± 0.033	0.047 ± 0.018
$t\bar{t}W$	23 ± 4	10.6 ± 2.0	3.8 ± 0.8
$t\bar{t}H$	7 ± 4	3.8 ± 2.0	1.5 ± 0.8
$t\bar{t}Z/\gamma$	12.6 ± 1.9	6.2 ± 1.0	2.6 ± 0.5
Int Conv	0.6 ± 0.4	1.8 ± 1.0	0.31 ± 0.18
Diboson	15 ± 5	6.0 ± 1.5	3.0 ± 0.5
HFμ	79 ± 13	20 ± 6	12.2 ± 2.2
HFel	1.2 ± 0.7	5.4 ± 2.0	1.6 ± 0.6
Mat Conv	1.4 ± 0.8	1.1 ± 0.5	1.6 ± 0.5
QMisID	0.26 ± 0.12	0.5 ± 0.4	0.37 ± 0.25
Other	5.1 ± 0.6	2.68 ± 0.28	0.81 ± 0.11
Total	146 ± 11	58 ± 4	27.8 ± 2.6
Data	150	57	28

Table 5.19: Event yields in the CRs resulting from the background-only fit performed over the CRs and the unblinded bins of the SRs.

5.7.2 Expected sensitivity

A "realistic" Asimov dataset containing pseudo-signal and pseudo-background events is built using different procedures for signal and background processes. Specifically:

- pseudo-background events related to non-prompt leptons, diboson, $t\bar{t}Z$ and $t\bar{t}W$ processes are generated following the results of the background-only fit performed on collision data reported in the previous section. Specifically, they have been obtained as Poissonian fluctuations using the fitted NFs as expectation values. Pseudo-background events related to the other background processes are generated according to the MC simulation;

- pseudo-signal events are generated according to the MC simulation, with the signal normalization set to the $t\bar{t}W$ excess (as described in Section 5.1.1).

Since the pseudo-background events of the "realistic" Asimov dataset are generated according to the results of the background-only fit described in the previous section, they act as a replica of collision data events in the CRs.

The Asimov dataset is employed to estimate the expected sensitivity of the analysis. For this purpose a maximum likelihood fit is performed on the Asimov pseudo-data following the signal+background (S+B) hypothesis over all CRs and SRs. The signal strength μ is associated to the same-sign top pairs production.

The Normalization Factors resulting from the fit on the Asimov dataset are reported in Figure 5.24. Since the S+B hypothesis has been used, the signal normalization factor is reported as well. As expected, the NFs related to $t\bar{t}Z$, VV and non-prompt leptons result in similar values with respect to the background-only fit reported in the previous section. The $t\bar{t}W$ NF exhibits an excess with respect to SM prediction. Its value is however different with respect to the previous fit and its associated error is reduced. This is due to the SRs, whose whole distributions have been employed in the Asimov fit instead of using only the first bins of the NN$^{\text{SvsB}}$ output.

The systematic uncertainties pulls and over-constraints are shown in Figure 5.25 and 5.26. Even though some NPs are pulled or over-constrained, the size of these effects is lower with respect to the background-only fit.

The expected sensitivity of the analysis is then assessed by evaluating the expected limit on the signal cross section following the Asimov fit results. The expected upper limit (UL) is estimated through the CL_s method [116] with the asymptotic approximation [117] based on the test statistic reported in eq.(5.8). For a given value of μ, values of the signal cross section that result in $CL_s < 0.05$ are excluded at $\geq 95\%$ of confidence level (CL). Both the test statistic and the UL are evaluated using the RooFit framework [118, 119].
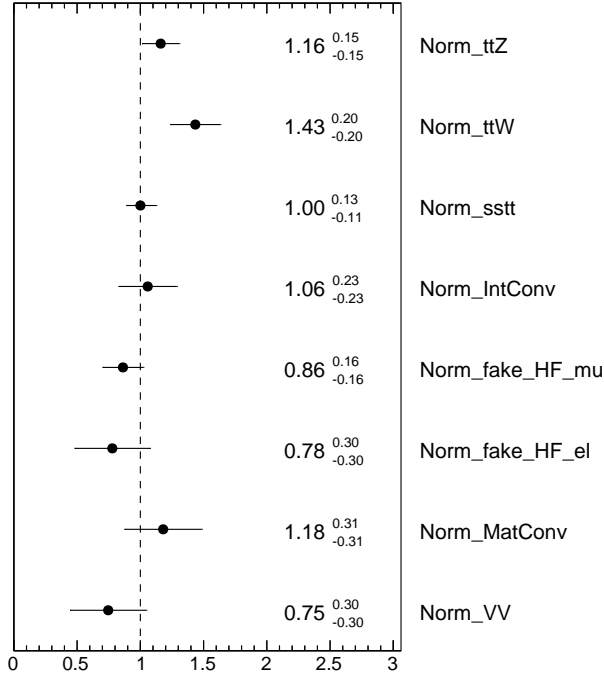
Figure 5.24: Normalization factors resulting from the S+B fit to the "realistic" Asimov dataset in all analysis regions with statistical and systematic uncertainties. The normalization factors are related to the non-prompt leptons, diboson, $t\bar{t}Z$ and $t\bar{t}W$ backgrounds and to the signal. All NFs are left free-floating in the fit.

The resulting expected upper limit on the signal strength parameter is: $0.031^{+0.014}_{-0.009}$. This corresponds to an expected upper limit on the signal cross section times Branching Ratio of:

$$\sigma(tt + \bar{t}\bar{t}) \times BR < 1.23 \text{ fb at } 95\% \text{ CL.} \tag{5.9}$$

A statistical test is performed following the Asimov fit results according to the background-only hypothesis. The level of disagreement between the observed (pseudo) signal events and the background-only hypothesis is quantified by the significance $\mathcal{Z}$ of the measurement, which is defined as

$$\mathcal{Z} = \Phi^{-1}(1 - p) \tag{5.10}$$

where Φ^{-1} is the quantile (the inverse of the cumulative distribution) of a standard Gaussian function and p is the $p - value$ associated to the measurement. The expected

significance has been evaluated using different normalization values for the signal. The value that resulted in $\mathcal{Z} = 3\sigma$ has been chosen as final signal normalization and employed in the unblinded data fit, described in the next section. The signal cross section value corresponding to the final normalization is reported in Section 5.1.1.
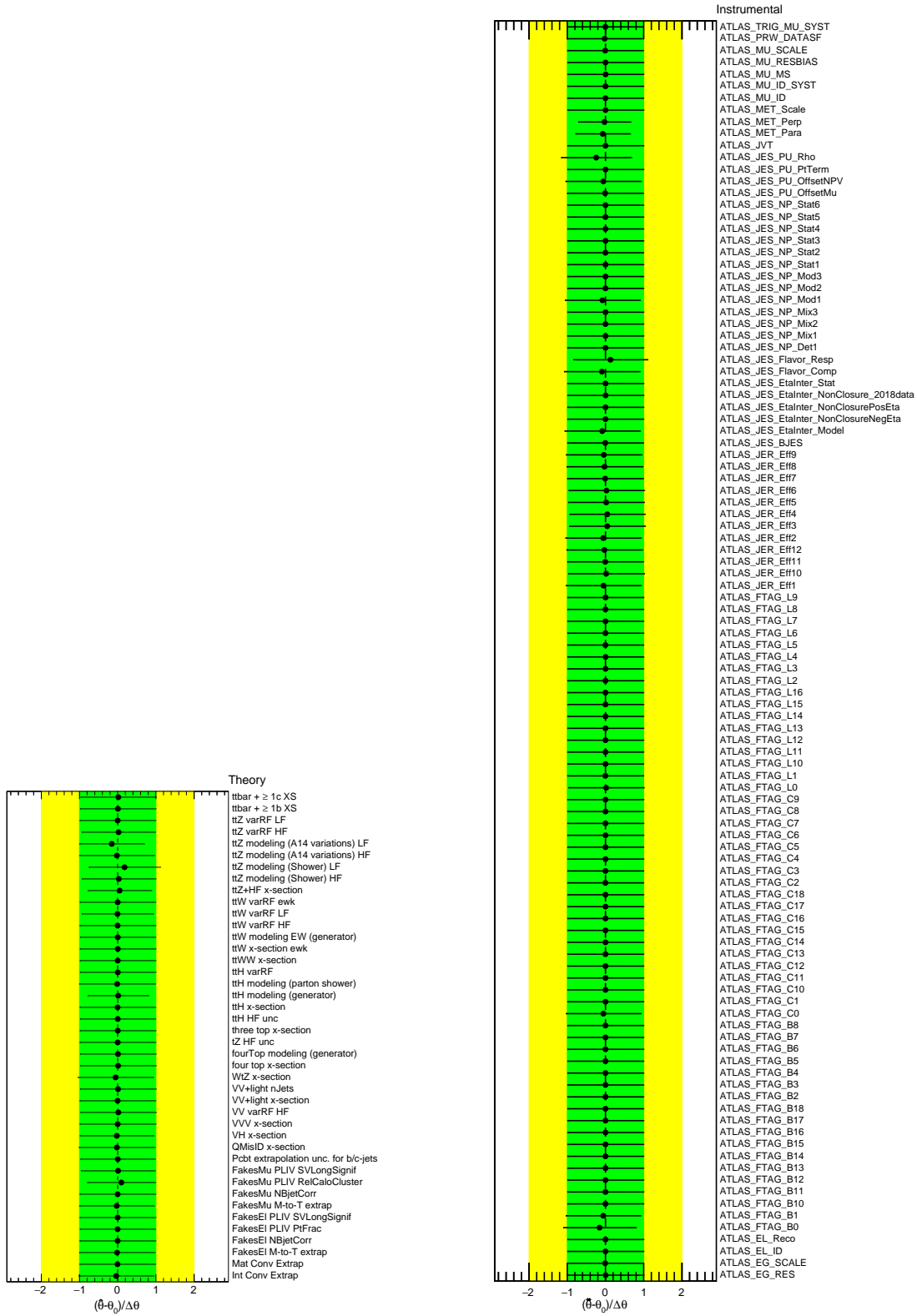
Figure 5.25: Pulls and constraints on the theory nuisance parameters (left) and on the instrumental nuisance parameters (right) resulting from a S+B fit to the Asimov dataset in all analysis regions.
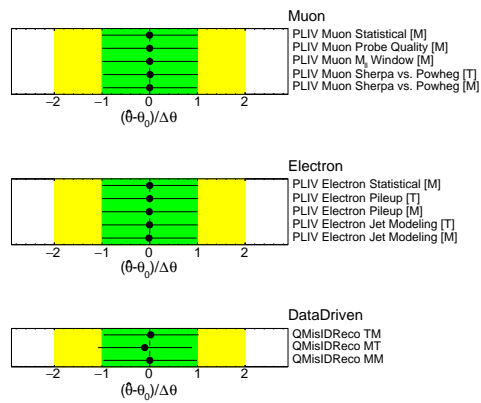
Figure 5.26: Pulls and constraints on the muon (top) and electron (middle) PLIV as well as on the data driven QMisID (bottom) related nuisance parameters resulting from a S+B fit to the Asimov dataset in all analysis regions.

5.8 Results

The search for same-sign top pairs is carried out by performing a maximum likelihood fit on the full Run 2 collision dataset over the 14 analysis regions (10 CRs and 4 SRs). The fit is performed assuming a signal+background hypothesis, with the expected SMEFT signal contribution normalized according to the results of the expected sensitivity study reported in the previous section. The signal strength μ is associated to same-sign top pairs production.

The distributions of the NN$^{\text{SvsB}}$ output in data and simulated events, for SRs and VRs, are reported in Figure 5.27 and 5.28 respectively. The distributions related to the CRs can be found in Section 5.5 instead.

The normalization factors (NFs) related to the signal and to the non-prompt lepton, diboson, $t\bar{t}Z$ and $t\bar{t}W$ backgrounds are left free floating in the fit. The resulting NFs values and related uncertainties are shown in Figure 5.29. The $t\bar{t}W$ NF is in tension with respect to SM prediction, as expected based on the excess measured in dedicated $t\bar{t}W$ analyses [87, 88]. Figure 5.30 and 5.31 show the pulls and constraints related to the systematic uncertainties resulting from the fit. Some deviations with respect to the nominal values are observed, however all of them are not significant.

The nuisance parameters, the normalization factors associated to the main backgrounds and the statistical uncertainties are ranked based on their impact on the signal strength μ resulting from the fit. Specifically, the effect of a parameter is evaluated by performing the maximum likelihood fit with the parameter value fixed to its $\pm 1\sigma$ variations. The shift in the resulting μ with respect to the nominal fit is then used to assess the importance of the parameter. This procedure is carried out individually for each parameter included in the fit. Statistical uncertainties are taken into account by defining one parameter per bin in all analysis regions.

The ranking of the fit parameters is reported in Figure 5.32. The main uncertainty is the one associated to the $t\bar{t}W$ normalization factor, which has a 8% impact on the signal strength measurement. The second highest uncertainty is associated to $t\bar{t}H$ modelling, with an impact of $\approx 3\%$, followed by the b-tagging extrapolation uncertainty at high p_T and the muon trigger uncertainty. The highest ranked statistical uncertainty is associated to the first bin of the SR_{RR}^{++} distribution.

The post-fit distributions in the CRs related to the variables employed in the fit are shown in Figure 5.33 and 5.34. The bottom panels display the post-fit ratios of data/MC yields, whose values are approximately 1 in each bin, therefore showing a good agreement between the background estimates and the data. A summary of the pre- and post-fit yields in the CRs is reported in Figure 5.35. The post-fit distributions in

the Validation Regions are employed to further assess the goodness of the background estimates resulting from the fit, as can be seen from Figure 5.36. The post-fit event yields related to the different processes are reported in Table 5.20 and 5.21 for CRs and VRs. Good agreement between expected event yields and data can be observed in all regions.
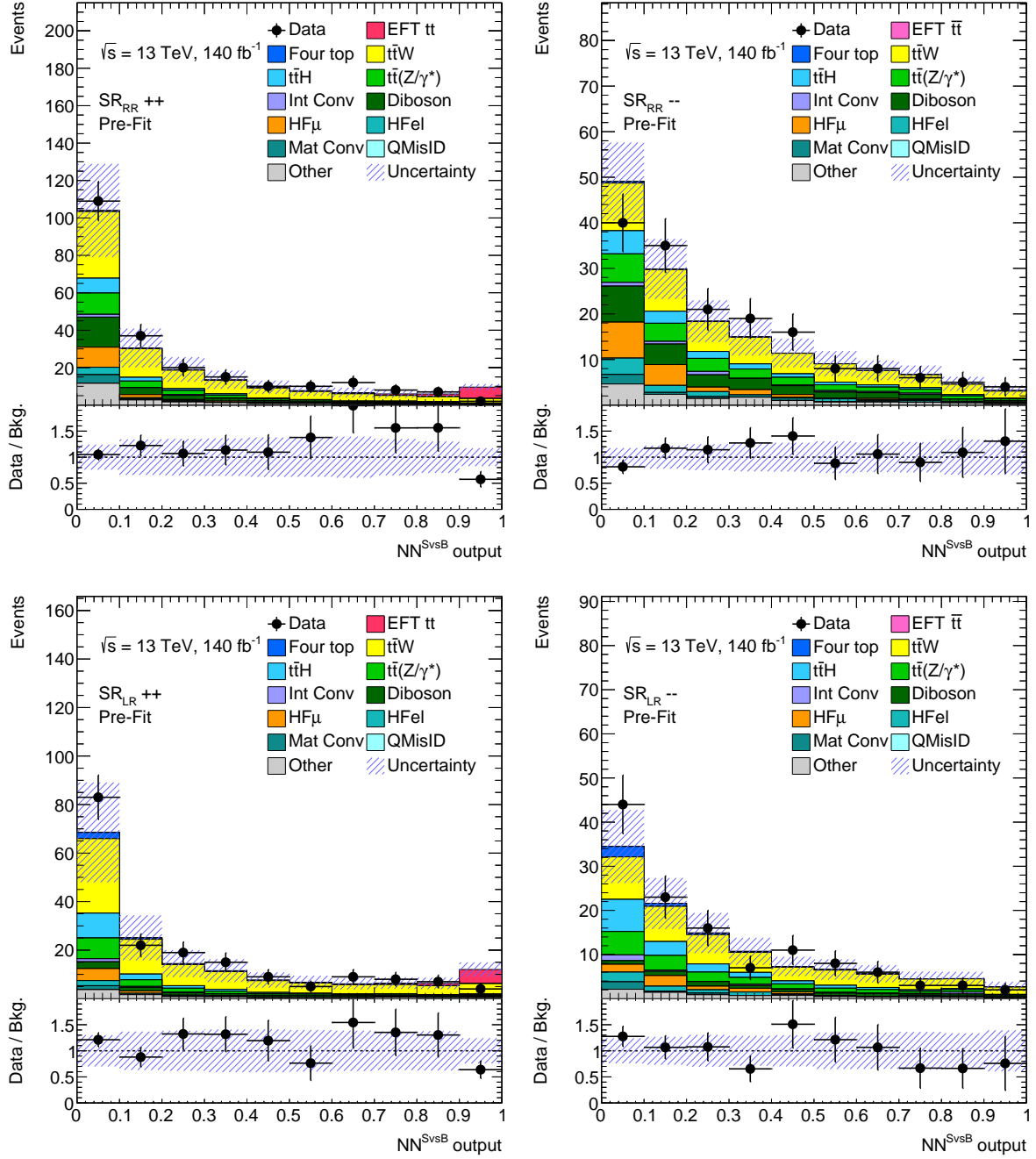
Figure 5.27: Unblinded distributions of the NN$^{\text{SvsB}}$ output in the analysis SRs. The signal prediction is normalized according to the analysis expected sensitivity. The blue hashed bands include both statistical and systematic uncertainties. The bottom panels show the ratio between data and background prediction.
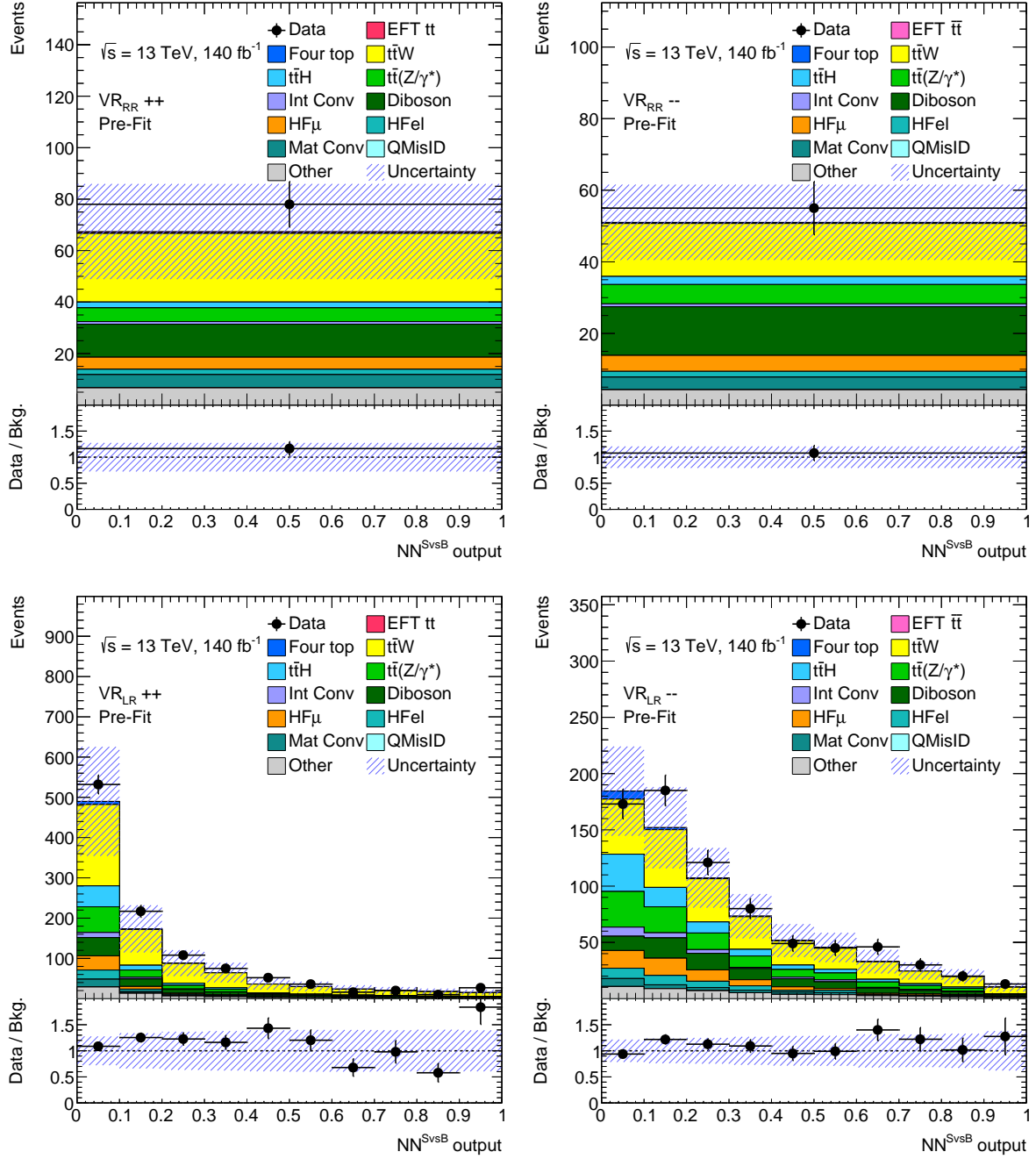
Figure 5.28: Distributions of the NN$^{\mathrm{SvsB}}$ output in the analysis VRs. The signal prediction is normalized according to the analysis expected sensitivity. The blue hashed bands include both statistical and systematic uncertainties. The bottom panels show the ratio between data and background prediction.
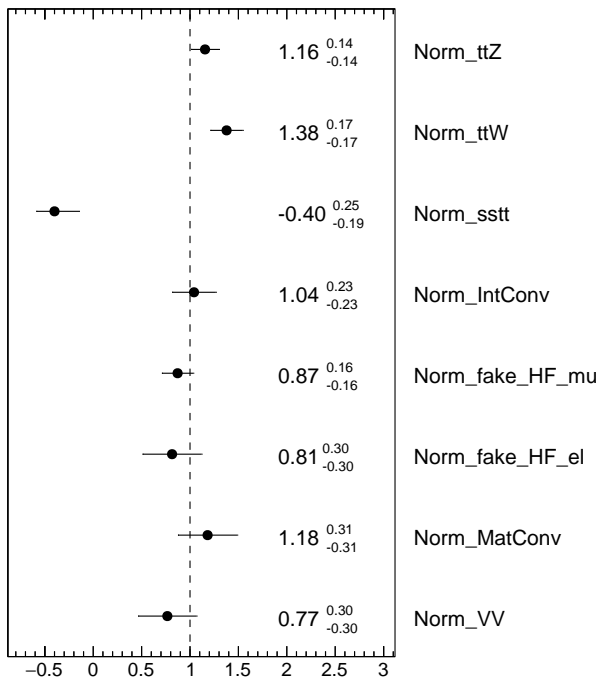
Figure 5.29: Normalization factors resulting from the S+B fit to Run 2 collision data performed over all analysis regions including statistical and systematic uncertainties. The normalization factors are related to the signal and to non-prompt leptons, diboson, $t\bar{t}Z$ and $t\bar{t}W$ backgrounds. All NFs and are left free-floating in the fit.
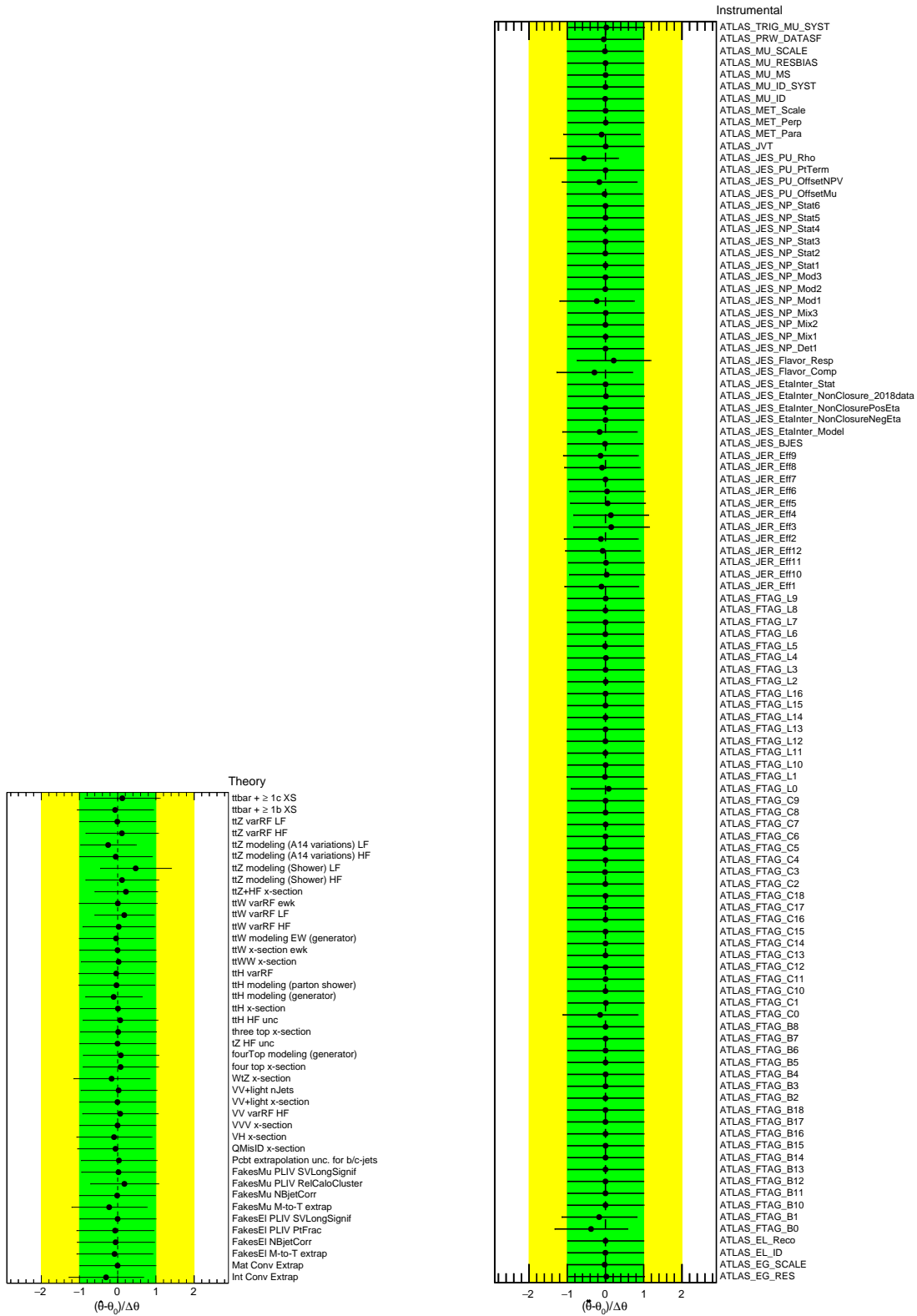
Figure 5.30: Pulls and constraints on the theory nuisance parameters (left) and on the instrumental nuisance parameters (right) resulting from the S+B fit to the Run 2 collision data performed over all analysis regions.
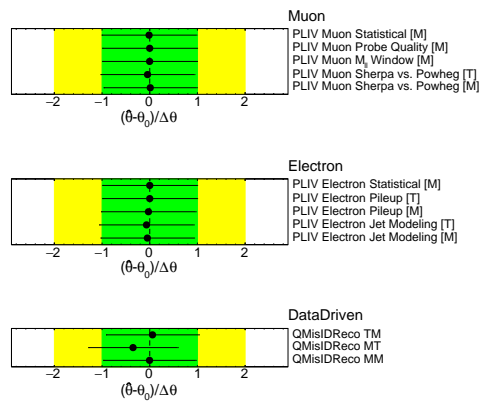
Figure 5.31: Pulls and constraints on the muon (top) and electron (middle) PLIV as well as on the data driven QMisID (bottom) related nuisance parameters resulting from the S+B fit to the Run 2 collision data performed over all analysis regions.
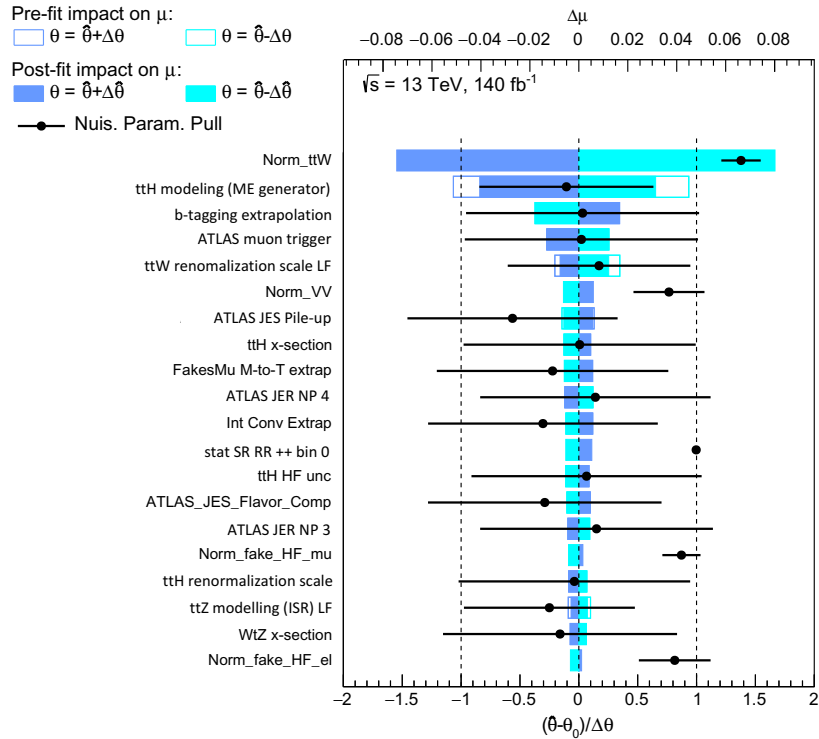
Figure 5.32: Ranking of the fit parameters resulting from the S+B fit to the Run 2 collision data performed over all analysis regions. The parameters are ranked based on their impact on the signal strength μ resulting from the fit. Pre- and post-fit impacts are shown as empty and filled colored bands respectively. The pulls of the parameters are also shown as black dots with associated uncertainties. The lower $x-$axis label is only referred to the systematic uncertainties, while for normalization factors and statistical uncertainties the black dots show the parameters post-fit values and associated errors.

The NN$^{\text{SvsB}}$ output distributions in the analysis SRs resulting from the fit are shown in Figure 5.37, with the bottom panels displaying the ratio between data and MC expected yields. The post-fit event yields in the SRs, related to the different processes, are reported in Table 5.22 and summarized in Figure 5.38, where the pre-fit yields in the SRs are also shown.

	CR IntCO 3l	CR MatCO 3l	CR ttZ 3l	CR VV 3l,
Four top	0 (0)	0 (0)	1.63 ± 0.32	0.094 ± 0.035
$t\bar{t}W$	0 (0)	0 (0)	8.0 ± 1.2	25.2 ± 3.0
$t\bar{t}H$	0 (0)	0 (0)	11 ± 6	7 ± 4
$t\bar{t}Z/\gamma$	0 (0)	0 (0)	378 ± 31	234 ± 28
Int Conv	42 ± 7	15 ± 4	0.13 ± 0.07	1.5 ± 0.9
Diboson	0.036 ± 0.021	2.03 ± 0.26	32 ± 13	100 ± 40
tZ	0 (0)	0 (0)	29.4 ± 2.4	157.1 ± 3.2
HFμ	0 (0)	0 (0)	1.02 ± 0.32	7 ± 5
HFel	0 (0)	0 (0)	0.38 ± 0.27	8.0 ± 3.0
Mat Conv	1.4 ± 1.0	38 ± 8	0.50 ± 0.33	2.3 ± 0.8
QMisID	0 (0)	0 (0)	0.19 ± 0.14	0.9 ± 0.4
Other	0 (0)	0 (0)	41 ± 19	45 ± 22
Total	44 ± 7	55 ± 7	504 ± 21	590 ± 22
Data	44	55	494	605

	CR HFel TM 2lSS	CR HFel MT 2lSS	CR HFel MM 2lSS
Four top	0.071 ± 0.019	0.042 ± 0.016	0.036 ± 0.012
$t\bar{t}W$	15.3 ± 1.9	6.6 ± 0.9	2.7 ± 0.4
$t\bar{t}H$	4.7 ± 2.2	2.4 ± 1.2	1.0 ± 0.5
$t\bar{t}Z/\gamma$	8.5 ± 1.7	1.55 ± 0.35	1.89 ± 0.34
Int Conv	4.9 ± 2.8	2.5 ± 1.4	0.41 ± 0.26
Diboson	10.9 ± 2.4	3.7 ± 1.1	1.7 ± 0.5
HFμ	2.1 ± 1.1	8.7 ± 2.2	3.5 ± 1.5
HFel	33 ± 11	5.6 ± 2.2	4.0 ± 1.4
Mat Conv	4.3 ± 2.3	1.6 ± 1.3	1.4 ± 0.4
QMisID	5.2 ± 2.9	2.5 ± 1.7	1.5 ± 1.0
Other	4.2 ± 0.5	1.63 ± 0.18	0.61 ± 0.09
Total	93 ± 9	36.8 ± 3.2	18.8 ± 2.1
Data	95	32	19

	CR HFmu TM 2lSS	CR HFmu MT 2lSS	CR HFmu MM 2lSS
Four top	0.11 ± 0.04	0.068 ± 0.032	0.047 ± 0.018
$t\bar{t}W$	22.3 ± 2.8	10.3 ± 1.3	3.7 ± 0.6
$t\bar{t}H$	6.9 ± 3.4	3.7 ± 1.8	1.5 ± 0.7
$t\bar{t}Z/\gamma$	12.6 ± 1.9	6.3 ± 1.0	2.6 ± 0.5
Int Conv	0.56 ± 0.33	1.5 ± 0.9	0.27 ± 0.16
Diboson	16 ± 5	6.0 ± 1.5	3.0 ± 0.5
HFμ	80 ± 13	20 ± 6	12.3 ± 2.1
HFel	1.2 ± 0.7	5.5 ± 2.0	1.7 ± 0.6
Mat Conv	1.4 ± 0.8	1.1 ± 0.5	1.6 ± 0.5
QMisID	0.26 ± 0.12	0.5 ± 0.4	0.37 ± 0.25
Other	5.1 ± 0.6	2.68 ± 0.28	0.81 ± 0.11
Total	146 ± 11	58 ± 4	27.8 ± 2.6
Data	150	57	28

Table 5.20: Event yields in the CRs resulting from the fit performed on Run 2 data.

	VR_{RR} ++	VR_{RR} −	VR_{LR} ++	VR_{LR} −
EFT tt	-0.18 ± 0.10	0 (0)	-1.5 ± 0.8	0 (0)
EFT $\overline{tt}$	0 (0)	-0.018 ± 0.010	0 (0)	-0.10 ± 0.05
Four top	0.30 ± 0.07	0.29 ± 0.07	11.0 ± 2.3	11.2 ± 2.3
$t\bar{t}W$	37 ± 4	20.3 ± 2.3	630 ± 70	340 ± 40
$t\bar{t}H$	2.5 ± 1.3	2.5 ± 1.2	90 ± 40	90 ± 40
$t\bar{t}Z/\gamma$	6.2 ± 0.8	6.2 ± 0.8	125 ± 14	120 ± 13
Int Conv	0.9 ± 0.5	0.5 ± 0.5	17 ± 10	20 ± 11
Diboson	10.4 ± 3.0	11.4 ± 3.0	80 ± 22	65 ± 18
HFμ	4.0 ± 1.5	3.9 ± 1.8	40 ± 18	46 ± 19
HFel	1.6 ± 2.0	1.5 ± 1.0	26 ± 15	24 ± 13
Mat Conv	5.4 ± 2.6	4.2 ± 1.2	34 ± 10	26 ± 7
QMisID	0 (0)	0 (0)	0 (0)	0 (0)
Other	6.4 ± 0.9	4.1 ± 0.6	63 ± 7	45 ± 6
Total	74 ± 6	55 ± 4	1110 ± 50	781 ± 32
Data	78	55	1093	762

Table 5.21: Event yields in the VRs resulting from the fit performed on Run 2 data.
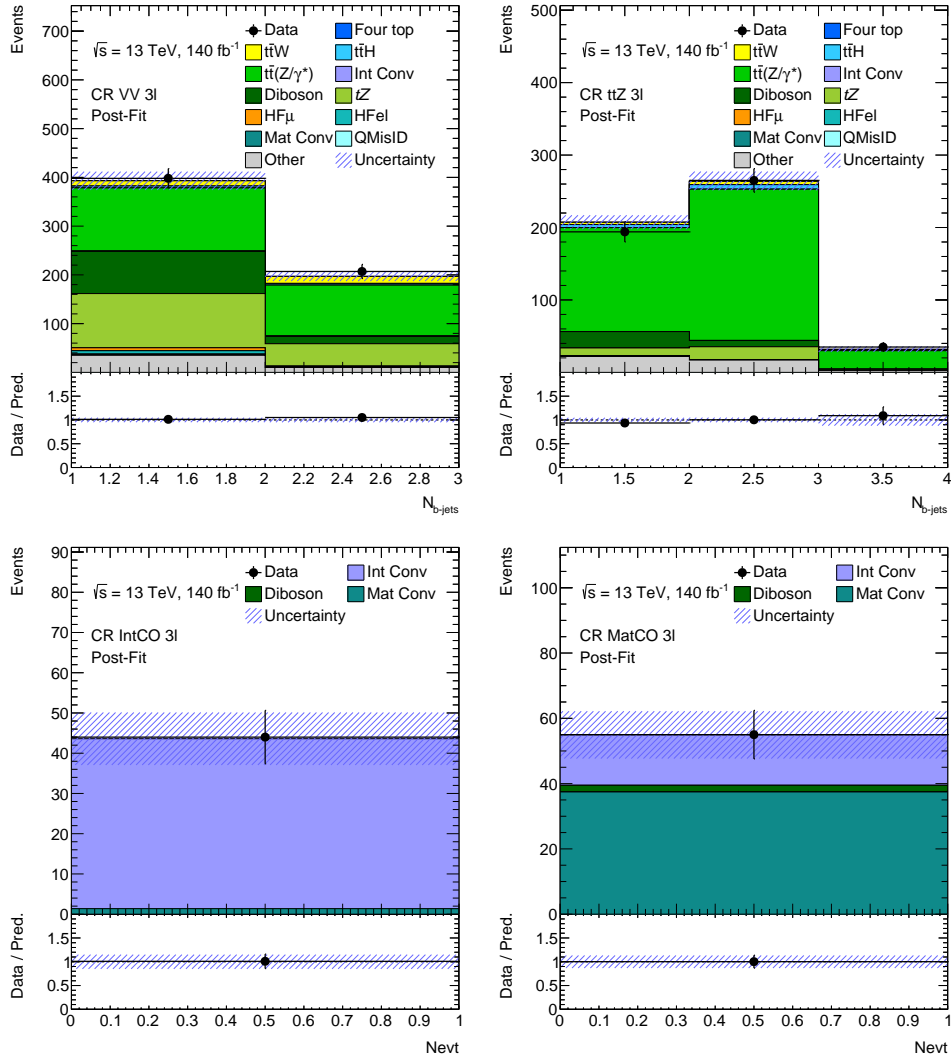
Figure 5.33: Post-fit distributions in the analysis VV, $t\bar{t}Z$, IntCO and MatCO CRs of the variables used in the fit performed on Run 2 data. The blue hashed bands include both statistical and systematic uncertainties. The bottom panels display the ratio between observed and expected event yields, used to assess the post-fit data/MC agreement.
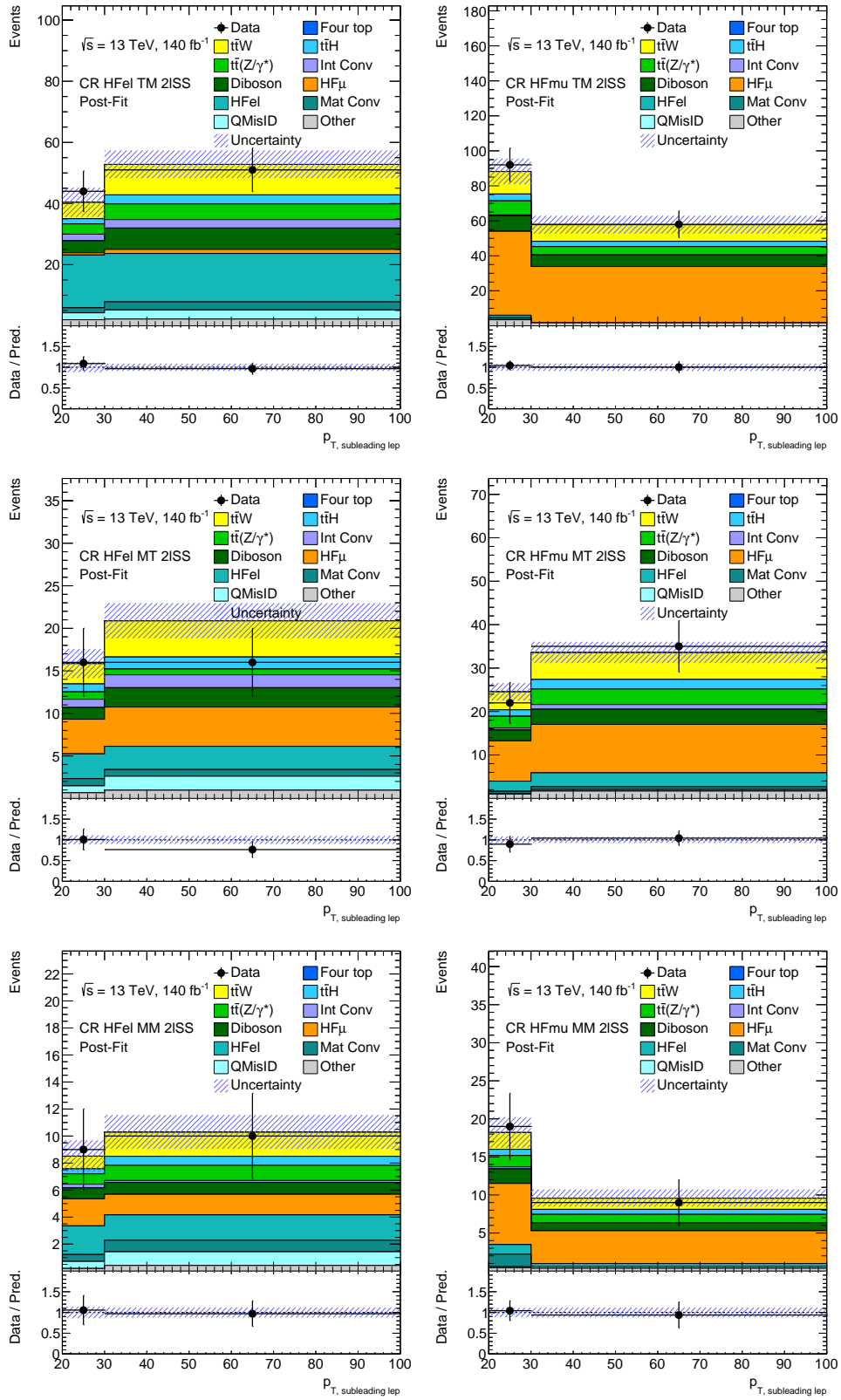
Figure 5.34: Post-fit distributions in the analysis *HF*-CRs of the variables used in the fit performed on Run 2 data. The blue hashed bands include both statistical and systematic uncertainties. The bottom panels display the ratio between observed and expected event yields, used to assess the post-fit data/MC agreement.
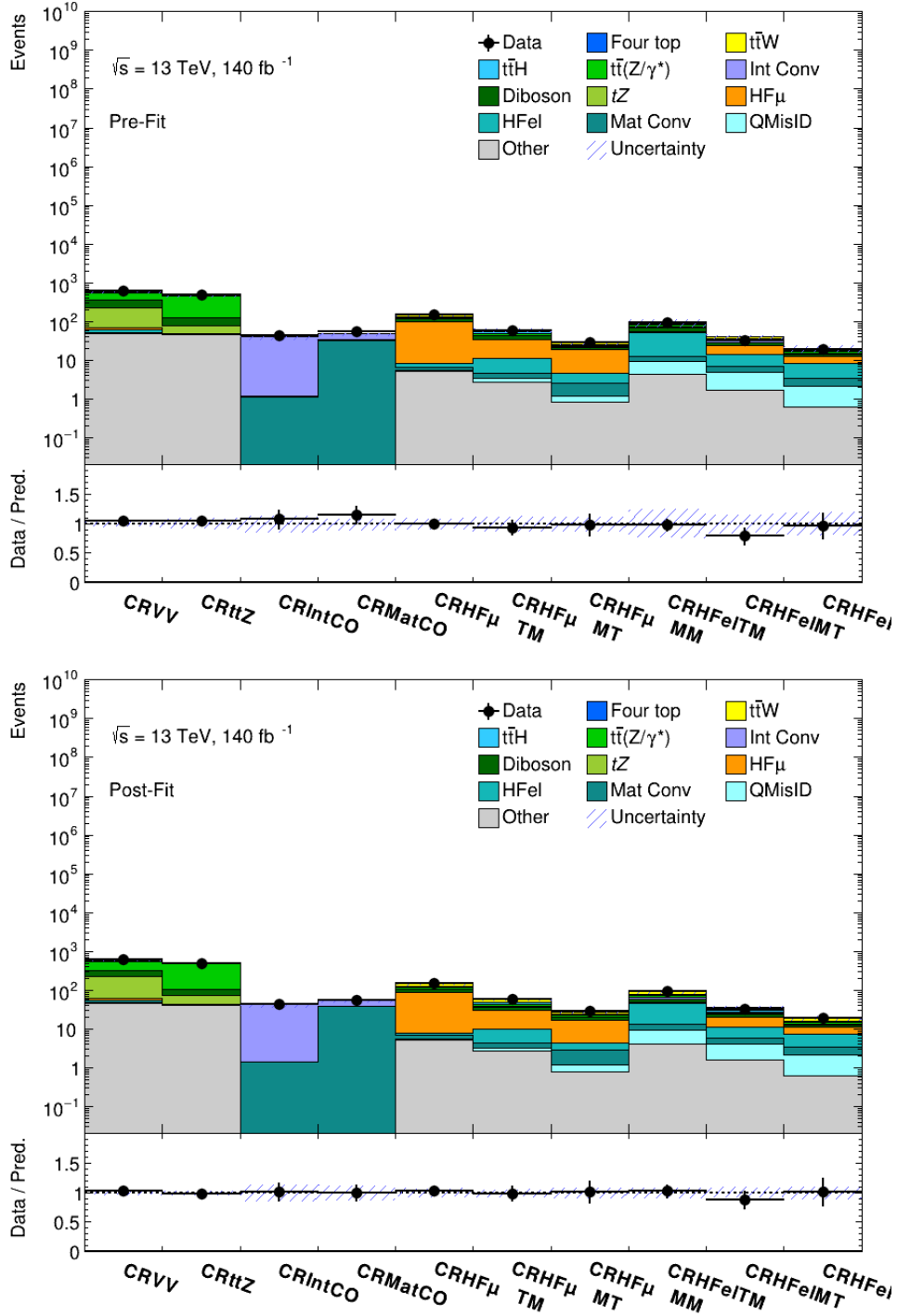
Figure 5.35: Summary of the pre-fit and post-fit data and MC yields in the analysis CRs. The post-fit yields are related to the fit performed on Run 2 data. The blue hashed bands include both statistical and systematic uncertainties. The bottom panels display the ratio between data and MC yields.

109
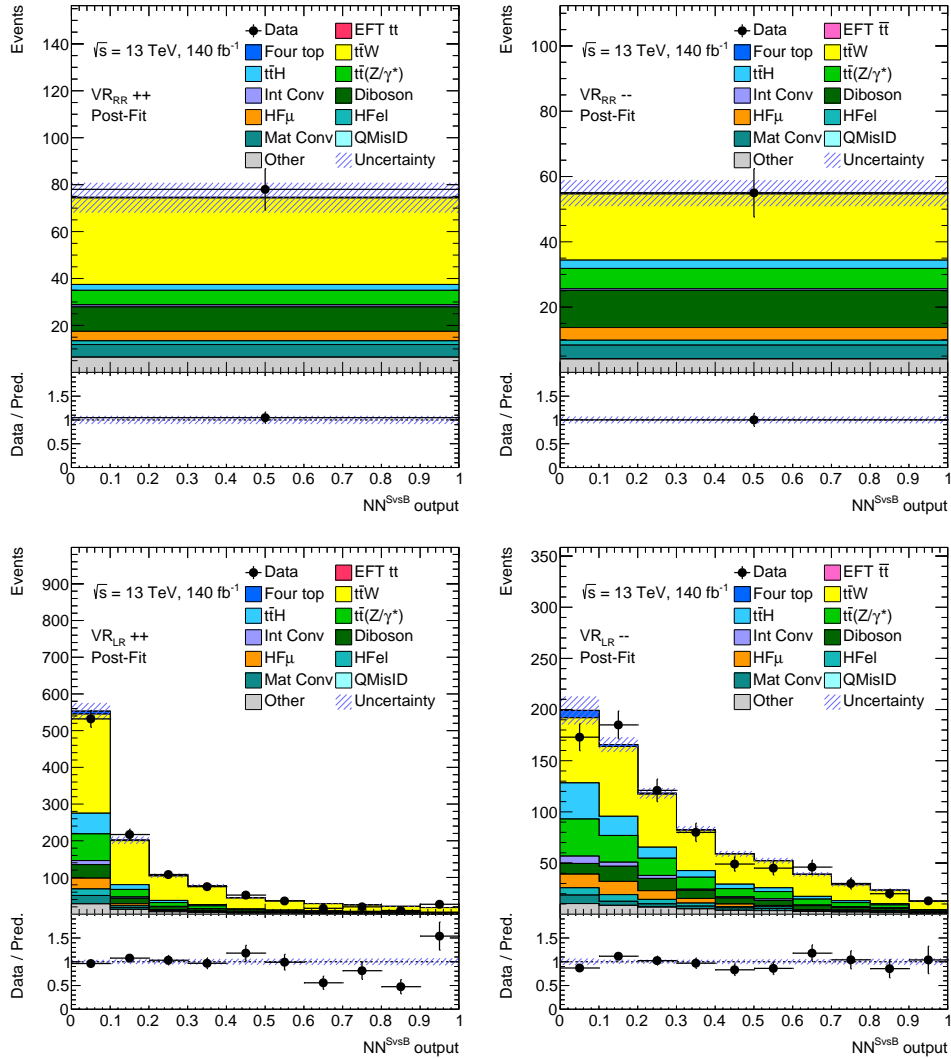
Figure 5.36: Post-fit distributions in the analysis VRs. The fit has been performed on Run 2 data events over all SRs and CRs. The blue hashed bands include both statistical and systematic uncertainties. The bottom panels display the ratio between observed and expected event yields, used to assess the post-fit data/MC agreement.
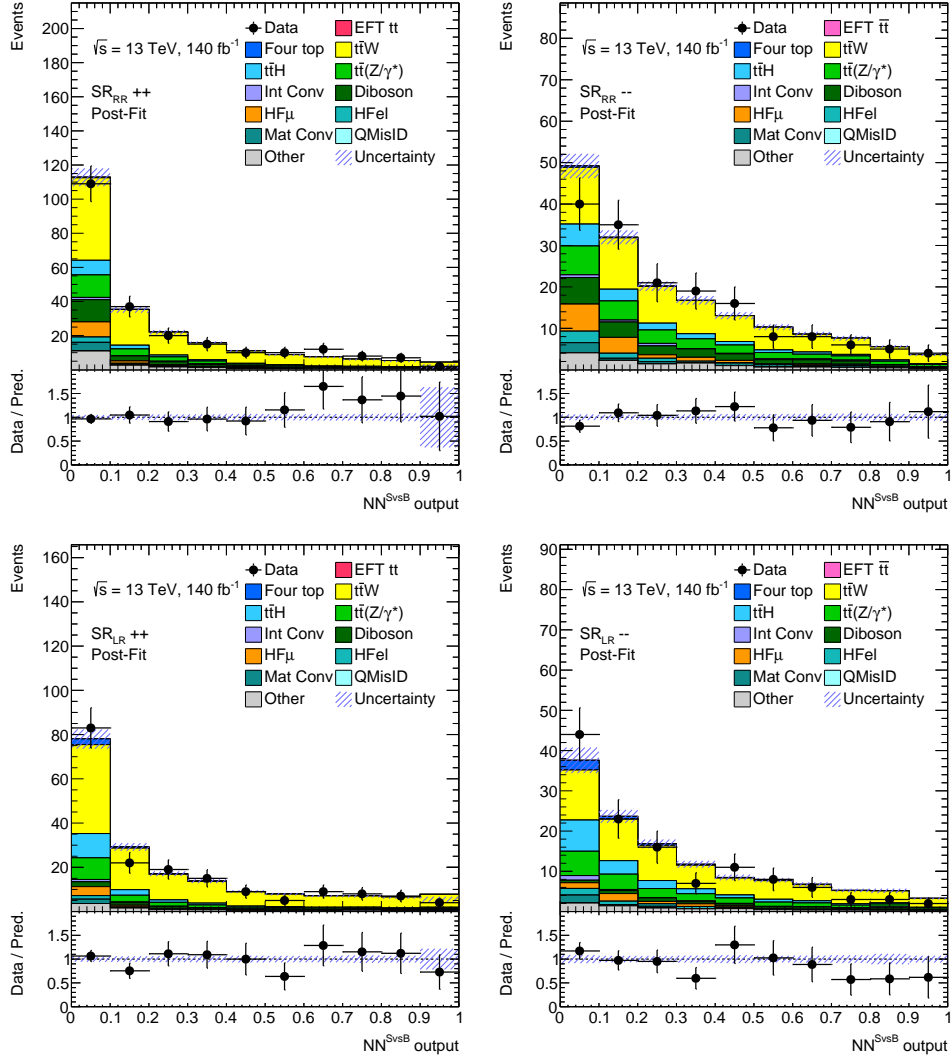
Figure 5.37: Post-fit distributions of the NN^{SvsB} output in the analysis SRs. The signal is normalized according to the analysis expected sensitivity. The fit is performed on Run 2 data. The blue hashed bands include both statistical and systematic uncertainties. The bottom panels show the ratio between data and MC yields.

No significant deviation with respect to SM predictions is found in the SRs, therefore a 95% confidence level upper limit on the same-sign top signal production cross section times Branching Ratio is evaluated using the CL_s method. The observed(expected) upper limit is:

$$\sigma(tt + \overline{tt}) \times BR < 0.86(1.34^{+0.60}_{-0.37}) \text{ fb at 95\% CL.} \quad (5.11)$$

	SR_{RR} ++	SR_{RR} −	SR_{LR} ++	SR_{LR} −
EFT tt	-4.3 ± 2.3	0 (0)	-3.3 ± 1.8	0 (0)
EFT $\bar{t}\bar{t}$	0 (0)	-0.19 ± 0.10	0 (0)	-0.08 ± 0.05
Four top	0.73 ± 0.16	0.70 ± 0.17	4.2 ± 0.9	4.1 ± 0.9
$t\bar{t}W$	122 ± 14	68 ± 8	113 ± 13	59 ± 7
$t\bar{t}H$	14 ± 7	14 ± 6	17 ± 9	17 ± 8
$t\bar{t}Z/\gamma$	25.4 ± 2.7	24.2 ± 2.8	19.4 ± 1.7	19.0 ± 1.8
Int Conv	2.5 ± 1.4	2.6 ± 1.5	1.8 ± 1.1	2.5 ± 1.4
Diboson	22 ± 6	19 ± 5	7.5 ± 2.2	5.1 ± 1.5
HFμ	12 ± 4	13 ± 6	5.5 ± 2.1	5.1 ± 1.9
HFel	4.1 ± 2.1	6 ± 4	2.7 ± 1.2	4.1 ± 3.2
Mat Conv	7.3 ± 2.3	5.5 ± 1.5	2.7 ± 0.8	3.3 ± 1.2
QMisID	$< 10^{-4}$	$< 10^{-4}$	$< 10^{-4}$	$< 10^{-4}$
Other	19.9 ± 3.0	13.0 ± 1.9	9.5 ± 1.3	7.5 ± 1.4
Total	225 ± 10	167 ± 6	181 ± 9	126 ± 6
Data	230	162	181	123

Table 5.22: Event yields in the SRs resulting from the fit performed on Run 2 data.

5.8.1 Limits on SMEFT parameters

Upper limits on SMEFT Wilson Coefficients are evaluated using different EFT benchmarks among the ones obtained through the reweighting procedure applied on the tt and $\bar{t}\bar{t}$ nominal samples, as reported in Section 5.1. Different signal assumptions are employed, corresponding to different values associated to the Wilson Coefficients c_{RR}, $c_{LR}^{(1)}$ and $c_{LR}^{(8)}$. The EFT benchmarks where only one of the three considered operators is responsible for the production of same-sign top pairs within the theory are employed, since the resulting limits on the signal cross section can be directly reinterpreted as limits on the associated Wilson Coefficients, following the EFT parametrization reported in eq(3.4). The resulting upper limits at 95% CL on the cross section times Branching Ratio are shown in Table 5.23. The limits associated to $\mathcal{O}_{LR}^{(1)}$ and $\mathcal{O}_{LR}^{(8)}$ are comparable, due to the kinematic similarity of signal events originating from the two LR operators.

The cross section limits reported in Table 5.23 correspond to individual limits on the three EFT operators reported in Table 5.24.

This is the first search for same-sign top pairs carried out using the SMEFT and proton-proton collision data at $\sqrt{s} = 13$ TeV. The resulting limit on the same-sign top pairs production cross section exhibits a significant improvement with respect to the most recent limits measured in analyses carried out by the ATLAS and CMS Collaborations [57, 64, 67]. Specifically, the limit on same-sign top pairs production cross section
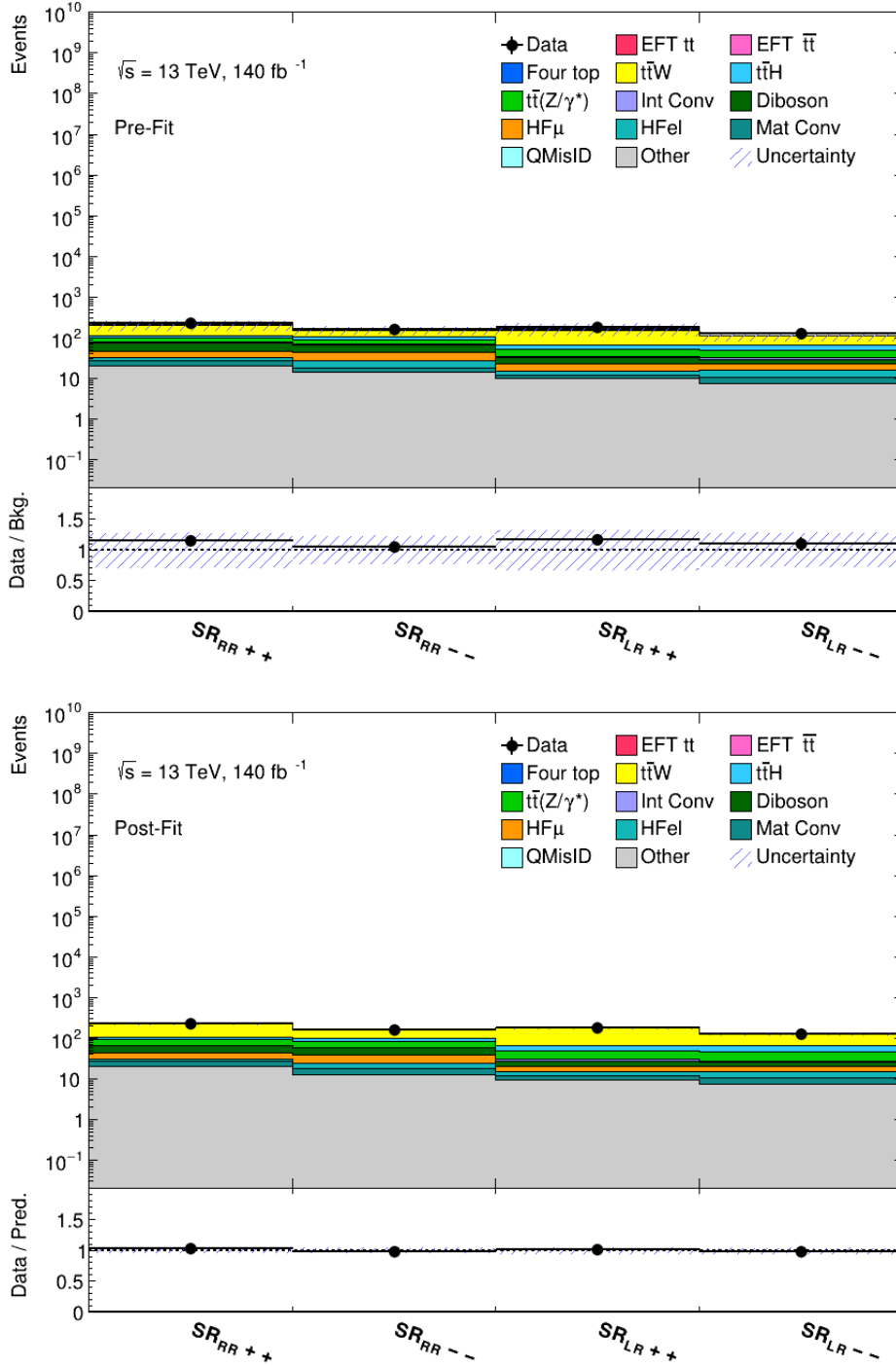
Figure 5.38: Summary of the pre-fit and post-fit data and MC yields in the analysis SRs. The post-fit yields are related to the fit performed on Run 2 data. The blue hashed bands include both statistical and systematic uncertainties. The bottom panels display the ratio between data and MC yields.

is improved by a factor of ~ 10 with respect to the latest ATLAS analysis targeting the same process [64]. This analysis resulted in $\sigma(uu \longrightarrow tt) = 89$ fb, as reported in Section 3.2, which corresponds to $\sigma(uu \longrightarrow tt) \times BR = 9.35$ fb to be compared with the

Cross section $\times BR$	observed upper limit at 95% CL (fb)	expected upper limit at 95% CL (fb)
σ_{RR}	0.82	$1.21^{+0.54}_{-0.034}$
$\sigma^{(1)}_{LR}$	0.91	$1.46^{+0.67}_{-0.42}$
$\sigma^{(8)}_{LR}$	0.93	$1.48^{+0.72}_{-0.41}$

Table 5.23: Observed and expected upper limits (with $\pm 1\sigma$ variations) at 95% CL on same-sign top pairs production cross section times Branching Ratio related to three EFT operators considered in the analysis.

Wilson Coefficient	observed upper limit at 95% CL $(\text{TeV}/\Lambda)^2$	expected upper limit at 95% CL $(\text{TeV}/\Lambda)^2$
c_{RR}	0.005	$0.006^{+0.001}_{-0.001}$
$c^{(1)}_{LR}$	0.015	$0.019^{+0.004}_{-0.003}$
$c^{(8)}_{LR}$	0.031	$0.040^{+0.009}_{-0.006}$

Table 5.24: Observed and expected upper limits (with $\pm 1\sigma$ variations) at 95% CL on the Wilson Coefficients in units of $(\text{TeV}/\Lambda)^2$ related to three EFT operators considered in the analysis.

0.86 fb limit resulting from the analysis reported in this thesis. Half of the improvement factor stems from the increase in the luminosity (from 36.1 fb^{-1} to 140 fb^{-1}), while the other half is associated to the improvement in the analysis sensitivity.

The individual limits placed on the Wilson Coefficients related to the four-fermion operators reported in Table 5.24 are more stringent with respect to the ones resulting from previous same-sign top searches carried out using the SMEFT, as reported in Section 3.2. However, a different basis related to the EFT model has been employed in this analysis. Therefore a direct comparison between the resulting limits on the WCs should be treated with caution.

Since at the present time the EFT basis employed in this analysis is widely used to perform EFT individual reinterpretation measurements as well as EFT global fits, the limits on the WCs derived in this analysis might be combined with other measurements in global EFT fits in the future.

Conclusions

The Standard Model Effective Field Theory (SMEFT) provides an excellent framework to search for new physics at the LHC by keeping a model independent approach. The SMEFT is a powerful tool to be employed in the interpretation of possible deviations with respect to Standard Model predictions, that might be observed not only in precision SM measurements but also in new physics searches. This is the case for same-sign top pairs production, a process that is highly suppressed by the SM theory, but allowed within the SMEFT via a four-fermion pointlike interaction.

A search for same-sign top quark pairs produced according to the SMEFT has been presented in this thesis. The analysis has been carried out within the ATLAS Collaboration using collision data at a center-of-mass energy of $\sqrt{s} = 13$ TeV, collected by the detector during the second run of the Large Hadron Collider (LHC) corresponding to an integrated luminosity of 140 fb^{-1}.

The signal associated to same-sign top pairs production is searched in the dilepton channel, with the top quarks decaying leptonically via the process $t \longrightarrow W^+ b \longrightarrow \ell^+ \nu b$. Three different EFT operators that can generate same-sign top quark pairs, namely $\mathcal{O}_{RR}$, $\mathcal{O}_{LR}^{(1)}$, and $\mathcal{O}_{LR}^{(8)}$, are considered in the analysis and the Warsaw basis is used for the operators definition. The final state signature associated with the searched signal is composed of a pair of high-transverse momentum same-sign leptons and b-jets. This signature is rarely produced in Standard Model processes. Nevertheless, backgrounds may arise from detector inefficiencies, as well as from the mis-reconstruction of physics objects, and are accurately estimated in the analysis.

Several mutually exclusive analysis regions are defined in order to be enriched in either signal or background events. A preliminary selection of events that exhibit characteristics consistent with the signal is performed, imposing strict requirements on the b-tagging of jets and the isolation of the two same-sign leptons. A first Deep Neural Network (DNN) is trained using the events that satisfy these requirements to build separate Signal Regions, enriched in same-sign top quark events resulting from different EFT operators. The defined Signal Regions are then further split based on the charge of the same-

sign leptons, and a second DNN is trained to perform signal-background discrimination within each individual region. An additional selection requirement is imposed on signal-like events, based on the azimuthal distance between the same-sign leptons, $\Delta\Phi(\ell,\ell)$, to increase the purity of the defined Signal Regions and to build Validation Regions that are used to validate the background estimates resulting from the statistical analysis.

The expected background contributions to the selected event samples are estimated employing different techniques, combining both simulation and data. Different Control Regions are defined in order to be enriched in specific background processes while having an expected negligible contamination from signal events. The extraction of the signal and of the estimates related to the main expected backgrounds, such as $t\bar{t}W$, $t\bar{t}Z$, diboson and non-prompt leptons, are simultaneously performed through a statistical maximum likelihood fit on the full Run 2 dataset. Various sources of systematic uncertainties affecting the measurement are taken into account in the analysis.

No significant excess with respect to the Standard Model predictions is observed, therefore upper limits on the signal production cross section and on the Wilson Coefficients associated to the considered EFT operators are derived. The observed upper limit at 95% of confidence level on same-sign top pairs production cross section times Branching Ratio is 0.86 fb. This result exhibits a factor of ~ 10 of improvement with respect to the latest same-sign top pairs search carried out by the ATLAS Collaboration [64].

The observed upper limits on the Wilson Coefficients related to the three four-fermion operators considered in the analysis are: $c_{RR} \leq 0.005$, $c_{LR}^{(1)} \leq 0.015$ and $c_{LR}^{(8)} \leq 0.031$ ($[\text{TeV}/\Lambda]^2$). These limits can be combined with other measurements in global EFT fits, which may be carried out within and outside the ATLAS Collaboration. Furthermore, due to the model independent approach of the Standard Model Effective Field Theory, the results obtained in this analysis might be reinterpreted using different BSM theories.

This is the first search for same-sign top quark pairs carried out within the ATLAS Collaboration using the SMEFT and proton-proton collision data at $\sqrt{s} = 13$ TeV.

Appendices

Appendix A

Search for heavy Higgs bosons from a g2HDM in multilepton plus b-jets final states

Researchers belonging to the team that carried out the analysis presented in Chapter 5 also contributed to another analysis within the ATLAS Collaboration titled "Search for heavy Higgs bosons from a g2HDM in multilepton plus b-jets final states in pp collisions at 13 TeV with the ATLAS detector" [120], summarized in this Appendix.

I contributed to the analysis by performing some studies related to the same-sign top signal production, which is one among the several targeted BSM processes, as reported in Section A.2. I also evaluated the product of acceptance times efficiency for all searched production modes and signal regions.

The *general Two Higgs Doublet Model* (g2HDM) search shares several features with the analysis presented in the main body of this document and has been employed as a reference for the SMEFT same-sign top quark pairs search for developing the global analysis strategy.

A.1 The general Two Higgs Doublet Model (g2HDM)

Among the many different BSM theories formulated, several are based on an extension of the SM Higgs sector by the addition of a second complex Higgs doublet. These models are referred as Two Higgs Doublet Models (2HDMs) [121, 122]. The addition of a new scalar doublet in the theory gives rise to new particles. Specifically, five massive particles result from the SM SSB: two CP-even scalar particles h and H, one CP-odd

pseudo-scalar A and two charged scalar particles $H^{\pm}$. The two fields associate to the scalar neutral particles are expected to mix. However, precise measurements of the SM Higgs boson proprieties carried out using LHC collision data show no deviations with respect to SM predictions, forcing the extra scalar particle arising from the 2HDM to be either very heavy or to have a vanishingly small mixing with the SM Higgs boson [35]. These two assumptions are referred as *decoupling limit* and *alignment limit* respectively. Analyses working with 2HDMs are usually carried out imposing a discrete Z_2 symmetry on the model. Following this additional assumption, flavor changing neutral current (FCNC) processes mediated by the scalar bosons are forbidden. On the other hand, if no additional requirements are placed on the 2HDM, the alignment limit is naturally reached and the BSM scalar particles can give rise to FCNC processes with the h scalar preserving its SM-like nature instead [60]. This model is referred as *general* 2HDM (g2HDM).

A.2 Summary of the g2HMD search

The analysis summarized in this section is a search for events originating by several processes involving a BSM scalar particle H from a g2HDM. The analysis is carried out using LHC proton-proton collision data at $\sqrt{s} = 13$ TeV collected by the ATLAS detector during the Run 2, corresponding to an integrated luminosity of 139 fb^{-1}.

Final state signatures associated to the BSM processes shown in Figure A.1 are searched in the analysis. Specifically, the processes considered in the analysis are: tt, ttq, $t\bar{t}t(\bar{t}t\bar{t})$, $t\bar{t}tq(\bar{t}t\bar{t}q)$ and $t\bar{t}t\bar{t}$.

Several Signal Regions are defined in the analysis related to the multi-lepton and multi b-jet final states generated by the processes reported in Figure A.1.

After performing a preselection on the events, the search strategy is defined based on two DNNs. One first NN is employed to categorize different signal processes in mutually exclusive Signal Regions. Specifically, categories associated to final states with either 2 same-sign leptons or 3 leptons are defined. Separate categories are defined for the five BSM process considered and based on the lepton charge associated to the same-sign lepton pair in the event ($++$ or $--$). One last category is defined related to events with 4 leptons originating from $t\bar{t}t\bar{t}$. Each defined category acts as a Signal Region in the analysis, for a total number of 17 SRs. A summary of the Signal Regions selection requirements is presented in Table A.1. It can be noticed that the $2\ell SS$ regions share common requirements with respect to the Signal Regions defined for the SMEFT same-sign top pairs search presented in the main body of this work (see Section 5.4). The lepton categories defined in Section 5.2.3 are employed here as well.
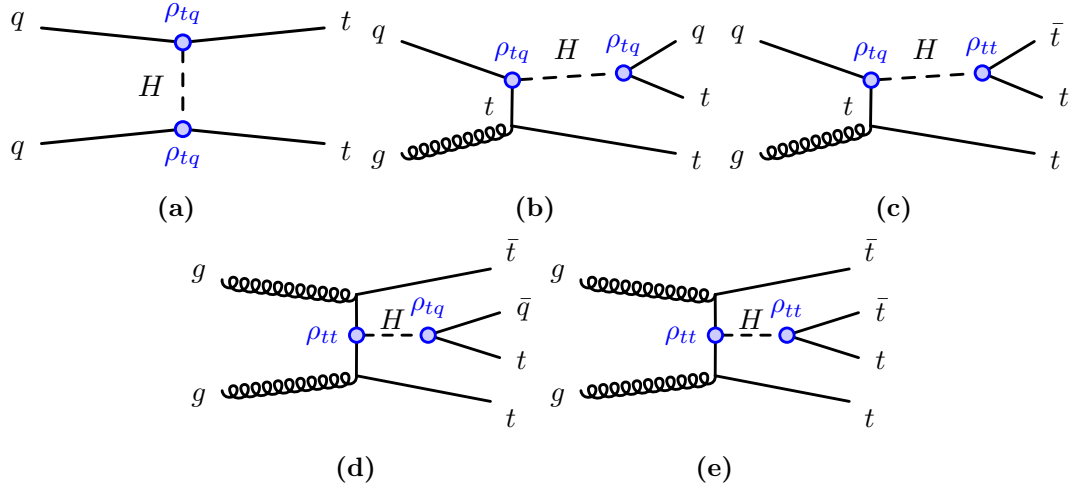
Figure A.1: Signal diagrams for the production and decay modes of the heavy scalar considered in the analysis. The couplings of the heavy H with SM particles are shown as well.

Lepton category	2ℓ SS	3ℓ	4ℓ
Lepton definition	(T, T) with ≥ 1 b-jet at 60% WP $\|\|$ (T, M) with ≥ 2 b-jet at 77% WP	(L, T, M) with ≥ 1 b-jet at 60% WP $\|\|$ (L, M, M) with ≥ 2 b-jet at 77% WP	(L, L, L, L)
Lepton p_T [GeV]	(20, 20)	(10, 20, 20)	(10, 10, 10, 10)
$m_{\ell^+\ell^-}^{OS-SF}$ [GeV]	–	>12	
$\|m_{\ell^+\ell^-}^{OS-SF} - m_Z\|$ [GeV]	–	>10	
N_{jets}		≥ 2	
N_{b-jets}		≥ 1 b-jet at 60% $\|\|$ ≥ 2 b-jet at 77%	
Region split	(sstt, ttq, ttt, tttq, tttt) $\times$ (Q^{++}, Q^{--})	(ttt, tttq, tttt) $\times$ (Q^+, Q^-)	–
Region naming	2ℓ SS ++ CAT sstt	3ℓ ++ CAT ttt	4ℓ
	2ℓ SS ++ CAT ttq	3ℓ ++ CAT tttq	
	2ℓ SS ++ CAT ttt	3ℓ ++ CAT tttt	
	2ℓ SS ++ CAT tttq	3ℓ −− CAT ttt	
	2ℓ SS ++ CAT tttt	3ℓ −− CAT tttq	
	2ℓ SS −− CAT sstt	3ℓ −− CAT tttt	
	2ℓ SS −− CAT ttq		
	2ℓ SS −− CAT ttt		
	2ℓ SS −− CAT tttq		
	2ℓ SS −− CAT tttt		

Table A.1: Summary of the event selection in the Signal Regions defined for the g2HDM search.

The background estimation is carried out following the same strategy employed for the SMEFT same-sign top pairs search, therefore a detailed description of the procedure has been already outlined in Section 5.5.

The extraction of the signal yields, and of the yields related to the background processes estimated in Control Regions, is performed through a maximum likelihood method, similarly to what has been reported in Section 5.7. One signal strength parameter is associated to all the signal processes. A summary of the post-fit results in SRs and CRs is shown in Figure A.2. No significant excess with respect to SM prediction has been found. Consequently, exclusion limits at 95% confidence level are placed on the g2HDM parameters. Specifically, exclusion limits have been placed on the mass value of the BSM H scalar boson, as shown in Figure A.3 for different coupling scenarios, and on the g2HDM couplings, as reported in Figure A.4.

Figure A.2: Comparison between data and the background prediction for the event yields in (a) the 17 Signal Regions and (b) the 10 Control Regions. The total background prediction before the likelihood fit to data is shown as a dashed blue histogram in the top panels. The ratio of the data to the total prediction is shown in the bottom panels, separately for post-fit (black points) and pre-fit background (dashed blue line).

Figure A.3: Observed and expected exclusion limits at 95% CL on the heavy Higgs boson mass for the g2HDM signal model for different couplings benchmarks. The yellow and green bands around the expected limit are respectively the $\pm 1\sigma$ and $\pm 2\sigma$ variations including all uncertainties. The predicted signal production cross section is shown as a red line. The production cross section is the sum of the five signal processes considered in the search.

(a)

(b)

(c)

(d)
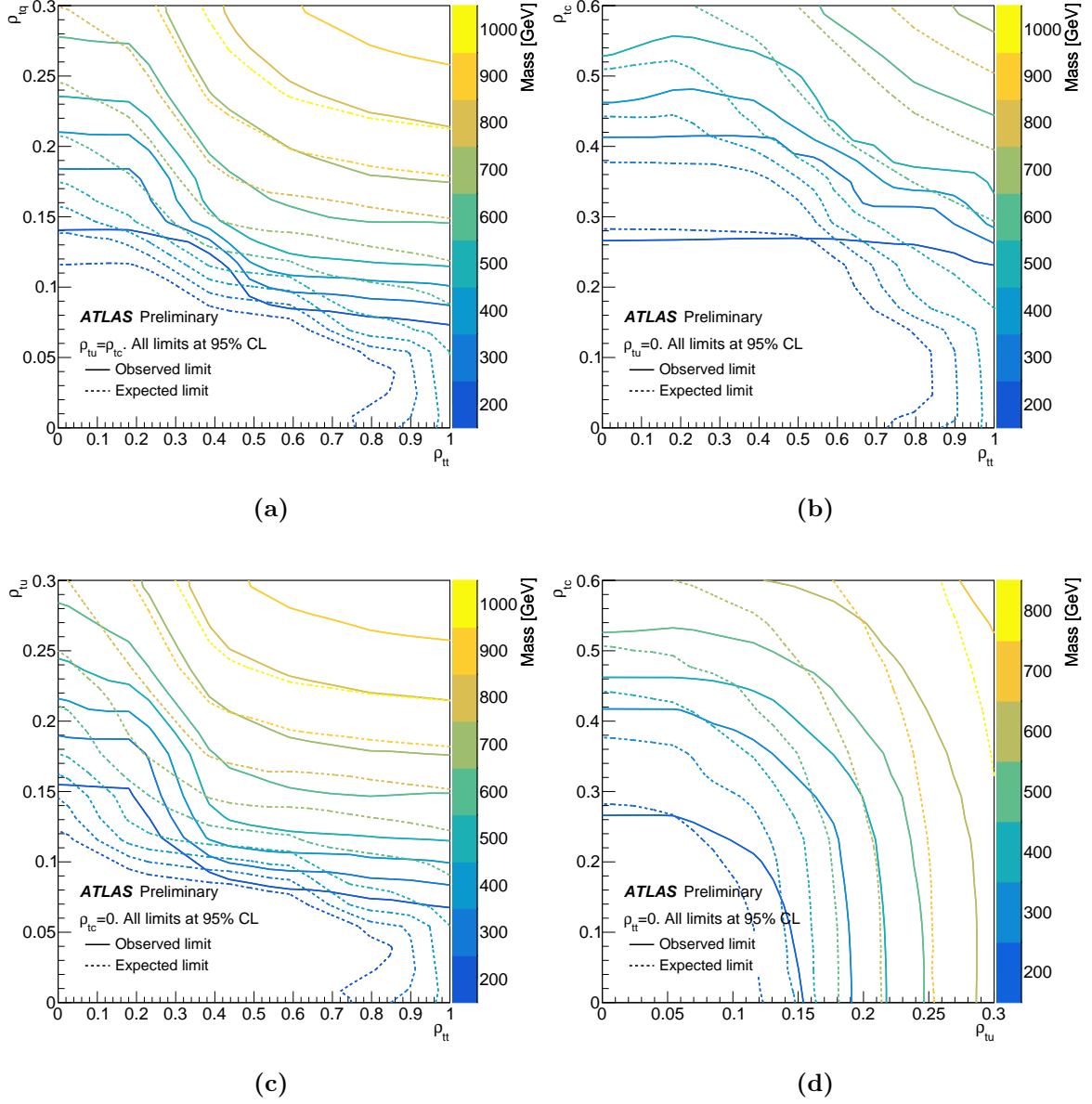
Figure A.4: Observed (solid line) and expected (dashed line) exclusion limits at 95% CL on the heavy Higgs boson mass for the g2HDM as a function of the couplings under different signal benchmarks.

Appendix B

Muon reconstruction efficiency and momentum calibration

Several physics analyses carried out by the ATLAS Collaboration, such as the one reported in this document, target final states involving muons. An accurate reconstruction and identification of muon candidates is therefore required for the Collaboration physics program to advance. Analyses targeting final states with muons rely on precise identification of candidates based on the measured tracks in the various ATLAS subdetectors. This is achieved thanks to the high level detector performance as well as through the implementation of thorough reconstruction and identification algorithms, as reported in Section 5.2. A correct calibration of the muon transverse momentum is also required to maximize the precision of physics measurements.

In the following section, the procedure adopted during the LHC Run 2 to measure the muon reconstruction and identification efficiency is outlined [97], with a specific focus on the low-p_T regime, where the background contamination coming from hadrons decay is higher.

The calibration of muon momentum is described in Section B.2, focusing on the determination and of scale and resolution corrections [109].

B.1 Muon reconstruction efficiency studies

The evaluation of muon reconstruction efficiencies is performed in the $|\eta| < 2.5$ region, where muon detection is carried out independently in the ID and the MS[1], through the

---

[1]The acronyms associated to the ATLAS subdetectors and to the different muon types defined in Chapter 4 and Section 5.2 will be used in this Appendix.

"tag-and-probe" method[2]. $Z \longrightarrow \mu\mu$ and $J/\psi \longrightarrow \mu\mu$[3] events are employed to evaluate the efficiencies in different p_T regimes with collision data and simulated events. Efficiency scale factors (SFs) are then derived based on the resulting efficiencies and applied to simulations in physics analyses, to match the muon reconstruction performance observed on collision data.

B.1.1   The tag-and-probe method

The tag-and-probe method is based on dimuon events resulting from the decay of Z and J/ψ resonances. One of the two muons is required to trigger the online event selection and to satisfy stringent identification criteria. This muon is referred as *tag*. The other muon candidate in the event, called *probe*, is employed to determine the efficiency of a given reconstruction algorithm or identification Working Point selection among the ones reported in Section 5.2.1. Several types of probes are defined as muons reconstructed from a specific subdetector and used to determine the efficiencies related to another independent subsystem (e.g. muon probes reconstructed using information from the MS are employed to evaluate the reconstruction efficiency related to the ID, and viceversa). Muon reconstruction and identification efficiencies are determined using the following probe types:

- ID probes, defined as ID tracks and employed to measure the reconstruction efficiency related to the MS or to specific identification WPs.

- MS probes, defined as ME tracks and used to determine the ID reconstruction efficiency.

- CT probes, defined as ID tracks that also satisfy the calo-tagging requirements. These probes are used to measure the reconstruction efficiency related to the MS and to the identification WPs.

- ST probes, defined as ID tracks also satisfying the segment-tagging requirements. As the ID and CT probes, these are employed to measure the reconstruction efficiency related to the MS and to specific identification WPs.

- Two-track probes, defined as MS tracks within $\Delta R = 0.05$ of an ID track. These probes are employed to measure the ID and MS combined efficiency in $Z \longrightarrow \mu\mu$ events and to determine the reconstruction efficiency for identification WPs.

---

[2]A different technique is implemented to evaluate muon reconstruction and identification efficiencies in the $2.5 < |\eta| < 2.7$ region, as reported in [97]

[3]The electric charges of the two muons are from now on omitted for simplicity.

Starting from the selected tag-and-probe muon pairs, the reconstruction efficiency of a given WP or subsystem X is evaluated as the ratio of the number of probes P matched to X to the total number of selected probes:

$$\epsilon(X|P) = \frac{N_P^X}{N_P^{All}} \tag{B.1}$$

A probe muon is defined as matched if a reconstructed muon candidate identified with the algorithm of interest is found within a $\Delta R = 0.05$ cone around the probe track. The number of probes N_P is evaluated in data samples after subtracting background events, following the procedure reported in Section B.1.2 for J/ψ events. Since both the tag and probe are required to be prompt muons in the simulated samples, no background subtraction is required for MC events. The agreement between the muon reconstruction efficiencies evaluated using collision data and MC events, $\epsilon(X|P)^{Data}$ and $\epsilon(X|P)^{MC}$ is assessed through the efficiency scale factor, defined as:

$$SF = \frac{\epsilon(X|P)^{Data}}{\epsilon(X|P)^{MC}} \tag{B.2}$$

SFs are evaluated for all the muon identification WPs defined in Section 5.2.1 and employed in physics analyses to correct the simulation.

B.1.2 Muon reconstruction efficiency with J/ψ events

While $Z \longrightarrow \mu\mu$ events are employed for the determination of muon reconstruction efficiencies for probes with $p_T > 10$ GeV, J/ψ tag and probe events are used to target the low-p_T region between 3 and 20 GeV. The tag muon is required to be a `Tight` muon with $p_T > 6$ GeV, while the probe is required to have $p_T > 3$ GeV and is defined as matched if a selected muon is found within $\Delta R = 0.05$ from the probe track. Additional selection criteria are placed on the difference between the longitudinal impact parameters of the tag and probe muons $|z_0^T - z_0^P| < 5$ mm as well as on the invariant mass of the dimuon system $m_{\mu\mu}$, that is required to be in the $2.7 - 3.5$ GeV window.

The muon reconstruction and identification efficiency is defined for the different WPs ($X = $ `Loose, Medium, Tight` and `Low-`p_T) using conditional probabilities and different

probe types [123, 124]:

$$\epsilon(X) = \epsilon(X \mid \mathrm{ID}) \times \epsilon(\mathrm{ID} \mid \mathrm{MS})$$
$$= \frac{\epsilon(X \mid \mathrm{ST})}{\epsilon(\mathrm{ST} \mid X)} \times \epsilon(\mathrm{ST} \mid \mathrm{ID}) \times \epsilon(\mathrm{ID} \mid \mathrm{MS}) \tag{B.3}$$
$$= \frac{\epsilon(X \mid \mathrm{ST})}{\epsilon(\mathrm{ST} \mid X)} \times \epsilon\left(\mathrm{ST} \mid \mathrm{ID} \wedge \mathrm{CT} \text{ if } p_\mathrm{T} > 5 \text{ GeV}\right) \times \epsilon(\mathrm{ID} \mid \mathrm{MS})$$

The first line in eq.(B.3) shows the elementary expression for the efficiency evaluation, based on the independence of ID and MS track measurements. Segment-tagged (ST) probes are used instead of ID probes in the second line to better deal with the high background contribution at low-p_T values, that causes a drop in the ID probes purity. To exploit the efficiency based on ST probes $\epsilon(X|ST)$, the efficiency related to the selection of ST probes $\epsilon(ST|ID)$ has to be taken into account as well. Since CT probes have lower background contamination with respect to ID probes, they are employed as a substitute to ID for $p_T > 5$ GeV (CT probes are not defined below this threshold), as reported in the third line of eq.(B.3). All efficiency terms in eq.(B.3) are evaluated separately using tag and probe samples, according to eq.(B.1).

In order to get the efficiency from collision data events by taking also into account the background contamination, a simultaneous maximum-likelihood fit is performed on the invariant mass distribution of the dimuon system in probe and matched events (where the probe has been matched to a muon candidate). The signal peak is modelled following a Crystal Ball function, while a second, third or fourth order polynomial function is used to model the background. Specifically, the polynomial resulting in the best χ^2/N_{dof} value is employed. An example of the simultaneous fit result related to the `low-`p_T cut-based WP is reported in Figure B.1, for ST probes with $3 < p_T < 3.5$ GeV and $-1.3 < \eta < -1.05$.

B.1.3   Systematic uncertainties

Several different sources of systematic uncertainties affecting the evaluation of the reconstruction efficiencies with $J/\psi \longrightarrow \mu\mu$ events, and therefore the determination of the SFs, are taken into account. An uncertainty related to possible biases introduced by the tag-and-probe method is defined as half of the observed difference between the measured MC reconstruction efficiency and the fraction of generator-level muons that are successfully reconstructed.

Another source of systematic uncertainty is taken into account related to the probe-matching procedure. This uncertainty is defined as the difference between the fraction
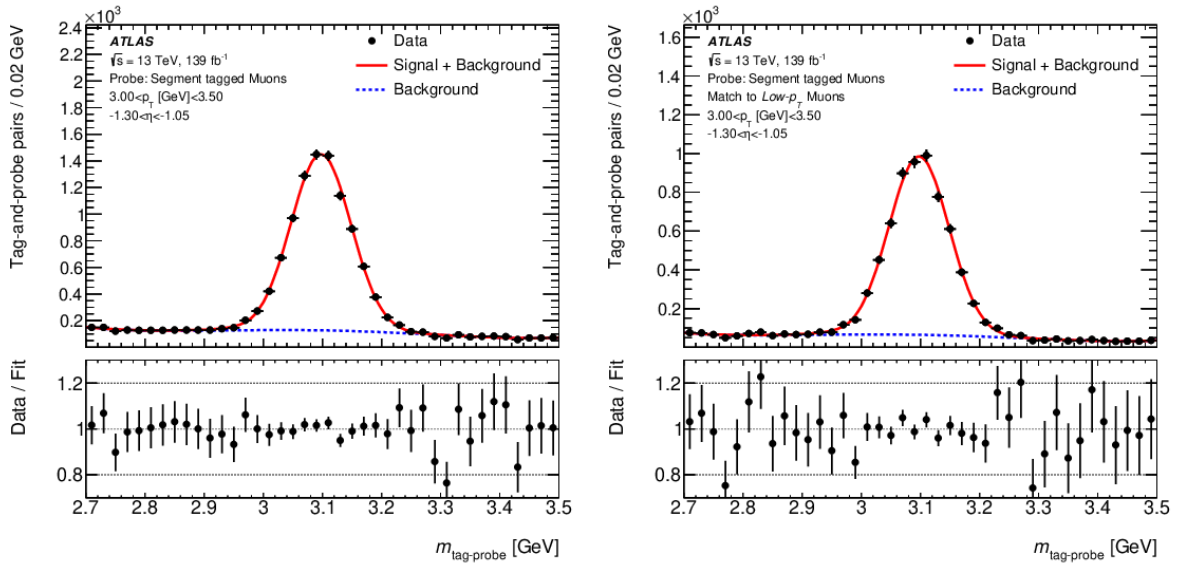
Figure B.1: Fit on the invariant mass distribution of the tag and probe muon pair for ST probes with $3 < p_T < 3.5$ GeV and $-1.3 < \eta < -1.05$. The fit is performed on probe muons on the left and on probes matched to the `low-`p_T cut-based WP on the right. The function resulting from the fit is reported as a red line, while the background-only component is showed as a dashed blue line. The bottom panels show the ratio of the data to the fit result.

of matched probes and the fraction of probe tracks that were reconstructed successfully as muons.

Finally, a systematic uncertainty related to possible biases introduced by the fitting procedure is taken into account. This uncertainty is estimated through the generation of pseudo-data samples built to mimic the background contribution observed in real data. Each pseudo-data sample is built by generating background-like events following the fit function related to the background resulting from the fit on real data. These background-like events are then injected into the invariant mass distribution of simulated events. The simultaneous fit is then performed on the pseudo-data probe and matched samples to get the reconstruction efficiency. The difference between the efficiencies obtained from the MC (as the ratio of the number of matched events to total number of probes) and from the pseudo-data fit is taken as the systematic uncertainty related to the fit procedure. The contributions to the reconstruction efficiency SFs associated to the different systematic uncertainties are reported in Figure B.2 for ST probes matched to low-p_T muons. The main contribution comes from the fit model related systematic.
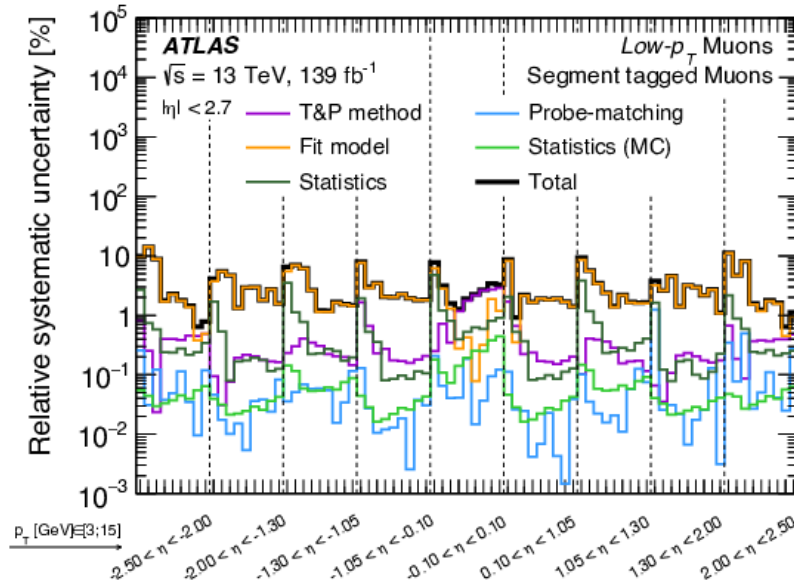
Figure B.2: Relative contribution of the different systematic uncertainties to the reconstruction efficiency SFs for ST probes matched to low-p_T muons in $J/\psi \longrightarrow \mu\mu$ events as a function of η and p_T. The total uncertainty on the SF values is obtained from the sum in quadrature of all the different contributions.

B.1.4 Results

Muon reconstruction and identification efficiencies obtained from $J/\psi \longrightarrow \mu\mu$ data collected by the ATLAS detector during LHC Run 2 and from simulated samples are reported in Figure B.3 for the `Loose, Medium` and `Tight` WPs as a function of p_T. The associated scale factors are reported in the bottom panel of the same figure and are consistent with one throughout the whole momentum range, except below $p_T = 5$ GeV, where muons do not have enough energy to cross the calorimeters and reach the second station pf precision chambers in the MS.
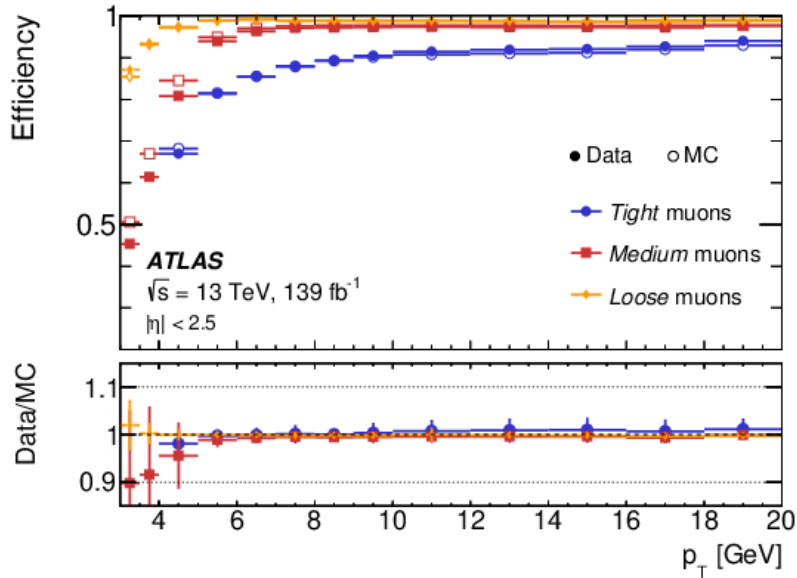
Figure B.3: Muon reconstruction and identification efficiencies for `Loose, Medium` and `Tight` muons from $J/\psi \longrightarrow \mu\mu$ events as a function of p_T. The scale factors are reported in the bottom panel.

Reconstruction efficiencies and associated SFs for `Low-`p_T muons are reported in Figure B.4, for both the cut-based and the MVA-based WP definitions, with the associated scale factors reported in the bottom panels. The two different WP definitions result in a similar performance for $p_T > 10$ GeV, while the MVA-based WP exhibits lower uncertainties with respect to the cut-based one at low p_T values, due to the better rejection of non prompt muon candidates.
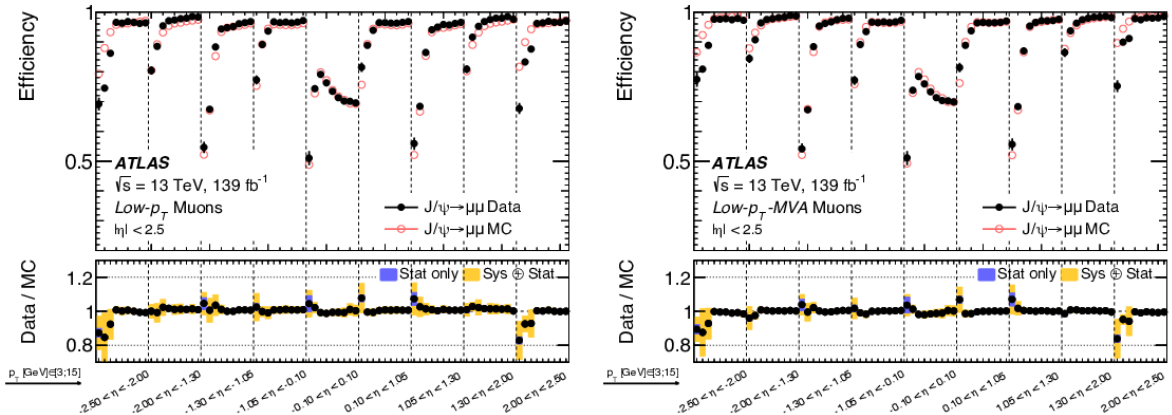
Figure B.4: Muon reconstruction and identification efficiency for `Low-`p_T muons with $J/\psi \longrightarrow \mu\mu$ events as a function of η and p_T. The associated SFs are reported in the bottom panels.

B.2 Muon momentum calibration

Together with muon reconstruction and identification scale factors, corrections are also derived on the muon momentum scale and resolution and then employed in physics analyses. The procedure employed for the evaluation and validation of these corrections is referred as muon momentum calibration. Charge dependent biases related to residual unknown misalignment in the detector are derived from MC simulation of $Z \longrightarrow \mu\mu$ decays and applied to collision data events, as reported in Section B.2.1. Scale and resolution corrections on muon momentum measurements are instead derived from $Z \longrightarrow \mu\mu$ and $J/\psi \longrightarrow \mu\mu$ data events and then applied to simulations, following the procedure described in Section B.2.2. The derived corrections are validated using $Z \longrightarrow \mu\mu$, $J/\psi \longrightarrow \mu\mu$ and $\Upsilon \longrightarrow \mu\mu$ events by assessing the post-correction agreement between data and MC predictions.

Only dimuon events satisfying specific selection criteria are employed to derive and validate the corrections. Both muons are required to be CB muons satisfying the `Medium` WP selection criteria. Other requirements are placed on the longitudinal and transverse impact parameters (z_0 and d_0 respectively): $\frac{|d_0|}{\sigma(d_0)} < 3$ and $|z_0 \sin\theta| < 0.5$ mm, with $\sigma(d_0)$ being the uncertainty on d_0. The leading muon and the invariant mass of the dimuon system in $Z \longrightarrow \mu\mu$ events are required to satisfy $p_T > 27$ GeV and $70 < m_{\mu\mu} < 130$ GeV. In $J/\psi \longrightarrow \mu\mu$ and $\Upsilon \longrightarrow \mu\mu$ events, both muons are required to have $p_T > 6.25$ GeV. Only events with $2.6 < m_{\mu\mu} < 3.5$ GeV and $7 < m_{\mu\mu} < 14$ GeV are selected in J/ψ and Υ decays respectively.

132

B.2.1 Charge dependent corrections

Charge dependent biases in the measurement of muon momentum can be caused by residual effects linked to the ID and MS subdetectors misalignment, even after applying dedicated alignment procedures. The charge dependent bias δ_s is estimated using $Z \longrightarrow \mu\mu$ events and it is defined following the approximation:

$$\frac{q}{\hat{p}} = \frac{q}{p} + q \cdot \delta_s \tag{B.4}$$

with q being the muon electric charge and p ($\hat{p}$) being the (biased) muon momentum. The momentum bias has an effect on the invariant mass of the dimuon system as well. The biased $\hat{m}_{\mu\mu}$ can be expressed as:

$$\hat{m}_{\mu\mu}^2 = \frac{m_{\mu\mu}^2}{\left(1 + \delta_s p_{\mathrm{T}}^+\right)\left(1 - \delta_s p_{\mathrm{T}}^-\right)} \tag{B.5}$$

where p_T^+ and p_T^- are the transverse momenta of the positive and negative muon respectively. Eq.(B.5), under the assumption of δ_s being small, can be approximated as:

$$m_{\mu\mu}^2 = \hat{m}_{\mu\mu}^2 \left(1 + \delta_s(\eta, \phi)p_{\mathrm{T}}^+ - \delta_s(\eta, \phi)p_{\mathrm{T}}^-\right) \tag{B.6}$$

where the bias has been parametrized as a function of (η, ϕ) to minimize angular correlations between the two muons. Specifically, a grid of equally-sized 48×48 $\eta - \phi$ detector regions is employed. Since the charge dependent bias affects the resolution of the $m_{\mu\mu}$ peak, it can be estimated by minimizing the variance of the invariant mass $m_{\mu\mu}$ distribution in Z decays. Specifically, an iterative procedure is employed to derive the correction. The biases $\hat{\delta}_s(\eta, \phi)$ are obtained from minimizing the variance of the $m_{\mu\mu}$ distributions in $Z \longrightarrow \mu\mu$ events. The estimate is then employed to correct the muon transverse momentum in data, according to:

$$p_{\mathrm{T}} = \frac{\hat{p}_{\mathrm{T}}}{1 - q\hat{\delta}_s(\eta, \phi)\hat{p}_{\mathrm{T}}} \tag{B.7}$$

The corrected transverse momentum is then used to obtain an updated $m_{\mu\mu}$ distribution. This procedure is applied iteratively until the δ_s values from two successive iterations differ by less than 0.1%.

The charge dependent corrections derived for the LHC Run 2 dataset are reported in Figure B.5 for CB muons.
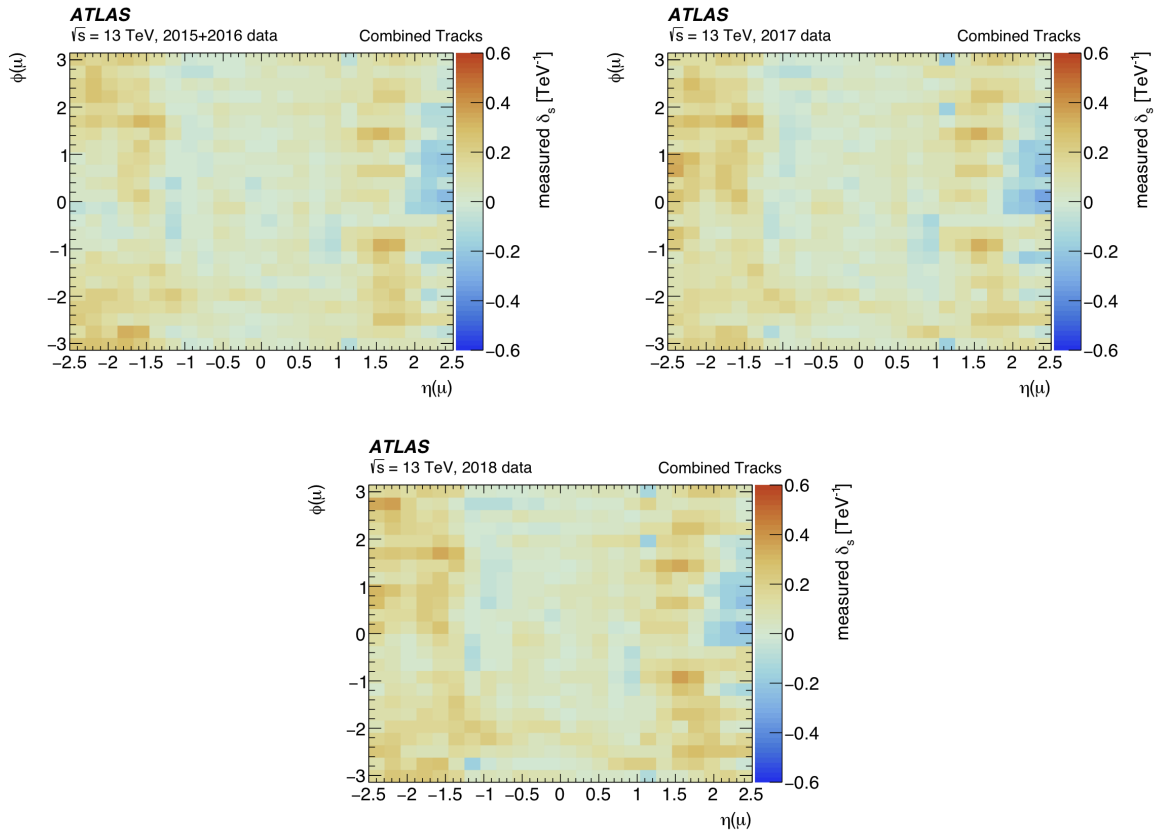
Figure B.5: Charge dependent bias on muon p_T evaluated for CB muons after applying the alignment procedures in Run 2 data for the different data taking years. The corrections have been derived using $Z \longrightarrow \mu\mu$ events.

B.2.2 Scale and resolution corrections

Corrections on the muon transverse momenta measurements are derived based on simulated $Z \longrightarrow \mu\mu$ and $J/\psi \longrightarrow \mu\mu$ events according to the following muon momentum calibration procedure, carried out after applying the charge dependent bias described in the previous section to collision data. Corrections are derived for CB muons, but also separately for the transverse momenta associated to muon tracks in the ID and in the MS, according to the following expression:

$$p_{\mathrm{T}}^{\mathrm{Cor,Det}} = \frac{p_{\mathrm{T}}^{\mathrm{MC,Det}} + \sum_{n=0}^{1} s_n^{\mathrm{Det}}(\eta,\phi) \left(p_{\mathrm{T}}^{\mathrm{MC,Det}} \right)^n}{1 + \sum_{m=0}^{2} \Delta r_m^{\mathrm{Det}}(\eta,\phi) \left(p_{\mathrm{T}}^{\mathrm{MC,Det}} \right)^{m-1} g_m}, \tag{B.8}$$

where $p_T^{Cor,Det}$ and $p_T^{MC,Det}$ are the corrected and uncorrected muon transverse momenta respectively, with $p_T^{MC,Det}$ measured using simulated events. Random variables normally distributed with zero mean and unit width are referred as g_m in eq.(B.8). The transverse momentum is corrected separately for $Det = $ CB, ID, MS. Both scale s_n^{Det} and smearing Δr_m^{Det} corrections on the transverse momentum are derived in $\eta - \phi$ detector regions homogeneous in performance.

Scale corrections s_n^{Det} on the transverse momentum are derived based on the numerator of eq.(B.8). Inaccuracies in the simulation of the muon energy loss in the calorimeter as well as in other detector materials are embedded into the s_0^{Det} term. Since the energy loss in the ID is negligible, s_0^{Det} is set to zero for $Det = $ ID. Inaccuracies in the description of the magnetic field and of the geometry of the detector in the transverse plane with respect to the magnetic field direction are taken into account with the s_1^{Det} term.

The denominator of eq.(B.8) is instead related to corrections on the smearing of the muon transverse momentum, based on the following parametrization of the momentum resolution:

$$\frac{\sigma(p_{\mathrm{T}})}{p_{\mathrm{T}}} = r_0/p_{\mathrm{T}} \oplus r_1 \oplus r_2 \cdot p_{\mathrm{T}} \tag{B.9}$$

with $\oplus$ being the sum in quadrature. The first term in eq.(B.9) is related to fluctuations of the muon energy loss in the transversed detector material. Since these fluctuations have a negligible impact on the momentum resolution in the range related to Z and J/ψ selected events, the corresponding term Δr_0^{Det} in eq.(B.8) is set to zero. Uncertainties on the modelling of the magnetic field and its inhomogeneities may affect the momentum resolution. These effects, together with the multiple scattering, are taken into account with the second term of eq.(B.9), corresponding to Δr_1^{Det}. The last term in the expression is related to residual misalignment in the detector and to the spatial resolution of the

hit measurements. This corresponds to the Δr_2^{Det} term in eq.(B.8).

Determination of scale and smearing corrections

Scale and smearing corrections for ID, MS and CB tracks are extracted from data by comparing the dimuon invariant mass distribution $m_{\mu\mu}$ in data and MC events. A fit on $m_{\mu\mu}$ is performed in two mutually exclusive p_T regions for Z and J/ψ events, to enhance sensitivity to p_T dependent effects. Specifically, the transverse momentum of the leading muon is used to define the regions related to the Z resonance as $20 < p_T^{lead} < 50$ GeV and $p_T^{lead} > 50$ GeV, while the subleading muon p_T is instead employed to define the J/ψ related regions as $6.3 < p_T^{sublead} < 9$ GeV and $p_T^{sublead} > 9$ GeV. Different detector $\eta - \phi$ regions are employed to extract the corrections.

Firstly, background contributions in Z and J/ψ events are estimated and added to the simulated signal templates. The background related to $Z \longrightarrow \mu\mu$ events is extracted from dedicated simulations. A data-driven method is instead employed in $J/\psi \longrightarrow \mu\mu$ events due to the complexity of the simulation for the associated background processes. Specifically, a fit is performed on J/ψ data events using a Crystal Ball and an exponential function to model the signal and the background respectively. The background model is finally added to the simulated signal templates following the fit result.

Scale and smearing corrections are then determined through an iterative procedure, where the corrections values are updated to gain the best match between the data $m_{\mu\mu}$ distributions and the simulated templates. Specifically, in each iteration corrections are applied on the muon p_T in MC events, then a binned χ^2 minimization is performed to compare data and simulation, resulting in updated values of the corrections. The procedure is repeated for 16 iteration, to ensure convergence. The averages of the last five iterations results are taken as final scale and smearing corrections.

Several sources of systematic uncertainties are taken into account, related to the modelling of the Z decay and to the choice of the two p_T regions as well as of the mass windows and the binning of the invariant mass distributions for the Z and J/ψ resonances. A dedicated systematic uncertainty related to the background modelling for J/ψ events has been evaluated. Furthermore, the fitting procedure has been performed by only employing Z or J/ψ events to evaluate the uncertainty related to the extrapolation of the correction values to p_T regions that are not dominated by the events related to the resonance considered.

Results and validation

The scale and smearing corrections derived following the procedure described in the previous section are validated using $Z \longrightarrow \mu\mu$ and $J/\psi \longrightarrow \mu\mu$ events within finer $\eta - \phi$ detector regions. Furthermore, $\Upsilon \longrightarrow \mu\mu$ events, that are not used to derive the corrections, are employed as well in the validation as an independent sample.

The validation is performed by comparing the invariant mass distributions $m_{\mu\mu}$ resulting from data and corrected simulation, since muon momentum scale and resolution are directly linked to the measurement of the dimuon system invariant mass $m_{\mu\mu}$ and its resolution $\sigma(m_{\mu\mu})$, under the assumptions of negligible angular effects and similar momentum resolution for both muons. Specifically, the relative mass resolution is proportional to the relative momentum resolution as

$$\frac{\sigma_{\mu\mu}}{m_{\mu\mu}} = \frac{1}{\sqrt{2}} \frac{\sigma_{p_\mu}}{p_\mu} \qquad (B.10)$$

while muon momentum scale $s = \left\langle \left(p^{\mathrm{meas}} - p^{\mathrm{true}} \right) / p^{\mathrm{true}} \right\rangle$ is related to the dimuon mass scale $s_{\mu\mu} = \left\langle \left(m_{\mu\mu}^{\mathrm{meas}} - m_{\mu\mu}^{\mathrm{true}} \right) / m_{\mu\mu}^{\mathrm{true}} \right\rangle$ as

$$s_{\mu\mu} = \sqrt{s_{\mu_1} s_{\mu_2}} \qquad (B.11)$$

The invariant mass distributions of the dimuon system obtained from data and from the corrected simulation are therefore compared to assess the goodness of the extracted momentum corrections, as it can be seen in Figure B.6 for Z, J/ψ and Υ. For all the considered resonances, the shapes of the peaks resulting from the corrected simulation (with the addition of background estimates) agree with the ones resulting from data within the statistical and systematic uncertainties, proving the effectiveness of the muon momentum calibration.

The assessment of the goodness of momentum corrections is also performed through the comparison of the mean and width values related to the dimuon mass distributions in data and in the corrected simulation. To extract those values, a fit is performed on $m_{\mu\mu}$ using J/ψ, Υ and Z events. The modelling of signal and background contributions has been separately optimised for each resonance.

The fit on $J/\psi \longrightarrow \mu\mu$ events is performed in a different mass window with respect to the one used to extract the momentum corrections. Specifically, only events with $2.8 < m_{\mu\mu} < 3.9$ GeV are considered, with the lower threshold increased to remove the spectrum related to trigger turn-on effects and the higher threshold increased to contain also the $\psi(2S)$ resonance in the distribution. Two double-sided Crystal Ball functions are
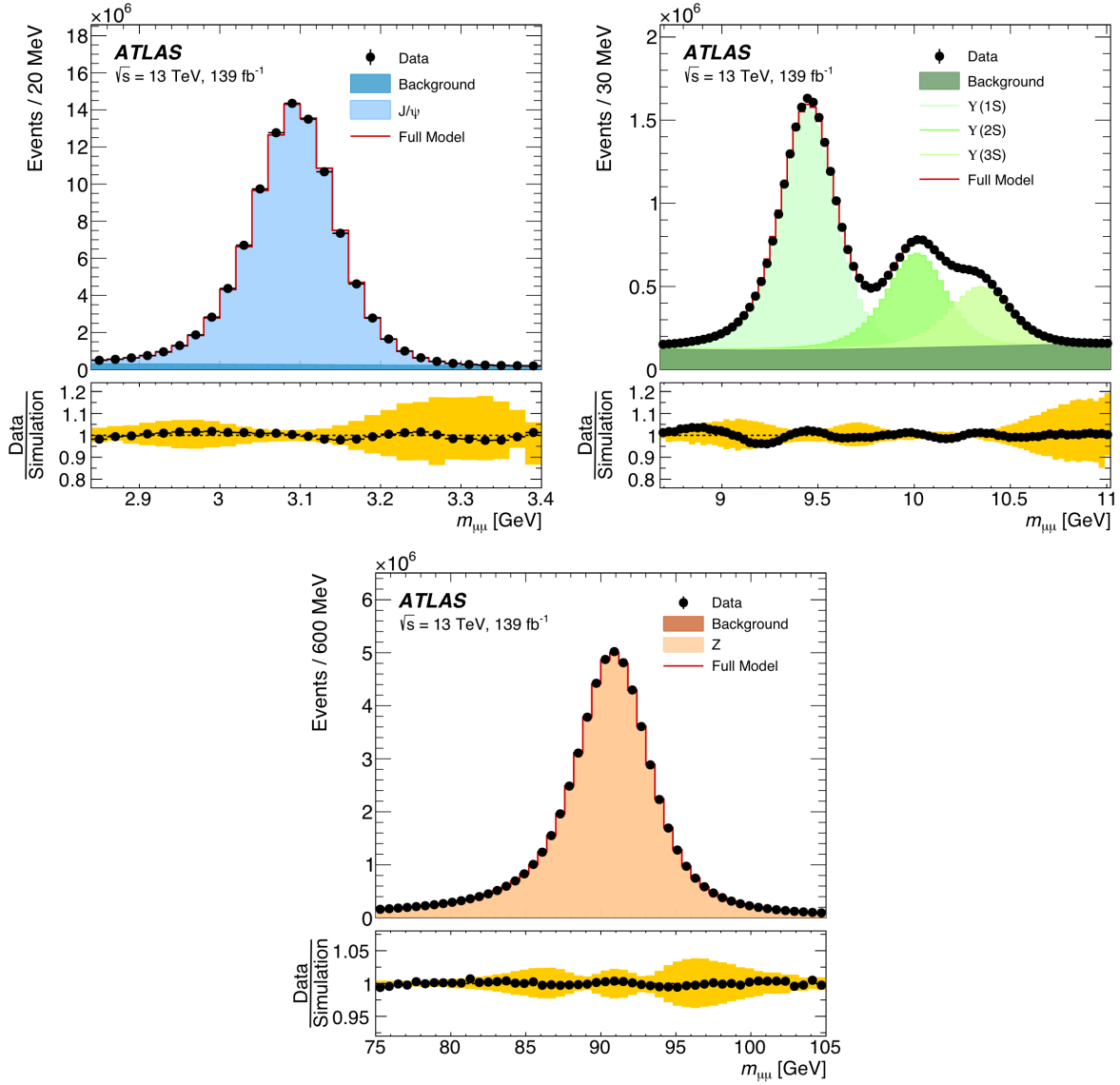
Figure B.6: Invariant mass distributions of the dimuon system in J/ψ, Υ and Z events. Both muons in the system are reconstructed as CB. The data events are shown as black dots while the MC signal simulation, corrected following the results of the momentum calibration, is reported together with the added background estimate as a continuous red line. The bottom panels show the data to MC ratios with related uncertainties.

employed in the fit to model the J/ψ and $\psi(2S)$ peaks. All fit parameters related to the two peaks are left free floating when fitting MC events, except the width of the $\psi(2S)$, which is constrained to scale linearly with respect to the width of the main resonance peak. When performing the fit on collision data, the eight parameters related to the Crystal Ball tails are fixed to the values resulting from the simulation. An exponential function is also added to the fit model to account for background events in the data distribution.

A similar procedure is employed when fitting $\Upsilon \longrightarrow \mu\mu$ events, taking also into account the $\Upsilon(2S)$ ans $\Upsilon(3S)$ resonances in the invariant mass window $8.7 < m_{\mu\mu} < 11$ GeV. Three double-sided Crystal Ball functions are employed to model the three resonances' peaks, with all the related parameters left free floating when fitting MC events. The widths of the $3S$ and $2S$ resonances are however constrained to scale linearly with respect to the widths of the $1S$ and $2S$ peaks respectively. In the data fit, a polynomial function is added to the model to account for background events, and all parameters related to the tails of the resonances' peaks are fixed to the values resulting from the MC fit.

In $Z \longrightarrow \mu\mu$ events, the resonance peak is modelled with a double-sided Crystal Ball function convoluted with a Breit-Wigner function, to account for both the experimental resolution and the natural width of the resonance, that is instead negligible in J/ψ and Υ decays. The invariant mass distribution in the $75 < m_{\mu\mu} < 105$ GeV window is used. All parameters are left free floating when fitting simulated events and the resulting values related to the parameters modelling the resonance tails are used as fixed values in the data fit. Background events are modelled following an exponential function in the data distribution.

The mean and width $m_{\mu\mu}$ and $\sigma(m_{\mu\mu})$ values related to the J/ψ, Υ and Z resonance peaks resulting from data and corrected simulation are compared to validate the muon momentum corrections, as reported in Figures B.7,B.8 and B.9 for CB muon tracks. For all three resonances it can be seen that the values obtained from data and corrected simulation are in agreement within the statistical and systematic errors. Specifically, the resulting mean values $m_{\mu\mu}$ as a function of the leading muon η show deviations of 0.05% in the barrel detector region for all resonances. These deviations increase in the detector end-caps up to 0.15%, 0.1% and 0.1% for J/ψ, Υ and Z events respectively. The dimuon invariant mass width values $\sigma(m_{\mu\mu})$ resulting from data and MC show agreement as well, with a deterioration of the resolution exhibited going from the barrel to the end-cap detector regions for all resonances.
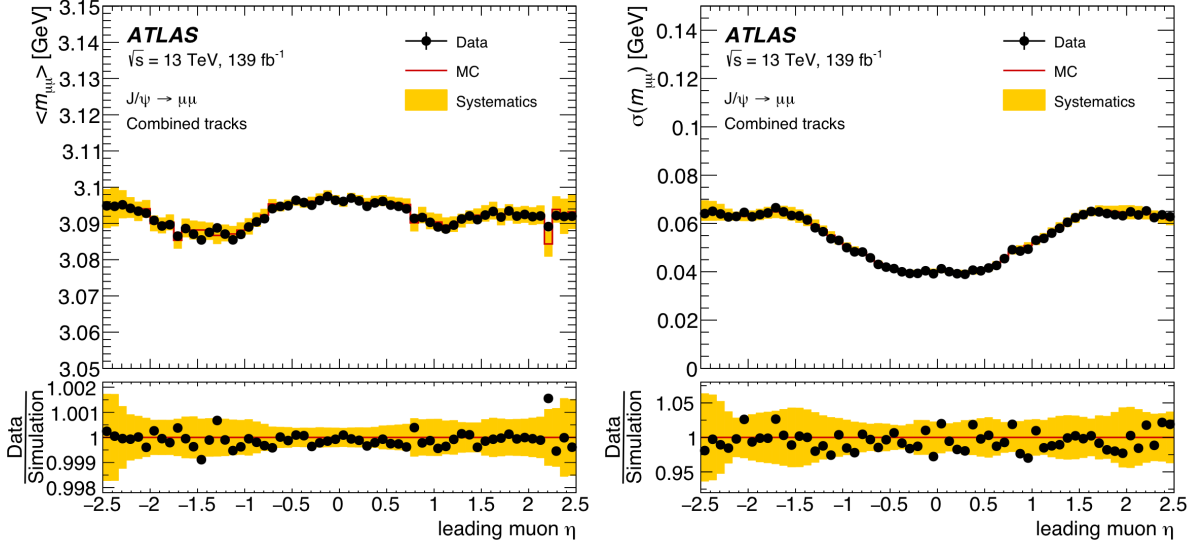
Figure B.7: Mean and width values resulting from the fit on data and corrected simulation using CB muons in $J/\psi \longrightarrow \mu\mu$ events. The values are shown as a function of the pseudorapidity of the leading muon with associated errors. The bottom panels show data/MC ratio.
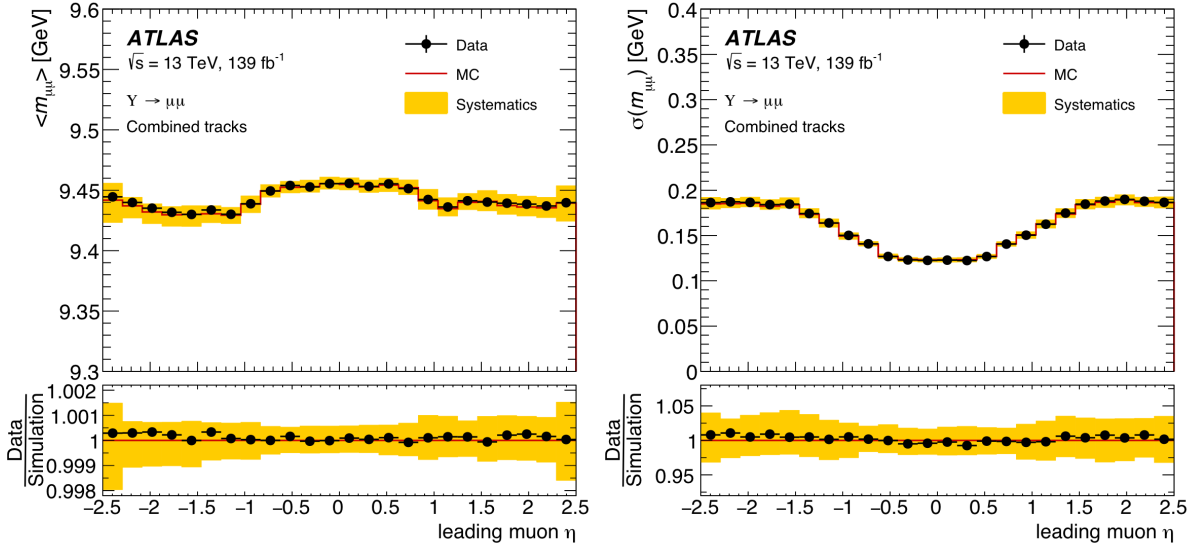
Figure B.8: Mean and width values resulting from the fit on data and corrected simulation using CB muons in $\Upsilon \longrightarrow \mu\mu$ events. The values are shown as a function of the pseudorapidity of the leading muon with associated errors. The bottom panels show data/MC ratio.
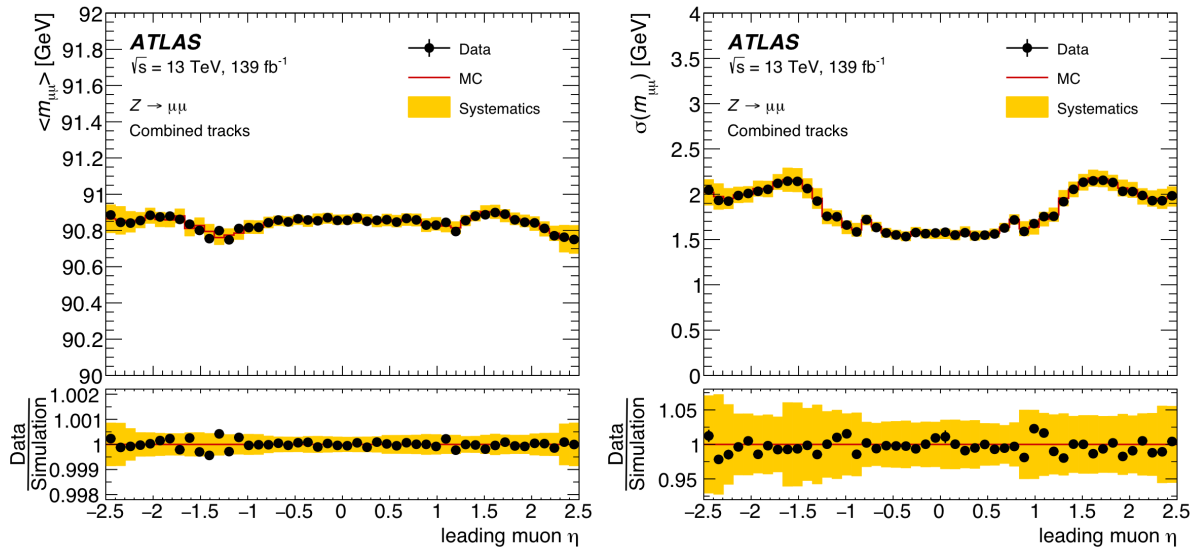
Figure B.9: Mean and width values resulting from the fit on data and corrected simulation using CB muons in $Z \longrightarrow \mu\mu$ events. The values are shown as a function of the pseudorapidity of the leading muon with associated errors. The bottom panels show data/MC ratio.

Appendix C

Validation of the EFT reweighting

The reweighting procedure applied to the signal samples employed in the analysis, as reported in Section 5.1, has been validated using the tt nominal sample and additional samples generated assuming different WC values for the three operators taken into account in the analysis: $\mathcal{O}_{RR}$, $\mathcal{O}_{LR}^{(1)}$ and $\mathcal{O}_{LR}^{(1)}$. Specifically, for each additional sample, the reweighting validation has been performed by comparing the resulting kinematic distributions associated to same-sign top events with the same distributions resulting from the nominal sample after applying the weights related to the matching EFT assumption. The validation has been performed both at *truth-* and *reco-level*. The WC values related to the additional samples employed are reported in Table C.1.

Figures C.1, C.2, C.3, C.4, C.5, C.6, C.7, C.8, C.9, C.10, C.13, C.14, C.11 and C.12 show the reweighting validation results at *truth-level*, while the validation plots at *reco-level* are reported in Figure C.15, C.16 and C.17. No significant discrepancy has been observed between the compared distributions on both levels.

c_{RR}	$c_{LR}^{(1)}$	$c_{LR}^{(1)}$	level
0.04	0	0	truth, reco
0	0.1	0	truth, reco
0	0	0.1	truth, reco
0	0.1	0.2	truth
0.01	0.05	0	truth
0.02	0	0.3	truth
0.01	0.1	0.3	truth

Table C.1: Values related to the WCs used to generate the additional tt samples employed for the reweighting validation at *truth-* and *reco-level*.
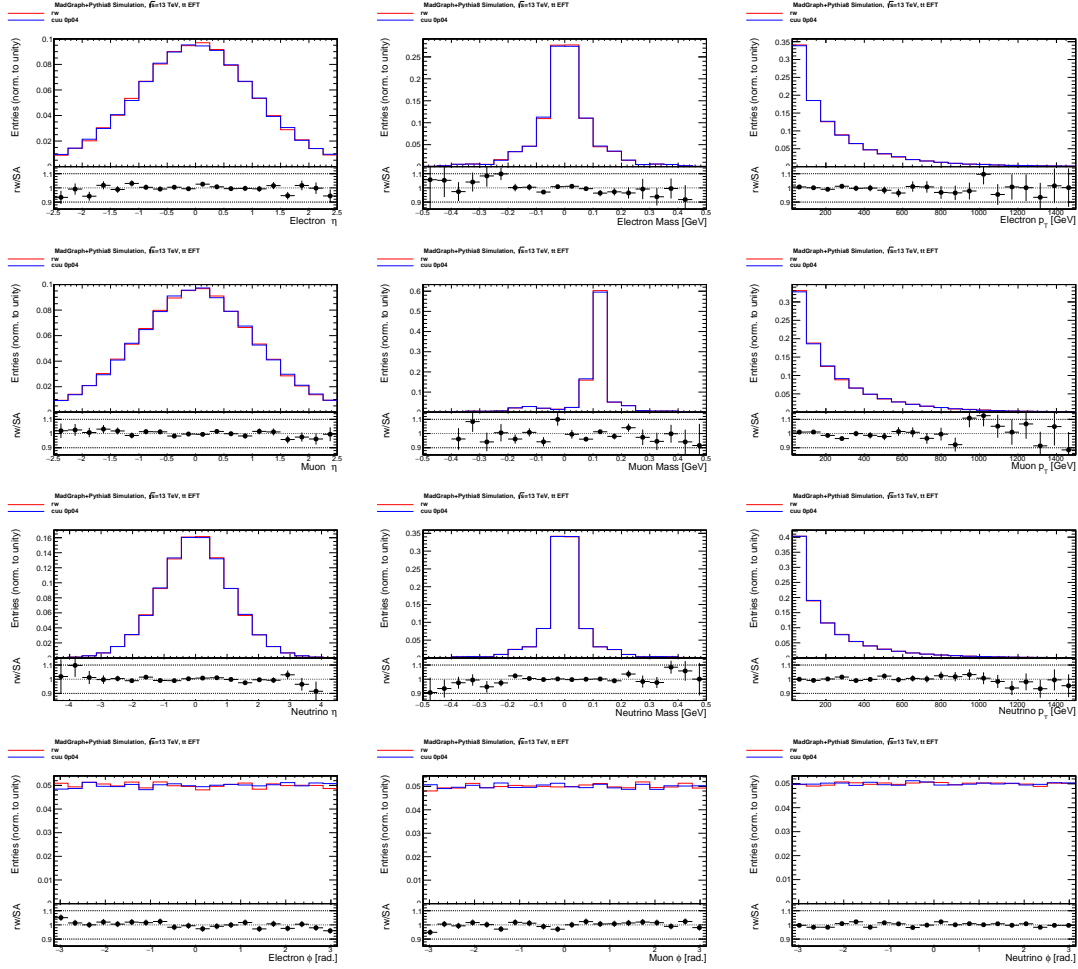
Figure C.1: Truth-level reweighting validation related to the additional $t\bar{t}$ sample generated with $c_{RR} = 0.04$, $c_{LR}^{(1)} = c_{LR}^{(8)} = 0$. The red and blue lines show the distribution resulting from the nominal and the reweighted samples respectively. All distributions are normalized to unity. The bottom panels show the ratio between the nominal and reweighted sample entries.
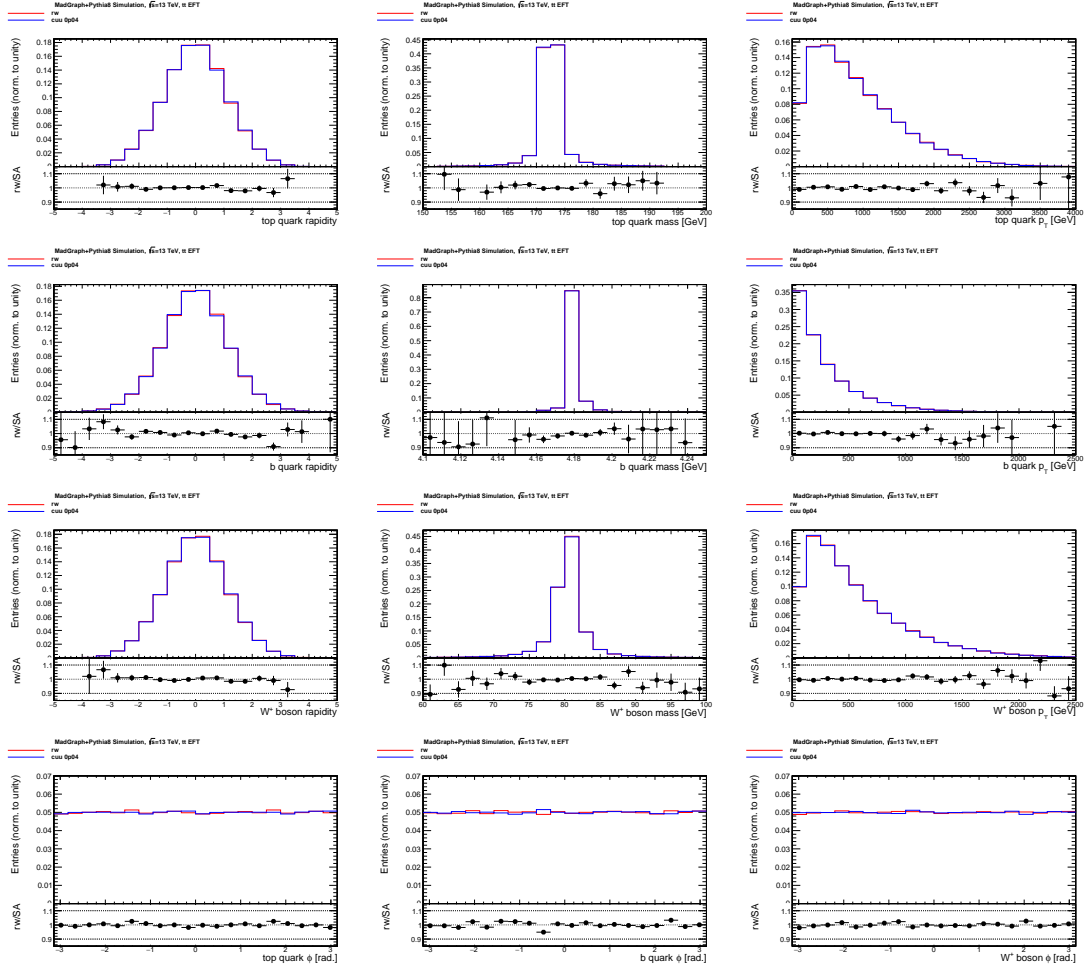
Figure C.2: Truth-level reweighting validation related to the additional $t\bar{t}$ sample generated with $c_{RR} = 0.04$, $c_{LR}^{(1)} = c_{LR}^{(8)} = 0$. The red and blue lines show the distribution resulting from the nominal and the reweighted samples respectively. All distributions are normalized to unity. The bottom panels show the ratio between the nominal and reweighted sample entries.
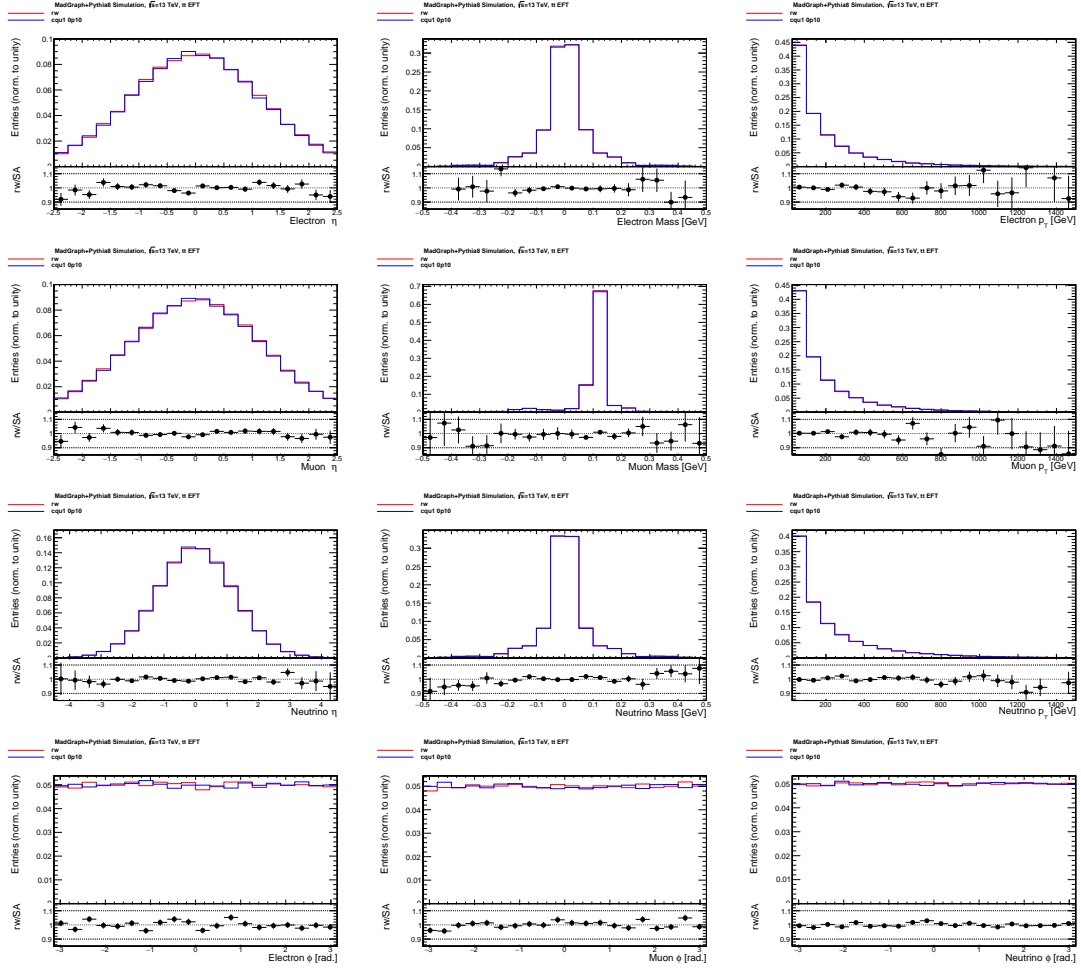
Figure C.3: Truth-level reweighting validation related to the additional $t\bar{t}$ sample generated with $c_{LR}^{(1)} = 0.1$, $c_{RR} = c_{LR}^{(8)} = 0$. The red and blue lines show the distribution resulting from the nominal and the reweighted samples respectively. All distributions are normalized to unity. The bottom panels show the ratio between the nominal and reweighted sample entries.
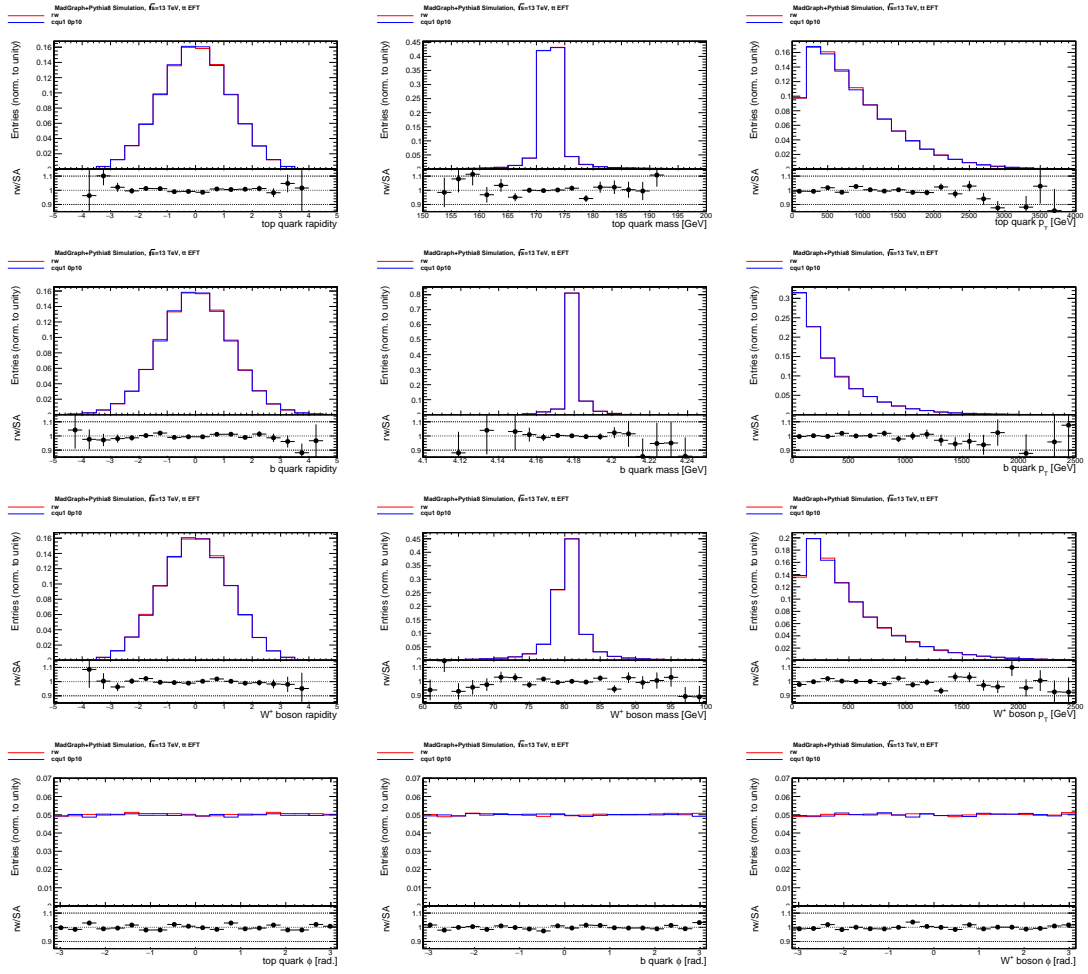
Figure C.4: Truth-level reweighting validation related to the additional tt sample generated with $c_{LR}^{(1)} = 0.1$, $c_{RR} = c_{LR}^{(8)} = 0$. The red and blue lines show the distribution resulting from the nominal and the reweighted samples respectively. All distributions are normalized to unity. The bottom panels show the ratio between the nominal and reweighted sample entries.

146
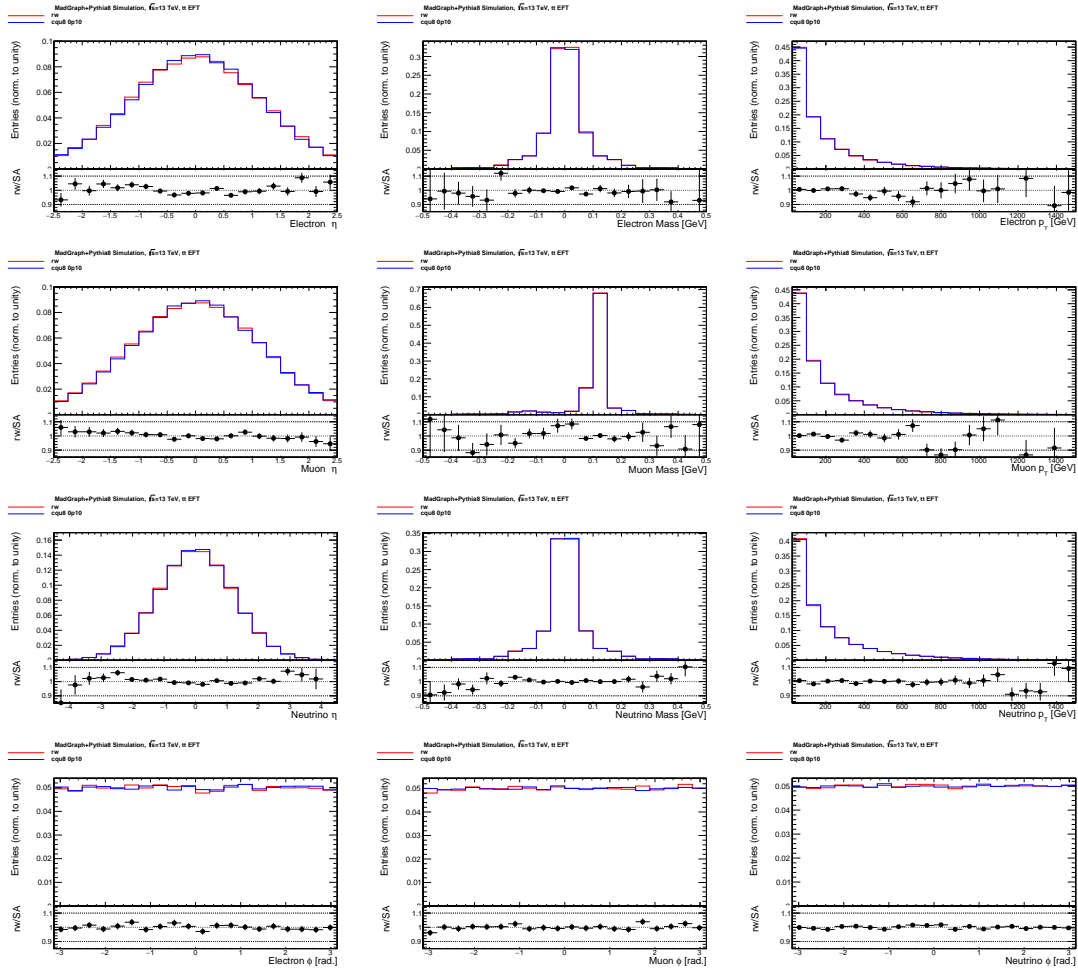
Figure C.5: Truth-level reweighting validation related to the additional tt sample generated with $c_{LR}^{(8)} = 0.1$, $c_{RR} = c_{LR}^{(1)} = 0$. The red and blue lines show the distribution resulting from the nominal and the reweighted samples respectively. All distributions are normalized to unity. The bottom panels show the ratio between the nominal and reweighted sample entries.
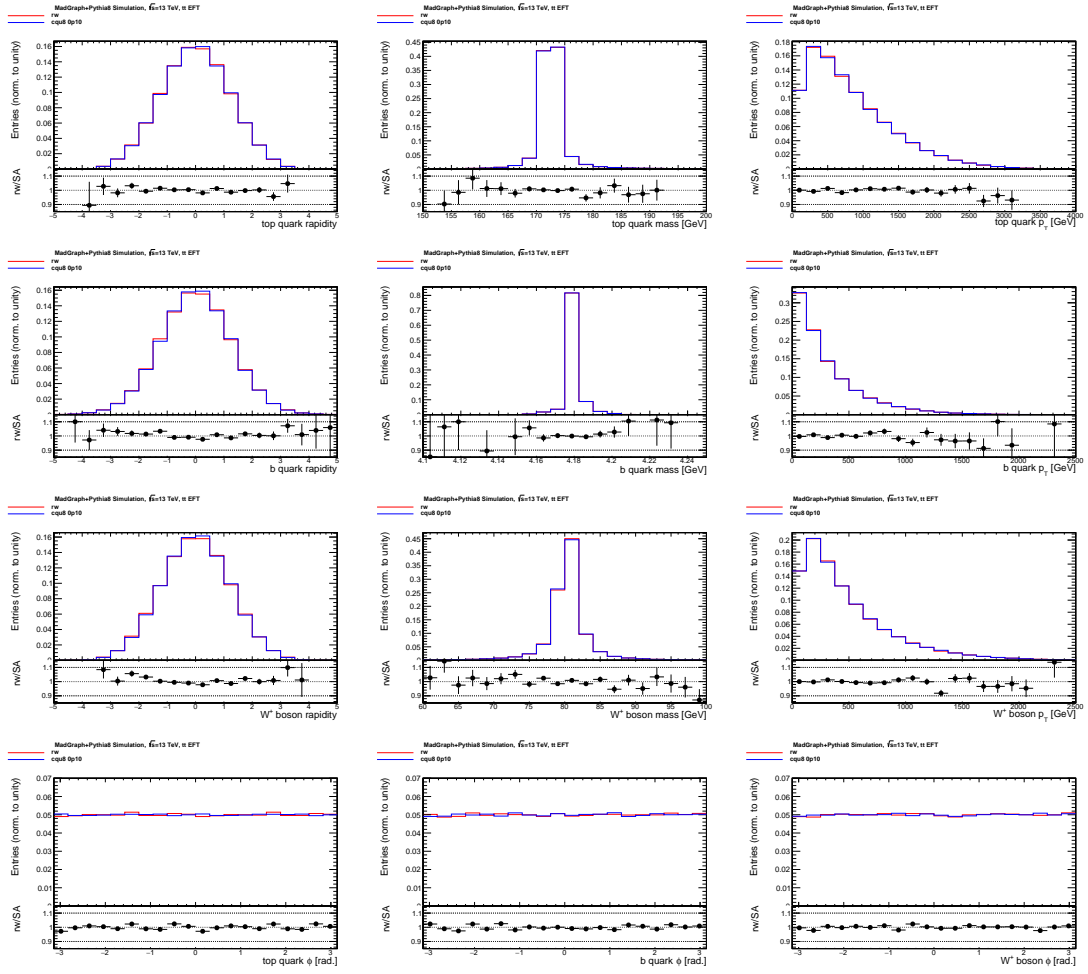
Figure C.6: Truth-level reweighting validation related to the additional tt sample generated with $c_{LR}^{(8)} = 0.1$, $c_{RR} = c_{LR}^{(1)} = 0$. The red and blue lines show the distribution resulting from the nominal and the reweighted samples respectively. All distributions are normalized to unity. The bottom panels show the ratio between the nominal and reweighted sample entries.
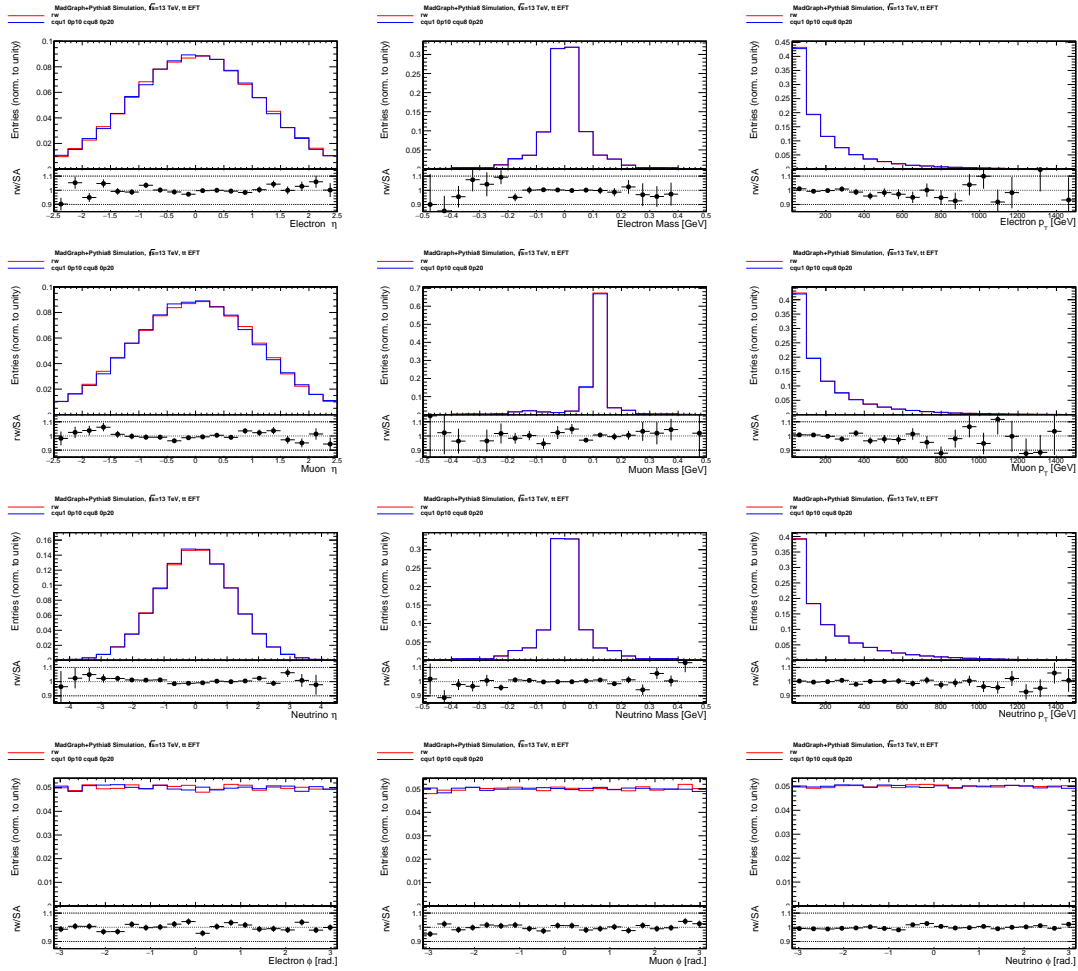
Figure C.7: Truth-level reweighting validation related to the additional tt sample generated with $c_{RR} = 0$, $c_{LR}^{(1)} = 0.1$, $c_{LR}^{(8)} = 0.2$. The red and blue lines show the distribution resulting from the nominal and the reweighted samples respectively. All distributions are normalized to unity. The bottom panels show the ratio between the nominal and reweighted sample entries.
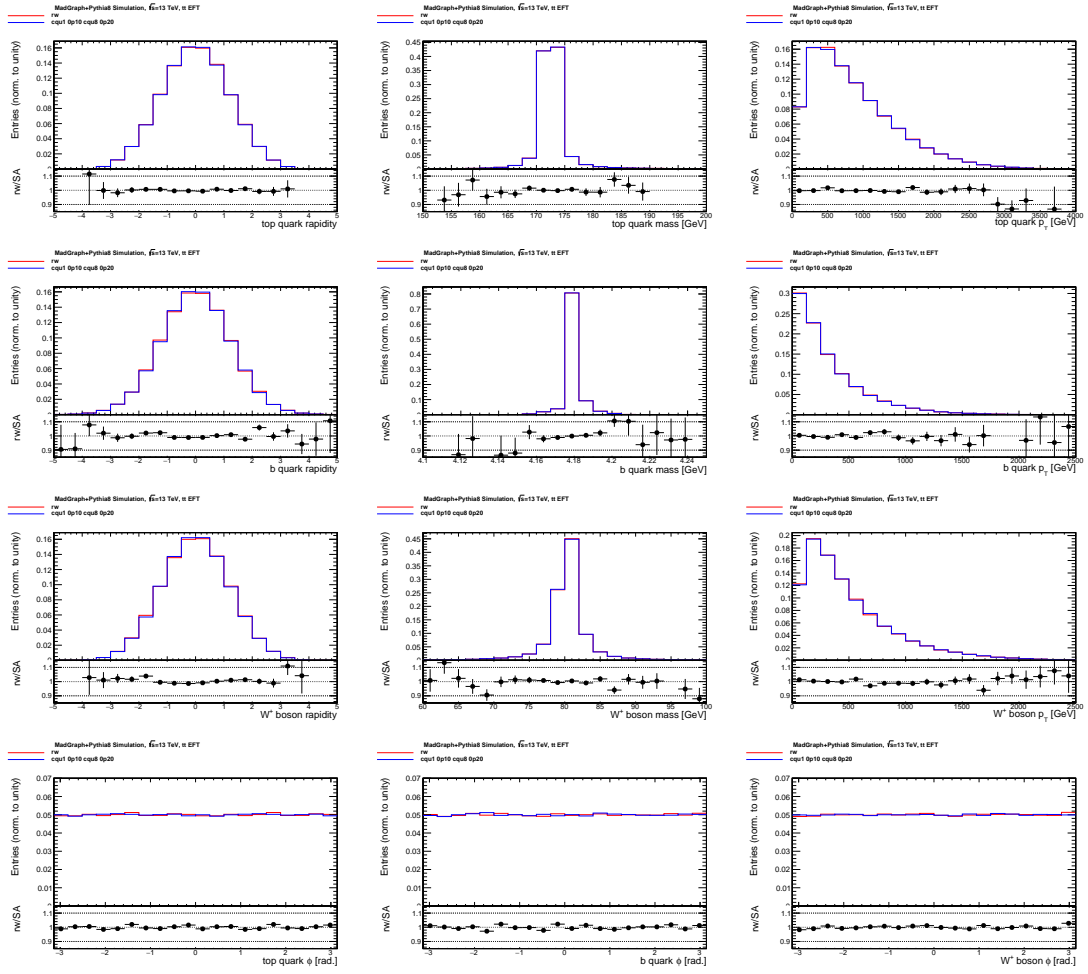
Figure C.8: Truth-level reweighting validation related to the additional $t\bar{t}$ sample generated with $c_{RR} = 0$, $c_{LR}^{(1)} = 0.1$, $c_{LR}^{(8)} = 0.2$. The red and blue lines show the distribution resulting from the nominal and the reweighted samples respectively. All distributions are normalized to unity. The bottom panels show the ratio between the nominal and reweighted sample entries.
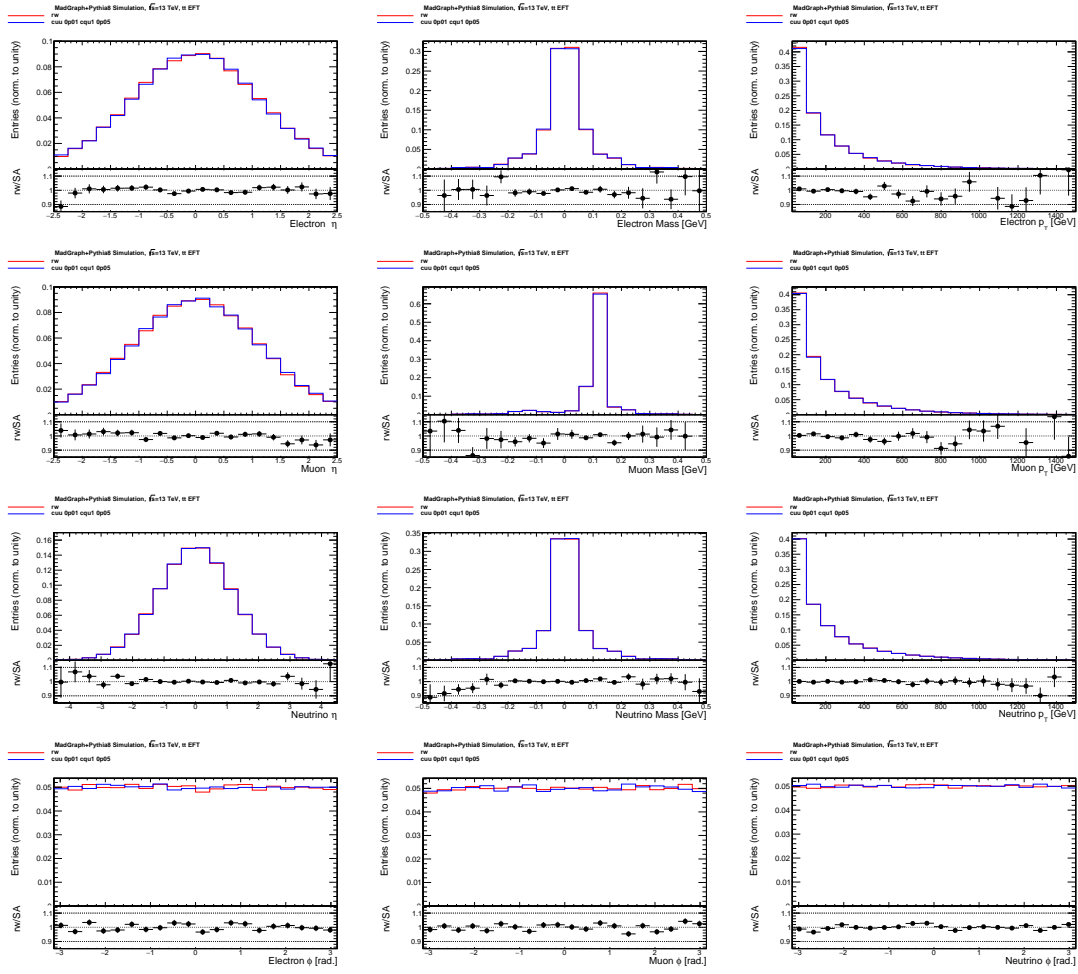
Figure C.9: Truth-level reweighting validation related to the additional tt sample generated with $c_{RR} = 0.01$, $c_{LR}^{(1)} = 0.05$, $c_{LR}^{(8)} = 0$. The red and blue lines show the distribution resulting from the nominal and the reweighted samples respectively. All distributions are normalized to unity. The bottom panels show the ratio between the nominal and reweighted sample entries.
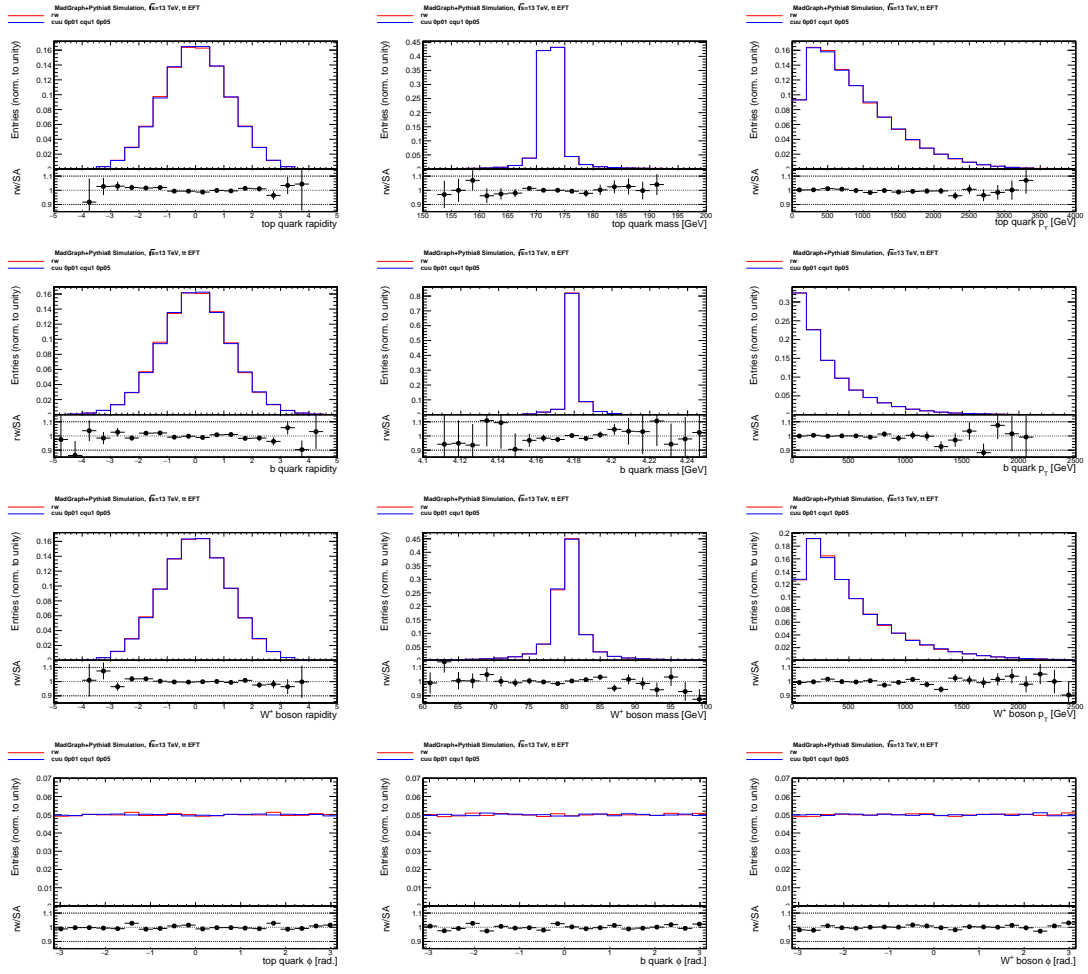
Figure C.10: Truth-level reweighting validation related to the additional $t\bar{t}$ sample generated with $c_{RR} = 0.01$, $c_{LR}^{(1)} = 0.05$, $c_{LR}^{(8)} = 0$. The red and blue lines show the distribution resulting from the nominal and the reweighted samples respectively. All distributions are normalized to unity. The bottom panels show the ratio between the nominal and reweighted sample entries.
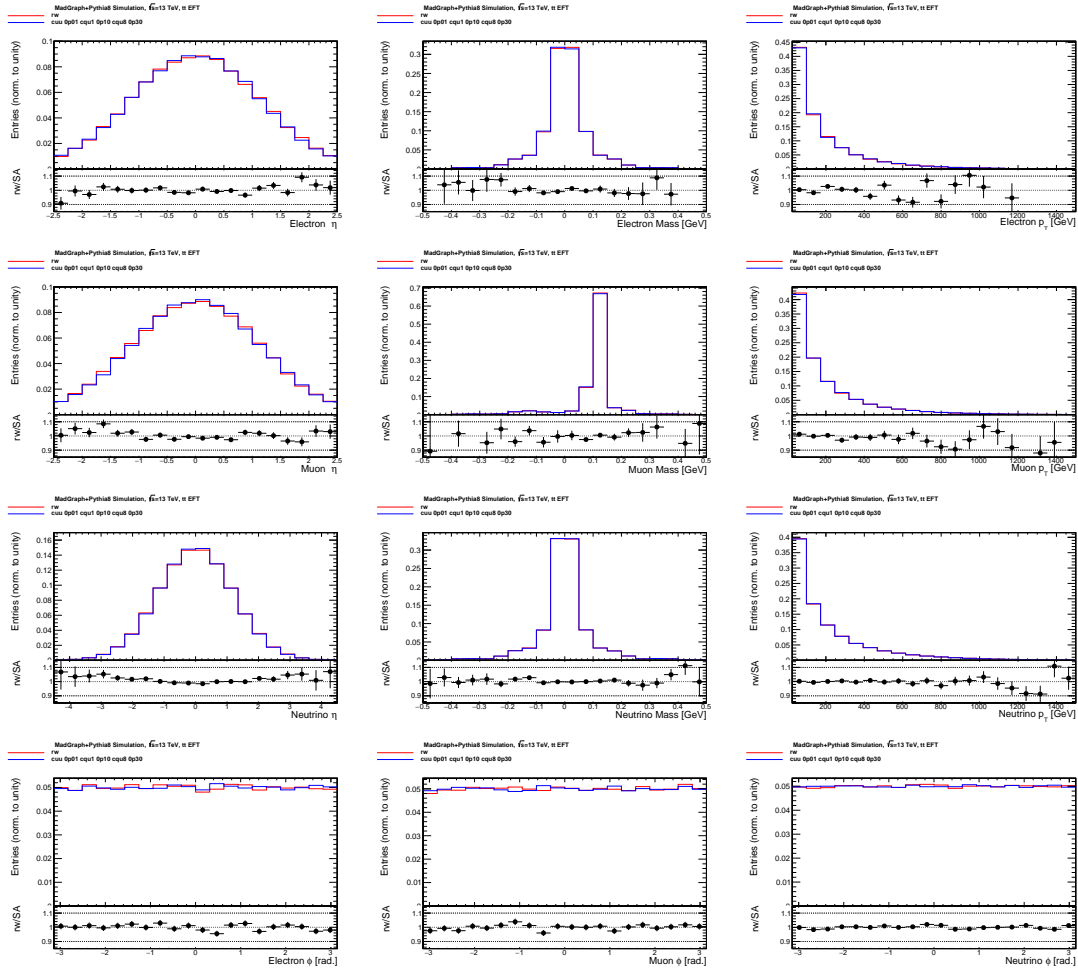
Figure C.11: Truth-level reweighting validation related to the additional $t\bar{t}$ sample generated with $c_{RR} = 0.01$, $c_{LR}^{(1)} = 0.1$, $c_{LR}^{(8)} = 0.3$. The red and blue lines show the distribution resulting from the nominal and the reweighted samples respectively. All distributions are normalized to unity. The bottom panels show the ratio between the nominal and reweighted sample entries.

153
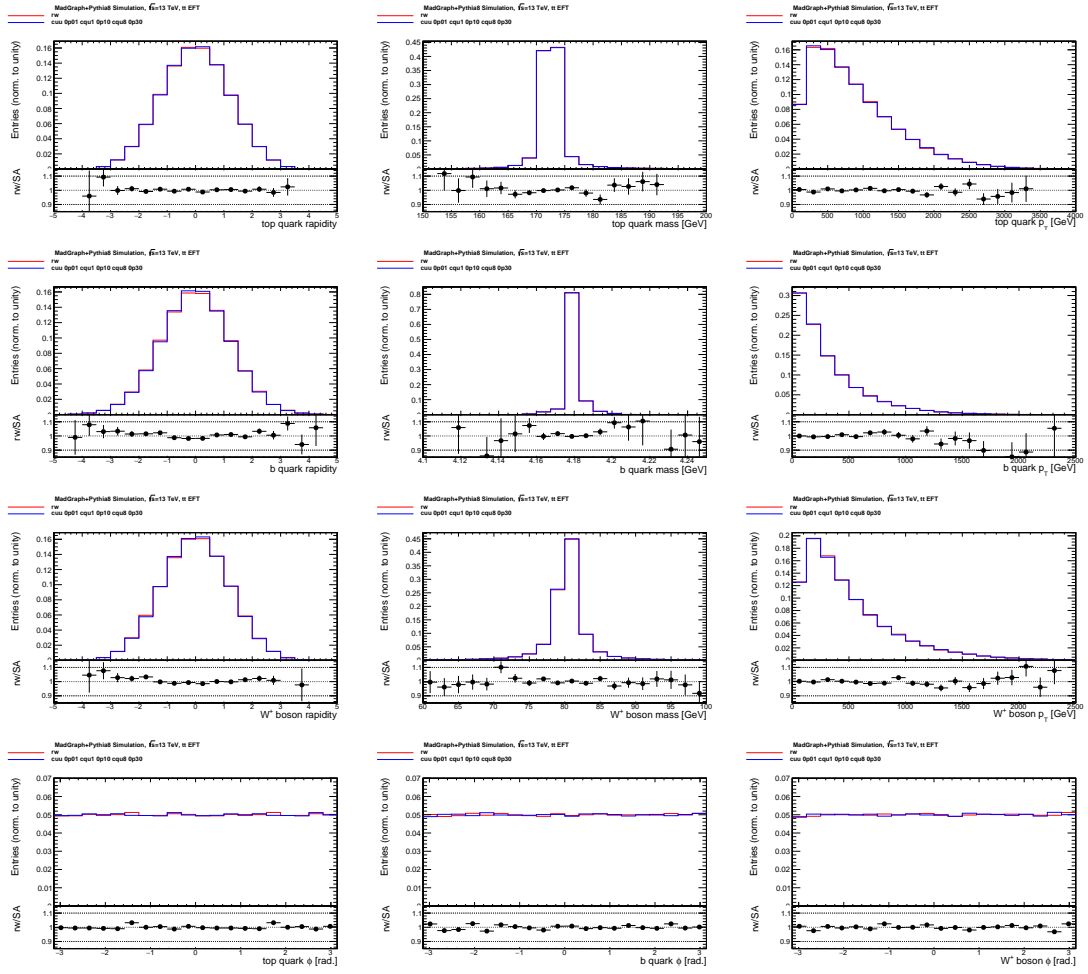
Figure C.12: Truth-level reweighting validation related to the additional $t\bar{t}$ sample generated with $c_{RR} = 0.01$, $c_{LR}^{(1)} = 0.1$, $c_{LR}^{(8)} = 0.3$. The red and blue lines show the distribution resulting from the nominal and the reweighted samples respectively. All distributions are normalized to unity. The bottom panels show the ratio between the nominal and reweighted sample entries.
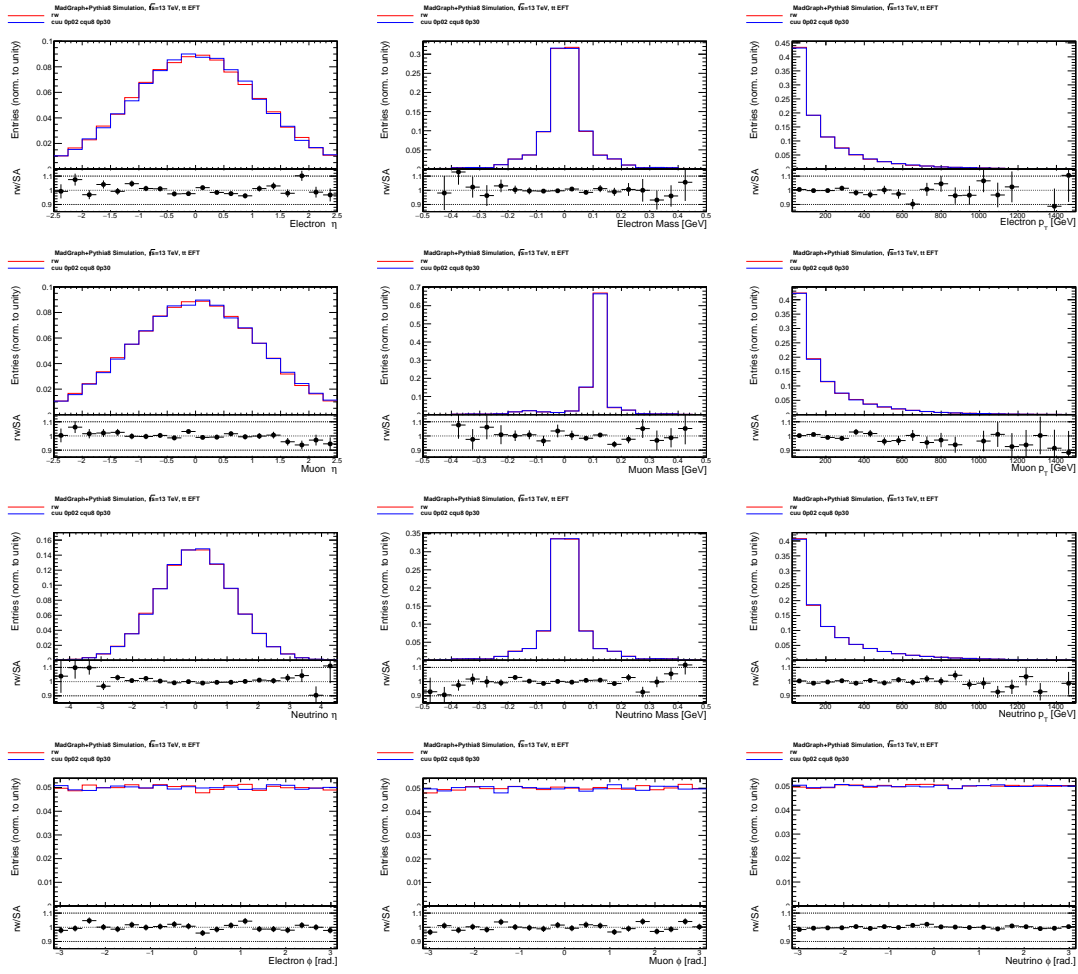
Figure C.13: Truth-level reweighting validation related to the additional tt sample generated with $c_{RR} = 0.02$ $c_{LR}^{(1)} = 0$, $c_{LR}^{(8)} = 0.3$. The red and blue lines show the distribution resulting from the nominal and the reweighted samples respectively. All distributions are normalized to unity. The bottom panels show the ratio between the nominal and reweighted sample entries.
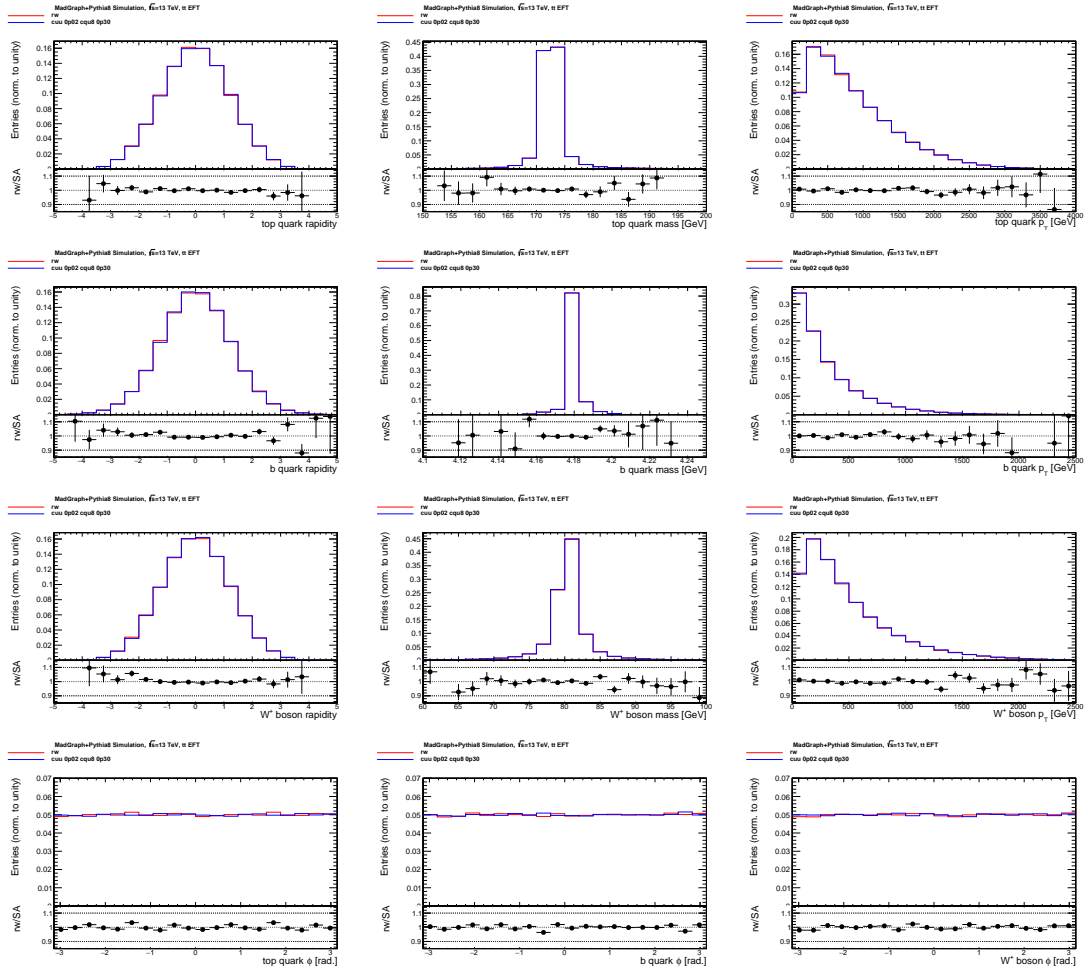
Figure C.14: Truth-level reweighting validation related to the additional tt sample generated with $c_{RR} = 0.02$ $c_{LR}^{(1)} = 0$, $c_{LR}^{(8)} = 0.3$. The red and blue lines show the distribution resulting from the nominal and the reweighted samples respectively. All distributions are normalized to unity. The bottom panels show the ratio between the nominal and reweighted sample entries.
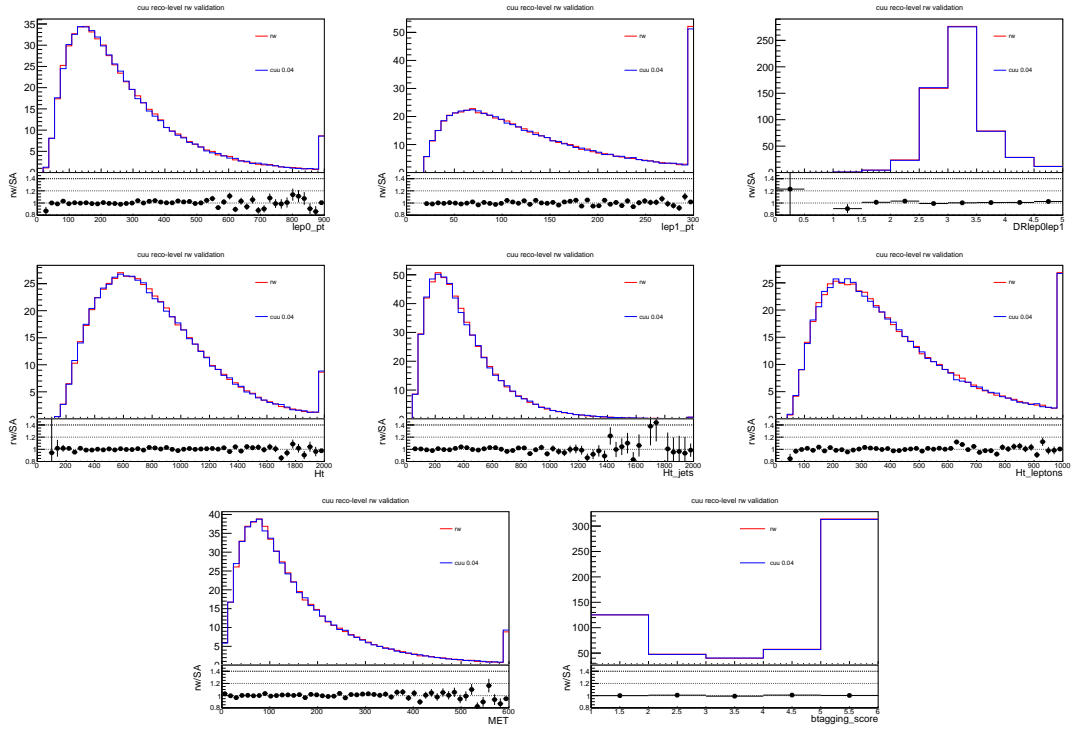
Figure C.15: Reco-level reweighting validation related to the additional tt sample generated with $c_{RR} = 0.04$, $c_{LR}^{(1)} = c_{LR}^{(8)} = 0$
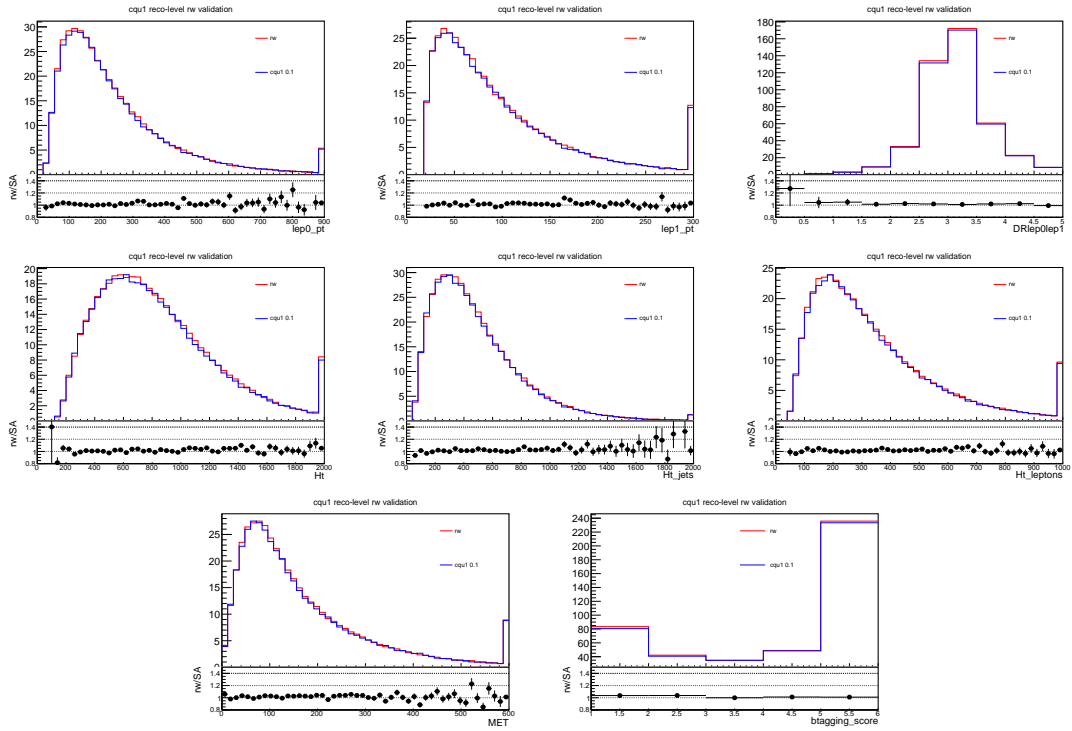
Figure C.16: Reco-level reweighting validation related to the additional tt sample generated with $c_{LR}^{(1)} = 0.1$, $c_{RR} = c_{LR}^{(8)} = 0$
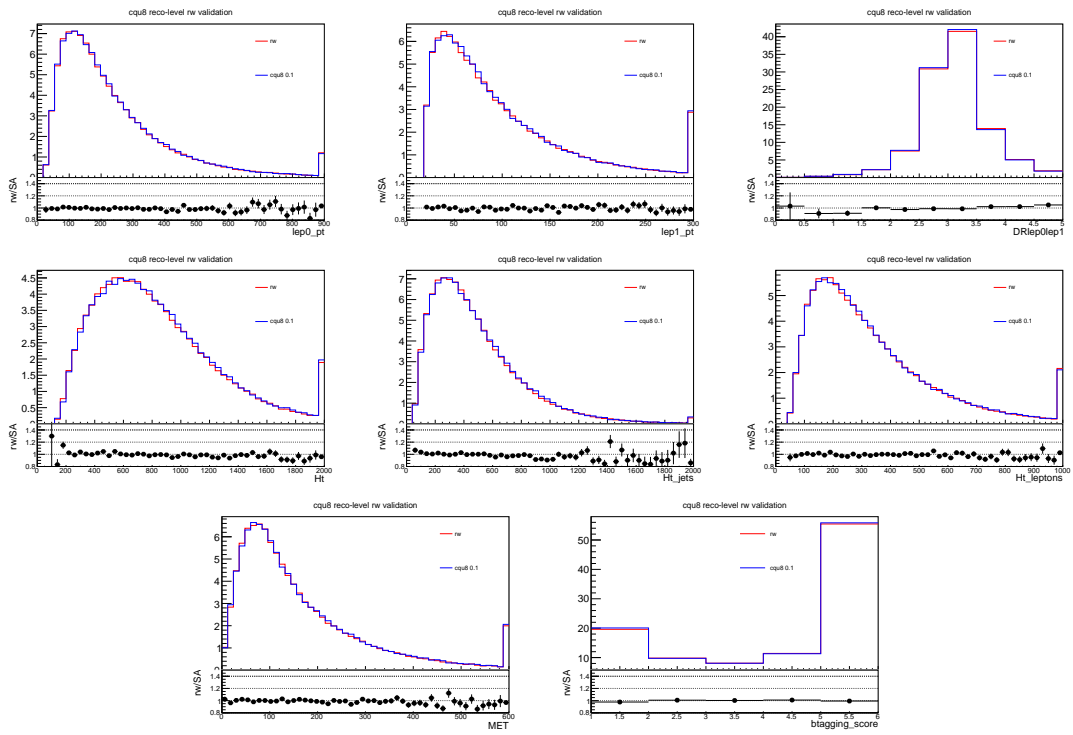
Figure C.17: Reco-level reweighting validation related to the additional tt sample generated with $c_{LR}^{(8)} = 0.1,\ c_{RR} = c_{LR}^{(1)} = 0$

Appendix D

Simulated background samples

The nominal $t\bar{t}W$ sample is generated using Sherpa-2.2.10 [125]. Both the factorization and renormalization scales are set to $M_T/2$, where M_T is defined as:

$$M_T = \Sigma_i m_{T,i} = \Sigma_i \sqrt{m_i^2 + p_{T,i}^2},$$ (D.1)

where the sum is performed over all outgoing partons in the matrix element calculation. The sample is generated using NLO accuracy for matrix elements for up to one additional jet and LO accuracy for up to two additional jets. The additional partons are matched and merged with the Sherpa parton shower based on Catani-Seymour dipole factorisation [126] using the MEPS@NLO prescription [127–130] with CKKW merging scale of 30 GeV[1]. The virtual QCD correction for matrix elements at NLO accuracy are provided by the OPENLOOPS 2 library [131, 132]. Samples are generated using the NNPDF3.0NNLO [82] PDF set. The LO electroweak contributions are obtained from a dedicated sample simulated with Sherpa-2.2.10 and then embedded to the NLO QCD sample described above. To evaluate the systematic uncertainty associated to the ME generator, an additional sample is generated with MADGRAPH5_AMC@NLO+PYTHIA8 at NLO accuracy. Two additional samples are instead generated to evaluate the systematic uncertainty associated to the parton shower generator. Specifically, the comparison between $t\bar{t}W$ events generated with POWHEG-BOX+PYTHIA8 and with POWHEG-BOX+HERWIG7 is taken as uncertainty.

The production of $t\bar{t}t\bar{t}$ events is modelled using the MADGRAPH5_AMC@NLO v2.6.2

---

[1]The CKKW merging is a procedure that allows to combine consistently tree-level matrix elements containing multiple partons with parton showers. The associated algorithm is implemented in Pythia [75].

generator [79] which provides matrix elements at NLO with the NNPDF3.1 NLO parton distribution function. The functional forms of the renormalization and factorization scales are set to $M_T/4$ where M_T is defined as reported in eq.(D.1). Top quark decays are generated at LO using MadSpin [133] to preserve all spin correlations. Pythia 8.230 [75] is employed for the parton shower and hadronisation, using the A14 set of tuned parameters and the NNPDF2.3 LO PDF set. An additional sample is generated to evaluate the modelling systematic uncertainty associate to the process. Specifically, four top events are generated with Sherpa 2.2.10 at NLO and compared with the nominal $t\bar{t}t\bar{t}$ sample.

The $t\bar{t}H$ samples are generated using Powheg-Box [134–136] at NLO. This sample uses the NNPDF3.0NLO PDF set. The h_{damp} parameter [2] is set to $3/4 \times (m_t + m_{\bar{t}} + m_H)$. The parton showering is generated with Pythia 8. Two additional samples related to the $t\bar{t}H$ process are generated to evaluate the systematic uncertainties associate to the modelling of the process. Specifically, in the first sample Powheg-Box is employed as ME generator instead of Madgraph5_aMC@NLO, while in the second sample Herwig 7 is used as parton shower generator, instead of Pythia 8.

The $t\bar{t}Z(\gamma)$ sample is generated using Madgraph5_aMC@NLO with a multileg configuration with +0,1 j at NLO and +2 j at LO. The NNPDF3.0 NNLO parton distribution functions are used. The invariant mass of the lepton pair (m_{ll}) is set to be greater than 1 GeV. Pythia 8 is employed to generate the parton showering. The systematic uncertainty related to the modelling of the process is evaluated using a $t\bar{t}Z(\gamma)$ sample generated with Madgraph5_aMC@NLO and Herwig 7. Uncertainties associated to the modelling of the initial-state radiation (ISR) are evaluated by employing two additional samples generated with the same settings as the nominal one, but with up- and down- variations of α_S in the A14 tune [137].

The $t\bar{t}$ events are generated using Powheg-Box v2.0 together with Pythia8 for the parton showering and fragmentation with the A14 tune. Single top events are simulated with Powheg-Box and Pythia8. The interference between Wt ad $t\bar{t}$ processes is taken into account as well. The modelling uncertainty associated to the process is evaluated using an additional sample, generated with Powheg-Box and Herwig 7.

A dedicated $t\bar{t}$ sample where one of the two top quarks undergoes rare $t \longrightarrow Wb\gamma^*$ ($\gamma^* \longrightarrow l^+l^-$) radiative decay is generated at LO requiring $m(l^+l^-) > 1$ GeV. In this sample the photon can be radiated from the top quark, the W boson, or the b-quark. The $t\bar{t}Z(\gamma)$ and $t\bar{t} \longrightarrow W^+bW^-\bar{b}l^+l^-$ samples are combined together. The contribution from internal photon conversion ($\gamma^* \longrightarrow l^+l^-$) with $m(l^+l^-) < 1$ GeV is modelled by

---

[2]The h_{damp} parameter controls the p_T of the first additional emission beyond the leading-order Feynman diagram in the parton showering.

QED multiphoton radiation in an inclusive $t\bar{t}$ sample.

Diboson backgrounds are generated using Sherpa 2.2.2 with the NNPDF3.0NNLO parton distribution functions. The same settings and generators are employed to generate VVV samples as well.

Rare background processes (tZ, $ttWW$, $ttHH$, $ttWH$, $ttZZ$, WtZ) have been generated either with MADGRAPH at LO or with MG5_AMC at NLO.

A summary of the MC samples generation is reported in Table D.1 together with further information concerning the alternative Monte Carlo samples used to estimate systematic uncertainties.

Process	Generator	ME order	Parton shower	PDF	Tune
$t\bar{t}W$	Sherpa 2.2.10	NLO	Sherpa	NNPDF3.0 NNLO	Sherpa default
	(MG5_AMC)	(NLO)	(Pythia 8)	(NNPDF3.0 NLO)	(A14)
	(Powheg-BOX)	(NLO)	(Pythia 8)	(NNPDF2.3 LO)	(A14)
	(Powheg-BOX)	(NLO)	(Herwig 7.1.6)	(NNPDF3.0 NLO)	(H7-UE-MMHT)
$t\bar{t}t\bar{t}$	MG5_AMC	NLO	Pythia 8	NNPDF3.1 NLO	A14
	(Sherpa 2.2.10)	(NLO)	(Sherpa)	(NNPDF3.0 NNLO)	(Sherpa default)
$t\bar{t}H$	Powheg-BOX	NLO	Pythia 8	NNPDF3.0 NLO	A14
	(Powheg-BOX)	(NLO)	(Herwig7)	(NNPDF3.0 NLO)	(H7-UE-MMHT)
	(MG5_AMC)	(NLO)	(Pythia 8)	(NNPDF3.0 NLO)	(A14)
$t\bar{t}Z(\gamma)$	MG5_AMC	NLO	Pythia 8	NNPDF3.0 NNLO	A14
	(MG5_AMC)	(NLO)	(Herwig 7)	(NNPDF3.0 NLO)	(H7-UE-MMHT)
$t\bar{t} \longrightarrow W^+bW^-\bar{b}l^+l^-$	MG5_AMC	LO	Pythia 8	NNPDF3.0 LO	A14
$t(Z/\gamma^*)$	MG5_AMC	NLO	Pythia 8	NNPDF2.3 LO	A14
$tW(Z/\gamma^*)$	MG5_AMC	NLO	Pythia 8	NNPDF2.3 LO	A14
$t\bar{t}W^+W^-$	MG5_AMC	LO	Pythia 8	NNPDF2.3 LO	A14
$t\bar{t}$	Powheg-BOX	NLO	Pythia 8	NNPDF3.0 NLO	A14
	(Powheg-BOX)	NLO	(Herwig7.1.3)	(NNPDF3.0 NLO)	(H7-UE-MMHT)
$t\bar{t}t$	MG5_AMC	LO	Pythia 8	NNPDF2.3 LO	A14
s-, t-channel, Wt single top	Powheg-BOX	NLO	Pythia 8	NNPDF3.0 NLO	A14
VV, $qqVV$, low $m_{\ell\ell}$, VVV	Sherpa 2.2.2	NLO	Sherpa	NNPDF3.0 NNLO	Sherpa default
$Z \to l^+l^-$	Sherpa 2.2.1	NLO	Sherpa	NNPDF3.0 NLO	Sherpa default
$Z \to l^+l^-$ (matCO)	Powheg-BOX	NLO	Pythia 8	CTEQ6L1 NLO	A14
$Z \to l^+l^-+(\gamma*)$	Powheg-BOX	NLO	Pythia 8	CTEQ6L1 NLO	A14
W+jets	Sherpa 2.2.1	NLO	Sherpa	NNPDF3.0 NLO	Sherpa default
VH	Powheg-BOX	NLO	Pythia 8	NNPDF3.0 NLO	A14
$t\bar{t}ZZ$	Madgraph	LO	Pythia 8	NNPDF2.3 LO	A14
$t\bar{t}HH$	Madgraph	LO	Pythia 8	NNPDF2.3 LO	A14
$t\bar{t}WH$	Madgraph	LO	Pythia 8	NNPDF2.3 LO	A14

Table D.1: Summary of the configurations used for the generation of background processes. The samples used to estimate the systematic uncertainties are reported in between parentheses. V refers to production of an electroweak boson (W or Z/γ^*). The sets of parton distribution functions (PDFs) shown in the table are used for the matrix element (ME). Tune refers to the underlying-event tune of the parton shower generator. MG5_AMC refers to MadGraph5_aMC@NLO 2.2.X or 2.3.X [79]; Pythia 8 refers to version 8.2 [75]; Herwig7 refers to version 7.0.4 [138]. Samples using Pythia 8 have heavy flavour hadron decays modelled by EvtGen 1.2.0 [84]. All samples include leading-logarithm photon emission, either modelled by the parton shower generator or by PHOTOS [139]. The mass of the top quark and SM Higgs boson were set to 172.5 GeV and 125 GeV.

Appendix E

Neural Networks' input variables

The normalized distributions related to the input variables used in the training of the Neural Networks employed in the analysis are reported in this Appendix. The feature importance ranking plots related to the input variables are presented as well. The ranking of the input variables is evaluated by applying the "Permutation feature importance" method. After the NN has been trained, the values associated to one input variable are randomly permuted within the events, then the events are re-classified by the NN. The resulting classification accuracy is then used to assess the importance of the permuted variable, with a lower performance corresponding to an higher importance of the input feature. This procedure is individually performed for each input variable, therefore resulting in a importance ranking.

The plots showing the data/MC agreement of the input variables are reported in this Appendix as well. Since the NNs are trained on events belonging to a phase space region where signal events are expected to be the dominant contribution, the number of unblinded bins in the input variables distributions is not sufficient to assess the data/MC agreement. Therefore, the accordance between data and simulation is evaluated using the input variables distributions resulting after applying an additional selection requirement based on the azimuthal distance $\Delta\Phi(\ell^\pm, \ell^\pm)$ between the same-sign leptons in the events. Specifically, since the MC distributions of the background processes related to the NNs input variables have comparable shapes in the $\Delta\Phi(\ell, \ell) < 2.5$ and $\Delta\Phi(\ell, \ell) \geq 2.5$ regions, the distributions of the input variables in the low-$\Delta\Phi$ region have been employed to assess the data/MC agreement.

E.1 NN^{SvsS} Input Variables

The Deep Neural Network NN^{SvsS} is employed in the analysis to define separate Signal Regions, enriched in same-sign top events resulting from different EFT operators, as reported in Section 5.3.2.

The 9 input variables used to train the NN^{SvsS} are reported in Table E.1. The associated kinematic distributions for RR and LR signal events as well as for the backgrounds are reported in Figure E.1. The importance of the input variables for the NN-based categorization is shown in Figure E.2. It can be seen that the kinematic distributions related to the most important input variables, such as the invariant mass of the dilepton system $M(\ell, \ell)$ and $\Delta\Phi(\ell, \ell)$, are more similar for LR signal and background events. Therefore, background events are more likely to be classified by the NN^{SvsS} as LR-like, as reported in Figure 5.3a in Section 5.3.2.

The data/MC ratio in the unblinded bins of the input variables distributions in the $\Delta\Phi(\ell, \ell) < 2.5$ region is employed to assess the good modelling provided by the simulation, as reported in Figure E.3. The shapes related to the input variable distributions for background processes are comparable in the low- and high-$\Delta\Phi$ regions, as can be seen by comparing Figure E.3 and E.4.

Signal categorisation neural network input variables
$\Delta\Phi,\ \Delta R, \Delta\eta$ between the two same-sign leptons
Invariant mass $M_{\ell\ell}$ of the two same-sign leptons
Sum of the p_T of jets and leptons $(H_{T,jet}, H_{T,lep})$
p_T of the leading jet
Missing transverse momentum E_T^{miss}
Transverse mass of leptons and missing transverse momentum $(M_{T,lep-met})$ [1]

Table E.1: Input variables for NN^{SvsS}.

---

[1] The transverse mass is defined as: $M_T = \sqrt{E^2 - p_z^2}$
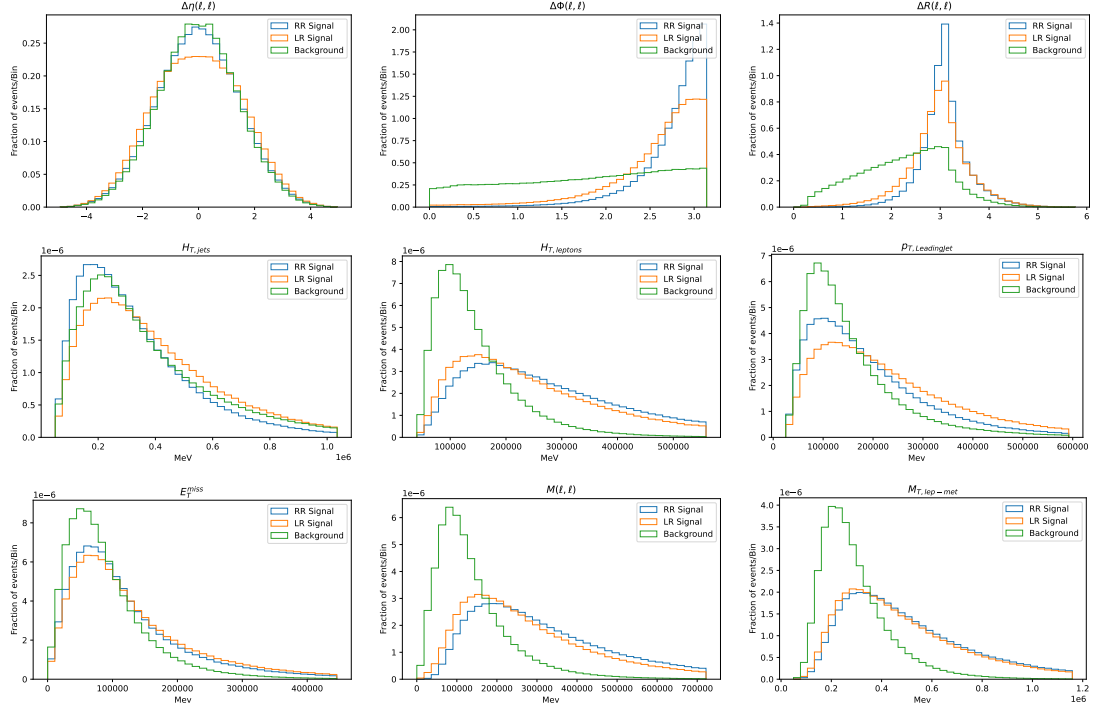
Figure E.1: Kinematic distributions related to the 9 input variables of NN$^{\text{SvsS}}$. From top left to bottom right: $\Delta\eta(\ell,\ell)$, $\Delta\Phi(\ell,\ell)$, $\Delta R(\ell,\ell)$, $H_{T,jets}$, $H_{T,leptons}$, $p_{T,LeadingJet}$, E_T^{miss}, $M(\ell,\ell)$ and $M_{T,lep-met}$. RR signal, LR signal and background distribution are reported in blue, orange and green respectively. All distribution are normalized to unity.
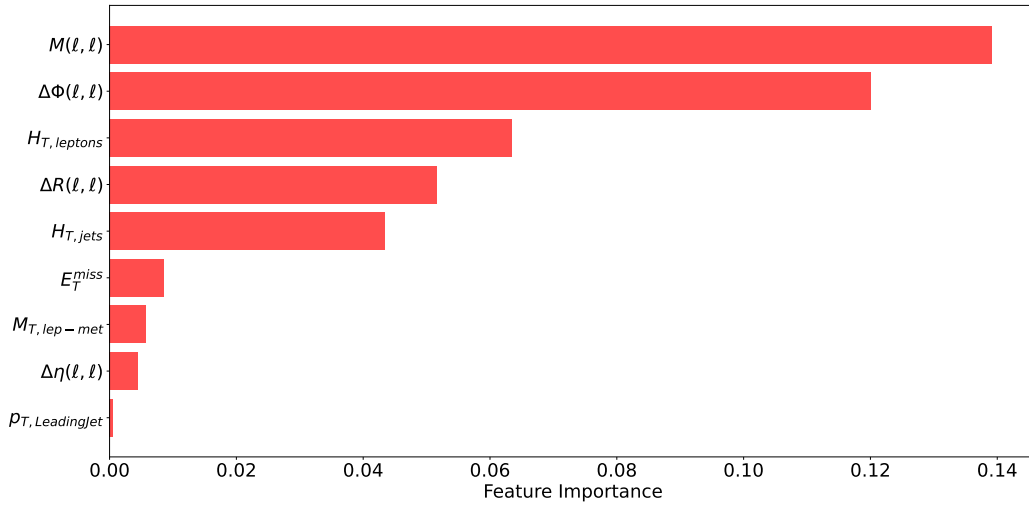
Figure E.2: NN$^{\text{SvsS}}$ input variable ranking. $M(\ell,\ell)$ and $\Delta\Phi(\ell,\ell)$ are the most important variable for the categorization of RR and LR signal events, followed by $H_{T,lep}$, $\Delta R(\ell,\ell)$ and $H_{T,jets}$. The leas discriminating variables are $E_T{}^m iss$, $M_{T,lep-met}$, $\Delta\eta(\ell,\ell)$ and $p_{T,LeadingJet}$
.
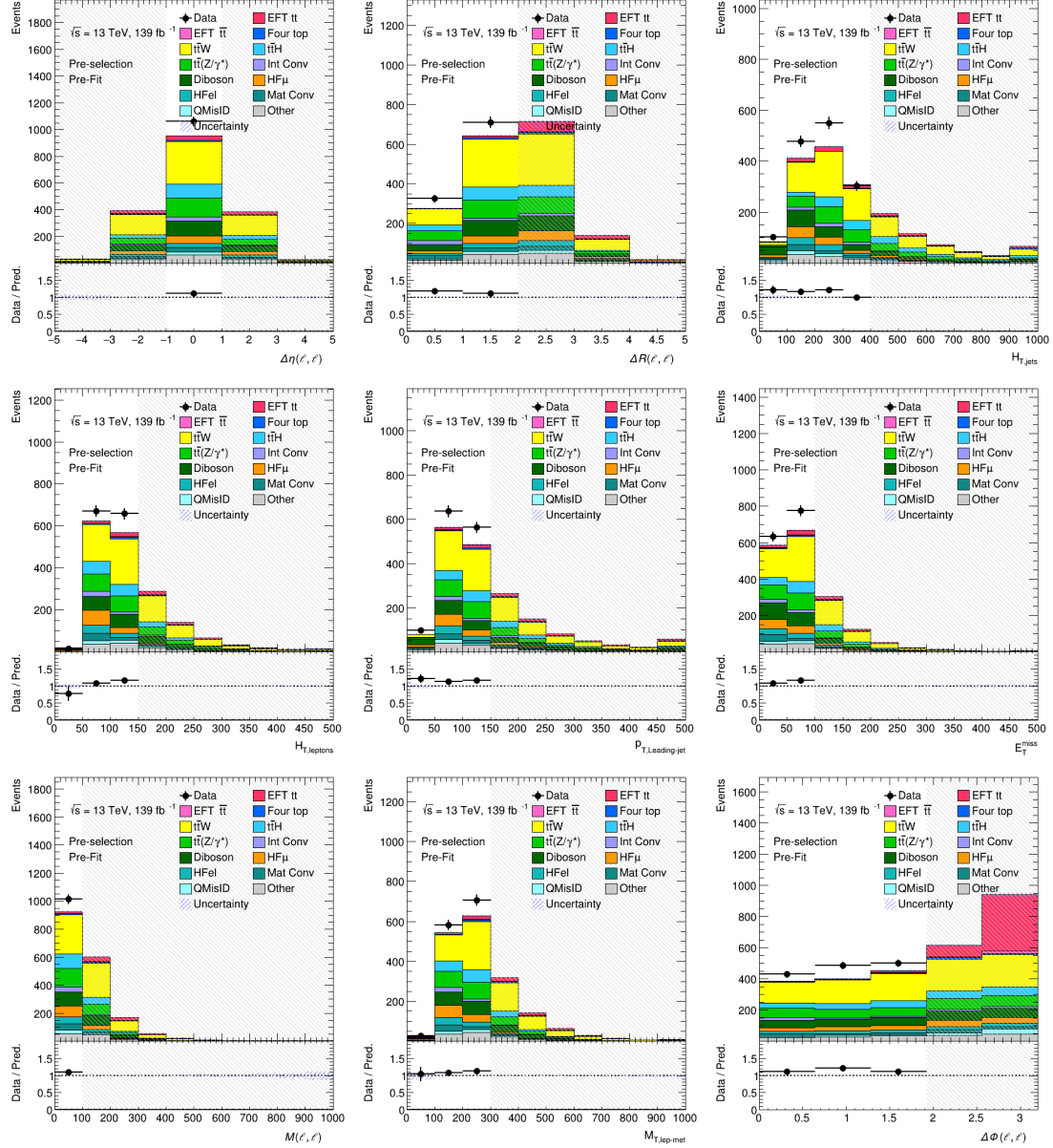
Figure E.3: Kinematic distributions of data and MC events related to the 9 input variables of NN$^{\text{SvsS}}$ in the $\Delta\Phi < 2.5$ region. From top left to bottom right: $\Delta\eta(\ell,\ell)$, $\Delta R(\ell,\ell)$, $H_{T,jets}$, $H_{T,leptons}$, $p_{T,LeadingJet}$, E_T^{miss}, $M(\ell,\ell)$ and $M_{T,lep-met}$. The distribution related to $\Delta\Phi(\ell,\ell)$ is obtained by only applying the preliminary signal-like event selection. The bottom panels display the ratio between data and MC yields. Data events are not shown in bins where $S/B \geq 5\%$.
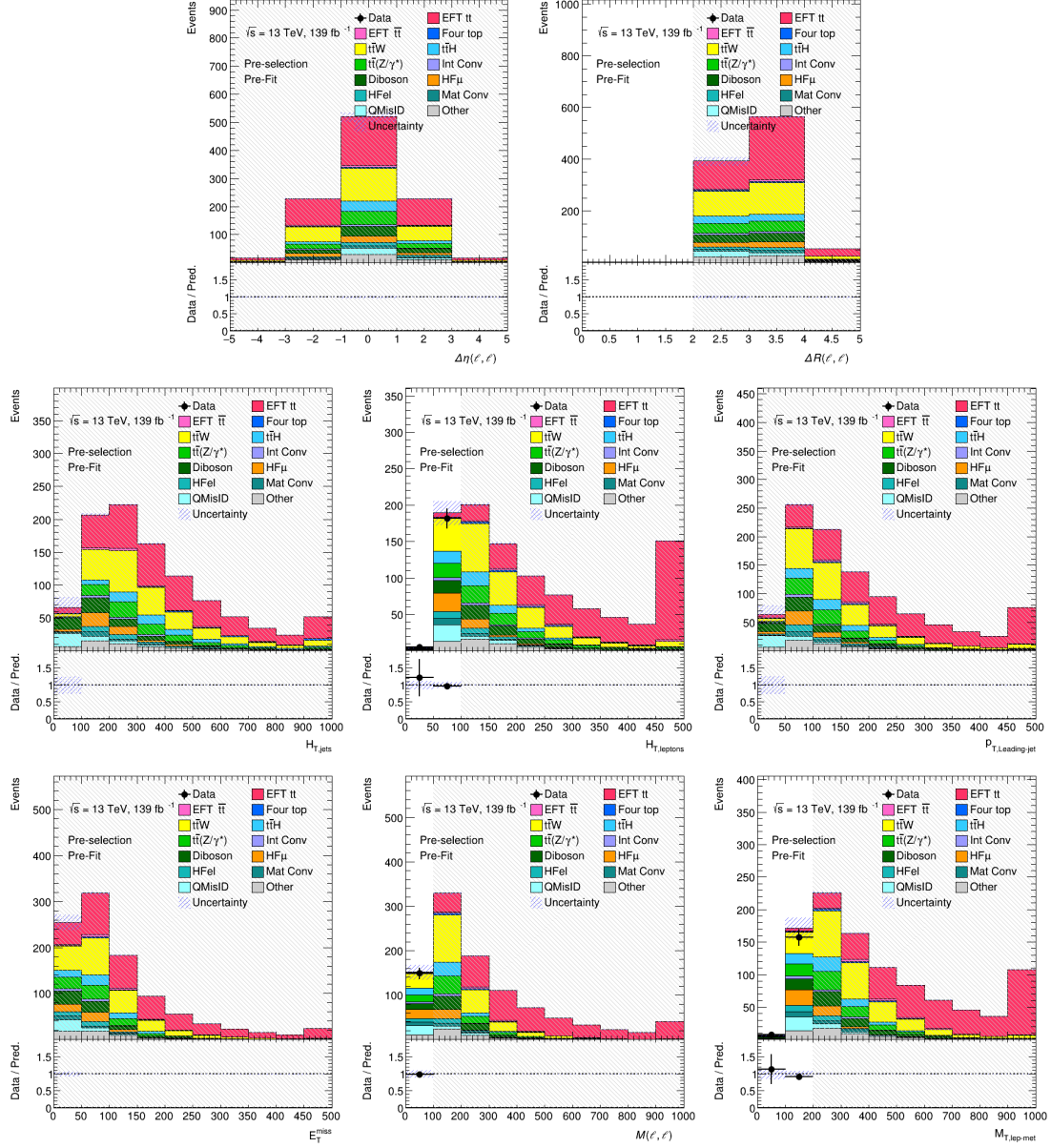
Figure E.4: Kinematic distributions of data and MC events related to the 8 input variables of NN$^{\mathrm{SvsS}}$ ($\Delta\Phi$ is not shown) in the $\Delta\Phi \geq 2.5$ region. From top left to bottom right: $\Delta\eta(\ell,\ell)$, $\Delta R(\ell,\ell)$, $H_{T,jets}$, $H_{T,leptons}$, $p_{T,LeadingJet}$, E_T^{miss}, $M(\ell,\ell)$ and $M_{T,lep-met}$. The bottom panels display the ratio between data and MC yields. Data events are not shown in bins where $S/B \geq 5\%$.

E.2 NN$^{\text{SvsB}}$ Input Variables

The Deep Neural Network NN$^{\text{SvsB}}$ is employed in the analysis to perform signal-background discrimination within the defined Signal Regions SR_{RR}^{++}, SR_{RR}^{--}, SR_{LR}^{++} and SR_{LR}^{--}, as reported in Section 5.3.3.

The 6 input variables used to train the NN$^{\text{SvsB}}$ are listed in Table E.2. The associated kinematic distributions for signal and background events belonging to SR_{RR} and SR_{LR} are reported in Figure E.5 and E.6. The importance of the input variables for the NN-based categorization is shown in Figure E.9.

Figure E.10 and E.11 show the NN$^{\text{SvsB}}$ input variables distributions for tt, $\overline{tt}$ and background events in SR_{RR} and SR_{LR} respectively. It can be seen that the distributions related to $\overline{tt}$ events are more similar to the background ones. Therefore the NN$^{\text{SvsB}}$ performance is lower in the negative Signal Regions SR_{RR}^{--} and SR_{LR}^{--} as stated in Section 5.3.3.

The data/MC agreement related to the input variables has been checked in the unblinded bins of the distributions in the $\Delta\Phi(\ell,\ell) < 2.5$ region to assess the good modelling provided by the simulation, as reported in Figure E.12, E.14, E.16 and E.18. The shapes related to the input variable distributions for background processes are comparable in the low- and high-$\Delta\Phi$ regions, as can be seen by comparing the previous figures with Figure E.13, E.15, E.17 and E.19.

Signal vs Background neural network input variables
Sum of the p_T of leptons ($H_{T,lep}$)
Pseudo-continuous b-tagging score of 1st, 2nd leading jet
p_T of the leading jet
Transverse mass of leptons and missing transverse momentum ($M_{T,lep-met}$)
Number of jets (N_{jets})

Table E.2: Input variables for NN$^{\text{SvsB}}$.
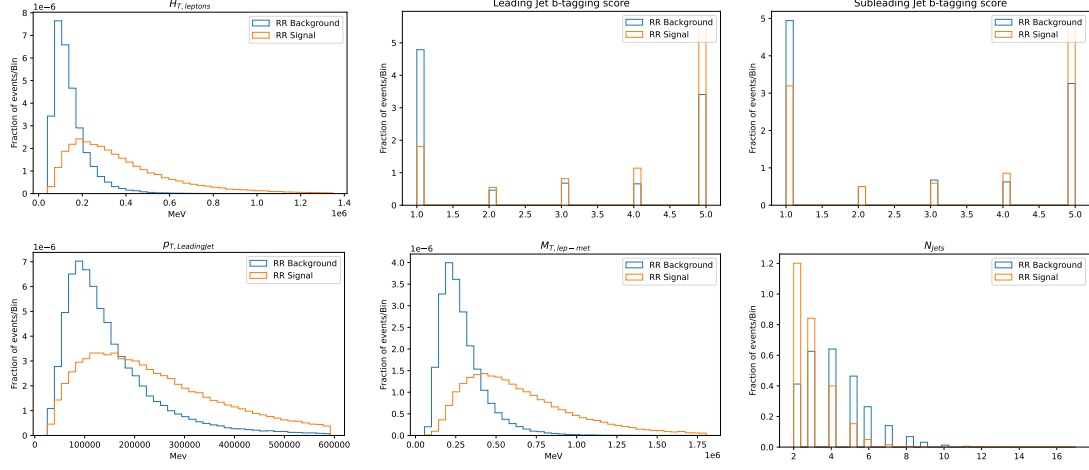
Figure E.5: Kinematic distributions related to the 6 input variables of NN$^{\text{SvsB}}$ for events in SR_{RR}. From top left to bottom right: $H_{T,leptons}$, b-tagging score of the leading jet, b-tagging score of the subleading jet, $p_{T,LeadingJet}$, $M_{T,lep-met}$ and n_{Jets}. Signal and background distributions are reported in orange and blue respectively. All distribution are normalized to unity.
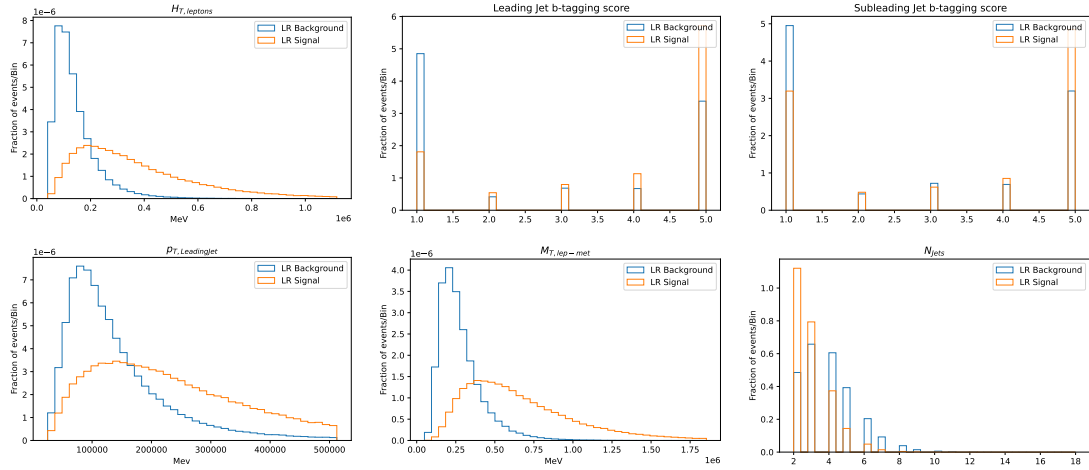
Figure E.6: Kinematic distributions related to the 6 input variables ob NN$^{\text{SvsB}}$ for events in SR_{LR}. From top left to bottom right: $H_{T,leptons}$, b-tagging score of the leading jet, b-tagging score of the subleading jet, $p_{T,LeadingJet}$, $M_{T,lep-met}$ and n_{Jets}. Signal and background distributions are reported in orange and blue respectively. All distribution are normalized to unity.
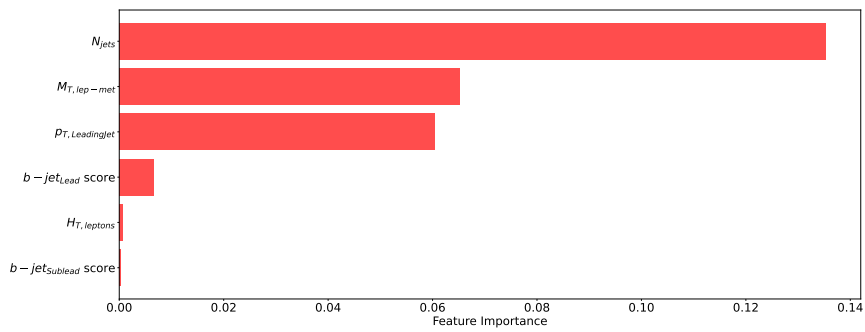
Figure E.7: NN$^{\mathrm{SvsB}}$ input variable ranking for SR_{RR}.
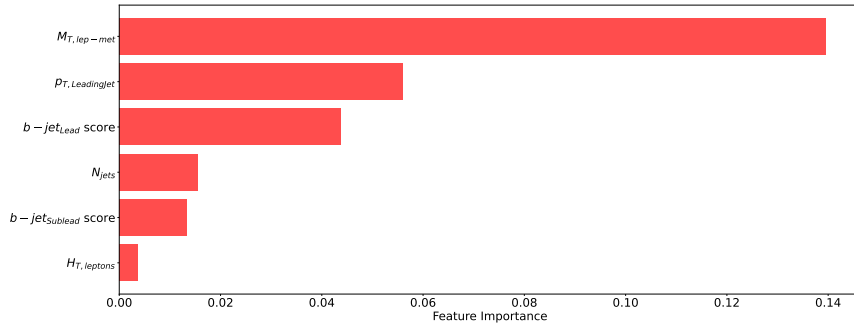
Figure E.8: NN$^{\mathrm{SvsB}}$ input variable ranking for SR_{LR}.

Figure E.9: NN$^{\mathrm{SvsB}}$ input variable ranking for SR_{RR} and SR_{LR}. $M_{T,lep-met}$, N_{jets} and $p_{T,Leagingjet}$ are the most important variable for signal-background discrimination.
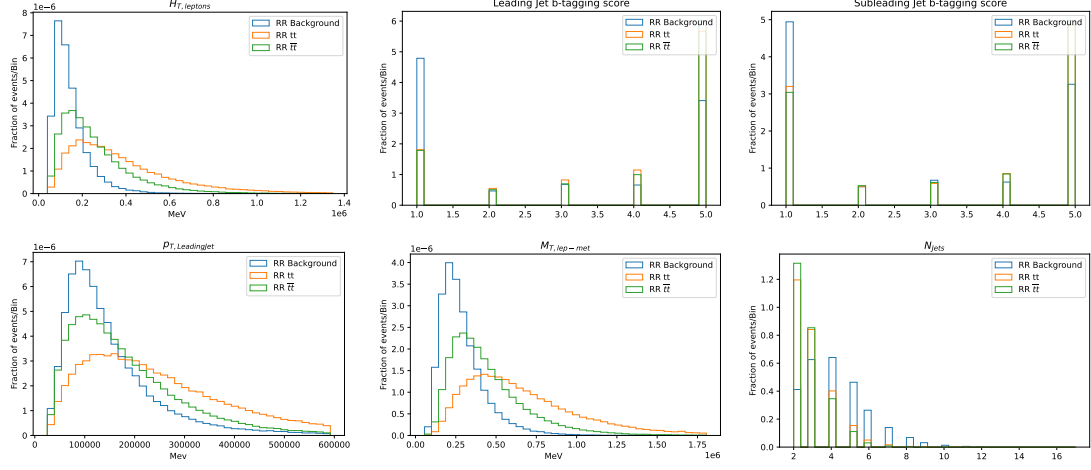
Figure E.10: Kinematic distributions related to the 6 input variables of NN$^{\text{SvsB}}$ for events in SR_{RR}. From top left to bottom right: $H_{T,leptons}$, b-tagging score of the leading jet, b-tagging score of the subleading jet, $p_{T,LeadingJet}$, $M_{T,lep-met}$ and n_{Jets}. The distributions related to tt, $\overline{tt}$ and background events are reported in orange, green and blue respectively. All distribution are normalized to unity.
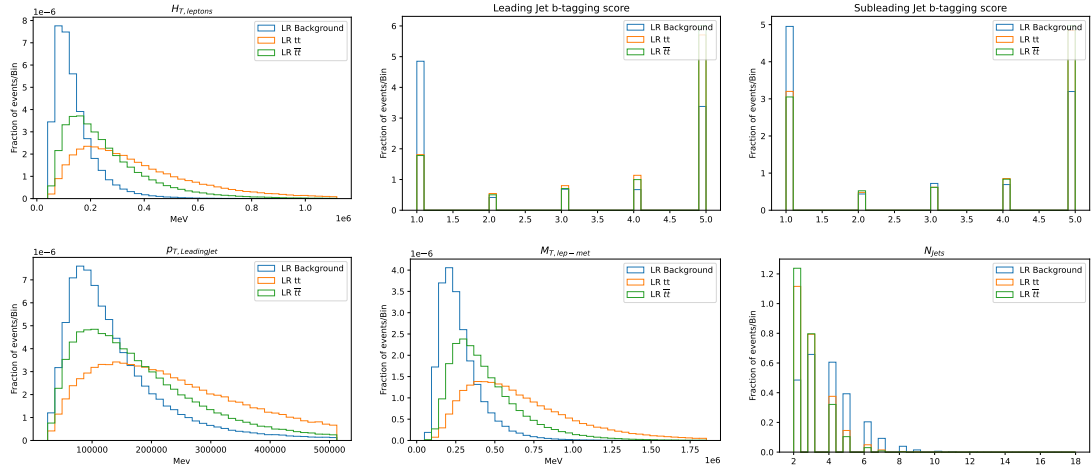
Figure E.11: Kinematic distributions related to the 6 input variables of NN$^{\text{SvsB}}$ for events in SR_{LR}. From top left to bottom right: $H_{T,leptons}$, b-tagging score of the leading jet, b-tagging score of the subleading jet, $p_{T,LeadingJet}$, $M_{T,lep-met}$ and n_{Jets}. The distributions related to tt, $\overline{tt}$ and background events are reported in orange, green and blue respectively. All distribution are normalized to unity.
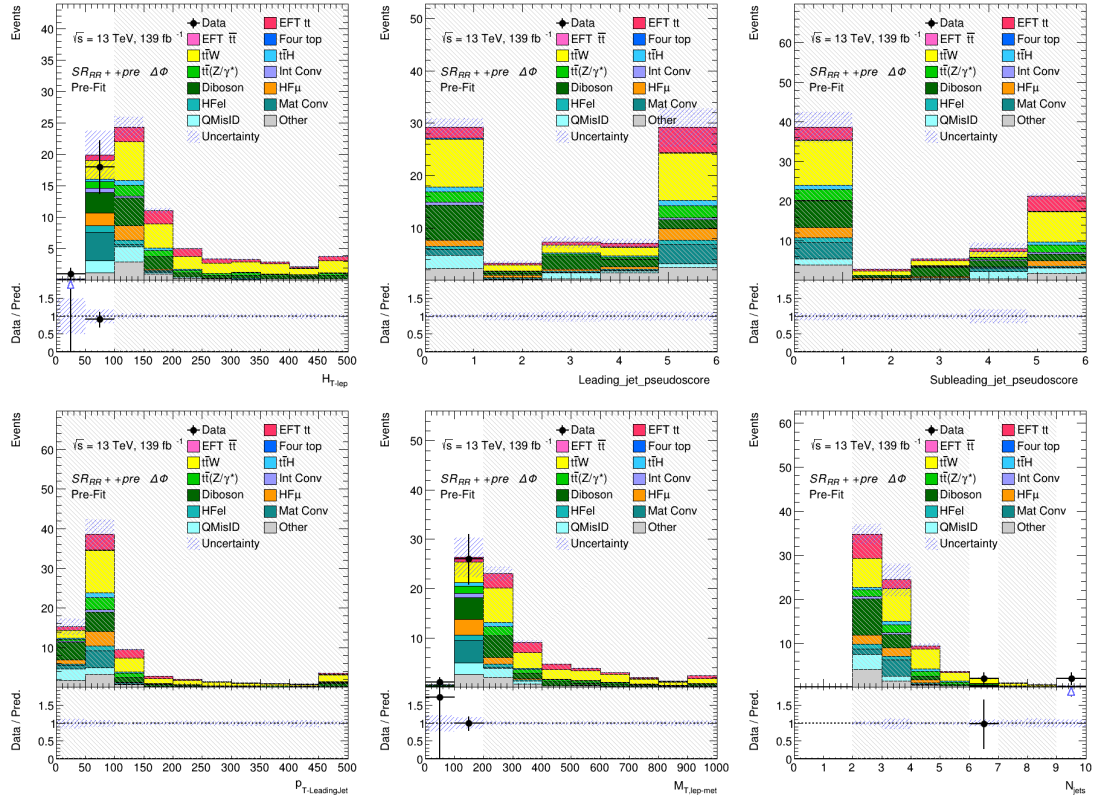
Figure E.12: Kinematic distributions for data and MC events in the $\Delta\Phi < 2.5$ region related to the 6 input variables of NN^{SvsB} for events in SR_{RR}^{++}. From top left to bottom right: $H_{T,leptons}$, b-tagging score of the leading jet, b-tagging score of the subleading jet, $p_{T,LeadingJet}$, $M_{T,lep-met}$ and n_{Jets}. The bottom panels display the ratio between data and MC yields. Data events are not shown in bins where $S/B \geq 5\%$.
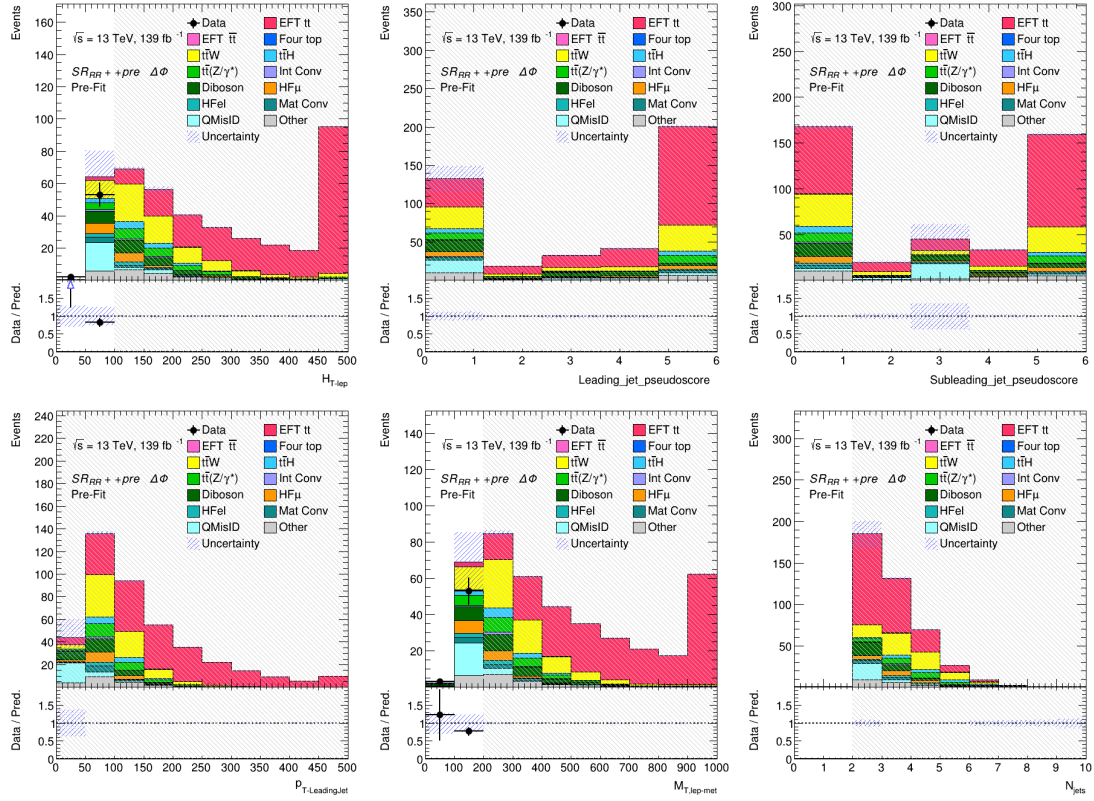
Figure E.13: Kinematic distributions for data and MC events in the $\Delta\Phi \geq 2.5$ region related to the 6 input variables of $\mathrm{NN^{SvsB}}$ for events in SR_{RR}^{++}. From top left to bottom right: $H_{T,leptons}$, b-tagging score of the leading jet, b-tagging score of the subleading jet, $p_{T,LeadingJet}$, $M_{T,lep-met}$ and n_{Jets}. The bottom panels display the ratio between data and MC yields. Data events are not shown in bins where $S/B \geq 5\%$.
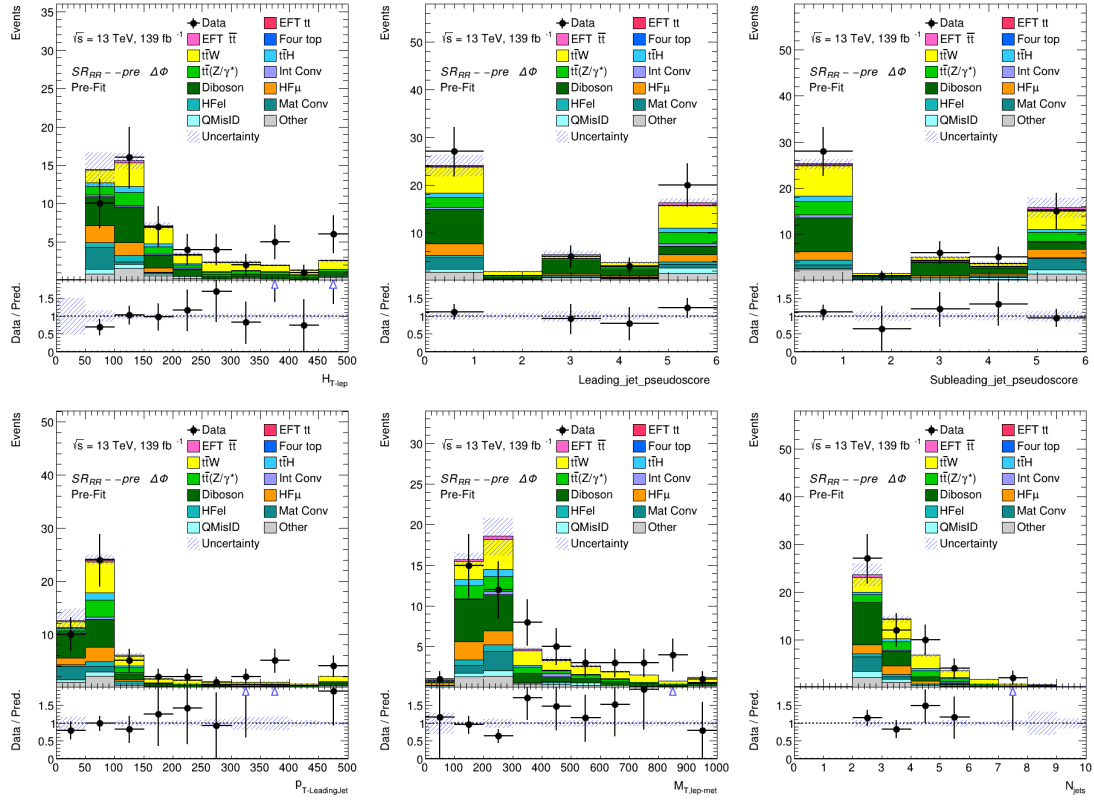
Figure E.14: Kinematic distributions for data and MC events in the $\Delta\Phi < 2.5$ region related to the 6 input variables of $\mathrm{NN^{SvsB}}$ for events in SR_{RR}^{--}. From top left to bottom right: $H_{T,leptons}$, b-tagging score of the leading jet, b-tagging score of the subleading jet, $p_{T,LeadingJet}$, $M_{T,lep-met}$ and n_{Jets}. The bottom panels display the ratio between data and MC yields. Data events are not shown in bins where $S/B \geq 5\%$.
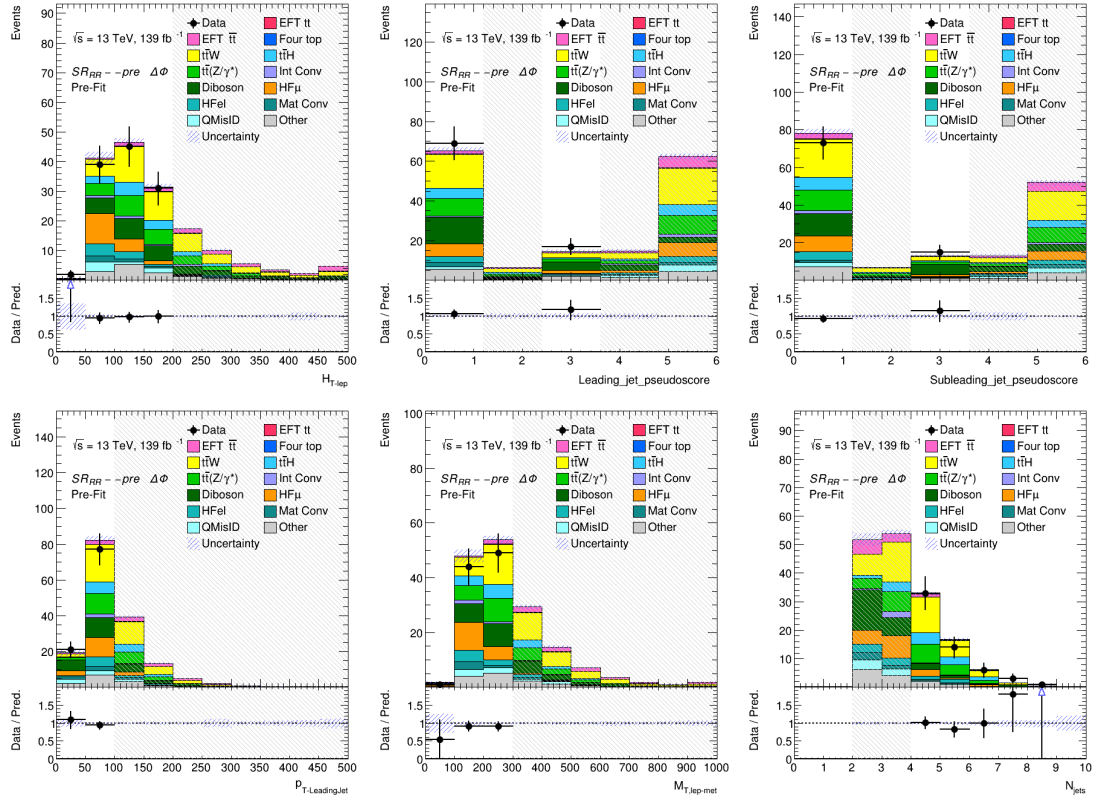
Figure E.15: Kinematic distributions for data and MC events in the $\Delta\Phi \geq 2.5$ region related to the 6 input variables of NN$^{\text{SvsB}}$ for events in SR_{RR}^{--}. From top left to bottom right: $H_{T,leptons}$, b-tagging score of the leading jet, b-tagging score of the subleading jet, $p_{T,LeadingJet}$, $M_{T,lep-met}$ and n_{Jets}. The bottom panels display the ratio between data and MC yields. Data events are not shown in bins where $S/B \geq 5\%$.
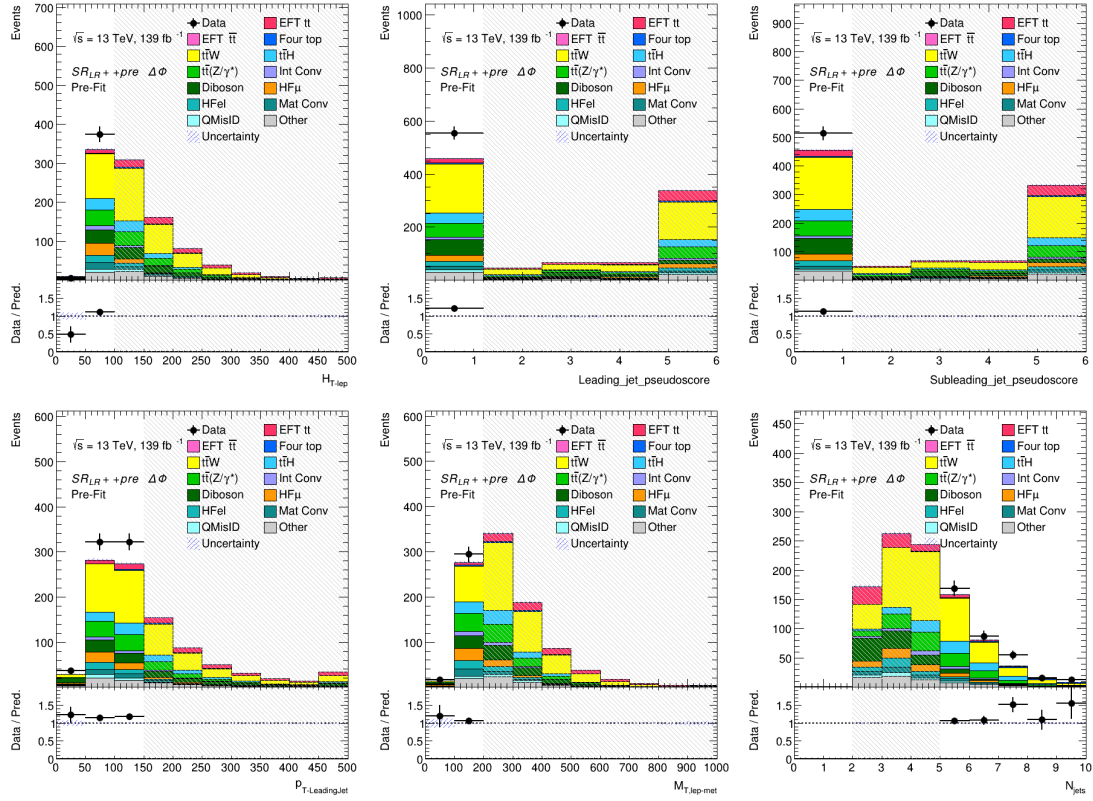
Figure E.16: Kinematic distributions for data and MC events in the $\Delta\Phi < 2.5$ region related to the 6 input variables of NN^{SvsB} for events in SR_{LR}^{++}. From top left to bottom right: $H_{T,leptons}$, b-tagging score of the leading jet, b-tagging score of the subleading jet, $p_{T,LeadingJet}$, $M_{T,lep-met}$ and n_{Jets}. The bottom panels display the ratio between data and MC yields. Data events are not shown in bins where $S/B \geq 5\%$.
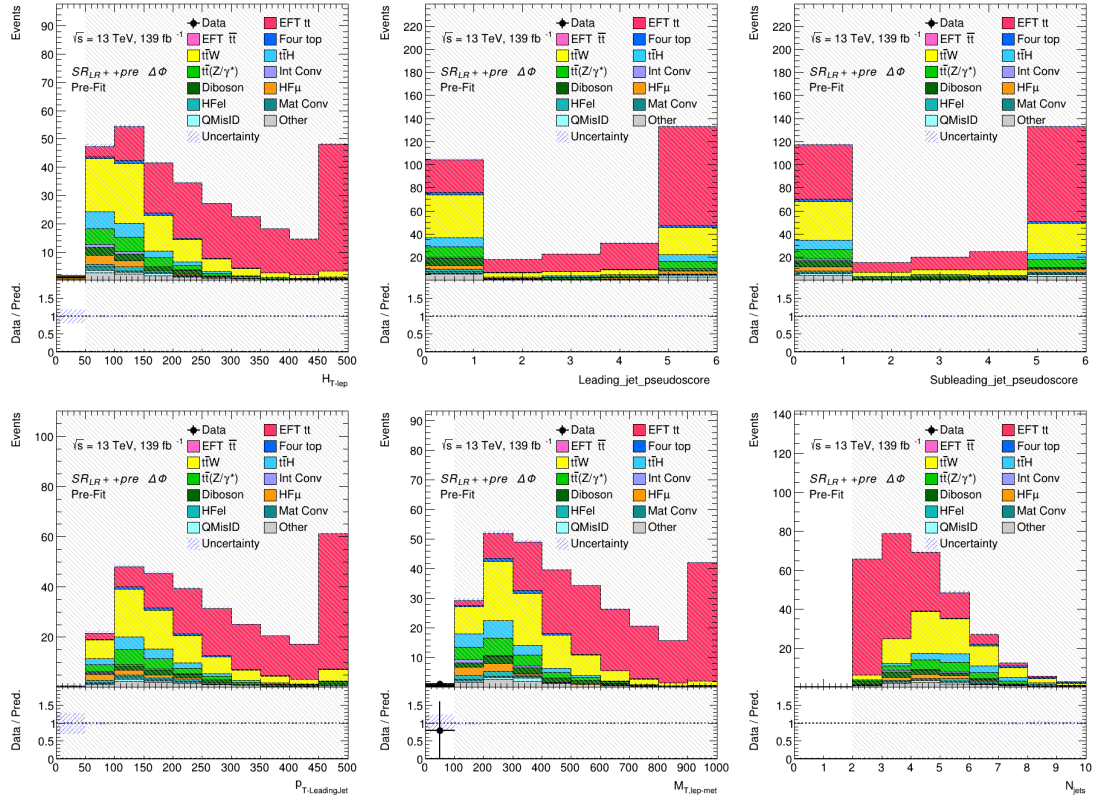
Figure E.17: Kinematic distributions for data and MC events in the $\Delta\Phi \geq 2.5$ region related to the 6 input variables of NN$^{\text{SvsB}}$ for events in SR_{LR}^{++}. From top left to bottom right: $H_{T,leptons}$, b-tagging score of the leading jet, b-tagging score of the subleading jet, $p_{T,LeadingJet}$, $M_{T,lep-met}$ and n_{Jets}. The bottom panels display the ratio between data and MC yields. Data events are not shown in bins where $S/B \geq 5\%$.
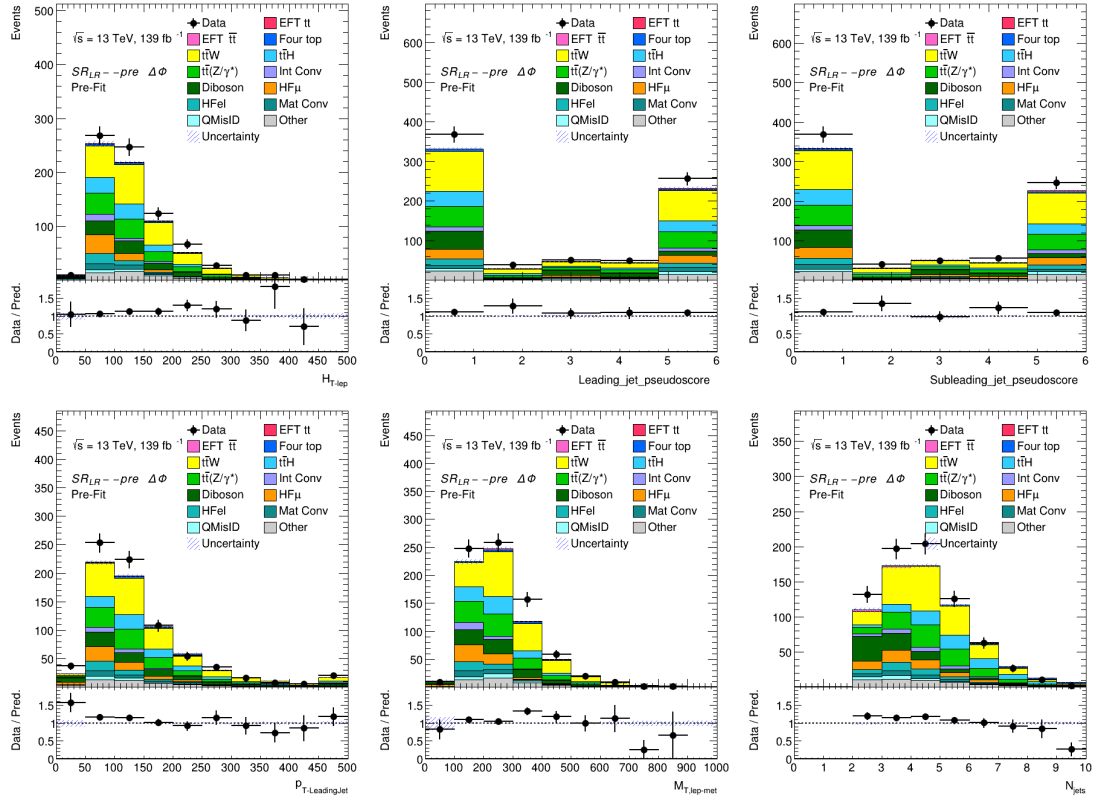
Figure E.18: Kinematic distributions for data and MC events in the $\Delta\Phi < 2.5$ region related to the 6 input variables of NN^{SvsB} for events in SR_{LR}^{--}. From top left to bottom right: $H_{T,leptons}$, b-tagging score of the leading jet, b-tagging score of the subleading jet, $p_{T,LeadingJet}$, $M_{T,lep-met}$ and n_{Jets}. The bottom panels display the ratio between data and MC yields. Data events are not shown in bins where $S/B \geq 5\%$.
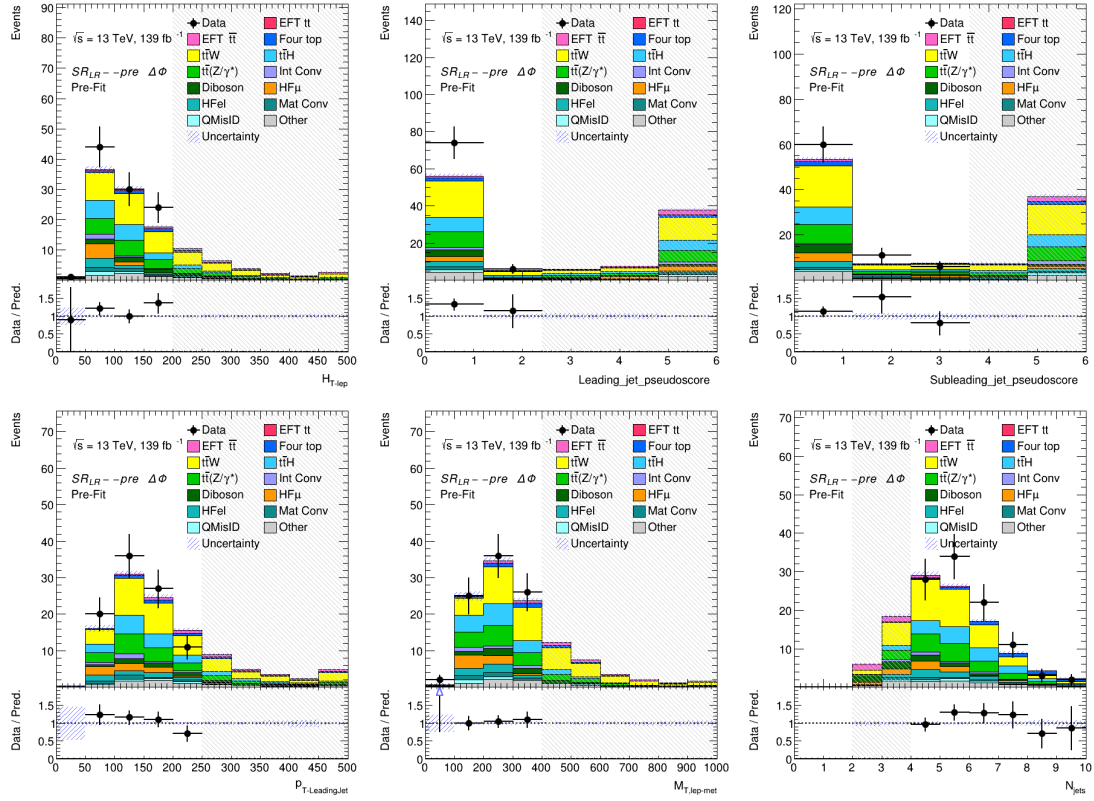
Figure E.19: Kinematic distributions for data and MC events in the $\Delta\Phi \geq 2.5$ region related to the 6 input variables of NN^{SvsB} for events in SR_{LR}^{++}. From top left to bottom right: $H_{T,leptons}$, b-tagging score of the leading jet, b-tagging score of the subleading jet, $p_{T,LeadingJet}$, $M_{T,lep-met}$ and n_{Jets}. The bottom panels display the ratio between data and MC yields. Data events are not shown in bins where $S/B \geq 5\%$.

Appendix F

Correction on jet multiplicity for diboson processes

In order to derive a correction on the jet multiplicity distribution for diboson processes, a dedicated Control Region enriched in diboson events, referred as *VV00* CR, has been defined. The same selection criteria defined for the diboson Control Region described in Section 5.5 are employed, excluding the requirements on the number of jets and b-tagged jets. Only events with no jets b-tagged at the 85% efficiency WP are selected in $VV00$ CR to suppress the $t\bar{t}Z$ contribution, which is not negligible in the high jet multiplicity region, as can be seen from Figure F.1. A summary of the selection requirements employed to define the $VV00$ CR is reported in Table F.1. This region is mutually exclusive with respect to all the other regions employed in the analysis.

	$VV00$ CR
N_ℓ	3
$\ell\ p_T$ [GeV]	>20 (SS pair), >10 (OS)
PLIV WPs (same-sign ℓ pair)	MincMinc (SS pair), LincLinc (OS)
Total charge	± 1
Electron CO candidate	!MatCO and !IntCO
Nbjets	0 b-jet at 85% WP
$|m_{SFOS} - m_Z|$	< 10 GeV

Table F.1: Summary of the event selection applied in the $VV00$ Control Region defined to derive the correction on the jet multiplicity distribution.

The correction on the jet multiplicity distribution is derived by fitting the ratio of data and diboson yields in $VV00$ CR (after subtracting the contribution coming from other backgrounds from collision data). A least chi square fit is performed following a
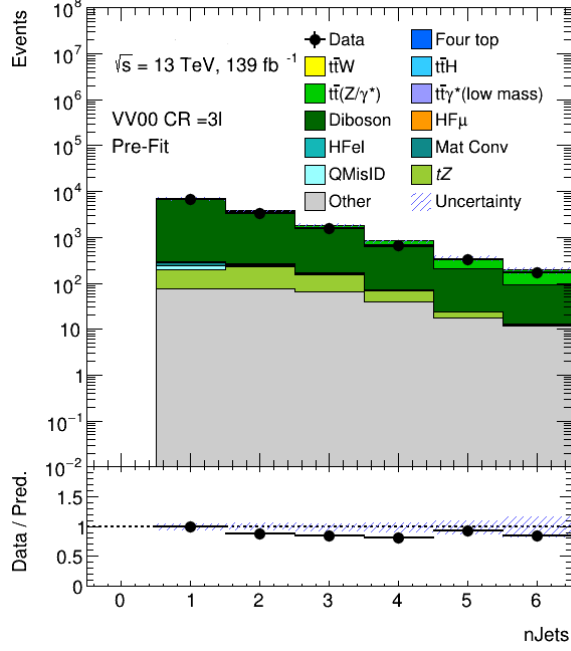
Figure F.1: Jet multiplicity distribution of data and simulated events in the defined $VV00$ CR without the b-jet selection requirement. It can be noticed that the $t\bar{t}Z$ contribution is not negligible at high multiplicity.

polynomial function

$$f(x) = \frac{(b \times 2^c - a)}{(2^c - 1)} + \frac{(b - a) \times 2^c}{(2^c - 1)\, x^c} \tag{F.1}$$

which is a re-parametrization of

$$f(x) = a + \frac{b}{x^c} \tag{F.2}$$

performed to reduce correlations between the a, b parameters. The a, b, c parameters values resulting from the fit are:

- $a = -0.693 \pm 0.012$

- $b = -0.563 \pm 0.014$

- $c = 0.264 \pm 0.018$

The N_{Jets} uncorrected and corrected distribution is shown in Figure F.3. It can be seen that no data/MC mis-modelling is exhibited after applying the derived correction.
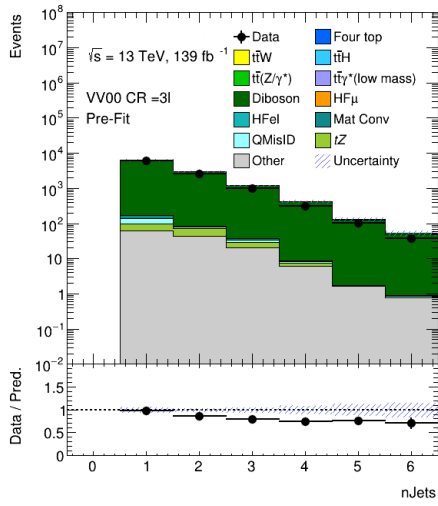
Figure F.2: Distribution of the jet multiplicity in the $VV00$ Control Region before correction.
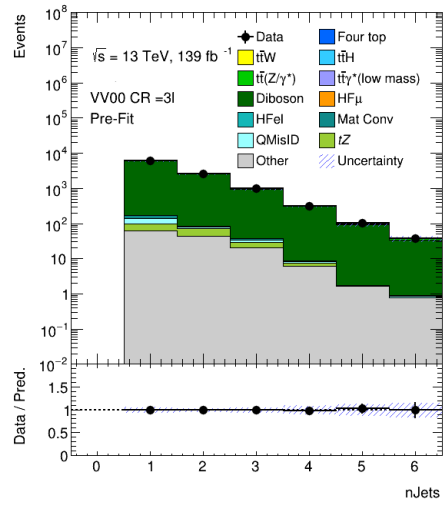
Figure F.3: Distribution of the jet multiplicity in the $VV00$ Control Region after correction.

Bibliography

[1]   S. L. Glashow. "Partial Symmetries of Weak Interactions". In: *Nucl. Phys.* 22 (1961), pp. 579–588. DOI: 10.1016/0029-5582(61)90469-2.

[2]   S. Weinberg. "A Model of Leptons". In: *Phys. Rev. Lett.* 19 (1967), pp. 1264–1266. DOI: 10.1103/PhysRevLett.19.1264.

[3]   A. Salam. "Weak and Electromagnetic Interactions". In: *Conf. Proc.* C680519 (1968), pp. 367–377. DOI: 10.1142/9789812795915_0034.

[4]   CDF Collaboration. "Observation of Top Quark Production in $\bar{p}p$ Collisions with the Collider Detector at Fermilab". In: *Phys. Rev. Lett.* 74 (Apr. 1995), pp. 2626–2631. DOI: 10.1103/PhysRevLett.74.2626.

[5]   D0 Collaboration. "Observation of the Top Quark". In: *Phys. Rev. Lett.* 74 (Apr. 1995), pp. 2632–2637. DOI: 10.1103/PhysRevLett.74.2632.

[6]   R. L. Workman et al. "Review of Particle Physics". In: *PTEP* 2022 (2022). DOI: 10.1093/ptep/ptac097.

[7]   G. Bertone, D. Hooper, and J. Silk. "Particle dark matter: evidence, candidates and constraints". In: *Physics Reports* 405.5 (2005), pp. 279–390. ISSN: 0370-1573. DOI: https://doi.org/10.1016/j.physrep.2004.08.031.

[8]   P. Salucci. "The distribution of dark matter in galaxies". In: *The Astronomy and Astrophysics Review* 27.1 (Feb. 2019). DOI: 10.1007/s00159-018-0113-1.

[9]   C. L. Bennett et al. "First-Year Wilkinson Microwave Anisotropy Probe – Observations: Preliminary Maps and Basic Results". In: *The Astrophysical Journal Supplement Series* 148.1 (Sept. 2003), pp. 1–27. DOI: 10.1086/377253.

[10]   A. D. Sakharov. "Violation of CP Invariance, C asymmetry, and baryon asymmetry of the universe". In: *Pisma Zh. Eksp. Teor. Fiz.* 5 (1967), pp. 32–35. DOI: 10.1070/PU1991v034n05ABEH002497.

[11] R. D. Peccei. "The Strong CP Problem and Axions". In: *Lecture Notes in Physics*. Springer Berlin Heidelberg, 2008, pp. 3–17. DOI: `10.1007/978-3-540-73518-2_1`.

[12] W. A. Bardeen. "On naturalness in the standard model". In: *Ontake Summer Institute on Particle Physics*. Aug. 1995.

[13] R. Aaij et al. "Test of lepton universality in beauty-quark decays". In: (Mar. 2021). arXiv: `2103.11769 [hep-ex]`.

[14] B. Abi et al. "Measurement of the Positive Muon Anomalous Magnetic Moment to 0.46 ppm". In: *Phys. Rev. Lett.* 126.14 (2021), p. 141801. DOI: `10.1103/PhysRevLett.126.141801`. arXiv: `2104.03281 [hep-ex]`.

[15] Muon g-2 Collaboration. "Final report of the E821 muon anomalous magnetic moment measurement at BNL". In: *Phys. Rev. D* 73 (Apr. 2006), p. 072003. DOI: `10.1103/PhysRevD.73.072003`.

[16] H. Georgi. "Effective Field Theory". In: *Annual Review of Nuclear and Particle Science* 43.1 (1993), pp. 209–252. DOI: `10.1146/annurev.ns.43.120193.001233`.

[17] S. Weinberg. "Phenomenological Lagrangians". In: *Physica A* 96.1-2 (1979). Ed. by S. Deser, pp. 327–340. DOI: `10.1016/0378-4371(79)90223-1`.

[18] S. Weinberg. "Effective gauge theories". In: *Physics Letters B* 91.1 (1980), pp. 51–55. ISSN: 0370-2693. DOI: `https://doi.org/10.1016/0370-2693(80)90660-7`.

[19] A. Grozin. *Effective field theories*. 2020. DOI: `10.48550/ARXIV.2001.00434`.

[20] A. Pich. *Effective Field Theory*. 1998. DOI: `10.48550/ARXIV.HEP-PH/9806303`.

[21] A. Pich. *Effective Field Theory with Nambu-Goldstone Modes*. 2018. DOI: `10.48550/ARXIV.1804.05664`.

[22] E. Fermi. "An attempt of a theory of beta radiation. 1." In: *Z. Phys.* 88 (1934), pp. 161–177. DOI: `10.1007/BF01351864`.

[23] A. A. Petrov and A. E. Blechman. *Effective Field Theories*. WSP, 2016. ISBN: 978-981-4434-92-8, 978-981-4434-94-2. DOI: `10.1142/8619`.

[24] W. Buchmuller and D. Wyler. "Effective Lagrangian Analysis of New Interactions and Flavor Conservation". In: *Nucl. Phys. B* 268 (1986), pp. 621–653. DOI: `10.1016/0550-3213(86)90262-2`.

[25] I. Brivio and M. Trott. "The standard model as an effective field theory". In: *Physics Reports* 793 (Feb. 2019), pp. 1–98. DOI: `10.1016/j.physrep.2018.11.002`.

[26] J. Aguilar-Saavedra. "A minimal set of top anomalous couplings". In: *Nuclear Physics B* 812.1 (2009), pp. 181–204. ISSN: 0550-3213. DOI: https://doi.org/10.1016/j.nuclphysb.2008.12.012.

[27] C. Zhang and S. Willenbrock. "Effective-field-theory approach to top-quark production and decay". In: *Phys. Rev. D* 83 (Feb. 2011), p. 034006. DOI: 10.1103/PhysRevD.83.034006.

[28] B. Grzadkowski and M. Iskrzyński and M. Misiak and J. Rosiek. "Dimension-six terms in the Standard Model Lagrangian". In: *Journal of High Energy Physics* 2010.10 (Oct. 2010). DOI: 10.1007/jhep10(2010)085.

[29] S. Fichet, A. Tonero, and P. R. Teles. "Sharpening the shape analysis for higher-dimensional operator searches". In: *Phys. Rev. D* 96 (Aug. 2017), p. 036003. DOI: 10.1103/PhysRevD.96.036003.

[30] J. A. A. Saavedra et al. *Interpreting top-quark LHC measurements in the standard-model effective field theory.* 2018. DOI: 10.48550/ARXIV.1802.07237.

[31] N. Hartland et al. "A Monte Carlo global analysis of the Standard Model Effective Field Theory: the top quark sector". In: *Journal of High Energy Physics* 2019 (Apr. 2019). DOI: 10.1007/JHEP04(2019)100.

[32] A. Buckley et al. "Constraining top quark effective theory in the LHC Run II era". In: *Journal of High Energy Physics* 2016.4 (Apr. 2016), pp. 1–32. DOI: 10.1007/jhep04(2016)015.

[33] ATLAS Collaboration. "Measurement of the polarisation of single top quarks and antiquarks produced in the t-channel at $\sqrt{} = $ 13 TeV and bounds on the tWb dipole operator from the ATLAS experiment". In: *Journal of High Energy Physics* 2022.11 (Nov. 2022). DOI: 10.1007/jhep11(2022)040.

[34] ATLAS Collaboration. "Measurement of the $t\bar{t}Z$ and $t\bar{t}W$ cross sections in proton-proton collisions at $\sqrt{s} = 13$TeV with the ATLAS detector". In: *Phys. Rev. D* 99 (Apr. 2019), p. 072009. DOI: 10.1103/PhysRevD.99.072009. arXiv: 1901.03584 [hep-ex].

[35] ATLAS Collaboration. "A portrait of the Higgs boson by the CMS experiment ten years after the discovery". In: *Nature* 607.7917 (July 2022), pp. 60–68. DOI: 10.1038/s41586-022-04892-x. URL: https://doi.org/10.1038%5C%2Fs41586-022-04892-x.

[36] CMS Collaboration. "Probing effective field theory operators in the associated production of top quarks with a Z boson in multilepton final states at $\sqrt{s} = 13$ TeV". In: *Journal of High Energy Physics* 2021.12 (Dec. 2021). DOI: 10.1007/jhep12(2021)083.

[37] CMS Collaboration. "Measurement of the inclusive and differential $t\bar{t}\gamma$ cross sections in the dilepton channel and effective field theory interpretation in proton–proton collisions at $\sqrt{s} = 13\,$TeV". In: *JHEP* 05 (2022), p. 091. DOI: 10.1007/JHEP05(2022)091. arXiv: 2201.07301 [hep-ex].

[38] CMS Collaboration. "Measurement of top quark pair production in association with a Z boson in proton–proton collisions at $\sqrt{s} = 13\,$TeV". In: *JHEP* 03 (2020), p. 056. DOI: 10.1007/JHEP03(2020)056. arXiv: 1907.11270 [hep-ex].

[39] CMS Collaboration. "Search for new physics in top quark production with additional leptons in proton–proton collisions at $\sqrt{s} = 13\,$TeV using effective field theory". In: *JHEP* 03 (2021), p. 095. DOI: 10.1007/JHEP03(2021)095. arXiv: 2012.04120 [hep-ex].

[40] ATLAS and CMS Collaborations. "Combination of the W boson polarization measurements in top quark decays using ATLAS and CMS data at $\sqrt{s} = 8\,$TeV". In: *JHEP* 08 (2020), p. 051. DOI: 10.1007/JHEP08(2020)051. arXiv: 2005.03799 [hep-ex].

[41] CMS Collaboration. "Search for new physics in top quark production in dilepton final states in proton–proton collisions at $\sqrt{s} = 13\,$TeV". In: *Eur. Phys. J. C* 79 (2019), p. 886. DOI: 10.1140/epjc/s10052-019-7387-y. arXiv: 1903.11144 [hep-ex].

[42] CMS Collaboration. "Measurement of the top quark polarization and $t\bar{t}$ spin correlations using dilepton final states in proton–proton collisions at $\sqrt{s} = 13\,$TeV". In: *Phys. Rev. D* 100 (2019), p. 072002. DOI: 10.1103/PhysRevD.100.072002. arXiv: 1907.03729 [hep-ex].

[43] CMS Collaboration. "Search for the production of four top quarks in the single-lepton and opposite-sign dilepton final states in proton–proton collisions at $\sqrt{s} = 13\,$TeV". In: *JHEP* 11 (2019), p. 082. DOI: 10.1007/JHEP11(2019)082. arXiv: 1906.02805 [hep-ex].

[44] ATLAS Collaboration. "Measurement of the energy asymmetry in $t\bar{t}j$ production at 13 TeV with the ATLAS experiment and interpretation in the SMEFT framework". In: *Eur. Phys. J. C* 82 (2022), p. 374. DOI: 10.1140/epjc/s10052-022-10101-w. arXiv: 2110.05453 [hep-ex].

[45] ATLAS Collaboration. "Search for flavour-changing neutral current top-quark decays $t \rightarrow qZ$ in proton–proton collisions at $\sqrt{s} = 13\,\mathrm{TeV}$ with the ATLAS detector". In: *JHEP* 07 (2018), p. 176. DOI: `10.1007/JHEP07(2018)176`. arXiv: `1803.09923 [hep-ex]`.

[46] ATLAS Collaboration. "Search for flavour-changing neutral currents in processes with one top quark and a photon using $81\,\mathrm{fb^{-1}}$ of pp collisions at $\sqrt{s} = 13\,\mathrm{TeV}$ with the ATLAS experiment". In: *Phys. Lett. B* 800 (2020), p. 135082. DOI: `10.1016/j.physletb.2019.135082`. arXiv: `1908.08461 [hep-ex]`.

[47] ATLAS Collaboration. "Search for flavour-changing neutral-current interactions of a top quark and a gluon in pp collisions at $\sqrt{s} = 13\,\mathrm{TeV}$ with the ATLAS detector". In: *Eur. Phys. J. C* 82 (2021), p. 334. DOI: `10.1140/epjc/s10052-022-10182-7`. arXiv: `2112.01302 [hep-ex]`.

[48] S. L. Glashow, J. Iliopoulos, and L. Maiani. "Weak Interactions with Lepton-Hadron Symmetry". In: *Phys. Rev. D* 2 (Oct. 1970), pp. 1285–1292. DOI: `10.1103/PhysRevD.2.1285`.

[49] G. Durieux, F. Maltoni, and C. Zhang. "Global approach to top-quark flavor-changing interactions". In: *Physical Review D* 91.7 (Apr. 2015), p. 074017. DOI: `10.1103/physrevd.91.074017`.

[50] I. Brivio et al. "O new physics, where art thou? A global search in the top sector". In: *Journal of High Energy Physics* 2020.2 (Feb. 2020). DOI: `10.1007/jhep02(2020)131`.

[51] J. J. Ethier et al. *Combined SMEFT interpretation of Higgs, diboson, and top quark data from the LHC*. 2021. arXiv: `2105.00006 [hep-ph]`.

[52] V. Hirschi and O. Mattelaer. *Automated event generation for loop-induced processes*. 2015. DOI: `10.48550/ARXIV.1507.00020`. URL: `https://arxiv.org/abs/1507.00020`.

[53] G. Durieux, J.-M. Gérard, F. Maltoni, and C. Smith. "Three-generation baryon and lepton number violation at the LHC". In: *Physics Letters B* 721.1-3 (Apr. 2013), pp. 82–85. DOI: `10.1016/j.physletb.2013.02.052`.

[54] C. Degrande et al. "An effective approach to same sign top pair production at the LHC and the forward–backward asymmetry at the Tevatron". In: *Physics Letters B* 703.3 (2011), pp. 306–309. ISSN: 0370-2693. DOI: `https://doi.org/10.1016/j.physletb.2011.08.003`.

187

[55] M. Bona et al. "Model-independent constraints on $\Delta F = 2$ operators and the scale of new physics". In: *Journal of High Energy Physics* 2008.03 (Mar. 2008), pp. 049–049. DOI: 10.1088/1126-6708/2008/03/049.

[56] S. Cho et al. "Top FCNC induced by a Z' boson". In: *Phys. Rev. D* 101 (Mar. 2020), p. 055015. DOI: 10.1103/PhysRevD.101.055015.

[57] CMS Collaboration. "Search for same-sign top-quark pair production at $\sqrt{s} = 7\,\text{TeV}$ and limits on flavour changing neutral currents in the top sector". In: *JHEP* 08 (2011), p. 005. DOI: 10.1007/JHEP08(2011)005. arXiv: 1106.2142 [hep-ex].

[58] J. Ebadi, F. Elahi, M. Khatiri, and M. Mohammadi Najafabadi. "Same-sign top pair plus W production in flavor changing vector and scalar models". In: *Phys. Rev. D* 98 (Oct. 2018), p. 075012. DOI: 10.1103/PhysRevD.98.075012.

[59] O. M. Ozsimsek, V. Ari, and O. Cakir. *Studying Same-Sign Top Pair Production in Flavor Changing Scalar Models at the HL-LHC*. 2021. DOI: 10.48550/ARXIV.2105.03982.

[60] W.-S. Hou and M. Kikuchi. "Approximate alignment in two-Higgs-doublet model with extra Yukawa couplings". In: *EPL (Europhysics Letters)* 123.1 (Aug. 2018), p. 11001. DOI: 10.1209/0295-5075/123/11001. arXiv: 1706.07694 [hep-ph]. URL: https://doi.org/10.1209%5C%2F0295-5075%5C%2F123%5C%2F11001.

[61] S. Kraml and A. R. Raklev. "Same-sign top quarks as signature of light stops". In: *AIP Conference Proceedings* 903.1 (2007), pp. 225–228. DOI: 10.1063/1.2735166. eprint: https://aip.scitation.org/doi/pdf/10.1063/1.2735166.

[62] F. Larios and F. Peñuñuri. "Flavour changing neutral current production of same sign top quark pairs at the LHC". In: *Journal of Physics G: Nuclear and Particle Physics* 30.7 (May 2004), p. 895. DOI: 10.1088/0954-3899/30/7/006.

[63] CMS Collaboration. "Search for physics beyond the standard model in events with jets and two same-sign or at least three charged leptons in proton–proton collisions at $\sqrt{s} = 13\,\text{TeV}$". In: *Eur. Phys. J. C* 80 (2020), p. 752. DOI: 10.1140/epjc/s10052-020-8168-3. arXiv: 2001.10086 [hep-ex].

[64] ATLAS Collaboration. "Search for new phenomena in events with same-charge leptons and b-jets in pp collisions at $\sqrt{s} = 13\,\text{TeV}$ with the ATLAS detector". In: *JHEP* 12 (2018), p. 039. DOI: 10.1007/JHEP12(2018)039. arXiv: 1807.11883 [hep-ex].

[65] CMS Collaboration. "Search for physics beyond the standard model in events with two leptons of same sign, missing transverse momentum, and jets in proton–proton collisions at $\sqrt{s} = 13\,\text{TeV}$". In: *Eur. Phys. J. C* 77 (2017), p. 578. DOI: 10.1140/epjc/s10052-017-5079-z. arXiv: 1704.07323 [hep-ex].

[66] ATLAS Collaboration. "Search for same-sign top-quark production and fourth-generation down-type quarks in *pp* collisions at $\sqrt{s} = 7\,\text{TeV}$ with the ATLAS detector". In: *JHEP* 04 (2012), p. 069. DOI: 10.1007/JHEP04(2012)069. arXiv: 1202.5520 [hep-ex].

[67] ATLAS Collaboration. "Analysis of events with *b*-jets and a pair of leptons of the same charge in *pp* collisions at $\sqrt{s} = 8\,\text{TeV}$ with the ATLAS detector". In: *JHEP* 10 (2015), p. 150. DOI: 10.1007/JHEP10(2015)150. arXiv: 1504.04605 [hep-ex].

[68] E. Yazgan. *Flavor changing neutral currents in top quark production and decay.* 2013. DOI: 10.48550/ARXIV.1312.5435.

[69] L. Evans and P. Bryant. "LHC Machine". In: *JINST* 3 (2008), S08001. DOI: 10.1088/1748-0221/3/08/S08001.

[70] J. T. Boyd. *LHC Run-2 and Future Prospects.* 2020. DOI: 10.48550/ARXIV.2001.04370.

[71] ATLAS Collaboration. "The ATLAS Experiment at the CERN Large Hadron Collider". In: *JINST* 3 (2008), S08003. DOI: 10.1088/1748-0221/3/08/S08003.

[72] B. Abbott et al. "Production and integration of the ATLAS Insertable B-Layer". In: *JINST* 13 (2018), T05008. DOI: 10.1088/1748-0221/13/05/T05008. arXiv: 1803.00844 [physics.ins-det].

[73] ATLAS Collaboration. *ATLAS Insertable B-Layer: Technical Design Report.* ATLAS-TDR-19; CERN-LHCC-2010-013. 2010. URL: https://cds.cern.ch/record/1291633.

[74] ATLAS Collaboration. "Performance of the ATLAS trigger system in 2015". In: *Eur. Phys. J. C* 77 (2017), p. 317. DOI: 10.1140/epjc/s10052-017-4852-3. arXiv: 1611.09661 [hep-ex].

[75] T. Sjöstrand, S. Mrenna, and P. Skands. "A brief introduction to PYTHIA 8.1". In: *Comput. Phys. Commun.* 178 (2008), p. 852. DOI: 10.1016/j.cpc.2008.01.036. arXiv: 0710.3820 [hep-ph].

[76] *The Pythia 8 A3 tune description of ATLAS minimum bias and inelastic measurements incorporating the Donnachie-Landshoff diffractive model.* Tech. rep. Geneva: CERN, Aug. 2016. URL: https://cds.cern.ch/record/2206965.

[77] ATLAS Collaboration. "The ATLAS Simulation Infrastructure". In: *Eur. Phys. J. C* 70 (2010), p. 823. DOI: 10.1140/epjc/s10052-010-1429-9. arXiv: 1005.4568 [physics.ins-det].

[78] S. Agostinelli et al. "GEANT4: A Simulation toolkit". In: *Nucl. Instrum. Meth.* A506 (2003), pp. 250–303. DOI: 10.1016/S0168-9002(03)01368-8.

[79] J. Alwall et al. "The automated computation of tree-level and next-to-leading order differential cross sections, and their matching to parton shower simulations". In: *JHEP* 07 (2014), p. 079. DOI: 10.1007/JHEP07(2014)079. arXiv: 1405.0301 [hep-ph].

[80] I. Brivio, Y. Jiang, and M. Trott. "The SMEFTsim package, theory and tools". In: *Journal of High Energy Physics* 2017.12 (Dec. 2017). DOI: 10.1007/jhep12(2017)070. URL: https://doi.org/10.1007%5C%2Fjhep12%5C%282017%5C%29070.

[81] I. Brivio. "SMEFTsim 3.0 — a practical guide". In: *Journal of High Energy Physics* 2021.4 (Apr. 2021). DOI: 10.1007/jhep04(2021)073.

[82] R. D. Ball et al. "Parton distributions for the LHC Run II". In: *JHEP* 04 (2015), p. 040. DOI: 10.1007/JHEP04(2015)040. arXiv: 1410.8849 [hep-ph].

[83] ATLAS Collaboration. *ATLAS Pythia 8 tunes to 7 TeV data.* ATL-PHYS-PUB-2014-021. 2014. URL: https://cds.cern.ch/record/1966419.

[84] D. J. Lange. "The EvtGen particle decay simulation package". In: *Nucl. Instrum. Meth. Phys. Res. A* 462 (2001), p. 152. DOI: 10.1016/S0168-9002(01)00089-4.

[85] O. Mattelaer. "On the maximal use of Monte Carlo samples: re-weighting events at NLO accuracy". In: *The European Physical Journal C* 76.12 (Dec. 2016). DOI: 10.1140/epjc/s10052-016-4533-7.

[86] P. Artoisenet, V. Lemaitre, F. Maltoni, and O. Mattelaer. "Automation of the matrix element reweighting method". In: *Journal of High Energy Physics* 2010.12 (Dec. 2010). DOI: 10.1007/jhep12(2010)068.

[87] ATLAS Collaboration. *Analysis of $t\bar{t}H$ and $t\bar{t}W$ production in multilepton final states with the ATLAS detector.* ATLAS-CONF-2019-045. 2019. URL: https://cds.cern.ch/record/2693930.

[88] ATLAS Collaboration. "Measurement of the $t\bar{t}Z$ and $t\bar{t}W$ cross sections in proton–proton collisions at $\sqrt{s} = 13\,\text{TeV}$ with the ATLAS detector". In: *Phys. Rev. D* 99 (2019), p. 072009. DOI: `10.1103/PhysRevD.99.072009`. arXiv: `1901.03584` `[hep-ex]`.

[89] A. Collaboration. *Inclusive and differential cross-sections for dilepton $t\bar{t}$ production measured in $\sqrt{s} = 13$ TeV pp collisions with the ATLAS detector*. 2023. arXiv: `2303.15340` `[hep-ex]`.

[90] A. Collaboration. *Measurement of single top-quark production in the s-channel in proton−proton collisions at $\sqrt{s} = 13$ TeV with the ATLAS detector*. 2022. arXiv: `2209.08990` `[hep-ex]`.

[91] A. Collaboration. "Measurement of the inclusive cross-sections of single top-quark and top-antiquark t-channel production in pp collisions at s = 13 TeV with the ATLAS detector". In: *Journal of High Energy Physics* 2017.4 (Apr. 2017). DOI: `10.1007/jhep04(2017)086`.

[92] A. Collaboration. "Measurement of the cross-section for producing a W boson in association with a single top quark in pp collisions at s = 13 TeV with ATLAS". In: *Journal of High Energy Physics* 2018.1 (Jan. 2018). DOI: `10.1007/jhep01(2018)063`.

[93] A. Collaboration. "Measurement of W± and Z-boson production cross sections in pp collisions at $\sqrt{s} = 13$ TeV with the ATLAS detector". In: *Physics Letters B* 759 (Aug. 2016), pp. 601–621. DOI: `10.1016/j.physletb.2016.06.023`.

[94] R. Frederix and I. Tsinikos. "On improving NLO merging for $t\bar{t}W$ production". In: *Journal of High Energy Physics* 2021.11 (Nov. 2021). DOI: `10.1007/jhep11(2021)029`.

[95] A. Collaboration. "Measurement of the t $\bar{t}t\bar{t}$ production cross section in pp collisions at $\sqrt{s}$= 13 TeV with the ATLAS detector". In: *Journal of High Energy Physics* 2021 (2021). DOI: `https://doi.org/10.1007/JHEP11(2021)118`.

[96] CERN. *CERN Yellow Reports: Monographs, Vol 2 (2017): Handbook of LHC Higgs cross sections: 4. Deciphering the nature of the Higgs sector*. en. 2017. DOI: `10.23731/CYRM-2017-002`. URL: `https://e-publishing.cern.ch/index.php/CYRM/issue/view/32`.

[97] ATLAS Collaboration. "Muon reconstruction and identification efficiency in ATLAS using the full Run 2 *pp* collision data set at $\sqrt{s} = 13\,\text{TeV}$". In: *Eur. Phys. J. C* 81 (2021), p. 578. DOI: `10.1140/epjc/s10052-021-09233-2`. arXiv: `2012.00578` `[hep-ex]`.

[98] ATLAS Collaboration. "Electron and photon performance measurements with the ATLAS detector using the 2015–2017 LHC proton–proton collision data". In: *JINST* 14 (2019), P12006. DOI: 10.1088/1748-0221/14/12/P12006. arXiv: 1908.00005 [hep-ex].

[99] M. Cacciari, G. P. Salam, and G. Soyez. "The anti-k_t jet clustering algorithm". In: *JHEP* 04 (2008), p. 063. DOI: 10.1088/1126-6708/2008/04/063. arXiv: 0802.1189 [hep-ph].

[100] M. Cacciari and G. P. Salam. "Dispelling the N^3 myth for the k_t jet-finder". In: *Phys. Lett. B* 641 (2006), pp. 57–61. DOI: 10.1016/j.physletb.2006.08.037. arXiv: hep-ph/0512210.

[101] *JetVertexTagger for Run-2 in reco and analysis.* https://twiki.cern.ch/twiki/bin/view/AtlasProtected/JetVertexTaggerTool. Accessed: 2021-04-13.

[102] ATLAS Collaboration. "ATLAS b-jet identification performance and efficiency measurement with $t\bar{t}$ events in pp collisions at $\sqrt{s}$=13 TeV". In: *The European Physical Journal C* 79.11 (Nov. 2019). ISSN: 1434-6052. DOI: 10.1140/epjc/s10052-019-7450-8.

[103] ATLAS Collaboration. "Performance of missing transverse momentum reconstruction in proton–proton collisions at $\sqrt{s} = 7$ TeV with ATLAS". In: *Eur. Phys. J. C* 72 (2012), p. 1844. DOI: 10.1140/epjc/s10052-011-1844-6. arXiv: 1108.5602 [hep-ex].

[104] ATLAS Collaboration. *Development of ATLAS Primary Vertex Reconstruction for LHC Run 3.* ATL-PHYS-PUB-2019-015. 2019. URL: https://cds.cern.ch/record/2670380.

[105] F. Chollet et al. *Keras.* 2015. URL: https://github.com/fchollet/keras.

[106] *TensorFlow: Large-Scale Machine Learning on Heterogeneous Systems.* Software available from tensorflow.org. 2015. URL: https://www.tensorflow.org/.

[107] D. Kingma and J. Ba. *Adam: A Method for Stochastic Optimization.* 2017. arXiv: 1412.6980.

[108] F. Pedregosa et al. "Scikit-learn: Machine Learning in Python". In: *Journal of Machine Learning Research* 12 (2011), p. 2825.

[109] ATLAS Collaboration. *Studies of the muon momentum calibration and performance of the ATLAS detector with pp collisions at $\sqrt{s}$=13 TeV.* 2022. DOI: 10.48550/ARXIV.2212.07338.

[110] ATLAS Collaboration. "Performance of electron and photon triggers in ATLAS during LHC Run 2". In: *Eur. Phys. J. C* 80 (2020), p. 47. DOI: `10.1140/epjc/s10052-019-7500-2`. arXiv: `1909.00761` `[hep-ex]`.

[111] ATLAS Collaboration. "Performance of the ATLAS muon triggers in Run 2". In: *JINST* 15 (2020), P09015. DOI: `10.1088/1748-0221/15/09/p09015`. arXiv: `2004.13447` `[hep-ex]`.

[112] ATLAS Collaboration. "Jet energy scale and resolution measured in proton–proton collisions at $\sqrt{s} = 13$ TeV with the ATLAS detector". In: *Eur. Phys. J. C* 81 (2020), p. 689. DOI: `10.1140/epjc/s10052-021-09402-3`. arXiv: `2007.02645` `[hep-ex]`.

[113] ATLAS Collaboration. *Luminosity determination in pp collisions at $\sqrt{s} = 13$ TeV using the ATLAS detector at the LHC*. ATLAS-CONF-2019-021. 2019. URL: `https://cds.cern.ch/record/2677054`.

[114] *TRexFitter framework documentation*. URL: `https://trexfitter-docs.web.cern.ch/trexfitter-docs/`.

[115] K. Cranmer et al. *HistFactory: A tool for creating statistical models for use with RooFit and RooStats*. Tech. rep. New York: New York U., Jan. 2012. URL: `https://cds.cern.ch/record/1456844`.

[116] A. L. Read. "Presentation of search results: The CL(s) technique". In: *J. Phys. G* 28 (2002), p. 2693. DOI: `10.1088/0954-3899/28/10/313`.

[117] G. Cowan, K. Cranmer, E. Gross, and O. Vitells. "Asymptotic formulae for likelihood-based tests of new physics". In: *Eur. Phys. J. C* 71 (2011), p. 1554. DOI: `10.1140/epjc/s10052-011-1554-0`. arXiv: `1007.1727` `[physics.data-an]`.

[118] W. Verkerke and D. P. Kirkby. "The RooFit toolkit for data modeling". In: *eConf* C0303241 (2003), MOLT007. arXiv: `physics/0306116` `[physics.data-an]`.

[119] W. Verkerke and D. Kirkby. *RooFit Users Manual*. URL: `http://roofit.sourceforge.net`.

[120] ATLAS Collaboration. *Search for heavy Higgs bosons from a g2HDM in multilepton plus b-jets final states in pp collisions at 13 TeV with the ATLAS detector*. ATLAS-CONF-2022-039. 2022. URL: `https://cds.cern.ch/record/2815674`.

[121] G. Branco et al. "Theory and phenomenology of two-Higgs-doublet models". In: *Physics Reports* 516.1-2 (July 2012), pp. 1–102. DOI: `10.1016/j.physrep.2012.02.002`. URL: `https://doi.org/10.1016%5C%2Fj.physrep.2012.02.002`.

[122]   J. F. Gunion and H. E. Haber. "CP-conserving two-Higgs-doublet model: The approach to the decoupling limit". In: *Physical Review D* 67.7 (Apr. 2003). DOI: 10.1103/physrevd.67.075019. URL: https://doi.org/10.1103%5C%2Fphysrevd.67.075019.

[123]   ATLAS Collaboration. "Measurement of the muon reconstruction performance of the ATLAS detector using 2011 and 2012 LHC proton–proton collision data". In: *Eur. Phys. J. C* 74 (2014), p. 3130. DOI: 10.1140/epjc/s10052-014-3130-x. arXiv: 1407.3935 [hep-ex].

[124]   ATLAS Collaboration. "Muon reconstruction performance of the ATLAS detector in proton–proton collision data at $\sqrt{s} = 13$ TeV". In: *Eur. Phys. J. C* 76.5 (2016), p. 292. DOI: 10.1140/epjc/s10052-016-4120-y. arXiv: 1603.05598 [hep-ex].

[125]   E. Bothmann et al. "Event generation with Sherpa 2.2". In: *SciPost Phys.* 7.3 (2019), p. 034. DOI: 10.21468/SciPostPhys.7.3.034. arXiv: 1905.09127 [hep-ph].

[126]   S. Schumann and F. Krauss. "A Parton shower algorithm based on Catani-Seymour dipole factorisation". In: *JHEP* 03 (2008), p. 038. DOI: 10.1088/1126-6708/2008/03/038. arXiv: 0709.1027 [hep-ph].

[127]   S. Höche, F. Krauss, M. Schönherr, and F. Siegert. "A critical appraisal of NLO+PS matching methods". In: *JHEP* 09 (2012), p. 049. DOI: 10.1007/JHEP09(2012)049. arXiv: 1111.1220 [hep-ph].

[128]   S. Hoeche, F. Krauss, M. Schonherr, and F. Siegert. "QCD matrix elements + parton showers: The NLO case". In: *JHEP* 04 (2013), p. 027. DOI: 10.1007/JHEP04(2013)027. arXiv: 1207.5030 [hep-ph].

[129]   S. Catani, F. Krauss, R. Kuhn, and B. R. Webber. "QCD Matrix Elements + Parton Showers". In: *JHEP* 11 (2001), p. 063. DOI: 10.1088/1126-6708/2001/11/063. arXiv: hep-ph/0109231.

[130]   S. Höche, F. Krauss, S. Schumann, and F. Siegert. "QCD matrix elements and truncated showers". In: *JHEP* 05 (2009), p. 053. DOI: 10.1088/1126-6708/2009/05/053. arXiv: 0903.1219 [hep-ph].

[131]   F. Cascioli, P. Maierhofer, and S. Pozzorini. "Scattering Amplitudes with Open Loops". In: *Phys. Rev. Lett.* 108 (2012), p. 111601. DOI: 10.1103/PhysRevLett.108.111601. arXiv: 1111.5206 [hep-ph].

[132] F. Buccioni et al. "OpenLoops 2". In: *The European Physical Journal C* 79.10 (Oct. 2019). DOI: 10.1140/epjc/s10052-019-7306-2. URL: https://doi.org/10.1140%5C%2Fepjc%5C%2Fs10052-019-7306-2.

[133] P. Artoisenet, R. Frederix, O. Mattelaer, and R. Rietkerk. "Automatic spin-entangled decays of heavy resonances in Monte Carlo simulations". In: *Journal of High Energy Physics* 2013.3 (Mar. 2013), p. 015. DOI: 10.1007/jhep03(2013)015. arXiv: 1212.3460 [hep-ph].

[134] S. Alioli, P. Nason, C. Oleari, and E. Re. "A general framework for implementing NLO calculations in shower Monte Carlo programs: the POWHEG BOX". In: *JHEP* 06 (2010), p. 043. DOI: 10.1007/JHEP06(2010)043. arXiv: 1002.2581 [hep-ph].

[135] S. Frixione, P. Nason, and C. Oleari. "Matching NLO QCD computations with Parton Shower simulations: the POWHEG method". In: *JHEP* 11 (2007), p. 070. DOI: 10.1088/1126-6708/2007/11/070. arXiv: 0709.2092 [hep-ph].

[136] P. Nason. "A New method for combining NLO QCD with shower Monte Carlo algorithms". In: *JHEP* 11 (2004), p. 040. DOI: 10.1088/1126-6708/2004/11/040. arXiv: hep-ph/0409146 [hep-ph].

[137] A. Collaboration. *Modelling of the $t\bar{t}H$ and $t\bar{t}V$ ($V = W, Z$) processes for $\sqrt{s}$=13 TeV ATLAS analyses*. ATL-PHYS-PUB-2016-005. 2016. URL: https://cds.cern.ch/record/2120826.

[138] J. Bellm et al. "Herwig 7.0/Herwig++ 3.0 release note". In: *Eur. Phys. J. C* 76 (2016), p. 196. DOI: 10.1140/epjc/s10052-016-4018-8. arXiv: 1512.01178 [hep-ph].

[139] P. Golonka and Z. Was. "PHOTOS Monte Carlo: A Precision tool for QED corrections in Z and W decays". In: *Eur. Phys. J. C45* (2006), pp. 97–107. DOI: 10.1140/epjc/s2005-02396-4. arXiv: hep-ph/0506026 [hep-ph].